Instituto Alberto Luiz Coimbra de
Pós-Graduação e Pesquisa de Engenharia
COPPE
UFRJ

IDENTIFICATION OF ANNULAR GAS SEAL COEFFICIENTS, ROTOR-STATOR CONTACT, AND NONLINEAR ANALYSIS OF A ROTORDYNAMIC SYSTEM

David Julián González Maldonado

Tese de Doutorado apresentada ao Programa de Pós-graduação em Engenharia Mecânica, COPPE, da Universidade Federal do Rio de Janeiro, como parte dos requisitos necessários à obtenção do título de Doutor em Engenharia Mecânica.

Orientador: Thiago Gamboa Ritto

Rio de Janeiro
Novembro de 2019

IDENTIFICATION OF ANNULAR GAS SEAL COEFFICIENTS, ROTOR-STATOR CONTACT, AND NONLINEAR ANALYSIS OF A ROTORDYNAMIC SYSTEM

David Julián González Maldonado

TESE SUBMETIDA AO CORPO DOCENTE DO INSTITUTO ALBERTO LUIZ COIMBRA DE PÓS-GRADUAÇÃO E PESQUISA DE ENGENHARIA (COPPE) DA UNIVERSIDADE FEDERAL DO RIO DE JANEIRO COMO PARTE DOS REQUISITOS NECESSÁRIOS PARA A OBTENÇÃO DO GRAU DE DOUTOR EM CIÊNCIAS EM ENGENHARIA MECÂNICA.

Examinada por:

Prof. Thiago Gamboa Ritto, D.Sc.

Prof. Fernando Augusto de Noronha Castro Pinto, Dr.Ing.

Prof. Fernando Alves Rochinha, D.Sc.

Prof. Americo Barbosa da Cunha Junior, D.Sc.

Prof. Katia Lucchesi Cavalca Dedini, D.Sc.

RIO DE JANEIRO, RJ – BRASIL
NOVEMBRO DE 2019

Maldonado, David Julián González

Identification of annular gas seal coefficients, rotor-stator contact, and nonlinear analysis of a rotordynamic system/David Julián González Maldonado. – Rio de Janeiro: UFRJ/COPPE, 2019.

XXI, 159 p.: il.; 29, 7cm.

Orientador: Thiago Gamboa Ritto

Tese (doutorado) – UFRJ/COPPE/Programa de Engenharia Mecânica, 2019.

Referências Bibliográficas: p. 127 – 137.

1. Rotordynamic. 2. Annular gas seals. 3. Rotor-seal rub. 4. Normal forms. I. Ritto, Thiago Gamboa. II. Universidade Federal do Rio de Janeiro, COPPE, Programa de Engenharia Mecânica. III. Título.

This thesis is dedicated to the most important people in my life. First and foremost, to my parents Pedro Antonio Gonzalez and Gloria Amparo Maldonado Giraldo. To my brothers Monica Gonzalez Maldonado and Fabian Andres Gonzalez Maldonado. To my wife Jennifer Garzon Espinosa. And to my daughter Valeria Gonzalez Garzon. I love you all.

Acknowledgments

I would first like to thank my PARENTS for the unconditional support and endless encouragement in my entire life, specially during the development of this thesis. YOU have been indispensable for me.

Secondly, I would like to thank two professors from the department: my advisor Prof. Thiago Gamboa Ritto and Prof. Fernando Augusto de Noronha Castro Pinto for the motivation and strong support along my studies.

I would like also to thank the Dynamic and Vibration Group, from the Techniche Universität Darmstadt, for the academic support, specially Prof. Peter Hagedorn, Artem Karev, Eoin Clerkin, Dominic Jekel and Alfredo Ramirez.

I would like to acknowledge my colleagues from the Acoustics and Vibration Laboratory, specially Diego Alejandro Godoy Diaz, Vinicius Ferreira Côrtes, Tiago Paulino dos Santos and Pedro Noronha.

People from CENPES/Petrobras: Leticia Tapajoz, Raphael Timbó and all the persons involved with the project.

To CAPES, CNPq and CENPES for the financial support.

To all the persons involved in the development of this thesis.

Resumo da Tese apresentada à COPPE/UFRJ como parte dos requisitos necessários para a obtenção do grau de Doutor em Ciências (D.Sc.)

IDENTIFICAÇÃO DE COEFICIENTES DE SELOS DE GÁS ANULARES, CONTATO ROTOR-ESTATOR, E ANÁLISE NÃO-LINEAR DE UM SISTEMA ROTODINÂMICO

David Julián González Maldonado

Novembro/2019

Orientador: Thiago Gamboa Ritto

Programa: Engenharia Mecânica

Nesta tese são realizadas investigações teóricas e experimentais de uma bancada usada para a identificação de coeficientes de gás anulares. O trabalho é dividido em três partes: (i) a identificação dos coeficientes de um selo anular; (ii) a simulação do movimento de um modelo de contato rotor-estator; (iii) a análise de um sistema rotodinâmico com mancais e eixo anisotrópicos, e um selo com rigidez e amortecimento cúbicos. Na primeira parte, os coeficientes são calculados excitando o rotor com atuadores magnéticos e medindo o deslocamento rotor-estator com sensores de proximidade. A Rigidez Dinâmica Complexa (RDC) é obtida como a função de transferência entre a força magnética e o deslocamento do rotor. Os coeficientes são diretamente obtidos da parte real e imaginária da RDC. Para o contato rotor-estator, modelos simplificados para o rotor e estator são usados. O contato é modelado como forças normais e tangenciais com atrito de Coulomb. Três simulações foram realizadas e diferentes formas de movimento foram observadas: direta, retrógrada, subsíncrona, supersíncrona e caótica. Os tipos de vibração são analisados usando gráficos de órbitas, mapas de Poincaré, espectros de potência e espectrogramas. A última parte da tese considera um rotor anisotrópico com mancais anisotrópicos e um selo anular com amortecimento e rigidez cúbica. Primeiro, o sistema é analisado mediante a teoria de Floquet e mostra o comportamento da combinação de ressonâncias com grau de anisotropia dos mancais e eixo. Depois, os pontos fixos do sistema são calculados usando um método semi-analítico conhecido como método das formas normais. Os resultados são comparados com uma integração numérica simples das equações.

Abstract of Thesis presented to COPPE/UFRJ as a partial fulfillment of the requirements for the degree of Doctor of Science (D.Sc.)

IDENTIFICATION OF ANNULAR GAS SEAL COEFFICIENTS, ROTOR-STATOR CONTACT, AND NONLINEAR ANALYSIS OF A ROTORDYNAMIC SYSTEM

David Julián González Maldonado

November/2019

Advisor: Thiago Gamboa Ritto

Department: Mechanical Engineering

This thesis deals with theoretical and experimental investigations of a test rig used for identification of annular gas seal coefficients. The work is divided in three parts: (i) the identification of coefficients from an annular seal; (ii) the simulation of the motion from a rotor-stator contact model; (iii) the analysis of rotordynamic system with anisotropic bearings and shaft, and a seal with cubic stiffness and damping. In the first part, the coefficients are computed by exciting the rotor with magnetic actuators and measuring the rotor-stator displacement with proximity sensors. The Complex Dynamic Stiffness (CDS) matrix is obtained as the transfer function between forces and displacements. The coefficients are obtained from the real and imaginary parts of the CDS matrix. For the rotor-stator contact, simplified models of the rotor and stator are used. The contact is modeled as tangential and normal forces with Coulomb friction. Three simulations are performed and different motion patterns are observed: forward, backward, subsynchronous, supersynchronous and chaotic vibration. The types of vibration are analyzed by orbits plots, Poincaré maps, full spectra and full spectrograms. The last part of thesis considers a simplified anisotropic rotor with anisotropic bearings and an annular seal with cubic damping and stiffness coefficients. First, the system is analyzed by the Floquet theory, showing the behavior of the combination resonances with the degree of anisotropy from the bearings and rotor. Then, the fixed points of the system are computed by a semi-analytical method known as the Normal Forms method. The results are compared with a simple numerical integration of the equations.

Contents

List of Figures

List of Tables

List of Symbols

Electromagnetic model symbols

A_g	Gap area
$\mathbf{B} = [B_1, \ldots, B_8]^T$	Magnetic flux density
$\mathbf{C}$	Coil selection matrix
$\mathbf{f} = [f_x, f_y]^T$	Electromagnetic forces of the actuator
g_i,g_0	Air gap of the i-th pole, air gap of concentric rotor-stator
$\mathbf{H}$	Magnetic field
$\mathbf{I} = [i_1, \ldots, i_8]^T$	Coil currents
$\hat{\mathbf{I}} = [i_x, i_y, i_0]^T$	Perturbation currents and base current
$\mathbf{J}$	Current density
μ	Permeability
$\mathbf{N}$	Linkage matrix
N	Number of turns of each coil
$\mathbf{R}$	Reluctance matrix

Finite element model symbols

A_e	Cross section area
$\mathbf{C}_e, \mathbf{C}$	Local, global damping matrices
E_e	Young's modulus
$\boldsymbol{\eta}$	Modal state vector
$\mathbf{G}_e, \mathbf{G}$	Local, global gyroscopic matrices
G_e	Shear modulus
I_e	Second moment of area
$\mathbf{K}_e, \mathbf{K}$	Local, global stiffness matrices
κ_e	Dimensionless shear constant
L_e	Lagrangian
l_e	Length of element
$\mathbf{\Lambda}$	Eigenvalues matrix
$\mathbf{M}_e, \mathbf{M}$	Local, global mass matrices
$\mathbf{N}_e$	Shape function matrix

$N_{e1}, N_{e2}, N_{e3}, N_{e4}$	Shape functions
$\mathbf{\Phi}$	Modal matrix
$\boldsymbol{\psi}_e(\xi, t) = [\alpha_e, \beta_e]^T$	Shear angles vector
ν_e	Poisson's ratio
Ω	Rotor speed
T_{Ge}	Kinetic energy due to gyroscopic effects
T_{Le}	Kinetic energy due to bending
$\mathbf{u}_e(\xi, t) = [u_{xe}, u_{ye}]^T$	Displacement vector inside the element e
$\mathbf{u}_{ek}(t) = [u_{xe1}, \theta_{xe1}, u_{ye1},$ $\phi_{e1}, u_{xe2}, \theta_{e2}, u_{ye2}, \phi_{e2}]^T$	Generalized nodal displacement vector
$u_{xe1}, u_{ye1}, u_{xe2}, u_{ye2}$	Nodal linear displacements along the x and y directions
$\theta_{xe1}, \phi_{e1}, \theta_{e2}, \phi_{e2}$	Nodal angular displacements along the x and y directions
u_{xe}, u_{ye}	Displacement along the x and y direction
U_e	Strain energy
$\mathbf{\Theta}_e(\xi, t) = [\theta_e, \phi_e]^T$	Bending angles vector
ζ_i, ω_i	Damping factor and frequency of the i-th mode

Identification methodology symbols

$\mathbf{F}_a$	Actuators' force matrix
$\mathbf{f}_a$	Actuators' force vector
$\mathbf{f}_{a1}, \mathbf{f}_{a2}$	Actuators' force vectors
$\mathbf{f}_{s,ij}$	Excitation along the j-direction and measured along the i-direction
γ_{fu}	Coherence function between force and displacement signals
$\mathbf{H}$	Complex Dynamic Stiffness matrix
$\bar{\mathbf{H}}$	Rearranged Complex Dynamic Stiffness matrix
$\bar{\mathbf{H}}_R$	Rearranged Complex Dynamic Stiffness matrix of the rotor
$\mathbf{H}_{Rij}$	Submatrices of the rotor's Complex Dynamic Stiffness matrix
$\mathbf{H}_s$	Average Complex Dynamic Matrix of the seal
$\mathbf{H}_{s1}, \mathbf{H}_{s2},$	Complex Dynamic Stiffness matrix at the proximity sensors' location
$\mathbf{H}_{s12}$	Augmented Complex Dynamic Stiffness at the proximity sensors' location
$\mathbf{H}_s^{\text{base}}, \mathbf{F}_a^{\text{base}}, \mathbf{U}_s^{\text{base}}$	CDS, force and displacement matrices of the seal for the baseline tests

$\mathbf{H}_s^{\text{over}}, \mathbf{F}_a^{\text{over}}, \mathbf{U}_s^{\text{over}}$	CDS, force and displacement matrices of the seal for the overall tests
$\mathbf{i}_a$	Coils' current vector
$\hat{\boldsymbol{\imath}}_a$	Measured coils' current vector
$\hat{\mathbf{p}} = [K_{xx}, K_{xy}, K_{yx}, K_{yy}, C_{xx}, C_{xy}, C_{yx}, C_{yy}]^T$	Parameters vector
$K_{xx}, K_{xy}, K_{yx}, K_{yy}$	Direct and cross-coupled stiffness coefficients
$C_{xx}, C_{xy}, C_{yx}, C_{yy}$	Direct and cross-coupled damping coefficients
$\mathbf{S}_{ff}, \mathbf{S}_{fu}$	Power spectral density and cross power spectral density
$\bar{\mathbf{u}}$	Rearranged displacement vector
$\mathbf{U}_s$	Displacement matrix
$\mathbf{u}, \mathbf{u}_s$	Rotor, seals' displacement
$\hat{\mathbf{u}}_s$	Measured seals' displacement
$\mathbf{u}_{s1}, \mathbf{u}_{s2}$	Displacement vector at the sensors' location
$\mathbf{u}_{s,ij}$	Displacement measured along the i-direction for an excitation along the j-direction
$\mathbf{v}$	Excitation voltage vector

Rotor-stator contact model symbols

b_r, b_S	Damping of the rotor and stator
d	Minimum rotor-stator clearance
η	Dimensionless rotor speed
$\mathbf{f}_c = \mathbf{f}_{ct} + \mathbf{f}_{cn}$	Contact force vector
$\mathbf{f}_{cn}$	Normal contact force vector
$\mathbf{f}_{ct}$	Tangent contact force vector
$\mathbf{f}_u = [f_{ux}, f_{uy}]^T$	Unbalance forces vector
k_C, b_C	Stiffness and damping of the contact model
k_R, k_S	Stiffness of the rotor and stator
κ	Stator-to-rotor stiffness ratio
κ_C	Contact-to-rotor stiffness ratio
m_R, m_S	Mass of the rotor and stator
μ_F	Friction coefficient
ν_R, ν_S, ν_C	Dimensionless damping of the rotor, stator and contact model
Ω	Rotor speed
ϕ_{BW}	Vibration phase of the backward precession of the rotor
ϕ_{FW}	Vibration phase of the forward precession of the rotor
ψ	Orientation angle of the minimal clearance
r_u	Unbalance radius

ρ	Stator-to-rotor mass ratio
s	Concentric rotor-stator clearance
σ	Ratio between the unbalance radius and concentric clearance
τ	Dimensionless time
U_{BW}	Vibration amplitude of the backward precession of the rotor
U_{FW}	Vibration amplitude of the forward precession of the rotor
$\mathbf{u}_R = [u_{Rx}, u_{Ry}]^T$	Rotor's displacement vector
$\hat{\mathbf{u}}_R = [\hat{u}_{Rx}, \hat{u}_{Ry}]^T$	Dimensionless rotor's displacement vector
$\hat{\mathbf{u}}_{Rx}, \hat{\mathbf{u}}_{Ry}$	
$\hat{\mathbf{u}}_{Sx}, \hat{\mathbf{u}}_{Sy}$	
x_{S0}, y_{S0}	Static eccentricity between rotor and stator
$\mathbf{u}_S = [u_{Sx}, u_{Sy}]^T$	Stator's displacement vector
$\hat{\mathbf{u}}_S = [\hat{u}_{Sx}, \hat{u}_{Sy}]^T$	Dimensionless stator's displacement vector

List of Abbreviations

CAD	Computer-Aided Design
CFD	Computer Fluid Dynamics
CDS	Complex Dynamic Stiffness
DFT	Digital Fourier Transform
FFT	Fast Fourier Transform
FRF	Frequency Response Function
LAVI	Acoustics and Vibration Laboratory
SFFT	Short-time Fast Fourier Transform
SNR	Signal-to-Noise Ratio
UFRJ	Federal University of Rio de Janeiro

Chapter 1

Introduction

Research on rotordynamics goes back more than 150 years, when Rankine [6], Durkeley [7], Jeffcott [8] and Föppl [9] studied the motion of a rotor. One of the main concerns was the critical speeds of rotating machinery due to the dangerous high vibrations. Later on, different problems have been addressed, namely, self-excited vibrations, internal damping, oil whirl, oil whip, parametrically excited systems, flow-induced vibrations, anisotropy and nonlinearity. Machines such as compressors, turbochargers and turbines have been relevant for different industries (oil extraction, aviation, etc.) and, thus, are the main motivation of research. Their correct functioning is vital to increase productivity and profitability. Their malfunctioning, due to different effects, must be reduced as much as possible. Such machines have components, such as seals or bearings, with a certain dynamic behavior. In the case of centrifugal compressors, annular gas seals are one of the components that may affect the overall dynamics of the machine depending on the operating condition (rotating speed, fluid, temperature, etc.). As an effort to analyze the seal dynamics, this thesis deals with the identification of rotordynamic coefficients from a seal of a prototype test rig. Moreover, since the rig operates with a small rotor-stator clearance, the contact between those parts is analyzed. Finally, the effects of anisotropy and smooth nonlinearities in the parameters are discussed.

1.1 Motivation

Petrobras is the Brazilian corporation of petroleum with several floating production storage and offloading units (SPSO). In one of them, located at the Campos basin and with a capacity of 180,000 barrels per day, a high vibration problem was found in January 2012, after a maintenance in the high power compressor of the unit, as related by Noronha et al. [10]. The amplitude of the synchronous vibration increased from 20 to 60 microns and the phase angle showed a rapid change as shown in Fig. 1.1. After some analysis, it was found that the stiffness and damping coefficients of a damper seal from the balance piston of the compressor changed after the closure of a recycle valve. Since the seals coefficients have a strong dependency on the pressure difference between the suction and discharge chambers, the closure of such valve caused a modification of the system dynamics, pushing the first critical speed to the operating condition. The solution to the problem was to change the geometry of the seal. This problem shows the importance to determine the seals coefficients under different operating conditions.

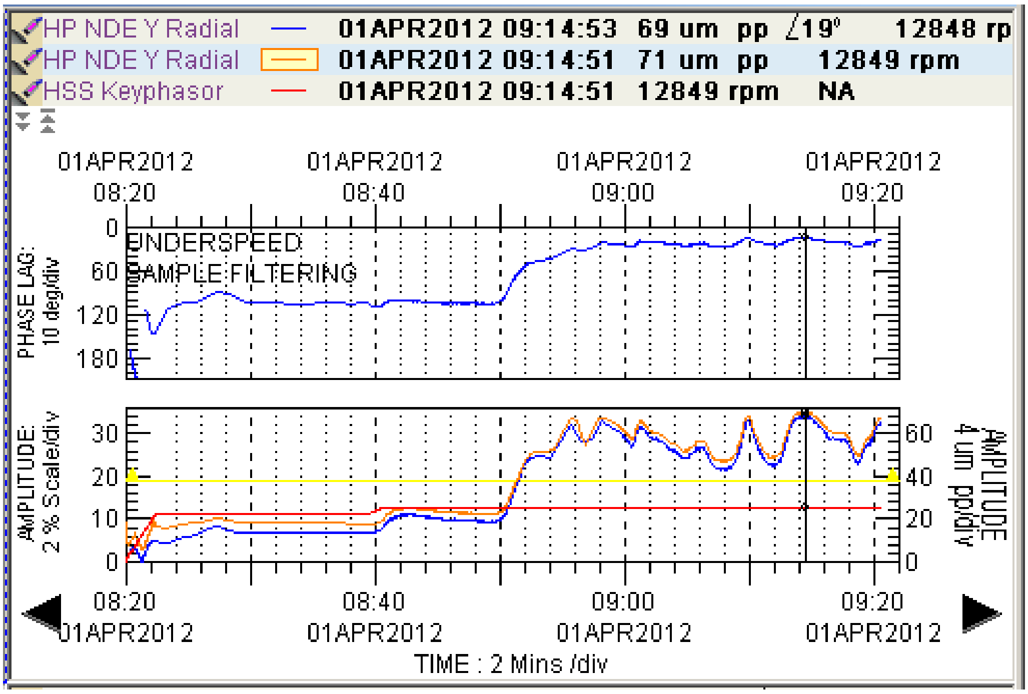

Figure 1.1: Overall vibration of a high power compressor from Petrobras (Noronha et al.[10]).

Another important source of dangerous vibrations in compressors is the contact between the stator and rotor, also known as rubbing and it involves impacts, friction, stiffening and coupling effects, thermal bow, among others effects. This condition causes different type of vibration such as forward whirl, backward whirl, sub-synchronous and super-synchronous vibration and chaotic motion.

The analysis of rotordynamic systems with nonlinear parameters is challenging. The dynamics of elements such as seals or bearings is nonlinear. However, for a certain operating condition with small vibration amplitude, it is possible to obtain equivalent linear stiffness and damping coefficients. This linear behavior comes from the truncation of a polynomial series expansion, which in most cases is reasonable. If the series is truncated up to a different order, a more complex dynamics arises. Nonlinear systems can be analyzed by different methods such as direct numerical integration, perturbation methods, harmonic balance, multiple scales, normal forms, among others. This thesis is based on the latter. The normal forms method consists in using several coordinate transformation to eliminate some nonlinear terms

1.2 Annular gas seals

Annular gas seals are one of the most important components in rotating machinery (turbines, compressors, etc). They are responsible for reducing the backward flux from a high-pressure stage to a previous stage, increasing the efficiency of the machine. In Fig. 1.2 a representation of a rotor-seal assembly is shown. During normal operation, the seal does not touch the rotor (in a seal-on-stator configuration), and thus, no rubbing is caused. On the other hand, velocity and pressure fields are created inside the clearance, and fluid-induced forces are created and applied to the rotor, affecting the dynamic behavior of the machine. Considering a small perturbations approach, the relation between fluid forces and seal-rotor displacements can be considered linear. Thus, the machine behavior is determined as a linear stiffness-damping system with frequency-dependent parameters. Although this approach disregards some nonlinear fluid effects, it is sufficient to explain important phenomena such as instabilities, added stiffness and damping, and modification of critical speeds.

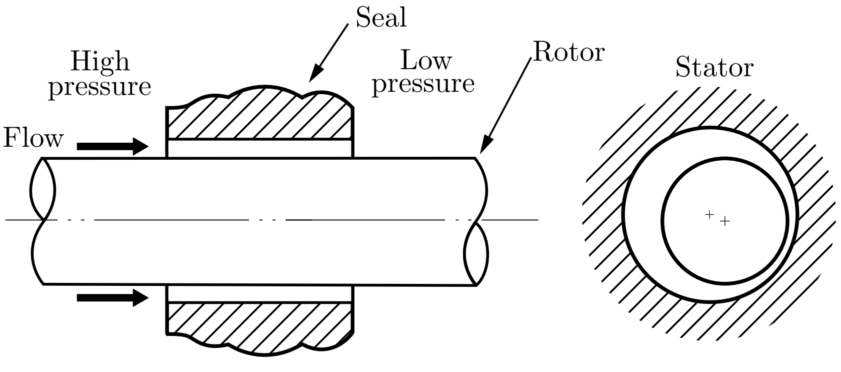

Figure 1.2: Schematic of a stator seal and a rotor. The stator moves inside the rotor and the fluid between them applies forces to it.

Annular gas seals play an important role in rotating machines used for petroleum extraction, such as the Petrobras 7-stage centrifugal compressor shown in Fig. 1.3. A simplified drawing of its principal components is shown in Fig. 1.4. When the fluid passes from a lower pressure stage to a higher pressure state, a leakage tends to flow back through the clearances between rotor and stator, i.e., the diffuser-rotor and the diffuser-impeller clearances. Also, there is a leakage through the balance piston as one side is connected to the last stage (discharge), and the other side to the first stage (intake). This fact makes necessary to have the interstage seals, eye-packing seals and balance piston seals shown in Fig. 1.4. Nevertheless, the use of these components may change the dynamic behavior of the rotor and, thus, their behavior under operating conditions must be known a priori.

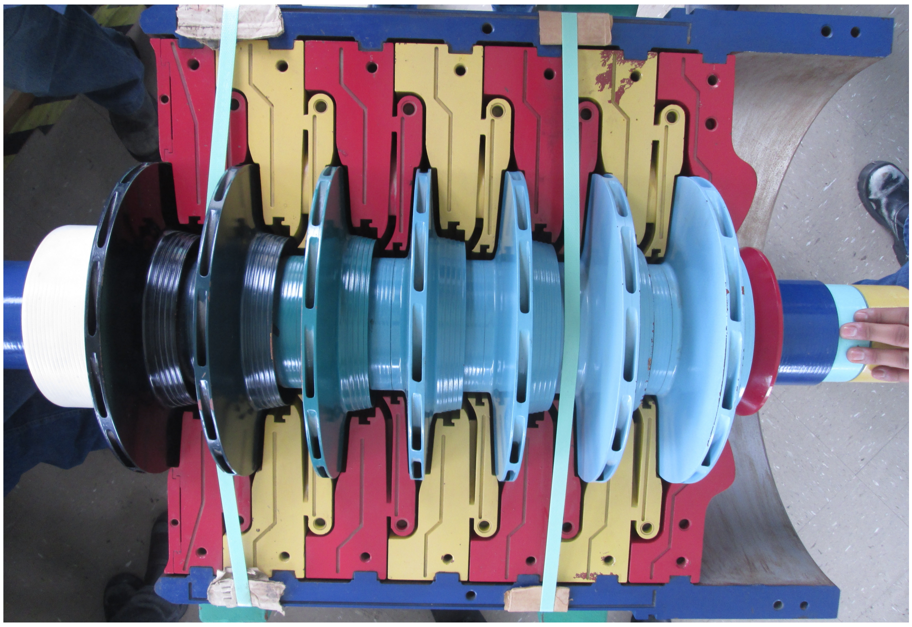

Figure 1.3: Cross section of a turbomachine from the Petrobras Turbomachinery Workshop in Macaé, Rio de Janeiro.

1.2.1 Type of seals

There are different annular gas seals used in centrifugal compressors, depending on their geometry (Fig. 1.6) and their inner surface (Fig. 1.5). If the rotor and seal are parallel to each other, as shown in Fig. 1.6a, it is called a straight seal. If the seal has a convergent geometry, it is a tapered seal (Fig. 1.6b). The seal can also have two different diameters, as shown in the stepped seal of Fig. 1.6c. In Figures 1.6d,

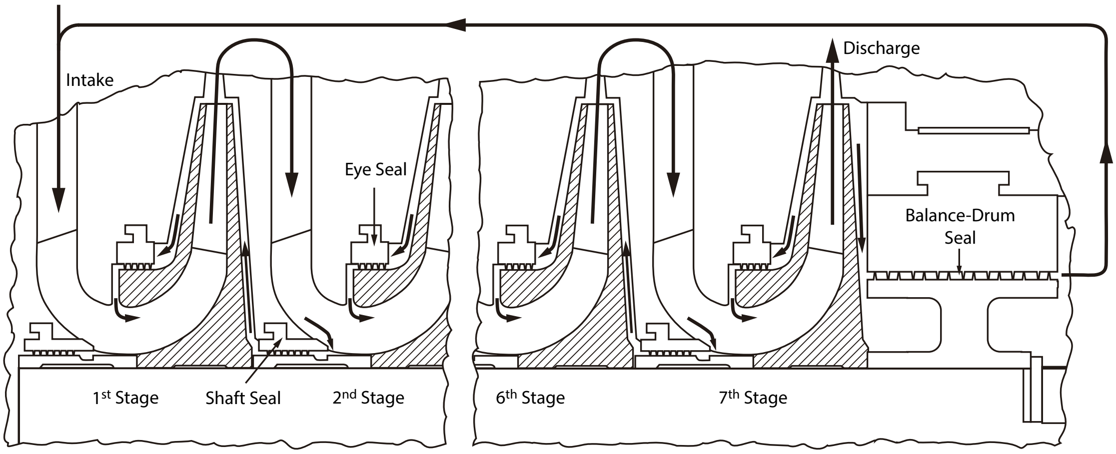

Figure 1.4: Typical seals in a centrifugal compressor [1].

1.6e, 1.6f 3 types of labyrinth seals are shown, namely, teeth-on-stator, teeth-on-rotor, and teeth-on-stator and teeth-on-rotor. In the honeycomb seal of Fig. 1.6g, a honeycomb pattern is machined on the inner seal surface.

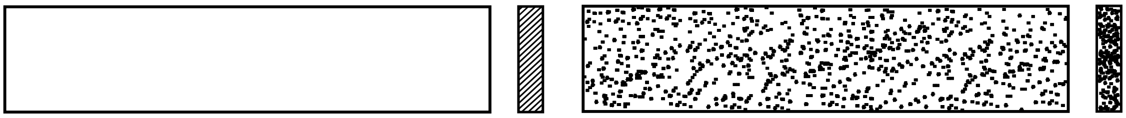

(a) Smooth seal surface. (b) Porous surface.

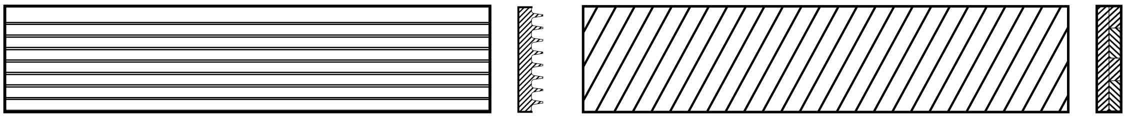

(c) Labyrinth surface. (d) Helically grooved surface.

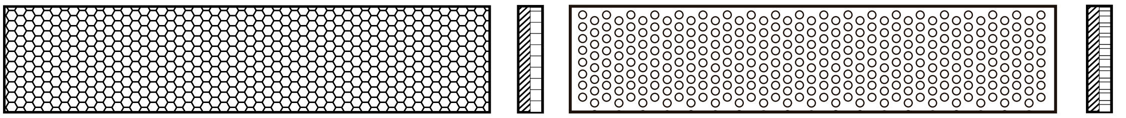

(e) Honeycomb surface. (f) Hole-pattern surface.

Figure 1.5: Annular gas seals surfaces [2].

1.2.2 Fluid-induced instabilities

Instabilities are one of the main concerns in rotordynamics. During this state, the rotor vibrations increase considerable until contact between rotor and stationary parts becomes considerably, leading to a failure. There are several causes of instabilities. Bearings and seals are affected by fluid-induced forces, where an external fluid, used either to lubricate or as a process fluid, applies forces on the rotor. In the former, the oil whirl and oil whip are common. In the latter, the instability is assessed by the eigenvalues of a linear model. Rotor internal damping (RID) instability, caused by the damping of a rotating structure, causes a whirling close to the first whirling mode (FWD) and the vibrations are maintained or increased without passing though with an acceleration or deceleration.

1.2.3 Identification methods

Coefficients of annular gas seals are obtained experimentally by using different test rigs. They are mainly composed of a rotor, a stator, seals in a back-to-back configuration pre-swirl rings, magnetic or hydraulic exciters, and supports such as hydrodynamic or active magnetic bearings. They are also instrumented and variables such as displacement, acceleration, force, pressure, mass flow and current are measured. In general, the identification methods consist in exciting the rotor (or stator) with a certain force and measuring the relative rotor-stator displacement; or vice-versa,

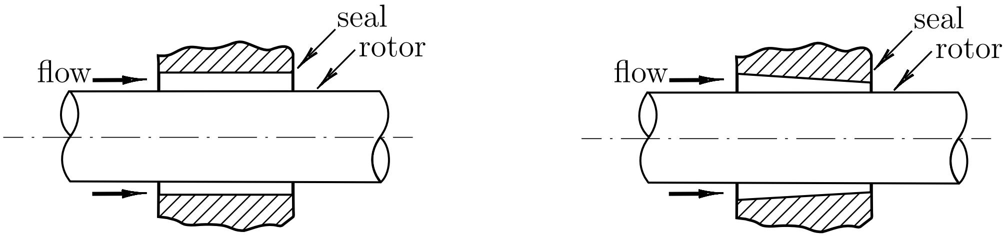

(a) Straight seal.

(b) Tapered seal.

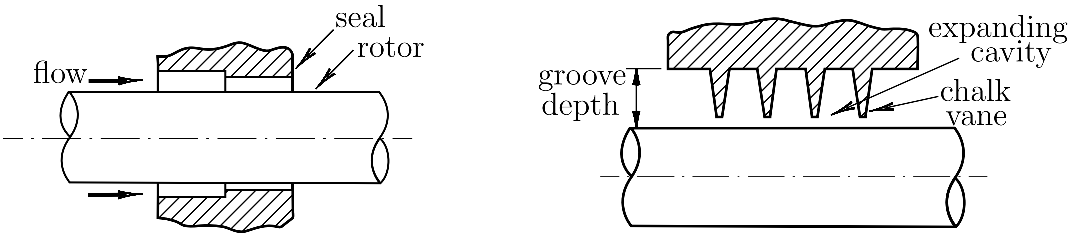

(c) Stepped seal.

(d) Teeth-on-stator labyrinth seal.

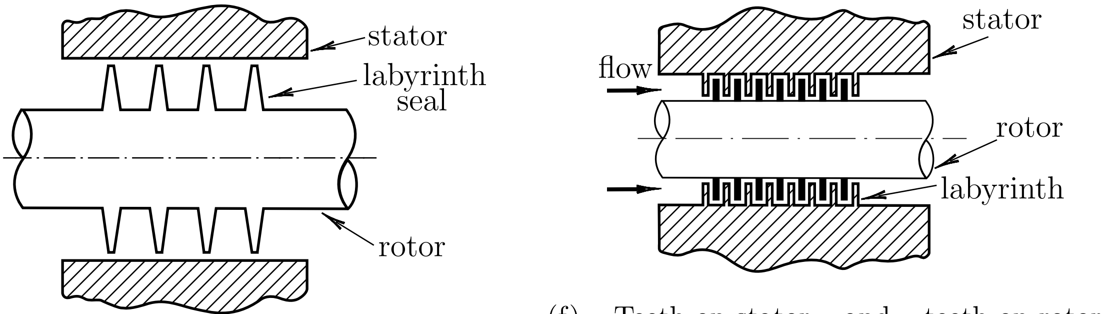

(e) Teeth-on-rotor labyrinth seal.

(f) Teeth-on-stator and teeth-on-rotor labyrinth seal.

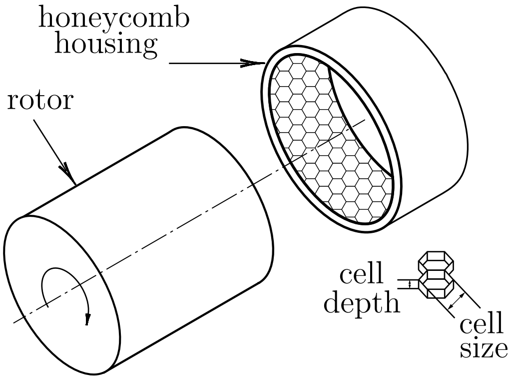

(g) Honeycomb seal.

Figure 1.6: Types of annular gas seals [2].

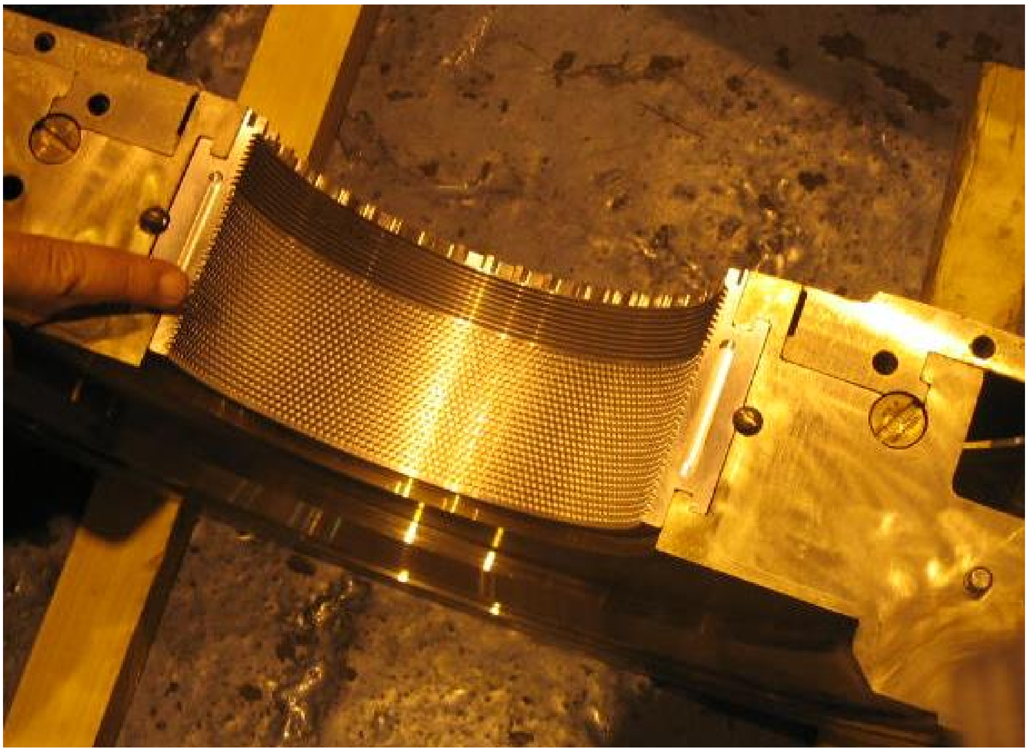

Figure 1.7: Hybrid annular gas seal from Petrobras (Noronha et al. [10]).

imposing a certain relative displacement and measuring the force. The coefficients are obtained either by a time-domain or frequency-domain approaches. In both cases, the seal is modeled as a linear system with direct and crossed-couple parameters. The experiments are carried out for different operating conditions such as inlet pressure, drop pressure, circumferential speed, rotor speed, excitation frequency. For validation purposes, the results are compared with previous validated models or experimental results in the literature.

1.2.4 Excitation signals

The quality of the estimates from the identification method strongly relies on the excitation signal used. Sufficient seal-to-rotor displacement must be applied in order to surpass the noise level in the sensors readings. If the excitation amplitude is small compared to the noise, the identification method output is not reliable.

In general, three types of excitation have been used. Instrumented hammers are used to apply impulsive signals to the structure (stator or rotor). In this case, a frequency band is excited. Hydraulic shakers and magnetic actuators are also used to apply a single frequency excitation, sweep excitation or multisine excitation. Recently, active magnetic bearings are widely used to both support the rotor and apply different excitation signals.

1.3 Stator-rotor contact

The efficiency of turbomachinery depends principally on their size, the diameter of the rotor, the angular speed and clearances between rotating and stationary parts. This thesis is focused on the latter. The smaller the clearance, the lower the leakage. Nevertheless, when a certain operating condition causes high level of vibrations, a contact, or rubbing, between those parts occur. Thus, improving the machinery performance leads to the risk of a different dynamics.

In some cases, the rubbing only causes wear of the parts but may change the dynamics of the machine. For example, when the rotor rubs slightly with a seal, the clearance may increase due to the material removal; the parameters of the seal may change considerably and also the dynamics of the overall machine. In other cases, severe damage may occur as a result of high contact and friction forces. In any case, the effects of the rubbing must be well understood to diminish the risk of hazardous events.

The rubbing can be divided into two effects: thermal deformation and contact forces. In the former, which is not considered in this thesis, a non-uniform temperature distribution causes a bending in the rotor. In the latter, which is addressed here, normal and tangential forces are applied to both parts. The interaction between the stator and rotor is simplified as mass-spring-damper systems. Nevertheless, the system is strongly nonlinear and its analysis turns complex.

Problems with rubbing were found in the test rig from the Laboratory of Acoustics and Vibration (LAVI). When a test above the first critical speed needs to be performed, the rotor must be accelerated quickly to avoid excessive vibrations due to its unbalance.

1.4 Anisotropy and nonlinearity

For simplicity, rotors are considered axisymmetric, which in most cases is reasonable due to the design and manufacturing processes. However, some of their components may introduce certain anisotropy to the system. For example, keyways grooved in circular shafts for coupling with other elements. However, the anisotropy can also comes from failures of the rotor, such as cracks, that modifies the initial geometry. Moreover, some other components may also introduce nonlinearities to the system. This is the case of bearings and seals that are affected by fluid-induced forces.

If a rotor has a noncircular cross section, the stiffness along two orthogonal axis is different. In this thesis, this configuration is called an anisotropic rotor. Similarly, if a bearing has different stiffness along orthogonal axis, it is called a anisotropic bearing. If the equations of motion are expressed in an inertial frame, a periodic stiffness matrix is obtained. On the other hand, if a non-inertial frame fixed in the rotor center of mass is used, a constant stiffness matrix is obtained. Moreover, if the rotor is supported by anisotropic bearings, it is not simple to obtain a constant stiffness matrix by expressing the equations in either frame. Such systems can be analyzed by Floquet or Hills theory. This thesis is focused on the former.

Nonlinearities in turbomachinery normally arises from fluid-induced forces. Considering small perturbation around an operating condition, the equations can be linearized to simplify the analysis. However, some effects may not be explained by linear systems theory. For example, if nonlinear stiffness and damping coefficients are considered a richer dynamics is obtained. Such systems can be addressed by different methods: perturbation methods, harmonic balance, multiple scales, normal forms, and others. This thesis makes use of the normal forms method. The objective of the method is to reduce as much nonlinear terms as possible by using a set of coordinate transformation that involves near-identity and polar coordinate transformations. Hereafter, the set of equations obtained is autonomous, without an explicit time dependency, and has fewer nonlinear terms. The new system exhibits a simpler form that is topologically equivalent to the original system.

1.5 Objectives of the Thesis

The objectives of the thesis are summarized in Fig. 1.8 and described below.

- *To analyze and test a rig for identifying annular gas seals coefficients.* An identification method is used to determine the seals coefficients of a labyrinth seal. The method consists in exciting the rotor with an optimal multisine signal and acquiring measurements of displacements and forces to create a complex matrix whose entries are directly related to the seals coefficients. This analysis considers only linear dynamics and the coefficients are only determined experimentally. Theoretical analysis such as computer fluid dynamics or bulk-flow are out of the scope.
- *To study the different motion patterns observed in a system with rotor-stator contact.* A Jeffcott rotor in contact with a flexible stator is used to perform a theoretical analysis of bifurcation. The effects of some parameters on the type of response are addressed. Some motion patterns are investigated through signal spectra, orbits and Poincaré maps.
- *To analyze a rotordynamic system with anisotropy and nonlinearity with Floquet theory and the normal forms method.* A rotordynamic system with anisotropic rotor and bearings, and a seal with cubic damping and stiffness is considered. A Floquet analysis is performed to account for the anisotropy.

Stability maps for the system are presented. The nonlinear analysis is carried out by the normal forms method. The effect of the nonlinear stiffness and damping on the fixed points is addressed.

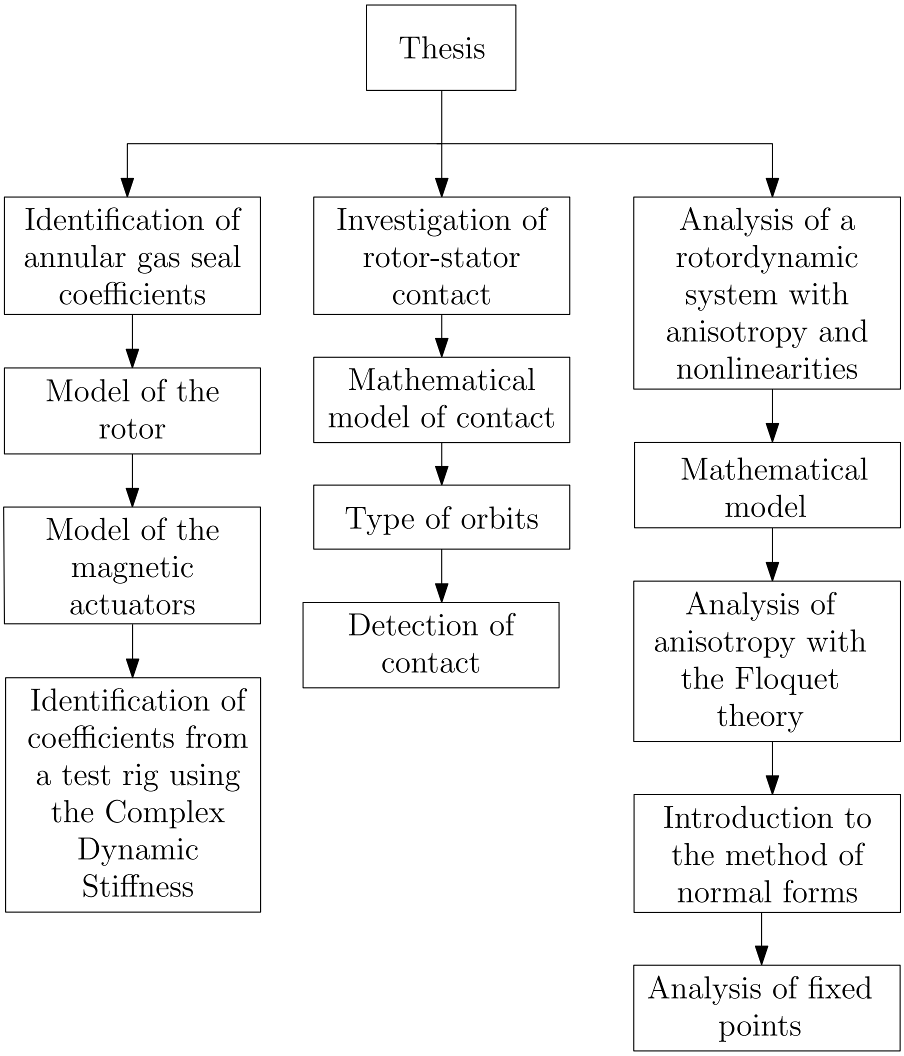

Figure 1.8: Overview of the thesis.

1.6 Thesis structure

The thesis is divided in nine chapters.

A review of literature in Chapter 2 shows the most relevant works regarding annular gas seals coefficients, rotor-stator contact models and the analysis of anisotropy and nonlinearities in the rotordynamic field. Chapter 3 presents some aspects and characteristics about the small-scale test rig built at LAVI. Chapter 4 is about the dynamic model of the rotor by means of the finite element method. Some preliminary analysis of the rig are performed based on this model. Chapter 5 is dedicated to the electromagnetic model of the actuators. The identification of seals coefficients is shown in Chapter 6. It is based on the Complex Dynamic Stiffness matrix, which is obtained experimentally with force and vibration data. Chapter 7 studies the behavior of the rotor under rotor-stator contact that eventually occurs during normal operation. Preliminary experiments are carried out to show the type of orbits set during contact in the test rig. Theoretical linear and nonlinear analyses of a rotor are performed in Chapter 8. First, the anisotropy influence on the stability is assessed by the Floquet theory. Then, the fixed points created by nonlinear stiffness and damping are analyzed by the normal form theory. In Chapter 9, the concluding remarks are presented.

Chapter 2

Literature Review

2.1 Overview of Literature

In this chapter, a review of the most relevant works about annular gas seals is presented. First, some works about annular gas seals are briefly exposed. Then, literature about rotor-stator contact problems in rotating machines is addressed. Finally, works regarding rotordynamic systems with anisotropy and nonlinear parameters is shown.

2.2 Annular gas seals

The model of labyrinth seals from Iwatsubo [11] is the base of subsequent models. The flow in the clearance is divided in two parts. One of them is the turbulent flow present in the seal cavities. The other part is the gas flow that is between the stator and the seal teeth, without entering in the cavities. Taking into account this flow behavior, the equations of continuity, circumferential moment and axial energy are formulated and solved by a method of perturbation. The results were compared with experimental data and showed good agreement for forward whirls.

Childs and Kim [12] determined the coefficients from a damping seal with a rough surface and a stator with a smooth surface. This configuration showed more damping with respect to a configuration with both stator and seal with rough surfaces.

Childs and Scharrer [13] determined the rotordynamic coefficients of teeth-on-rotor and teeth-on-stator. The stiffness and damping for both the configurations are insensitive to rotor speed variations. On the other hand, the coefficients are sensitive to the swirl and the pressure drop in both configurations. However, the teeth-on-stator seal is more stable in relation to the teeth-on-rotor configuration.

Dietzen and Nordmann [14] presented a model based on Naiver-Stokes equations for turbulent flow. The equations are computed at the center of the seal and a perturbation around it is applied. They solution is based on the method of finite differences.

Syssmann [15] compared theoretical and experimental results from a labyrinth seals. The predictions for the cross-coupled stiffness and direct damping were similar to those obtained from experiments. On the other hand, the results from the direct stiffness and cross-coupled damping differed significantly.

Childs and Scharrer [16] proposed a model with two control volumes to predict the behavior of labyrinth seals. The predictions were compared to experimental data and showed good agreement for the direct and cross-coupled stiffness.

For honeycomb seals, Kleynhans and Childs [17] proposed a model also with a two control volumes approach. The analysis showed that the honeycomb cells reduced the effective acoustic speed of the flow. This fact reduces the acoustic natural frequencies, which invalidates some previous models.

Yu and Childs [18] proposed a seal with a simpler manufacturing process than the honeycomb seals, but with similar damping characteristics. It is a seal with small holes around the surface, called hole-pattern seal. The results showed a leakage reduction of 12 % and a higher direct damping coefficient with respect to a honeycomb seal.

Childs et al. [19] presented three different types of seals: Honeycomb, labyrinth and smooth. For comparison purposes, the seals had the same diameter, length and clearance. The comparisons concluded that the honeycomb seal has the lower leakage, followed by the labyrinth and smooth seals. For a high swirl, the honeycomb seal showed a better rotordynamic stability in relation to the others. However, for a negative swirl, the labyrinth seal had a better stability, followed by the smooth and honeycomb seals.

Kwanka and Magel [20] explained the relevance of the forces induced by the flow in the interior of the labyrinth seals because they are capable of create unstable vibrations. The authors developed a identification method with a high sensitivity and reproducibility. The experiments showed that the crossed-couple stiffness increase linearly with the swirl and that the direct damping depends particularly of seal geometry. Another important conclusion is that for these type of seals the rotor speed has a minimum influence on the coefficients. However, the crossed-couple stiffness depends strongly on the pressure ration and swirl.

Picardo and Childs [21] studied teeth-on-stator labyrinth seals and shows the dependency of the clearance, pressure ration and swirl. The results of the experiments done are the following: The coefficients are independent of the frequency up to 150 Hz; the terms of crossed-coupled are equal in magnitude but with opposite sign; a reduction in the clearance does not affect significantly the damping or the stability; the coefficients magnitude of labyrinth seals are much smaller to those of the hole-pattern; the flow leakage is reduce to a half with a clearance reduction of 50%.

In the paper of Vannini et al. [22] a test rig built in General Electrics for seal coefficients identification is detailed. The rig is mainly composed of a rotor with 200 mm diameter, active magnetic bearings for support and excitation up to 330 Hz, rotation speeds up to 15000 RPM and nitrogen as the operating fluid. The system has an instrumentation to measure the relative displacement between the rotor and stator, inlet and outlet pressure, fluid temperature, circumferential speed of the fluid and mass flow. A labyrinth seal was tested and characterized in the rig to emulate a balance piston of a 12.5 MW submarine compressor in Norway [23]. The results were compared with a computational model and showed discrepancies in the direct stiffness at higher frequencies, while the direct damping values were more accurate.

The work of Wagner et al. [3] presents an identification method for labyrinth seals using a test rig developed by SIEMENS (see Fig. 2.1). It is driven by a motor with a frequency inverter and a gearbox connected to the test rotor through a quill shaft. The seals are arranged symmetrically in the high pressure region to balance the axial thrust. Two magnetic bearings support the test rotor and they can variate the static and dynamic eccentricity. Frequency, amplitude and whirl direction can be set for different tests. Moreover, the magnetic bearings serves as force transducers, so the tangential and radial forces can be obtained directly. The real scale of the test rig allows to test seals in conditions similar to those on centrifugal compressors. The inlet and outlet pressure are adjusted independently by electronic valves. In order to determine the swirl in labyrinth seals, the static and dynamic pressure are measured using pitot tubes.

The paper of Vannarsdall adn Childs [4] describes a identification of seals method tested in a test rig built in Texas A&M University. The rig works at a pressure of 70 bar and is composed of hydrostatic bearings, static and dynamic pressure sensors, load cells, temperature sensors, proximity sensors, asynchronous excitation, accelerometers and 3 different swirls. As the rig has no magnetic bearings, the seal eccentricity is imposed using hydraulic shakers connected to the rig casing. The test was initially developed to characterized hydrostatic bearings and, afterwards, modified for identification of annular gas seals. The rig is able to test seals with an inlet pressure of up to 70 bar. Hydraulic shakers are used to excite and control the relative position between stator and rotor. The high pressure air is supply to the center of stator by pre-swirl rings. The air that leaks through the outlet seal clearance can be regulated, allowing to impose different pressure ratios and leakage. During the test, the relative rotor-stator displacement and the shakers forces are measured. The measurement and excitation are realized in 2 orthogonal directions, parallel to the shakers. The temperature and pressure of the fluid are monitored

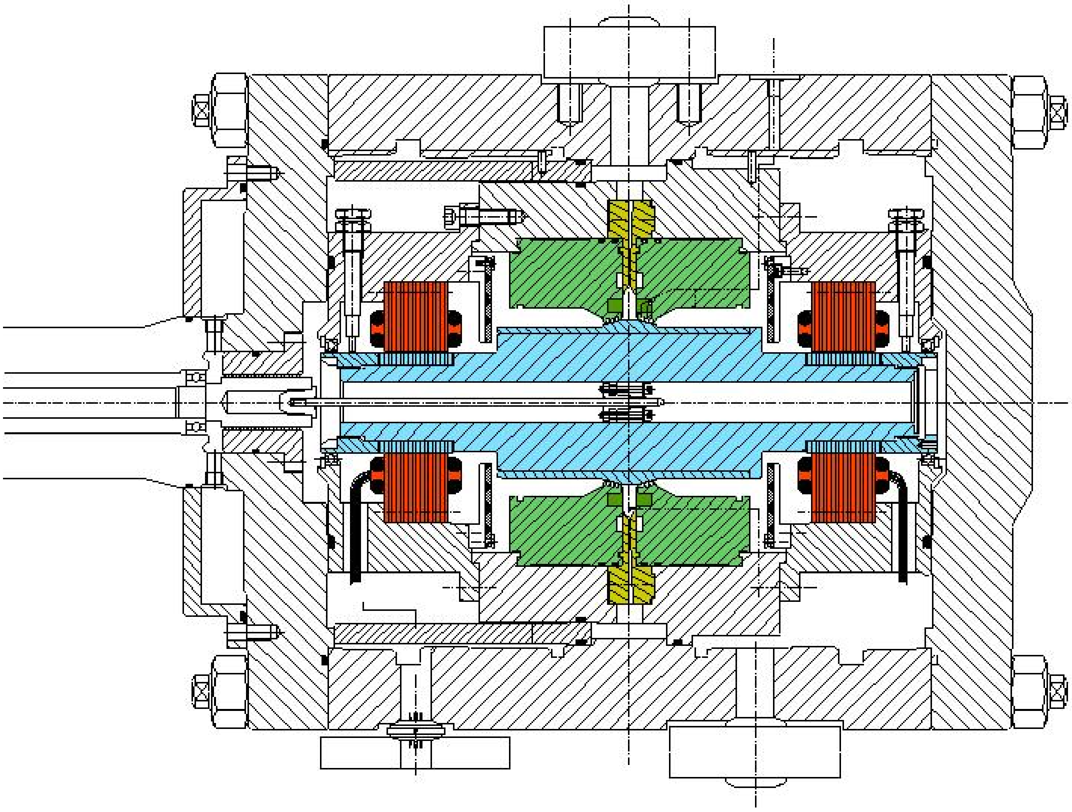

Figure 2.1: Test rig from SIEMENS [3].

and registered. The theoretical and experimental results of the direct stiffness from a hole-pattern seal is shown in Fig. 2.2.

From all the literature it was observed that the models are so complex that must be compared with experimental data. Moreover, the results found are valid only for the specific seals considered. This fact was a motivation for the construction of a small-scale test rig in the Acoustics and Vibration Laboratory (LAVI), from the Federal University of Rio de Janeiro. The characteristics and preliminary results can be found in Côrtes [24], Maldonado et al. [25–28], Diaz et al. [29–31] and Pinto et al. [32].

Further information about annular gas seals is found in Childs and Scharrer [16], Atkins and Perez [33], San Andrés [34], Childs and Hale [35], Kerr [36], Gupta et al. [37], Forte and Latini et al. [38], Kim and Lee [39], Burrows et al. [40], Lee et al. [41] et al. and Tiwari et al. [42].

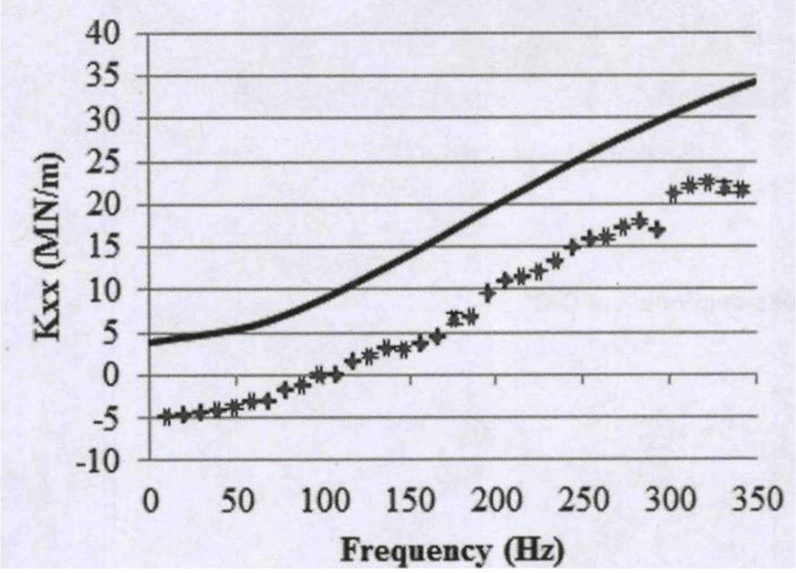

Figure 2.2: Experimental (cross) and theoretical (line) results from direct stiffness of a hole-pattern seal [4].

2.3 Rotor-stator contact models

The work of Ehrich [43] is one of the first investigations of rubbing between stator and rotor. The author described subsynchronous whirls excited by the nonlinearity of the contact. This vibration is a multiple of the critical speed, and becomes relevant when running the machine at twice the critical speed. Black [44] studied the change in the synchronous whirl by the intermittent interaction between the stator and unbalanced rotor. Different interaction zones were described and they may be different during a run-up or run-down. Counterwhirls were observed when considering dry friction.

Isaksson [45] conducted an intensive theoretical investigation about rubbing using Jeffcott rotors and finite element method models. Among the most important results are: jump phenomena during run-up and run-down, the improve of stability by adding external damping and low friction, subharmonic vibrations when friction is added and the influence of the stator offset.

In the work of Sawiki et al. [46], subharmonics, quasi-periodic and chaotic responses were encountered in a multi-disk rotor system. Bifurcation diagrams and Poincaré maps were used to analyze the vibrations.

Von Groll and Ewins [47] conducted experimental studies in which subharmonic and superharmonic vibrations were observed. It was shown that the parameter that determines the dominant frequency components depends on the resonance frequency of the rotor-stator system and the rotor speed.

Muszynska and Goldman [48] also showed the existence of chaotic vibrations zones of a rotor-bearinbg-stator system. Experimental results showed that the chaotic zones decrease with increasing damping.

Norrick et al. [49] used a analytical approach to predict backwhirl vibration during a rotor-stator contact.The influence of the gyroscope effects were taken into account.

Edwards et al. [50] carried out analyses on the influence of torsion in rotor-stator rubbing. In the results, periodic and chaotic motion were observed. Also, it was concluded that torsion has a considerable effect on the dynamics and should not be neglected.

The interaction of a mechanical seal contacting a rotor was investigated by Bently et al.[51]. Full annular rub was observed when increasing the mass unbalance of the rotor and seal-rotor friction. In this condition, a reverse precession is present. However, when the surfaces are lubricated, only synchronous motion is maintained. Also, the rotor foundation plays an important role. No reverse precessional rub was observed with flexible supports.

Lingener [52] studied reverse whirls when varying the rotor speed. The main result is that if this whirl excites a resonance of the coupled rotor-stator system any change of the rotational speed would not take the system out of this condition. In experiments conducted by Wilkes, conditions called dry whip and dry whirl were observed. The former is when the rotor rolls inside the stator without rolling. In the latter, the rotor slides inside the stator. When changing the speed of rotor, transitions from one condition to the other were observed.

In the work of Ehehalt et al. [5], the theoretical results of a model and the experimental results from a test rig (see Fig. 2.3) are shown. The motion patterns seen in the model were verified experimentally since parameters such as mass, stiffness and damping are able to be modified from the rig.

From all the literature found, few results related to contact in seals were found. In general, most of the rigs are simple systems with a flexible rotor and stator. This thesis tends to explore this phenomenon in a test rig for annular gas seals.

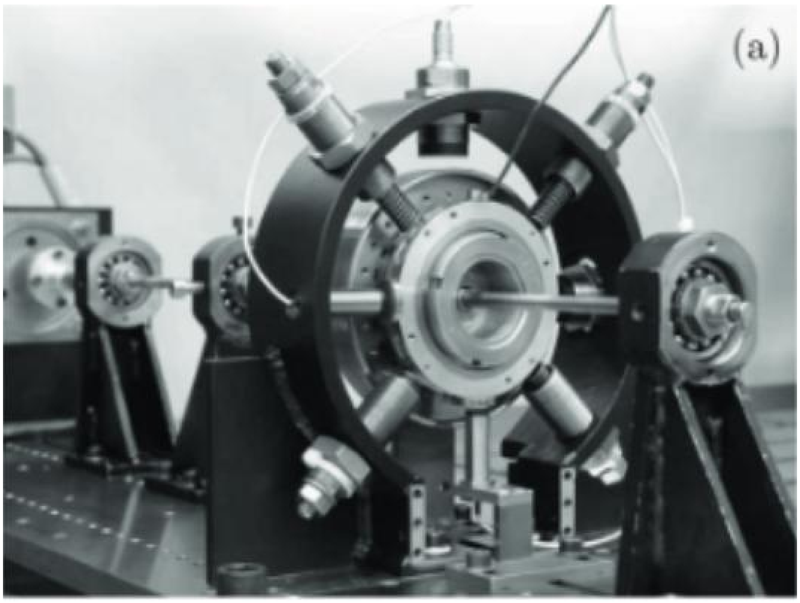

Figure 2.3: Test rig from the Technical University of Darmstadt [5]

2.4 Anisotropic rotor and bearings and nonlinear parameters

One of the first efforts in explaining the dynamics of rotating machines is the work of Jeffcott [8] and De Laval, showing that a flexible rotor is stable after surpassing the first critical speed. Although the rotor considered is symmetric, it motivated different research. A modified version of the Jeffcott rotor, considering asymmetries, were published by Prandtl [53], Foote [54] and Rogers [55]. They showed the existence of other resonant frequencies different from the critical speed.

Brosens and Crandall studied a symmetric rotor with an asymmetric disk mounted on anisotropic bearings. In this case, gyroscopic effects were taken into account. Experimental results validated some of the calculated unstable regions.

Yamamoto and Ōta [56] considered an asymmetric rotor and showed that the addition of external viscous damping tend to reduce the unstable regions.

Noah and Hopkins [57] presented a method, based on Hill's analysis, to study the stability of parametrically excited systems. Although they did not used rotordynamic models, those type of systems are obtained when considering anisotropy.

Genta [58] showed a model of a rotor using the finite element model. A stability analysis was performed by the Hill's method.

Jei and Lee [59] applied a modal analysis to a continuous asymmetrical rotor system. Resonances in forward and backward whirls are discussed.

Afolabi [60] presented a method to obtain a set of equations with constant coefficients for a non-circular rotor mounted on asymmetric bearings.

Oncescu et al. [61] studied a finite element model of an anisotropic rotor via

Floquet theory. A stability analysis showing the influence of the rotor and bearing anisotropy is addressed.

Hull [62] conducted experimental investigations in a test apparatus with a flatten rotor supported by asymmetric bearings. Regions of forward and backward whirls where observed for different frequencies.

Iwatsubo [63] analyzed continuous rotor-bearing system by using the Galerkin's method and perturbation method. Results were validated using an experimental apparatus. Results similar to other authors were found.

Ganesan [64] performed a non-stationary analysis of a system. The author focused to the motions near the critical speed.

Regarding nonlinear systems, different techniques are available (see [65–69]). For comparison purposes, Elliott et al. [70] and Hill et al. [71] showed backbones curves of a 2 degrees of freedom (2DOF) system via normal forms, multiple scales, harmonic balance and numerical continuation. Results from the normal forms and harmonic balance were more accurate, especially at frequencies far from the resonance. The method of averaging has a strong similarity with the normal forms [72].

Jezequel and Lamarque [73], Neild and Wagg [74], and Neild et al. [75] applied the method to different mechanical systems with satisfactory results.

Karev et al. [76] showed the occurrence of asynchronous parametric excitation of a disk brake system with good results compared to numerical integration.

The present work is based on the normal forms method. The general theory can be found in the books of Murdock [77], Guckenheimer and Holmes [78], Chow and Wang [79] and Nayfeh [66]. Nevertheless, the application of the method to rotordynamic systems has not been completely adopted.

Chapter 3

Test Rig Prototype Description

In this chapter, the main characteristics of a test rig for annular gas seals are presented. The purpose of the rig is to investigate the dynamics of a seal. Specifically, the equivalent damping and stiffness coefficients. The rig was designed and constructed in the Acoustics and Vibration Laboratory (LAVI) of the Federal University of Rio de Janeiro (UFRJ). The mechanical design was performed by Côrtes [24]. The instrumentation and design of excitation signals is based on the work of Diaz [29]. Some previous research about the test rig and the methodology of identification are presented by Maldonado et al. [25–28], Diaz et al. [29–31] and Pinto et al. [32]. A picture of the rig is shown in Fig. 3.1.

3.1 Overview of the system

The rig cross section and its main parts are shown in Fig. 3.2 and detailed in Tabs. 3.1 and 3.2. It is basically composed of three main parts: A high pressure chamber, where the inlet high pressure is connected; a low pressure chamber, where the gas leaks to the atmosphere; and the test section, a region between the high and low pressure chambers, where the seals are located.

The inlet pressure is connected to the high pressure chamber through the inlet ring (red part) which distributes the pressure radially. The gas passes through a swirl generator ring (yellow part) to impose a tangential speed to the flow. The seals (orange parts) are placed inside the seals support (green part) so that the inlet gas leaks through the clearance between the rotor and seals, at the test section. Once the gas exits the seals, through the low pressure chamber, it is discharged through a regulator valve to the atmosphere. The pressure and velocity field inside the clearance create tangential and radial forces that can be modeled as linear stiffness and damping, with direct and cross-coupled components. Those parameters are obtained by applying radial forces by means of two electromagnetic actuators (part No. 9). The clearance is measured by four proximity sensors (part No. 5). Two

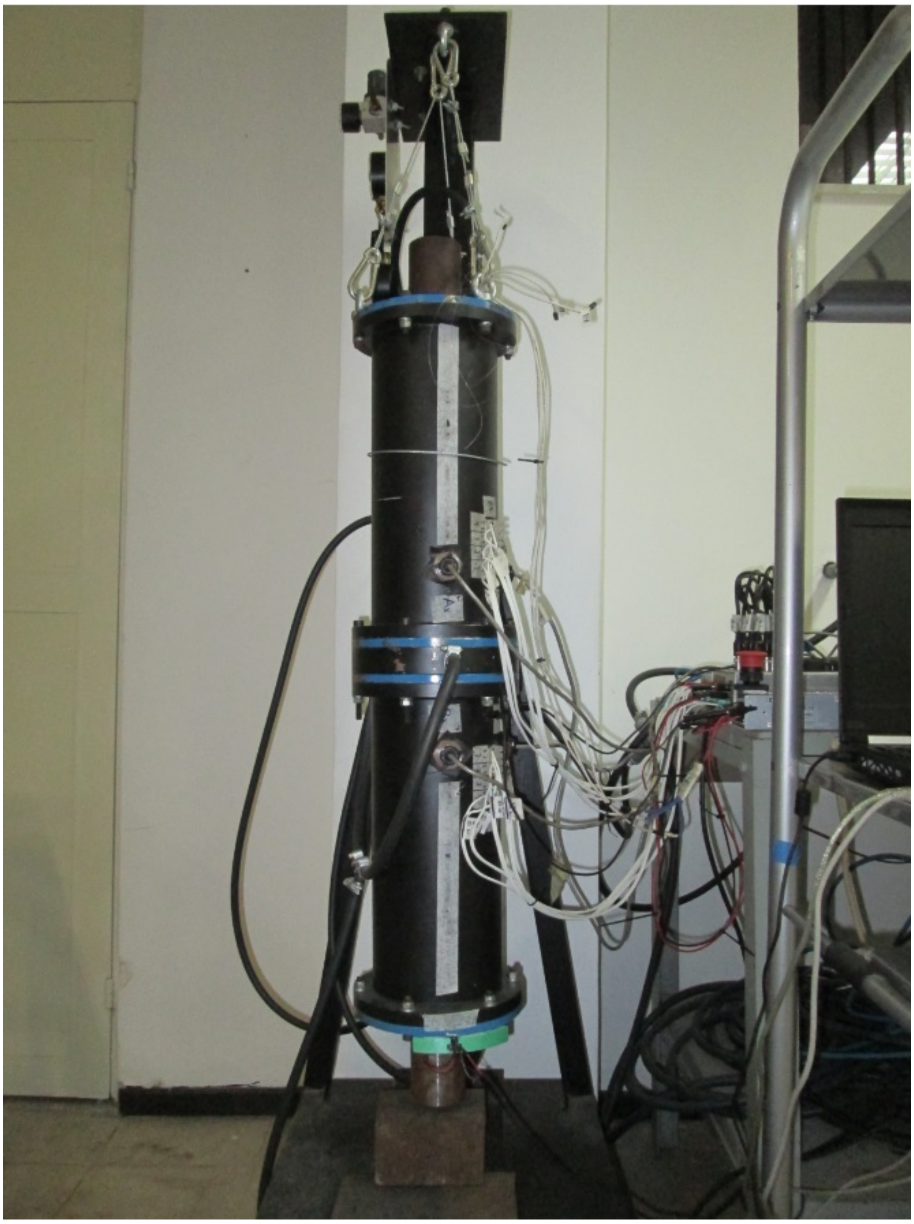

Figure 3.1: Test rig.

touchdown sleeves are used to avoid rubbing between rotor and seals, unbalance disks (blue parts) are used reduce the vibration coming from residual unbalance. Finally, the rotor is driven by a brushless DC motor (part No. 12).

The test rig is mainly built of steel. The touchdown sleeves are made of Teflon for a low friction factor and wear reduction. The seals are built of aluminum because it is less rigid than steel, which protects the rotor if the touchdown fails. The pressures in the high and low pressure chambers were limited to 4 MPa (40 bar) and 2.5 MPa (25 bar) to keep the mass below 70 Kg, facilitating the handling inside the laboratory facility. A swirl generator was used to emulate a typical characteristic of turbomachinery, where the inlet fluid has a circumferential velocity.

One of the most important characteristics of the test rig is the rotor flexibility.

Characteristics	Value
Maximum test pressure	4 MPa (40 bar)
Maximum counter-pressure	2.5 MPa (25 bar)
Maximum rotor speed	8500 RPM
Rotor length	800 mm
Test section diameter	40 mm
Test section length	120 mm
Seal radial gap	0.4 mm
Safety touchdown radial gap	0.25 mm
Approximate test rig weight	65 kgf

Table 3.1: Main characteristics of the test rig.

Number	Description	Qty.
1	Rotor	1
2	Bearing flange	2
3	Balancing disk	2
4	Center assembly	1
5	Distance sensor bushing	4
6	Low pressure chamber	2
7	Rotor speed sensor housing	1
8	O-ring	6
9	Electromagnetic actuator stator	2
10	Electromagnetic actuator rotor	2
11	Bearing	2
12	Motor	1

Table 3.2: Main components of the test rig.

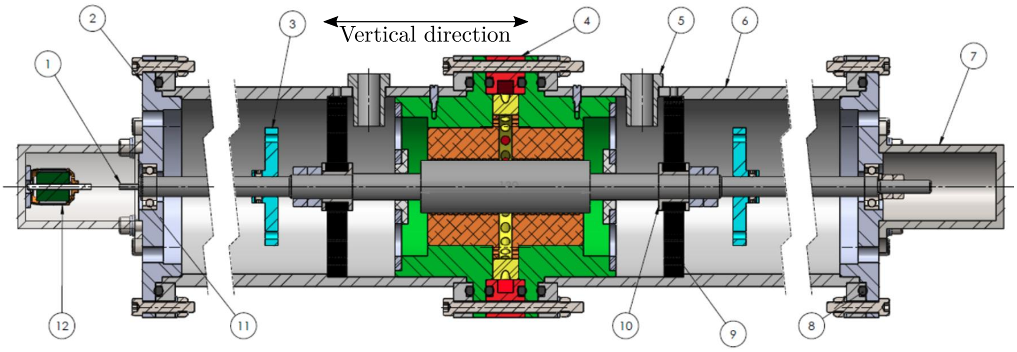

Figure 3.2: Test rig cross section; see Tab. 3.2.

Since most turbomachinery work above the first critical speed, a test rig with a flexible rotor would better represent the dynamics of such machines. Nevertheless, this is a challenge for several reasons. First, since the relative displacements are higher than in rigid rotors, the seals are more likely to touch the rotor, causing nonlinear vibration and wear. Second, if the rig is placed horizontally, the rotor will bend due to the gravity force and a different behavior will be set on the rotor. Third,

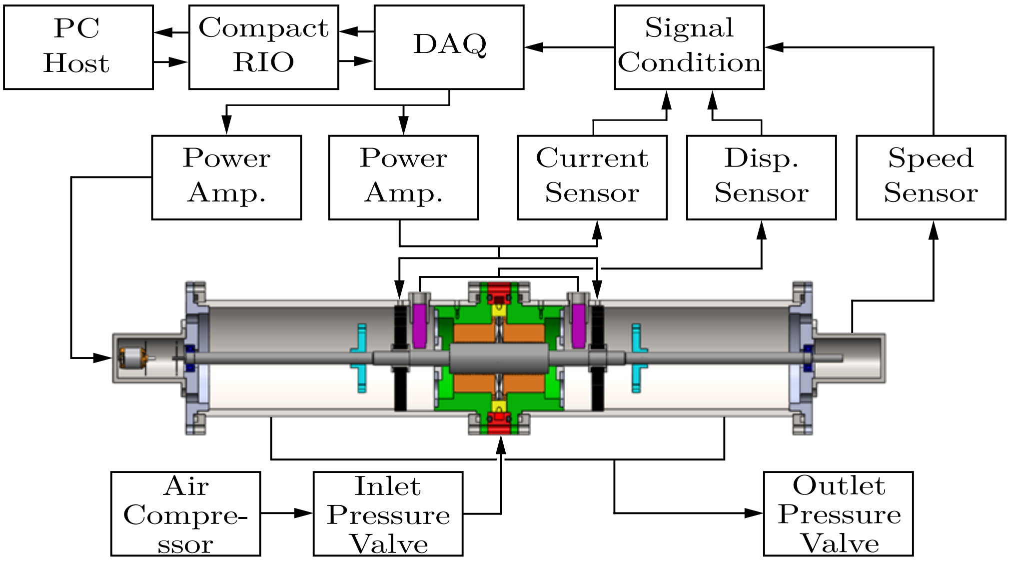

Figure 3.3: Test rig instrumentation and control scheme.

the second mode shape of a flexible rotor does not guarantee similar displacements measurements from sensors placed at equidistant locations.

3.1.1 Seals

The test seals used for the test are labyrinth type with 12 teeth (each one) and a depth of 1 mm, as shown in detail in Fig. 3.4.

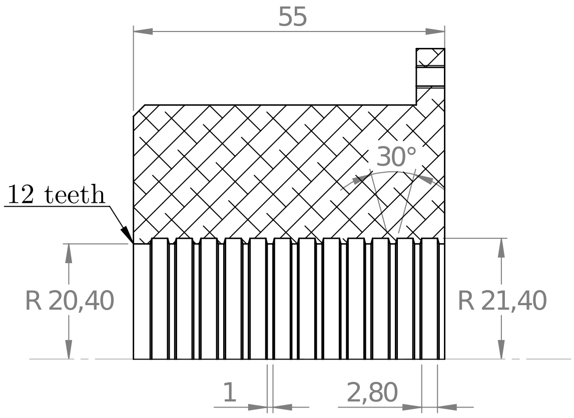

Figure 3.4: Cross section of the annular seal. Dimensions in mm.

3.2 Instrumentation

The instrumentation of the test rig is mainly made up of four proximity sensors, a rotor speed sensor, two electromagnetic actuators, eight current amplifiers and sensors, three pressure sensors, a brushless DC motor and a set of National Instruments boards (see Fig. 3.3). The gas is supplied by an air compressor with a capacity of 7 bar, and the inlet flow is controlled by a solenoid valve manually operated from a computer.

3.2.1 Sensors

A set of two orthogonal proximity sensors are located near the seal to measure the relative distance between rotor and stator. They are inductive-type sensors (Balluff BAW004). A static calibration was performed in a calibration stand by measuring a target at different distances and calibrating the values with a micrometer. The values were acquired by a 24-bit data acquisition module (NI 9239). The calibration curves are shown in Fig. 3.7a. Since the curves are not linear, a polynomial fitting was applied.

The current in the actuators' coils are measured by Hall effect-type sensors (ACS715-5A). A static calibration was performed by varying the voltage across a power resistor and measuring the current. The readings were calibrated with a precision current clamp. The calibration curves are shown in Fig. 3.7b. In this case, the curves are linear and only a linear fit was applied.

3.2.2 Actuators

The actuators are used to excite the rotor transversely based on induced electromagnetic forces. They are basically divided in two parts: a stator and a journal. The stator is made of several sheets of non-oriented ferromagnetic material that are stuck together to avoid power loss due to Eddy currents. They are shaped into an eight-pole configuration to accommodate eight coils as seen in Fig. 3.5. The journal is also made of stuck sheets but in a ring shape that is inserted in the shaft. The design of the actuator was based on Maslen [80]. A picture of one of the actuators is shown in Fig. 3.6.

The coils were placed in each of the stator poles. The interconnection between the coils are shown in Fig. 3.5. In this scheme, the coils in poles 1 and 2 are used to apply positive horizontal forces (to the right), while coils in poles 5 and 6 applies negative horizontal forces (to the left). A similar behavior applies to the coils in poles 3, 4, 7 and 8. This scheme is advantageous because the number of independent currents are reduced to four.

The coil currents are driven by H-bridge circuit amplifiers (VNH2SP30), which support up to 15A of continuous current. In total, four amplifiers were used per actuator (one per pair of interconnected coils). This type of amplifier is based on Pulse Width Modulation (PWM) in which the output voltage is varied in function of the duty cycle of a switched signal. The desired voltage is set from the computer through National Instruments boards.

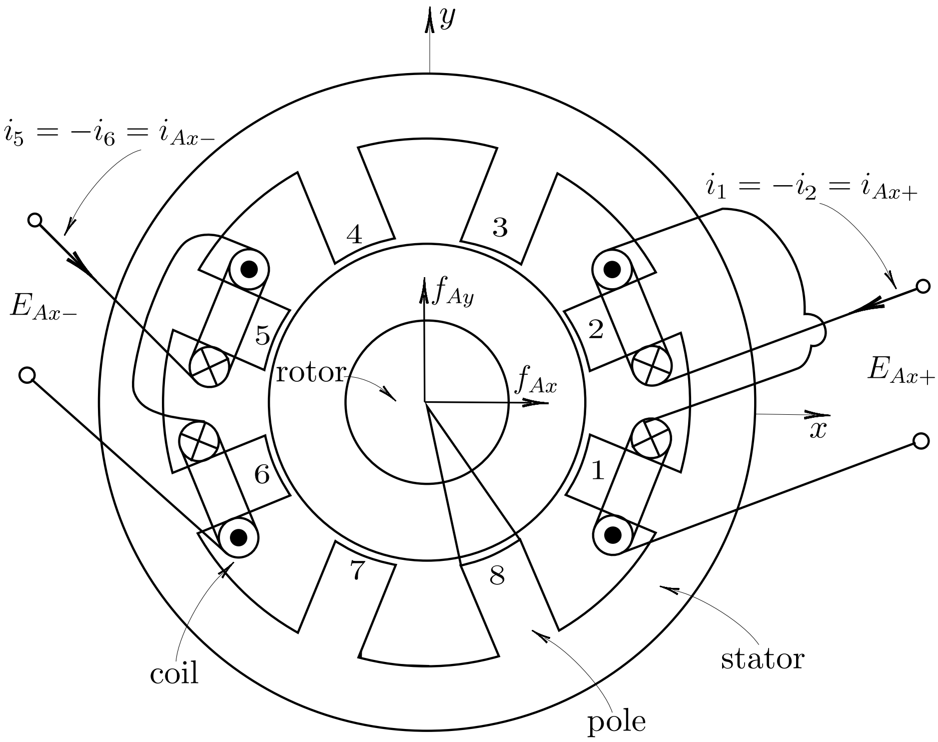

Figure 3.5: Eight-pole magnetic actuator.

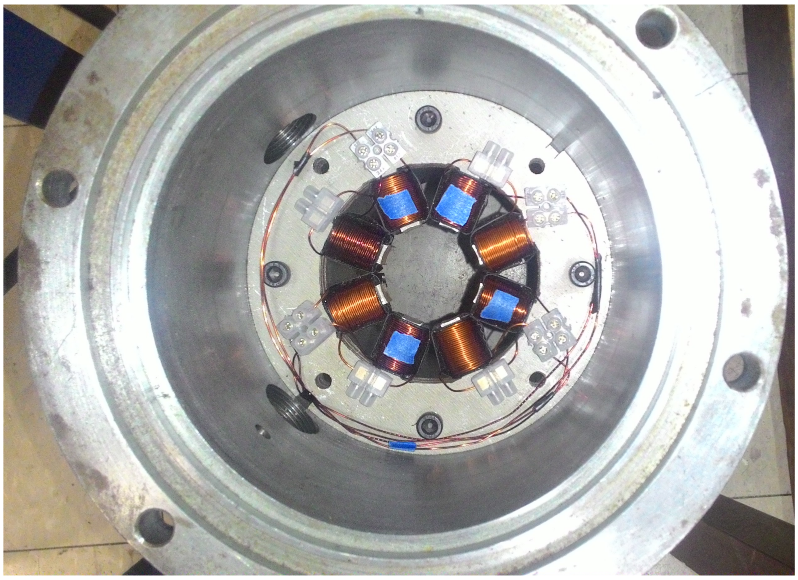

Figure 3.6: Picture of the magnetic actuator assembled in the stator.

3.2.3 Acquisition and excitation signals

The displacement of the rotor and currents of the coils measured by the sensors are acquired by Data Acquisition Boards from National Instruments.

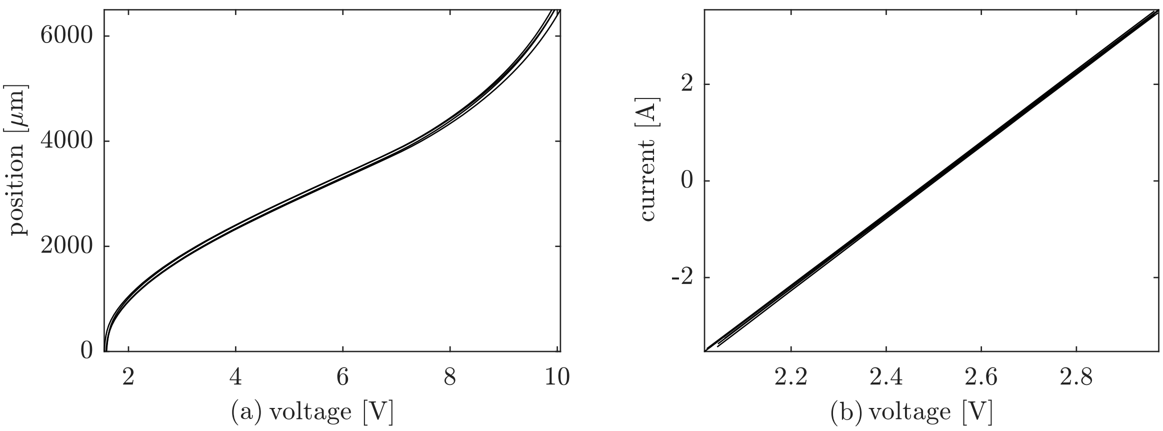

Figure 3.7: Calibration curves for all (a) position and (b) current sensors.

The excitation signals are created in Matlab and exported to a Field Programmable Gate Array (FPGA) controller (CompactRio 9030) capable of synchronization of the eight PWMs. Then, the signals are sent to the power amplifiers through analog and digital output boards (NI 9239 and NI 9474) with a frequency of 10 KHz.

3.2.4 Drive motor

The rig rotor is driven by a brushless DC motor linked with a flexible coupling. The speed is measured by an optical interrupter. The maximum rotation reached was 8500 RPM. This speed is enough to surpass the first critical speed of the rotor.

3.2.5 Labview interface

A graphical interface allows the visualization of the variables and the modification of some parameters (rotor speed, data storage, sampling rate, type of excitation signal, etc). The signals are shown in the time domain, frequency domain and as orbits. Also, it is used to save the data in a text file for post-processing.

Chapter 4

Finite element model of the rotor

In this chapter, the rotor of the rig modeled using the finite element method. The Timoshenko beam theory (Astley [81], Davis et al. [82], Inman [83], Petyt [84], Thomas et al. [85]) is used to model the dynamics of each element. Once the equations for each element is obtained, the overall equations of motions are derived by assembling the mass, stiffness and gyroscopic matrix. The damping matrix is obtained assuming a modal damping.

The equations of motion obtained are used to analyze some properties of the rotor, before the analysis of the annular seals. First, the Campbell diagram is plotted to visualize the first critical speeds and the influence of the gyroscopic effects. Second, the frequency response function is shown to observe behavior of the amplitude of vibration of a single point in the rotor when the rotation speed is varied. These analyses are useful to know a priori the critical speeds of the rig.

4.1 Finite element theory

The dynamics of the rig's rotor bending can be determined by applying a finite element method. The rotor is divided in several regions modeled with the Timoshenko beam theory. In this formulation, each node has four degrees of freedom represented by four generalized coordinates: two transversal displacements and two rotations. This section is based on the books of Lalanne and Ferraris [86], Nelson [87], and Nelson and McVaugh [88], and the thesis of Ritto [89].

The first step is to define the coordinates. In Fig. 4.1, a representative beam element e is shown in two orthogonal planes. In the x-z plane, the nodal displacements u_{xe1} and u_{xe2} are along the x axis, while the nodal angles θ_{e1} and θ_{e2} are measured around the y axis, with the positive direction defined by the right-hand rule between z and x. On the other hand, the nodal displacements u_{ey1} and u_{ey2} are along the y axis and the nodal angles ϕ_1 and ϕ_2 are measured around the x axis, with the positive direction defined by the right-hand rule between z and y. The element displacements u_{xe} and u_{ye} represents the transversal displacement of any point (x, y) in the element. This variables can be expressed in vector notation as

$$\mathbf{u}_e(\xi, t) = \begin{bmatrix} u_{xe}(\xi, t) \\ u_{ye}(\xi, t) \end{bmatrix}, \tag{4.1}$$

$$\mathbf{u}_{ek}(t) = \begin{bmatrix} u_{xe1}(t) & \theta_{e1}(t) & u_{ye1}(t) & \phi_{e1}(t) & u_{xe2}(t) & \theta_{e2}(t) & u_{ye2}(t) & \phi_{e2}(t) \end{bmatrix}^T. \tag{4.2}$$

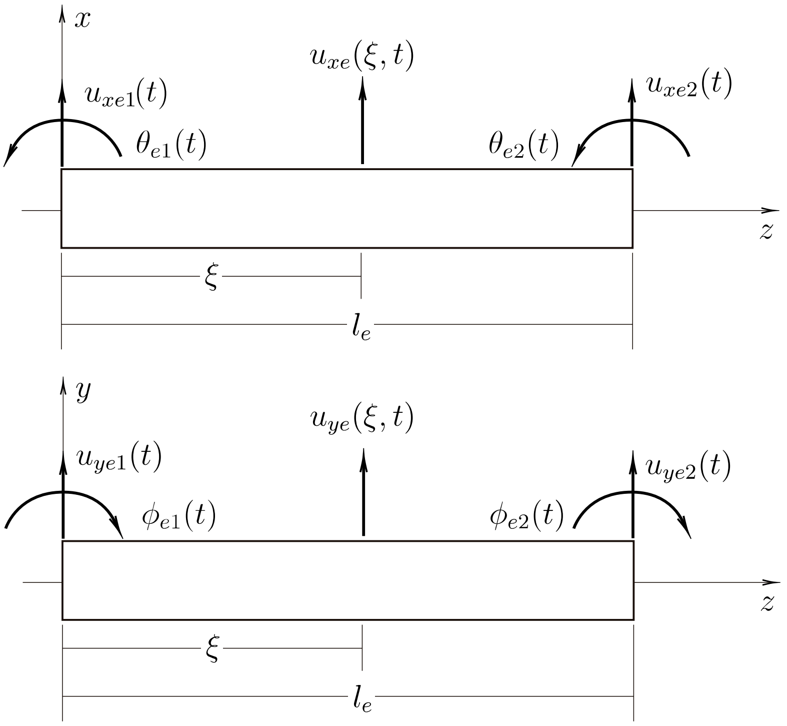

Figure 4.1: Local coordinates for a beam element.

Considering the Timoshenko beam theory, a small section of the element e is shown in Fig. 4.2. As opposed to the Euler-Bernoulli beam theory, the shear angles vector $\boldsymbol{\psi}_e = [\alpha_e,\ \beta_e]^T$ are considered. Thus, the angles vector $\boldsymbol{\Theta}_e = [\theta_e,\ \phi_e]^T$ of the beam element cross section is

$$\boldsymbol{\Theta}_e(\xi, t) = \mathbf{S}\frac{\partial \mathbf{u}_e(\xi, t)}{\partial \xi} + \boldsymbol{\psi}_e(\xi, t), \tag{4.3}$$

where the matrix

$$\mathbf{S} = \begin{bmatrix} 1 & 0 \\ 0 & -1 \end{bmatrix} \tag{4.4}$$

is used to account for the sign convention illustrated in Fig. 4.1, where a positive angle θ corresponds to a positive slope of the centerline (neutral axis or neutral plane) and a positive angle ϕ corresponds to a negative slope. The shear angles can

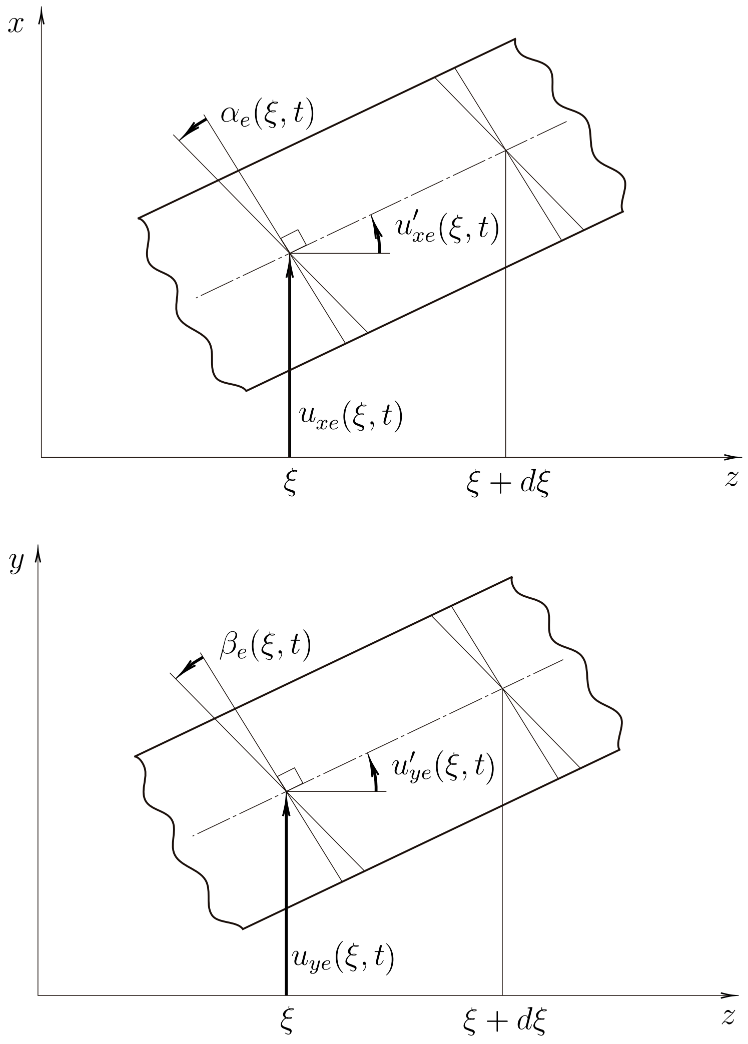

Figure 4.2: Local coordinates and share angles for a beam element.

be related ([83]) to the element displacements by using the following equation:

$$\frac{\partial}{\partial \xi}\left(E_e I_e \frac{\partial \boldsymbol{\Theta}_e(\xi,t)}{\partial \xi}\right) = \kappa_e G_e A_e \boldsymbol{\psi}_e(\xi,t), \tag{4.5}$$

where A_e is the area of the cross section,

$$\kappa_e = \frac{6(1+\nu_e)^2}{7+12\nu_e+4\nu_e^2} \tag{4.6}$$

is a shear constant, I_e is the second moment of area of the cross section about the neutral plane, E_e is the Young's modulus,

$$G_e = \frac{E_e}{2(1+\nu_e)} \tag{4.7}$$

is the shear modulus, ν_e is the Poisson's ratio. Considering a element with constant cross section, the substitution of Eq. (4.3) in Eq. (4.5) yields

$$\frac{\partial^2 \boldsymbol{\psi}_e(\xi,t)}{\partial \xi^2} + \mathbf{S}\frac{\partial^3 \mathbf{u}_e(\xi,t)}{\partial \xi^3} = \frac{\kappa_e G_e A_e}{E_e I_e}\boldsymbol{\psi}_e(\xi,t). \tag{4.8}$$

The solution of Eq. (4.8), for an uniform beam element, is approximated by

$$\boldsymbol{\psi}_e(\xi,t) = \frac{\gamma_e l_e^2}{12}\mathbf{S}\frac{\partial^3 \mathbf{u}_e(\xi,t)}{\partial \xi^3}, \tag{4.9}$$

where

$$\gamma_e = \frac{12 E_e I_e}{\kappa_e G_e A_e l_e^2}. \tag{4.10}$$

Thus, Eq. (4.3) turns to

$$\boldsymbol{\Theta}_e(\xi,t) = \mathbf{S}\frac{\partial \mathbf{u}_e(\xi,t)}{\partial \xi} + \frac{\gamma_e l_e^2}{12}\mathbf{S}\frac{\partial^3 \mathbf{u}_e(\xi,t)}{\partial \xi^3}. \tag{4.11}$$

The key idea of the finite element method is to eliminate the partial derivatives of the equations of motion by assuming a polynomial function for the displacement field inside the beam element. In this work, the third order polynomial

$$\mathbf{u}_e(\xi,t) = \mathbf{a}_0(t) + \mathbf{a}_1(t)\xi + \mathbf{a}_2(t)\xi^2 + \mathbf{a}_3(t)\xi^3 \tag{4.12}$$

is used, where $\mathbf{a}_i(t)$ depends on the nodal displacements and angles. Thus, considering the boundary conditions

$$u_{xe}(l_e) = u_{xe2}, \tag{4.13a}$$

$$u_{xe}(0) = u_{xe1}, \tag{4.13b}$$

$$\frac{\partial u_{xe}(0,t)}{\partial \xi} + \alpha_e(0,t) = \theta_{e1}(t), \tag{4.13c}$$

$$\frac{\partial u_{xe}(l_e,t)}{\partial \xi} + \alpha_e(l_e,t) = \theta_{e2}(t), \tag{4.13d}$$

$$u_{ye}(0) = u_{ye1}, \tag{4.13e}$$

$$u_{ye}(l_e) = v_{ye2}, \tag{4.13f}$$

$$\frac{\partial u_{ye}(l_e,t)}{\partial \xi} + \beta_e(l_e,t) = \phi_{e2}(t), \tag{4.13g}$$

$$\frac{\partial u_{ye}(l_e,t)}{\partial \xi} + \beta_e(l_e,t) = \phi_{e2}(t), \tag{4.13h}$$

the element displacement vector can be separated as

$$\mathbf{u}_e(\xi,t) = \mathbf{N}_e(\xi)\mathbf{u}_{ek}(t), \tag{4.14}$$

where,

$$\mathbf{N}_e(\xi) = \begin{bmatrix} N_{e1}(\xi) & N_{e2}(\xi) & 0 & 0 & N_{e3}(\xi) & N_{e4}(\xi) & 0 & 0 \\ 0 & 0 & N_{e1}(\xi) & -N_{e2}(\xi) & 0 & 0 & N_{e3}(\xi) & -N_{e4}(\xi) \end{bmatrix} \tag{4.15}$$

is called the shape function matrix with

$$N_{e1}(\xi) = \frac{1}{1+\gamma_e}\left(1+\gamma_e - \frac{\gamma_e}{l_e}\xi - \frac{3}{l_e^2}\xi^2 + \frac{2}{l_e^3}\xi^3\right), \tag{4.16a}$$

$$N_{e2}(\xi) = \frac{l_e}{1+\gamma_e}\left(\frac{2+\gamma_e}{2l_e}\xi - \frac{4+\gamma_e}{2l_e^2}\xi^2 + \frac{1}{l_e^3}\xi^3\right), \tag{4.16b}$$

$$N_{e3}(\xi) = \frac{1}{1+\gamma_e}\left(\frac{\gamma_e}{l_e}\xi + \frac{3}{l_e^2}\xi^2 - \frac{2}{l_e^3}\xi^3\right), \tag{4.16c}$$

$$N_{e4}(\xi) = \frac{l_e}{1+\gamma_e}\left(-\frac{\gamma_e}{2l_e}\xi - \frac{2-\gamma_e}{2l_e^2}\xi^2 + \frac{1}{l_e^3}\xi^3\right). \tag{4.16d}$$

The equations of motion for a beam element can be derived by using the Lagrange's equations. The first step is to define the Lagrangian L_e of an element e as

$$L_e = T_{Le} + T_{Ge} - U_e, \tag{4.17}$$

where T_{Le} is the kinetic energy due to bending, T_{Ge} is the kinetic energy due to rotation speed and U_e is the strain energy. Then, the equation of motion is derived as

$$\frac{d}{dt}\left(\frac{\partial L}{\partial \dot{\mathbf{u}}_e}\right) - \frac{\partial L}{\partial \mathbf{u}_e} = \mathbf{F}_{\text{ext}}. \tag{4.18}$$

The strain energy U_e is

$$U_e = \frac{1}{2}E_e I_e \int_0^{l_e} \left|\frac{\partial^2 \boldsymbol{\Theta}_e}{\partial \xi^2}\right|^2 d\xi + \frac{1}{2}\kappa_e^2 G_e A_e \frac{1}{2}\int_0^{l_e} |\boldsymbol{\psi}_e|^2 \, d\xi. \tag{4.19}$$

If the cross section of the element is uniform, the following equation holds

$$\frac{\partial \boldsymbol{\Theta}_e}{\partial \xi} = \mathbf{S}\frac{\partial^2 \mathbf{u}_e}{\partial \xi^2} + \frac{\partial \boldsymbol{\psi}_e}{\partial \xi} = \mathbf{S}\frac{\partial^2 \mathbf{u}_e}{\partial \xi^2}. \tag{4.20}$$

Thus, the strain energy is

$$
\begin{aligned}
&=\frac{1}{2}E_eI_e\int_0^{l_e}\left(\mathbf{S}\frac{\partial^2\left(\mathbf{N}_e\mathbf{u}_{ek}\right)}{\partial\xi^2}\right)^T\left(\mathbf{S}\frac{\partial^2\left(\mathbf{N}_e\mathbf{u}_{ek}\right)}{\partial\xi^2}\right)d\xi \\
&\quad+\frac{1}{2}\frac{E_eI_e\gamma_el_e^2}{12}\int_0^{l_e}\left(\mathbf{S}\frac{\partial^3(\mathbf{N}_e\mathbf{u}_{ek})}{\partial\xi^3}\right)^T\left(\mathbf{S}\frac{\partial^3(\mathbf{N}_e\mathbf{u}_{ek})}{\partial\xi^3}\right)d\xi \\
&=\frac{1}{2}\mathbf{u}_{ek}^T\left(E_eI_e\int_0^{l_e}\mathbf{N}_e''^T\mathbf{N}_e''d\xi+\frac{E_eI_e\gamma_el_e^2}{12}\int_0^{l_e}\mathbf{N}_e'''\mathbf{N}_e'''^Td\xi\right)\mathbf{u}_{ek} \\
&=\frac{1}{2}\mathbf{u}_{ek}^T\mathbf{K}_e\mathbf{u}_{ek},
\end{aligned}
\tag{4.21}
$$

where

$$
\mathbf{K}_e=E_eI_e\int_0^{l_e}\mathbf{N}_e''^T\mathbf{N}_e''d\xi+\frac{E_eI_e\gamma_el_e^2}{12}\int_0^{l_e}\mathbf{N}_e'''\mathbf{N}_e'''^Td\xi \tag{4.22}
$$

is the stiffness matrix of a beam element.

The kinetic energy due to the bending of the element is

$$
\begin{aligned}
T_{Le}&=\frac{1}{2}\rho_eA_e\int_0^{l_e}\left|\frac{\partial\mathbf{u}_e(\xi,t)}{\partial t}\right|^2d\xi+\frac{1}{2}\rho_eI_e\int_0^{l_e}\left|\frac{\partial\boldsymbol{\Theta}}{\partial t}\right|^2d\xi \\
&=\frac{1}{2}\rho_eA_e\int_0^{l_e}\left|\frac{\partial\mathbf{u}_e(\xi,t)}{\partial t}\right|^2d\xi+\frac{1}{2}\rho_eI_e\int_0^{l_e}\left|\frac{\partial\boldsymbol{\psi}}{\partial t}+\mathbf{S}\frac{\partial^2\mathbf{u}_e}{\partial\xi\partial t}\right|^2d\xi \\
&=\frac{1}{2}\rho_eA_e\int_0^{l_e}\left(\frac{\partial\mathbf{u}_e}{\partial t}\right)^T\left(\frac{\partial\mathbf{u}_e}{\partial t}\right)d\xi \\
&\quad+\frac{1}{2}\rho_eI_e\int_0^{l_e}\left(\frac{\partial\boldsymbol{\psi}}{\partial t}+\mathbf{S}\frac{\partial^2\mathbf{u}_e}{\partial\xi\partial t}\right)^T\left(\frac{\partial\boldsymbol{\psi}}{\partial t}+\mathbf{S}\frac{\partial^2\mathbf{u}_e}{\partial\xi\partial t}\right)d\xi \\
&=\frac{1}{2}\rho_eA_e\int_0^{l_e}\left(\frac{\partial\left(\mathbf{N}_e\mathbf{u}_{ek}\right)}{\partial t}\right)^T\left(\frac{\partial\left(\mathbf{N}_e\mathbf{u}_{ek}\right)}{\partial t}\right)d\xi \\
&\quad+\frac{1}{2}\rho_eI_e\int_0^{l_e}\left(\frac{\gamma_el_e^2}{12}\mathbf{S}\frac{\partial^4\left(\mathbf{N}_e\mathbf{u}_{ek}\right)}{\partial\xi^3\partial t}+\mathbf{S}\frac{\partial^2\left(\mathbf{N}_e\mathbf{u}_{ek}\right)}{\partial\xi\partial t}\right)^T \\
&\quad\cdot\left(\frac{\gamma_el_e^2}{12}\mathbf{S}\frac{\partial^4\left(\mathbf{N}_e\mathbf{u}_{ek}\right)}{\partial\xi^3\partial t}+\mathbf{S}\frac{\partial^2\left(\mathbf{N}_e\mathbf{u}_{ek}\right)}{\partial\xi\partial t}\right)d\xi \\
&=\frac{1}{2}\dot{\mathbf{u}}_{ek}^T\left(\rho_eA_e\int_0^{l_e}\mathbf{N}_e^T\mathbf{N}_ed\xi+\rho_eI_e\int_0^{l_e}\left(\frac{\gamma_el_e^2}{12}\mathbf{N}_e'''+\mathbf{N}_e'\right)^T\left(\frac{\gamma_el_e^2}{12}\mathbf{N}_e'''+\mathbf{N}_e'\right)d\xi\right)\dot{\mathbf{u}}_{ek} \\
T_{Le}&=\frac{1}{2}\dot{\mathbf{u}}_{ek}^T\mathbf{M}_e\dot{\mathbf{u}}_{ek},
\end{aligned}
\tag{4.23}
$$

where

$$
\mathbf{M}_e=\rho_eA_e\int_0^{l_e}\mathbf{N}_e^T\mathbf{N}_ed\xi+\rho_eI_e\int_0^{l_e}\left(\frac{\gamma_el_e^2}{12}\mathbf{N}_e'''+\mathbf{N}_e'\right)^T\left(\frac{\gamma_el_e^2}{12}\mathbf{N}_e'''+\mathbf{N}_e'\right)d\xi \tag{4.24}
$$

is defined as the mass matrix.

The kinetic energy due to the rotational speed is

$$T_{Ge} = -2\rho_e I_e \Omega \int_0^{l_e} \frac{\partial \theta_e(\xi,t)}{\partial t} \phi_e(\xi,t) d\xi, \tag{4.25}$$

or in matrix notation as

$$T_{Ge} = -\,2\rho_e I_e \Omega \int_0^{l_e} \dot{\boldsymbol{\Theta}}^T \mathbf{P} \boldsymbol{\Theta} d\xi, \tag{4.26}$$

where

$$\mathbf{P} = \begin{bmatrix} 0 & 1 \\ 0 & 0 \end{bmatrix}. \tag{4.27}$$

Thus, this kinetic energy is

$$\begin{aligned}
T_{Ge} =& -\,2\rho_e I_e \Omega \int_0^{l_e} \left(\mathbf{S}\dot{\mathbf{u}}'_e + \frac{\gamma_e l_e^2}{12} \mathbf{S}\dot{\mathbf{u}}'''_e \right)^T \mathbf{P} \left(\mathbf{S}\mathbf{u}'_e + \frac{\gamma_e l_e^2}{12} \mathbf{S}\mathbf{u}'''_e \right) d\xi \\
=& -\,2\rho_e I_e \Omega \int_0^{l_e} \left(\mathbf{S}\mathbf{N}'_e \dot{\mathbf{u}}_{ek} + \frac{\gamma_e l_e^2}{12} \mathbf{S}\mathbf{N}'''_e \dot{\mathbf{u}}_{ek} \right)^T \mathbf{P} \left(\mathbf{S}\mathbf{N}'_e \mathbf{u}_{ek} + \frac{\gamma_e l_e^2}{12} \mathbf{S}\mathbf{N}'''_e \mathbf{u}_{ek} \right) d\xi \\
=& -\,2\rho_e I_e \Omega \dot{\mathbf{u}}_{ek}^T \left(\int_0^{l_e} \mathbf{N}_e'^T \mathbf{S}\mathbf{P}\mathbf{S}\mathbf{N}'_e d\xi + \frac{\gamma_e l_e^2}{12} \int_0^{l_e} \mathbf{N}_e'^T \mathbf{S}\mathbf{P}\mathbf{S}\mathbf{N}'''_e d\xi \right. \\
& \left. + \frac{\gamma_e l_e^2}{12} \int_0^{l_e} \mathbf{N}_e'''^T \mathbf{S}\mathbf{P}\mathbf{S}\mathbf{N}'_e d\xi + \left(\frac{\gamma_e l_e^2}{12} \right)^2 \int_0^{l_e} \mathbf{N}_e'''^T \mathbf{S}\mathbf{P}\mathbf{S}\mathbf{N}'''_e d\xi \right) \mathbf{u}_{ek} \\
=& \dot{\mathbf{u}}_{ek}^T \mathbf{B}_e \mathbf{u}_{ek},
\end{aligned} \tag{4.28}$$

where

$$\begin{aligned}
\mathbf{B}_e =& -\,2\rho_e I_e \Omega \left(\int_0^{l_e} \mathbf{N}_e'^T \mathbf{S}\mathbf{P}\mathbf{S}\mathbf{N}'_e d\xi + \frac{\gamma_e l_e^2}{12} \int_0^{l_e} \mathbf{N}_e'^T \mathbf{S}\mathbf{P}\mathbf{S}\mathbf{N}'''_e d\xi \right. \\
& \left. + \frac{\gamma_e l_e^2}{12} \int_0^{l_e} \mathbf{N}_e'''^T \mathbf{S}\mathbf{P}\mathbf{S}\mathbf{N}'_e d\xi + \left(\frac{\gamma_e l_e^2}{12} \right)^2 \int_0^{l_e} \mathbf{N}_e'''^T \mathbf{S}\mathbf{P}\mathbf{S}\mathbf{N}'''_e d\xi \right).
\end{aligned} \tag{4.29}$$

The equations of motion are obtained by applying the Lagrange's equations in (4.18) based on Eqs. (4.22), (4.24) and (4.29):

$$\mathbf{M}_e \ddot{\mathbf{u}}_e(t) + \mathbf{G}_e \dot{\mathbf{u}}_e(t) + \mathbf{K}_e \mathbf{u}_e(t) = \mathbf{F}_{\text{ext}}(t), \tag{4.30}$$

where

$$\mathbf{K}_e = \frac{EI_e}{(1+\gamma_e)l_e^3}, \begin{bmatrix} k_1 & k_2 & 0 & 0 & -k_1 & k_2 & 0 & 0 \\ k_2 & k_3 & 0 & 0 & -k_2 & k_4 & 0 & 0 \\ 0 & 0 & k_1 & -k_2 & 0 & 0 & -k_1 & -k_2 \\ 0 & 0 & -k_2 & k_3 & 0 & 0 & k_2 & k_4 \\ -k_1 & -k_2 & 0 & 0 & k_1 & -k_2 & 0 & 0 \\ k_2 & k_4 & 0 & 0 & -k_2 & k_3 & 0 & 0 \\ 0 & 0 & -k_1 & k_2 & 0 & 0 & k_1 & k_2 \\ 0 & 0 & -k_2 & k_4 & 0 & 0 & k_2 & k_3 \end{bmatrix}, \tag{4.31}$$

with $k_1 = 12,\ k_2 = 6l_e,\ k_3 = (4+\gamma_e)l_e^2,\ k_4 = (2-\gamma_e)l_e^2,$

$$\begin{aligned} \mathbf{M}_e =& \frac{\rho A l_e}{840(1+\gamma_e)^2} \begin{bmatrix} m_1 & m_2 & 0 & 0 & m_3 & m_4 & 0 & 0 \\ m_2 & m_5 & 0 & 0 & -m_4 & m_6 & 0 & 0 \\ 0 & 0 & m_1 & -m_2 & 0 & 0 & m_3 & -m_4 \\ 0 & 0 & -m_2 & m_5 & 0 & 0 & m_4 & m_6 \\ m_3 & -m_4 & 0 & 0 & m_1 & -m_2 & 0 & 0 \\ n_4 & m_6 & 0 & 0 & -m_2 & m_5 & 0 & 0 \\ 0 & 0 & m_3 & m_4 & 0 & 0 & m_1 & m_2 \\ 0 & 0 & -m_4 & m_6 & 0 & 0 & m_2 & m_5 \end{bmatrix} \\ &+ \frac{\rho I_e}{30 l_e(1+\gamma_e)^2} \begin{bmatrix} m_7 & m_8 & 0 & 0 & -m_7 & m_8 & 0 & 0 \\ m_8 & m_9 & 0 & 0 & -m_8 & m_{10} & 0 & 0 \\ 0 & 0 & m_7 & -m_8 & 0 & 0 & -m_7 & -m_8 \\ 0 & 0 & -m_8 & m_9 & 0 & 0 & m_8 & m_{10} \\ -m_7 & -m_8 & 0 & 0 & m_7 & -m_8 & 0 & 0 \\ m_8 & m_{10} & 0 & 0 & -m_8 & m_9 & 0 & 0 \\ 0 & 0 & -m_7 & m_8 & 0 & 0 & m_7 & m_8 \\ 0 & 0 & -m_8 & m_{10} & 0 & 0 & m_8 & m_9 \end{bmatrix}, \end{aligned} \tag{4.32}$$

with

$$
\begin{aligned}
m_1 =& 312 + 588\gamma_e + 280\gamma_e^2, & m_6 =& -(6 + 14\gamma_e + 7\gamma_e^2)l_e^2, \\
m_2 =& (44 + 77\gamma_a + 35\gamma_e^2)l_e, & m_7 =& 36, \\
m_3 =& 108 + 252\gamma_e + 140\gamma_e^2, & m_8 =& (3 - 15\gamma_e)l_e, \\
m_4 =& -(26 + 63\gamma_e + 35\gamma_e^2)l_e, & m_9 =& (4 + 5\gamma_e + 10\gamma_e^2)l_e^2, \\
m_5 =& (8 + 14\gamma_e + 7\gamma_e^2)l_e^2, & m_{10} =& (-1 - 5\gamma_e + 5\gamma_e^2)l_e^2,
\end{aligned}
$$

$$
\mathbf{G}_e = \left(\mathbf{B}_e - \mathbf{B}_e^T\right) = \frac{\rho I_p \Omega}{15(1+\gamma_e)^2 l_e}
\begin{bmatrix}
0 & 0 & -g_1 & g_2 & 0 & 0 & g_1 & g_2 \\
0 & 0 & -g_2 & g_3 & 0 & 0 & g_2 & g_4 \\
g_1 & g_2 & 0 & 0 & -g_1 & g_2 & 0 & 0 \\
-g_2 & -g_3 & 0 & 0 & g_2 & -g_4 & 0 & 0 \\
0 & 0 & g_1 & -g_2 & 0 & 0 & -g_1 & -g_2 \\
0 & 0 & -g_2 & g_4 & 0 & 0 & g_2 & g_3 \\
-g_1 & -g_2 & 0 & 0 & g_1 & -g_2 & 0 & 0 \\
-g_2 & -g_4 & 0 & 0 & -g_2 & -g_3 & 0 & 0
\end{bmatrix}, \tag{4.33}
$$

where $g_1 = 36,\ g_2 = (3 - 15\gamma_e)l_e,\ g_3 = (4 + 5\gamma_e + 10\gamma_e^2)l_e^2,\ g_4 = (-1 - 5\gamma_e + 5\gamma_e^2)l_e^2$.

The mass, stiffness and gyroscopic matrices shown here were obtained using a symbolic computation code in Mathematica, which is shown in Appendix E.3.

4.1.1 Global matrix assembly

The equation of motion of the overall rotor is obtained by assembling the stiffness, mass and gyroscopic matrix according to the extended displacement vector $\mathbf{u}$ containing the overall nodes. The equation obtained is

$$
\mathbf{M}\ddot{\mathbf{u}}(t) + \mathbf{G}(\Omega)\dot{\mathbf{u}}(t) + \mathbf{K}\mathbf{u}(t) = \mathbf{f}(t), \tag{4.34}
$$

where $\mathbf{M} \in \mathbb{R}^{4(N_e+1)\times 4(N_e+1)}$, $\mathbf{K} \in \mathbb{R}^{4(N_e+1)\times 4(N_e+1)}$, $\mathbf{G} \in \mathbb{R}^{4(N_e+1)\times 4(N_e+1)}$ and $\mathbf{f} \in \mathbb{R}^{4(N_e+1)\times 1}$ are the global matrices and vector force and N_e the number of elements.

4.2 Modal damping

In the previous section, the damping forces were not considered. In this thesis, a modal damping approach is applied. The damped version of Eq. (4.34) is

$$
\mathbf{M}\ddot{\mathbf{u}}(t) + \mathbf{G}(\Omega)\dot{\mathbf{u}}(t) + \mathbf{C}\dot{\mathbf{u}}(t) + \mathbf{K}\mathbf{u}(t) = \mathbf{f}(t), \tag{4.35}
$$

where $\mathbf{C}$ is the damping matrix. Thereafter, the equation is written in the modal coordinates $\boldsymbol{\eta}$ by means of the transformation

$$\mathbf{u} = \boldsymbol{\Phi}\boldsymbol{\eta}, \tag{4.36}$$

where $\boldsymbol{\Phi}$ is a modal matrix obtained from the eigenvalue problem

$$\mathbf{K}\boldsymbol{\Phi} = \mathbf{M}\boldsymbol{\Phi}\boldsymbol{\Lambda}. \tag{4.37}$$

After substituting Eq. (4.36) in Eq. (4.35) and multiplying by $\boldsymbol{\Phi}^T$, the following equation is obtained:

$$\boldsymbol{\Phi}^T\mathbf{M}\boldsymbol{\Phi}\ddot{\boldsymbol{\eta}} + \boldsymbol{\Phi}^T\mathbf{G}\boldsymbol{\Phi}\dot{\boldsymbol{\eta}} + \boldsymbol{\Phi}^T\mathbf{C}\boldsymbol{\Phi}\dot{\boldsymbol{\eta}} + \boldsymbol{\Phi}^T\mathbf{K}\boldsymbol{\Phi}\boldsymbol{\eta} = \boldsymbol{\Phi}^T\mathbf{F}, \tag{4.38}$$

where it is assumed that the eigenvalue matrix $\boldsymbol{\Phi}$ diagonalizes the damping matrix. Since, $\boldsymbol{\Phi}$ diagonalizes $\mathbf{M}$ and $\mathbf{K}$, and considering negligible gyroscopic effects, the mode shapes from Eq. (4.38) are decoupled. Thus, the damping value of each mode shape is

$$\boldsymbol{\Phi}^T\mathbf{C}\boldsymbol{\Phi} = \mathrm{diag}(c_1, c_3, \ldots, c_n) = \mathrm{diag}(2\zeta_1\omega_1, 2\zeta_2\omega_2, \ldots, 2\zeta_n\omega_n) = \mathbf{c}, \tag{4.39}$$

where ζ_i and ω_i is the damping ratio and natural frequency of the i-th mode shape. When each mode shape is given a value, the damping matrix is obtained:

$$\mathbf{C} = \left(\boldsymbol{\Phi}^T\right)^{-1}\mathbf{c}\boldsymbol{\Phi}^{-1}. \tag{4.40}$$

4.3 Convergence analysis

The finite element method is an approximation of the exact solution of the rotor. By assuming shape functions, an approximation error is introduced in the equations. However, if the length of the element is small enough, the involved error may be reasonable depending on the type purpose of the analysis. In this thesis, the finite element method is used to model the rotor dynamics up to the second critical speed. Thus, a convergence analysis can be performed to assess the error. The approach used is to divide the rotor into the regions of constant area, which gives the N-th natural frequency $\omega_N(N_e)$. Then, each element is divided into two smaller elements, which gives the N-th natural frequency $\omega_N(N_e/2)$. Based on these results, the relative error is defined as

$$\mathrm{error}(N, N_e) \approx \frac{|\omega_N(N_e) - \omega_N(N_e/2)|}{\omega_N(N_e)}. \tag{4.41}$$

For thus thesis, this process is performed until the error of the second natural frequency is less than 5%. This is reached by dividing the rotor in 10 elements ($N_e = 10$).

4.4 Analysis of the rig's rotor

A representation of the rig is shown in Fig. 4.3. It is a flexible rotor with two bearings at the ends, two seals in the middle region and two radial forces. Based on Eq. (4.35), the system equations are:

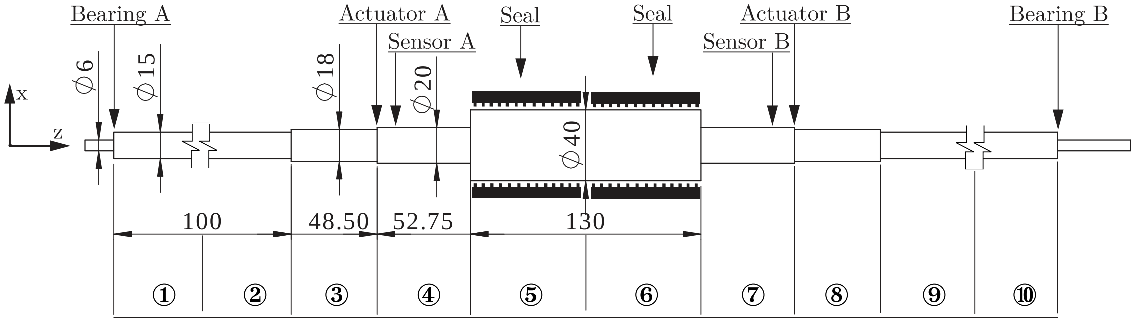

Figure 4.3: Representation of the test-rig. All dimensions are in millimeters.

$$\mathbf{M}\ddot{\mathbf{u}}(t) + (\mathbf{C} + \mathbf{G})\,\dot{\mathbf{u}}(t) + \mathbf{K}\mathbf{u}(t) = \mathbf{f}_a(t) + \mathbf{f}_u(t), \tag{4.42}$$

where $\mathbf{f}_a$ is the actuators forces and unbalancing force $\mathbf{f}_u$.

For certain analysis, such as mode shapes, frequency response functions and Campbell diagrams, the homogeneous first-order version of Eq. (4.42) is useful. This new equation is

$$\begin{bmatrix} \dot{\mathbf{u}} \\ \ddot{\mathbf{u}} \end{bmatrix} = \begin{bmatrix} \mathbf{0} & \mathbf{I} \\ -\mathbf{M}^{-1}\mathbf{K} & -\mathbf{M}^{-1}(\mathbf{C} + \mathbf{G}(\Omega)) \end{bmatrix} \begin{bmatrix} \mathbf{u} \\ \dot{\mathbf{u}} \end{bmatrix}. \tag{4.43}$$

This system leads to the eigenvalue problem

$$\mathbf{A}(\Omega)\boldsymbol{\nu}_k = \omega_k \boldsymbol{\nu}_k, \tag{4.44}$$

where $\mathbf{A}$ is the matrix of Eq. (4.43), $\boldsymbol{\nu}_k$ is the k-th eigenvector and ω_k the k-th eigenfrequency. The eigenvectors are related to the mode shapes of the rotor, while the eigenfrequencies are related to its critical speeds.

4.4.1 Mode shapes

The vibration of the test rig's rotor can be better visualized by plotting the mode shapes, which are obtained from the eigenvalue problem. In this analysis, only the first two modes are considered since the motor drive the rotor up to 8500 RPM. The mode shapes (bending modes) are shown Fig. 4.4. In the first mode, the displacement distribution is symmetric with respect to the center of the rotor; the readings of sensor A are the same as the readings of sensor B. In the second mode, the displacement distribution is anti-symmetric; the readings of both sensors have the same magnitude but with opposite sign.

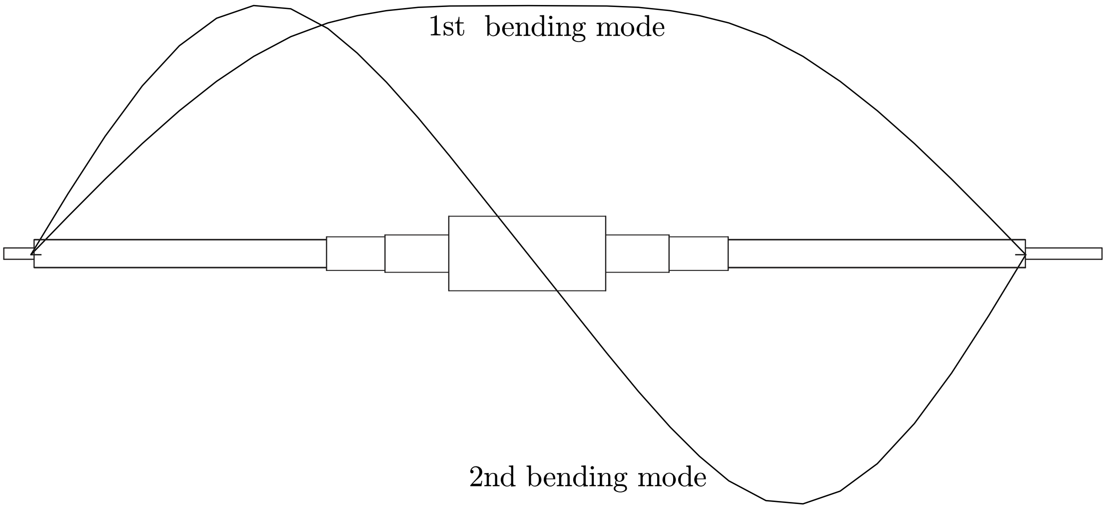

Figure 4.4: Mode shapes for the first two critical speeds of the rotor.

4.4.2 Campbell diagram

The Campbell diagram is based on the eigenfrequencies obtained from Eq. (4.44) the eigenvalue problem. It is shown in Fig. 4.5 for the first two bending modes. The eigenfrequencies are divided into two types: Forward whirl and Backward whirl. In the former, the rotor's orbit moves in the same direction of the rotor's angular velocity. In the latter, the orbit moves in the opposite direction. These two motion are represented as solid lines (forward) and dotted lines (backward) in Fig. 4.5. Also, the synchronous speed is represented as a dashed line. The crossing of the synchronous speed with an eigenfrequency represents a critical speed. The first two critical speeds are 2100 RPM and 8160 RPM, respectively. From the figure, it can be noted that the forward and backward whirl branches do not vary considerably with the frequency, which means that the gyroscopic effect is negligible. This is an expected behavior due to the symmetry of the rotor.

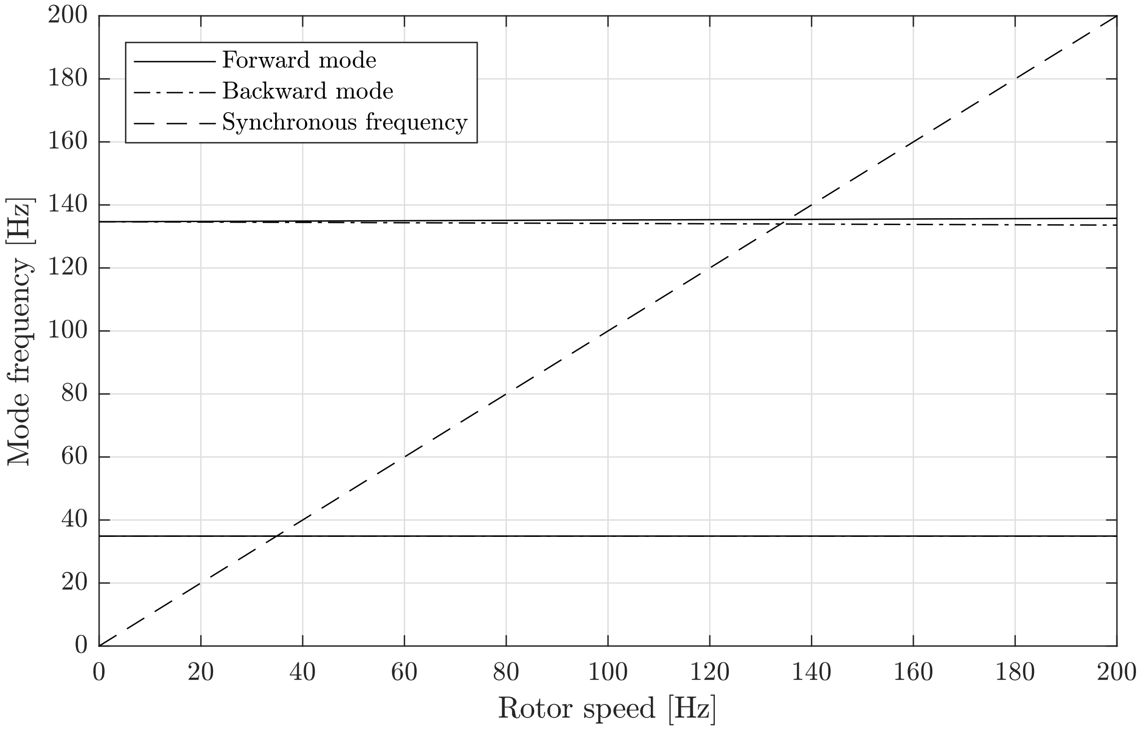

Figure 4.5: Campbell diagram of the rotor for the first two critical speeds.

4.4.3 Frequency response function

A Frequency Response Function (FRF) analysis can be obtained by considering the excitation force and displacement vectors

$$\begin{aligned} \mathbf{f}_a(t) &= \mathbf{F}_a(\omega)e^{-i\omega t+\phi_f}, \\ \mathbf{u}(t) &= \mathbf{U}(\omega)e^{-i\omega t+\phi_u}. \end{aligned} \tag{4.45}$$

The force vector is considered to be applied at the position of the actuators/sensors (nodes 4 and 8); both actuators applies the same force along each axis. The displacement vector is considered to be measured at the same nodes. This yields a system with two inputs and four outputs: one actuator force per axis and two points of measurements per axis. As a result of the symmetry of the rotor and applied forces, the displacements at node 4 is equal to that of node 8. In the case of symmetry, the displacements of both nodes can be averaged. Thus, the final system is represented by two input forces and two output displacements.

The substitution of Eq. (4.45) in Eq. (4.42) gives the following FRF matrix (length per unit force):

$$\mathbf{UF}_a^{-1} = \left(-\omega^2\mathbf{M} + i\omega\left(\mathbf{C} + \mathbf{G}(\Omega)\right) + \mathbf{K}\right)^{-1}. \tag{4.46}$$

This equation is a frequency-dependent matrix representing the FRF of the entire system, i.e., considering all nodes. For an excitation along one direction and measurements at the sensors' position, the FRF takes a single value for each frequency ω. The magnitude and phase of this function are shown in Figs. 4.6 and 4.7; they are valid for nodes 4 and 8. The magnitude shows the peak of the first critical speed. Although the second critical speed occurs at 136 Hz (see Fig. 4.5), it is not observed in the FRF. At this frequency, the left and right halves of the rotor are 180 degrees out of phase (see Fig. 4.4), and the left and right actuators forces are in phase. Thus, the excitation forces tends to excite the first mode. This is clarified in the next subsection. The phase of the FRF shows a rapid phase change near the first critical speed. However, as stated before, both FRFs for the 4 and 8 have similar phase for the first mode.

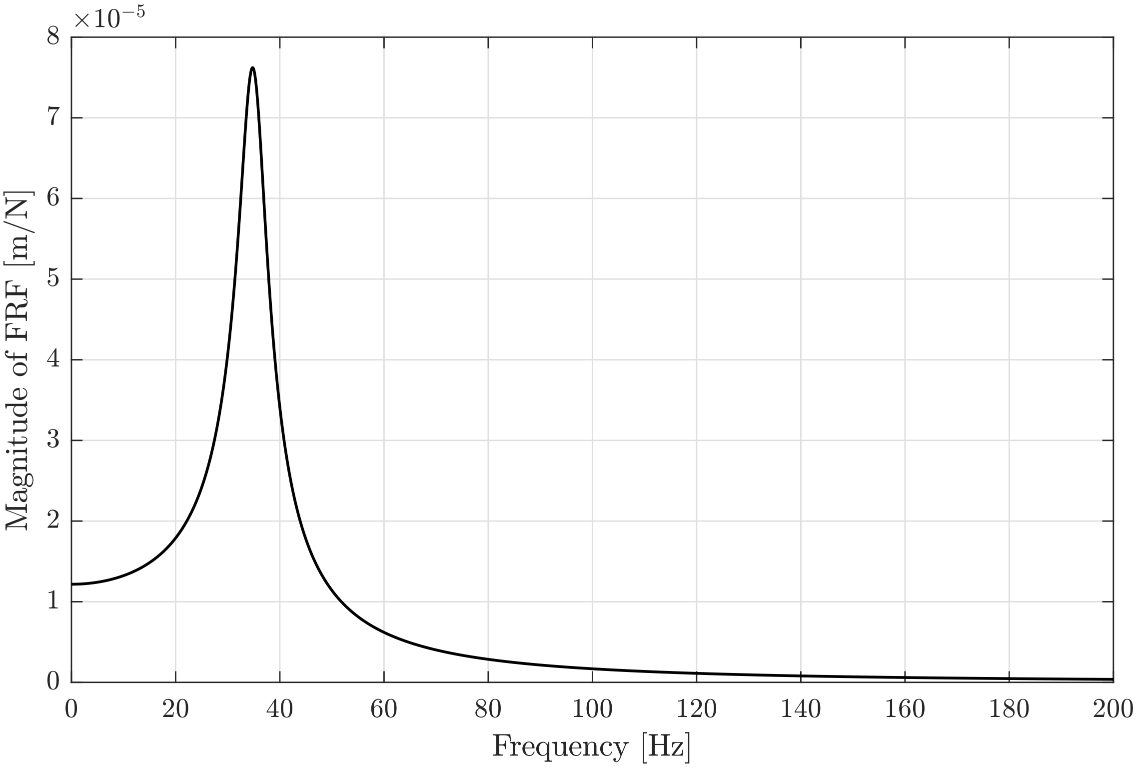

Figure 4.6: Magnitude of the FRF for an excitation at nodes 4 and 8, and displacements computed at node 4.

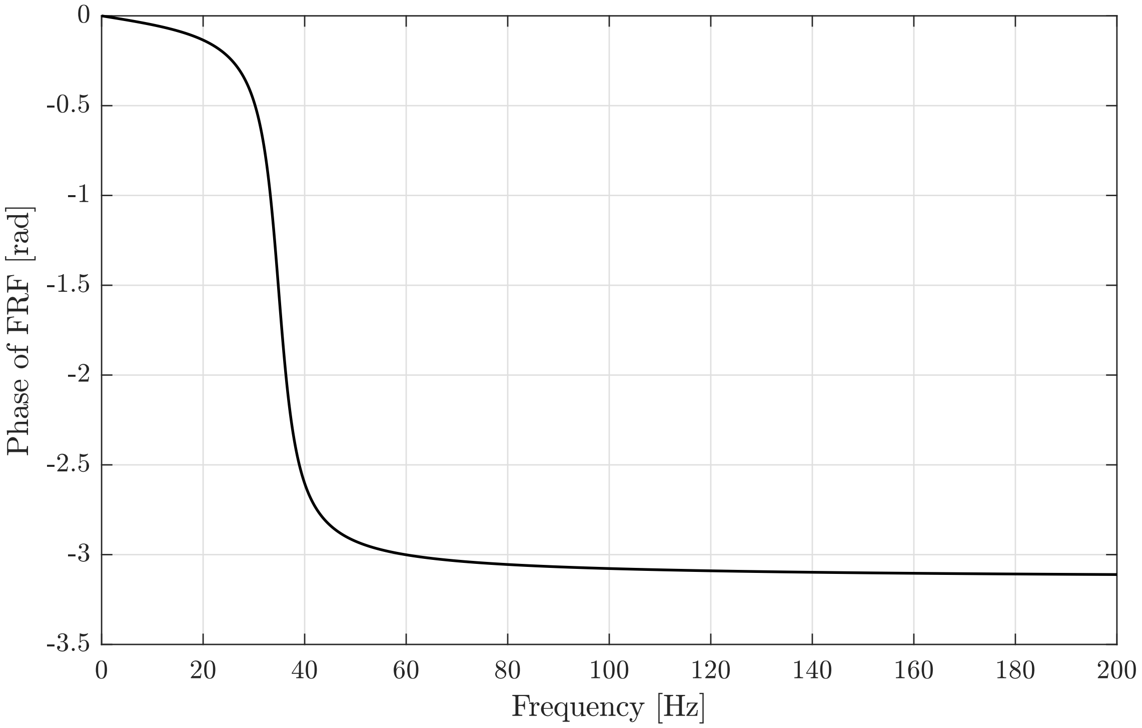

Figure 4.7: Phase of the FRF for an excitation at nodes 4 and 8, and displacements computed at node 4.

4.4.4 Unbalance response

An unbalance response in the frequency domain can be performed by considering two unbalancing masses m_{u3}, m_{u9} at the nodes 3 and 9. This is modeled as the following forces:

$$\begin{aligned}\mathbf{f}_{u3} &= \left[m_{u3} r_{u3} \Omega^2 \cos(\Omega t), m_{u3} r_{u3} \Omega^2 \sin(\Omega t)\right]^T, \\ \mathbf{f}_{u9} &= \left[m_{u9} r_{u9} \Omega^2 \cos(\Omega t), m_{u9} r_{u9} \Omega^2 \sin(\Omega t)\right]^T.\end{aligned}$$

Thus, by considering the excitation and displacement forces

$$\begin{aligned}\mathbf{f}_u(t) &= \left[\cdots, \mathbf{f}_{u3}, \cdots, \mathbf{f}_{u9}, \cdots\right]^T, \\ \mathbf{u}(t) &= \mathbf{U}(\omega) e^{-i\omega t + \phi_u},\end{aligned} \tag{4.47}$$

the unbalance response in the frequency domain is

$$\mathbf{U} = \left(-\omega^2 \mathbf{M} + i\omega\left(\mathbf{C} + \mathbf{G}(\Omega)\right) + \mathbf{K}\right)^{-1} \mathbf{f}_u. \tag{4.48}$$

This response is shown for three cases in Fig. 4.8. In the Case 1, a static unbalance was applied. Two identical unbalance masses were added in phase to the nodes 3 and 9. Similar to the FRF in Fig. 4.6, only the first mode is excited with a static unbalance. The Case 2 is simulated with a couple unbalance. A similar arrangement to the static unbalance was used, but the masses were located 180° opposite to each other. The response magnitude only excites the second critical speed. The Case 3 combines the static and couple unbalances. The masses are also located with a 180° phase, but the masses are different. This dynamic unbalance excites the first and second critical speeds.

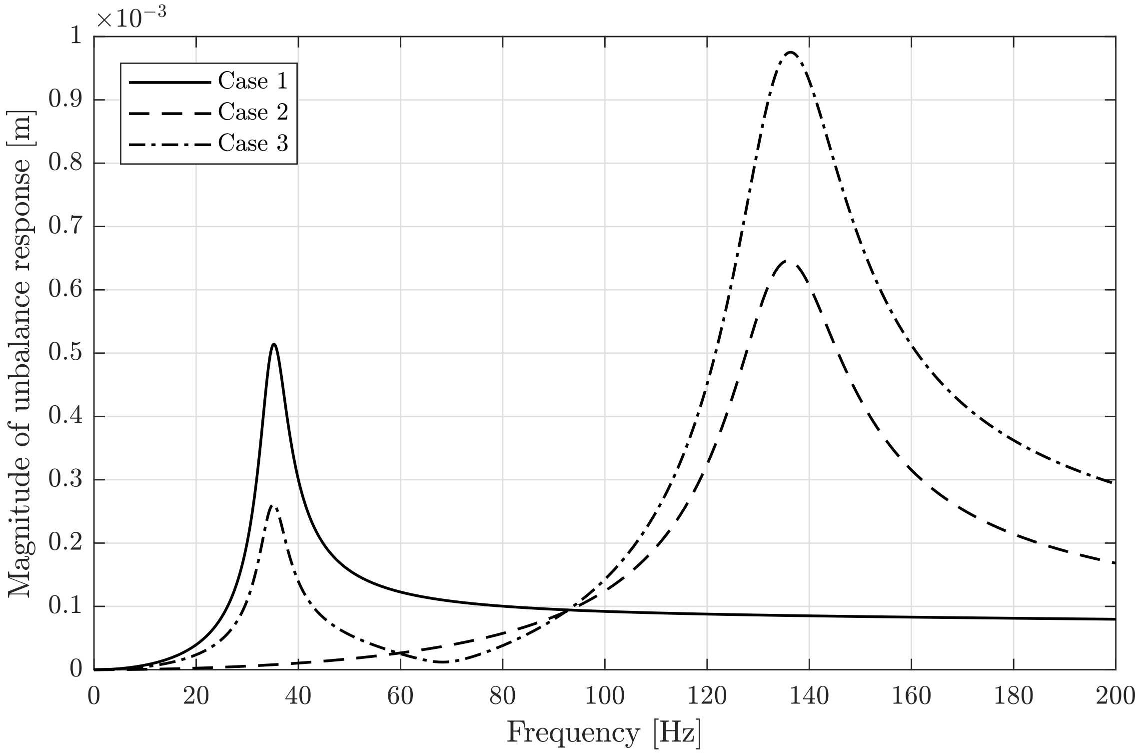

Figure 4.8: Magnitude of the system response due to unbalance forces. Three cases were tested. Case 1: Static unbalance. Case 2: Couple unbalance. Case 3: Dynamic unbalance.

4.4.5 Complex Dynamic Stiffness

The Complex Dynamic Stiffness (CDS) is defined as

$$\mathbf{H} = -\omega^2\mathbf{M} + i\omega\left(\mathbf{C} + \mathbf{G}(\Omega)\right) + \mathbf{K}, \tag{4.49}$$

which is the inverse of the FRF from Eq. (4.46). It is a convenient function because the system matrices are directly obtained from its real and imaginary parts. Fig. 4.9 shows the magnitude of the CDS computed at the left proximity sensor of the rig for an excitation along the x direction. The critical speeds correspond to points of minimum amplitude. The real part of the CDS corresponds to $\mathbf{K} - \omega^2\mathbf{M}$, which are quadratic equations with respect to the frequency. Fig. 4.9 shows this function computed at the left proximity sensor of the rig. The zeroes of this function corresponds to the critical speeds. On the other hand, the imaginary part of the CDS corresponds to $\omega\mathbf{C}$, which are linear equations with respect to the frequency. Fig. 4.9 shows this function computed at the left proximity sensor of the rig. Since the modal damping model was used in the finite element method, the slope of the curve correspond to the damping. The identification method explained in Chapter 6 is based on the CDS.

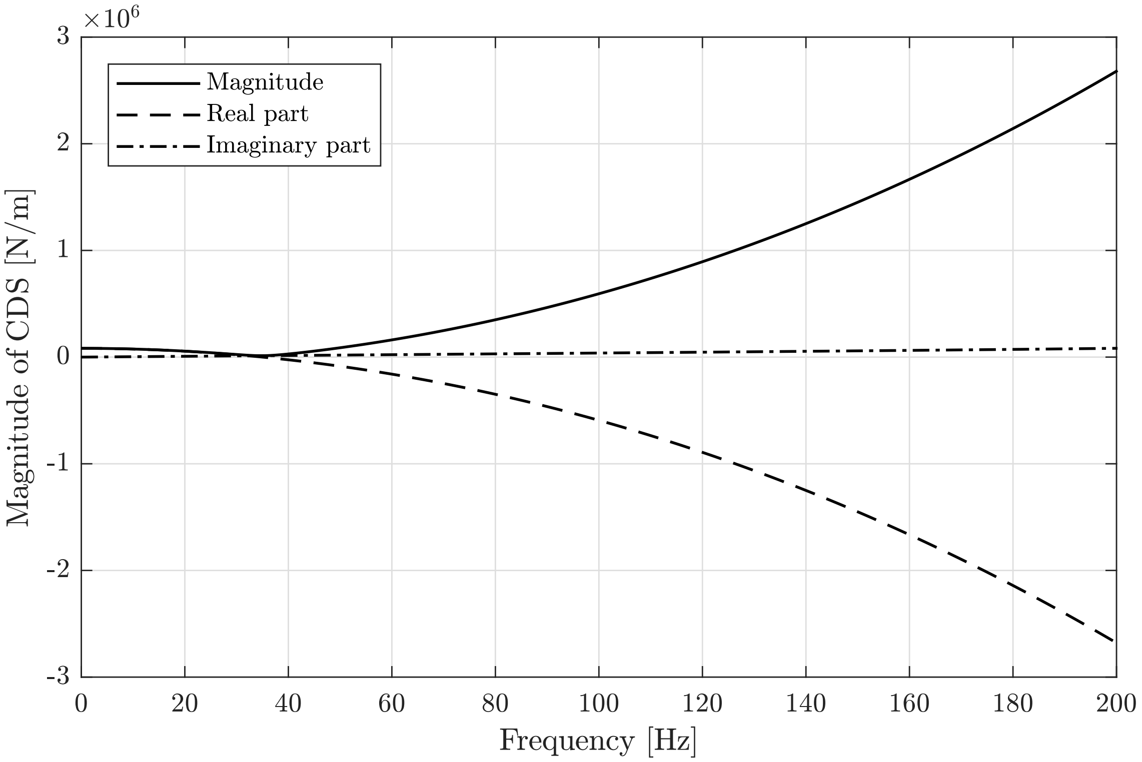

Figure 4.9: CDS for an excitation at nodes 4 and 8, and displacements computed at node 4.

Chapter 5

Electromagnetic model of the actuator

The actuator is formed basically by a rotor, an eight-pole stator and coils wound in each pole, as shown in Fig. 5.1. The excitation forces of the actuator are created due to the magnetic field imposed by electric currents carried by the coils. Considering a ferromagnetic material with high permeability μ_0, the electromagnetic forces acting on the body can be approximated as

$$\mathbf{f} = \frac{1}{2\mu_0} \oiint |\mathbf{B}|^2 d\mathbf{s}, \tag{5.1}$$

where $\mathbf{s}$ is a surface enclosing the body. The purpose of this section is to determine the magnetic flux density $\mathbf{B}$ in order to obtain the actuator's electromagnetic forces in terms of the coils currents and the material properties.

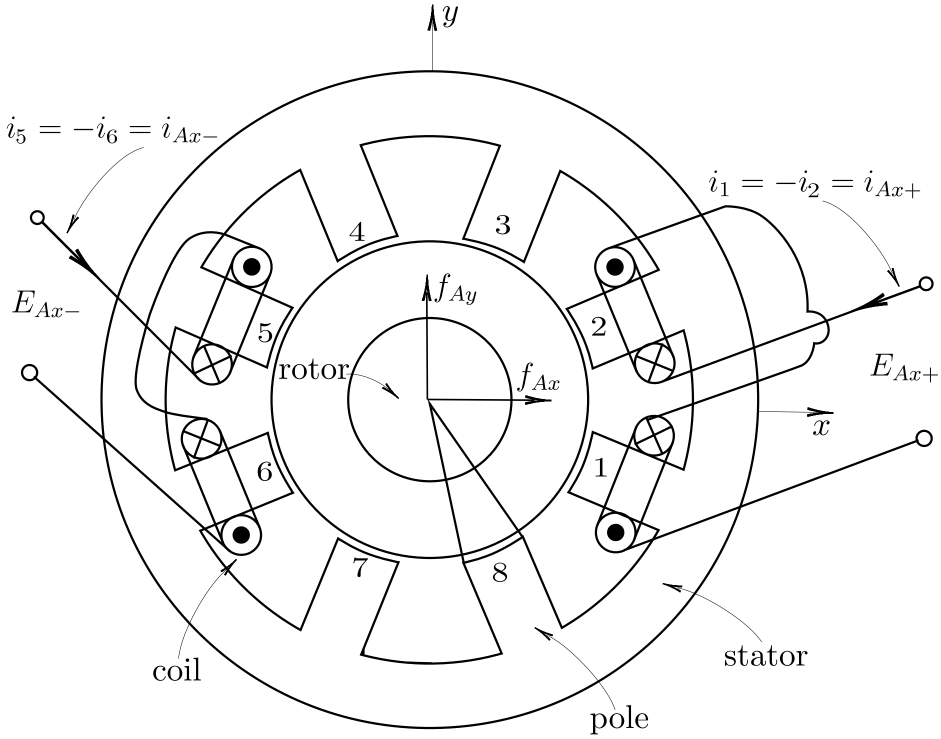

Figure 5.1: Magnetic actuator with an eight poles electromagnet.

5.1 Constitutive law of the material

An electric current creates a magnetic field intensity $\mathbf{H}$ (A/m), regardless the type of material inserted in the field. The magnetic flux density $\mathbf{B}$ (Tesla) is a response of the material to the magnetic field $\mathbf{H}$. For an isotropic material and low frequency excitation, they are related by

$$\mathbf{B}(t) = \mu(t)\mathbf{H}(t), \tag{5.2}$$

where μ is known as permeability. A typical B-H curve for a silicon iron is shown in Fig. 5.2. Two important properties can be observed. The permeability is the slope of the curve. The curve has an asymptotic behavior or saturation. This last property means that, when a certain magnetizing force is achieved, the material can no longer amplify the applied field.

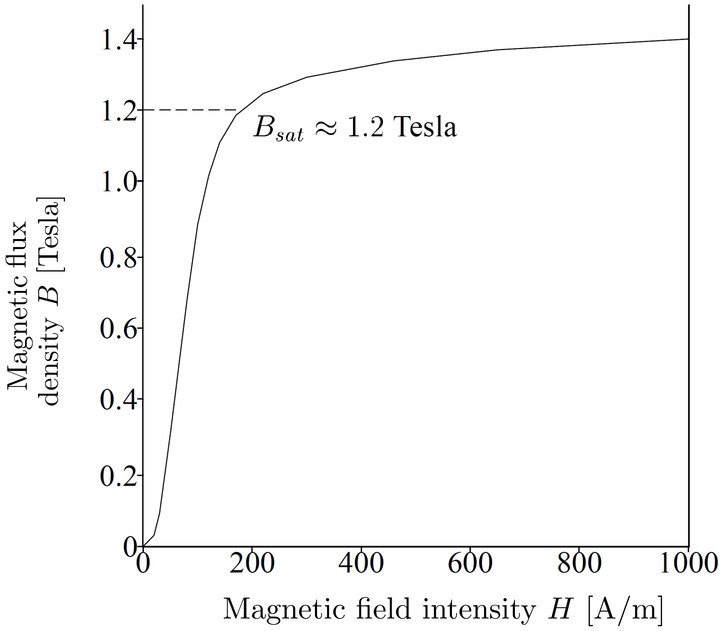

Figure 5.2: *B*-*H* curve for a silicon iron (from Maslen [80]).

5.2 Governing equations

The Maxwell's equations are useful to describe the magnetic quantities, specially the Ampere's and Gauss's Law.

Ampère's law

Considering a two dimension model of the actuator shown in Fig. 5.3, the Ampère's law is expressed as

$$\oint_L \mathbf{H} \cdot d\boldsymbol{\ell} = \int_A \mathbf{J} \cdot d\mathbf{a}, \tag{5.3}$$

where L is a closed path around an open surface and $d\boldsymbol{\ell}$ a length vector of an infinitesimal element of L with the direction defined by the tangent to L. The vector $\mathbf{J}$ is the current density.

In order to simplify this law, one can make the following assumptions:

1. The vector $d\boldsymbol{\ell}$ is parallel to $\mathbf{H}$.
2. The path L can be broken into discrete segments n_s where $\mathbf{H}$ is constant.
3. The current density $\mathbf{J}$ is confined to the coils.
4. $\mathbf{J}$ is uniform along the coil.
5. The permeability is constant along each segment.

Thus, considering a stator with n_c coils, each one with N_k turns and carrying a curent i_k, the Ampère's law is simplified as:

$$\sum_{i=1}^{n_s} \frac{B_i \ell_i}{g_i} = \sum_{k=1}^{n_c} N_k i_k. \tag{5.4}$$

Considering the eight paths of the actuator, the following equations hold:

$$\frac{B_1 g_1}{\mu_0} - \frac{B_2 g_2}{\mu_0} = N(i_1 - i_2) \longrightarrow \text{for the loop between coils 1 and 2,} \tag{5.5a}$$

$$\frac{B_2 g_2}{\mu_0} - \frac{B_3 g_3}{\mu_0} = N(i_2 - i_3) \longrightarrow \text{for the loop between coils 2 and 3,} \tag{5.5b}$$

$$\frac{B_3 g_3}{\mu_0} - \frac{B_4 g_4}{\mu_0} = N(i_3 - i_4) \longrightarrow \text{for the loop between coils 3 and 4,} \tag{5.5c}$$

$$\frac{B_4 g_4}{\mu_0} - \frac{B_5 g_5}{\mu_0} = N(i_4 - i_5) \longrightarrow \text{for the loop between coils 4 and 5,} \tag{5.5d}$$

$$\frac{B_5 g_5}{\mu_0} - \frac{B_6 g_6}{\mu_0} = N(i_5 - i_6) \longrightarrow \text{for the loop between coils 5 and 6,} \tag{5.5e}$$

$$\frac{B_6 g_6}{\mu_0} - \frac{B_7 g_7}{\mu_0} = N(i_6 - i_7) \longrightarrow \text{for the loop between coils 6 and 7,} \tag{5.5f}$$

$$\frac{B_7 g_7}{\mu_0} - \frac{B_8 g_8}{\mu_0} = N(i_7 - i_8) \longrightarrow \text{for the loop between coils 7 and 8.} \tag{5.5g}$$

Gauss's Law (Conservation of flux)

From Fig. 5.3, the Gauss's law is expressed as

$$\oiint_S \mathbf{B} \cdot d\mathbf{s} = 0, \tag{5.6}$$

where S is a closed surface surrounding a certain volume and $d\mathbf{s}$ is a vector area of an infinitesimal element of S. The direction of $d\mathbf{s}$ is normal to S.

This law can also be simplified assuming that total surface enclosing the magnetic circuit can be divided into n_p discrete patches where $\mathbf{B}$ is parallel to $d\mathbf{s}$. Thus, the Gauss's law is reduced to:

$$\sum_{i=1}^{n_p} B_i A_i = 0. \tag{5.7}$$

Considering a constant area A_g, the equation of conservation of flux are

$$A_g(B_1 + B_2 + B_3 + B_4 + B_5 + B_6 + B_7 + B_8) = 0. \tag{5.8}$$

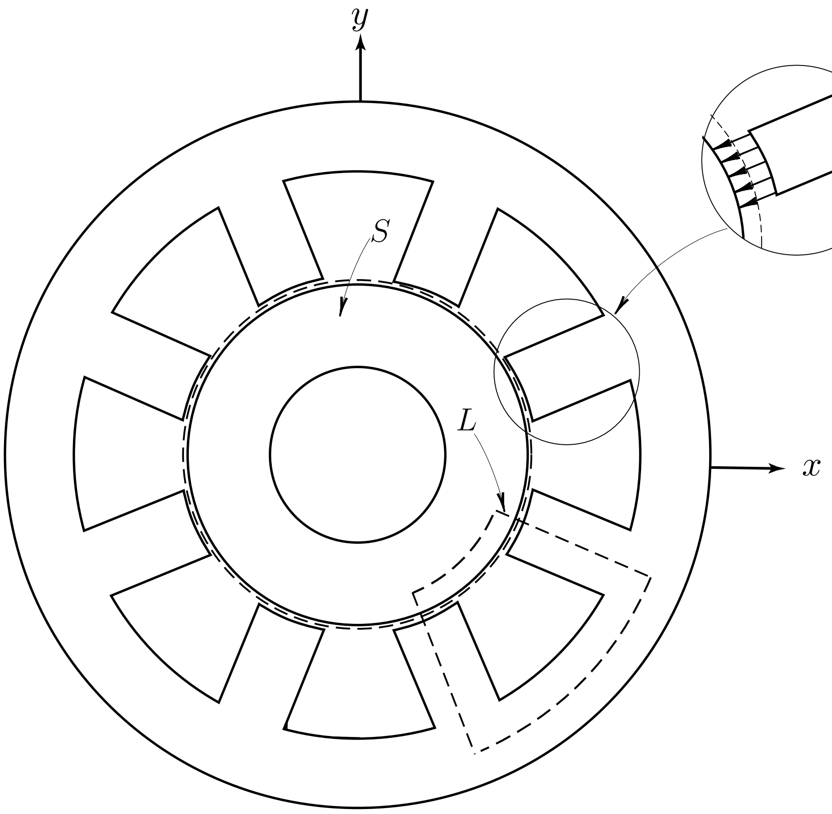

Figure 5.3: Gauss's and Ampère's law applied to one patch and one path.

5.2.1 Force model

The force vector of Eq. (5.1) is also simplified by using the previous assumptions. It is expressed as:

$$\mathbf{f} = \frac{1}{2\mu_0}\sum_{i=1}^{n_p} B_i^2 A_i \mathbf{n}_{A_i} = \begin{bmatrix} f_x \\ f_y \end{bmatrix} = \begin{bmatrix} \frac{1}{2\mu_0}\sum_{i=1}^{n_p} B_i^2 A_i \cos(\frac{\pi}{4}i - \frac{3\pi}{8}) \\ \frac{1}{2\mu_0}\sum_{i=1}^{n_p} B_i^2 A_i \sin(\frac{\pi}{4}i - \frac{3\pi}{8}) \end{bmatrix}, \tag{5.9}$$

where $\mathbf{n}_{A_i}$ is an unitary vector perpendicular to the patch's area A_i. In matrix notation, the magnetic forces, expressed in an inertial frame with coordinates (x, y), are:

$$\mathbf{f} = \begin{bmatrix} \mathbf{B}^T \mathbf{A}_x \mathbf{B} \\ \mathbf{B}^T \mathbf{A}_y \mathbf{B} \end{bmatrix}. \tag{5.10}$$

where

$$\mathbf{A}_x = \frac{A_g}{2\mu_0}\begin{bmatrix} 1 & 0 & 0 & 0 & 0 & 0 & 0 & 0 \\ 0 & \frac{1}{\sqrt{2}} & 0 & 0 & 0 & 0 & 0 & 0 \\ 0 & 0 & 0 & 0 & 0 & 0 & 0 & 0 \\ 0 & 0 & 0 & \frac{-1}{\sqrt{2}} & 0 & 0 & 0 & 0 \\ 0 & 0 & 0 & 0 & -1 & 0 & 0 & 0 \\ 0 & 0 & 0 & 0 & 0 & \frac{-1}{\sqrt{2}} & 0 & 0 \\ 0 & 0 & 0 & 0 & 0 & 0 & 0 & 0 \\ 0 & 0 & 0 & 0 & 0 & 0 & 0 & \frac{1}{\sqrt{2}} \end{bmatrix}, \tag{5.11}$$

$$\mathbf{A}_y = \frac{A_g}{2\mu_0}\begin{bmatrix} 0 & 0 & 0 & 0 & 0 & 0 & 0 & 0 \\ 0 & \frac{1}{\sqrt{2}} & 0 & 0 & 0 & 0 & 0 & 0 \\ 0 & 0 & 1 & 0 & 0 & 0 & 0 & 0 \\ 0 & 0 & 0 & \frac{1}{\sqrt{2}} & 0 & 0 & 0 & 0 \\ 0 & 0 & 0 & 0 & 0 & 0 & 0 & 0 \\ 0 & 0 & 0 & 0 & 0 & \frac{-1}{\sqrt{2}} & 0 & 0 \\ 0 & 0 & 0 & 0 & 0 & 0 & -1 & 0 \\ 0 & 0 & 0 & 0 & 0 & 0 & 0 & \frac{-1}{\sqrt{2}} \end{bmatrix}, \tag{5.12}$$

are the air gap area matrices.

For the actuator of Fig. 5.1, the governing equations can be expressed in matrix notation as

$$\mathbf{RB} = \mathbf{Ni}, \tag{5.13}$$

where

$$\mathbf{B} = \begin{bmatrix} B_1 & B_2 & B_3 & B_4 & B_5 & B_6 & B_7 & B_8 \end{bmatrix}^T, \tag{5.14}$$

$$\mathbf{N} = N\begin{bmatrix} 1 & -1 & 0 & 0 & 0 & 0 & 0 & 0 \\ 0 & 1 & -1 & 0 & 0 & 0 & 0 & 0 \\ 0 & 0 & 1 & -1 & 0 & 0 & 0 & 0 \\ 0 & 0 & 0 & 1 & -1 & 0 & 0 & 0 \\ 0 & 0 & 0 & 0 & 1 & -1 & 0 & 0 \\ 0 & 0 & 0 & 0 & 0 & 1 & -1 & 0 \\ 0 & 0 & 0 & 0 & 0 & 0 & 1 & -1 \\ 0 & 0 & 0 & 0 & 0 & 0 & 0 & 0 \end{bmatrix}, \tag{5.15}$$

$$\mathbf{i} = \begin{bmatrix} i_1 & i_2 & i_3 & i_4 & i_5 & i_6 & i_7 & i_8 \end{bmatrix}^T, \tag{5.16}$$

$$
\mathbf{R} = \frac{1}{\mu_0}\begin{bmatrix} -g_1 & g_2 & 0 & 0 & 0 & 0 & 0 & 0 \\ 0 & -g_2 & g_3 & 0 & 0 & 0 & 0 & 0 \\ 0 & 0 & -g_3 & g_4 & 0 & 0 & 0 & 0 \\ 0 & 0 & 0 & -g_4 & g_5 & 0 & 0 & 0 \\ 0 & 0 & 0 & 0 & -g_5 & g_6 & 0 & 0 \\ 0 & 0 & 0 & 0 & 0 & -g_6 & g_7 & 0 \\ 0 & 0 & 0 & 0 & 0 & 0 & -g_7 & g_8 \\ \mu_0 A_g & \mu_0 A_g & \mu_0 A_g & \mu_0 A_g & \mu_0 A_g & \mu_0 A_g & \mu_0 A_g & \mu_0 A_g \end{bmatrix}, \tag{5.17}
$$

with

$$
\begin{aligned}
g_1 =& g_0 - x, && (5.18)\\
g_2 =& g_0 - \frac{1}{\sqrt{2}}x - \frac{1}{\sqrt{2}}y, && (5.19)\\
g_3 =& g_0 - y, && (5.20)\\
g_4 =& g_0 + \frac{1}{\sqrt{2}}x - \frac{1}{\sqrt{2}}y, && (5.21)\\
g_5 =& g_0 + x, && (5.22)\\
g_6 =& g_0 + \frac{1}{\sqrt{2}}x + \frac{1}{\sqrt{2}}y, && (5.23)\\
g_7 =& g_0 + y, && (5.24)\\
g_8 =& g_0 - \frac{1}{\sqrt{2}}x + \frac{1}{\sqrt{2}}y. && (5.25)
\end{aligned}
$$

$\mathbf{R}$ is the reluctance matrix, $\mathbf{N}$ is the linkage matrix, and $\mathbf{i}$ the current vector and $\mathbf{B}$ is the magnetic flux density vector.

Thus, the magnetic flux density vector can be obtained by:

$$
\mathbf{B} = \mathbf{R}^{-1}\mathbf{N}\mathbf{i}. \tag{5.26}
$$

Substituting Eq. (5.26) in Eq. (5.10), the magnetic force vector in terms of the current vector, linkage matrix, reluctance matrix and area matrices is

$$
\mathbf{f} = \begin{bmatrix} \mathbf{i}^T\mathbf{N}^T\mathbf{R}^{-T}\mathbf{A}_x\mathbf{R}^{-1}\mathbf{N}\mathbf{i} \\ \mathbf{i}^T\mathbf{N}^T\mathbf{R}^{-T}\mathbf{A}_y\mathbf{R}^{-1}\mathbf{N}\mathbf{i} \end{bmatrix}. \tag{5.27}
$$

For small displacements inside the gap, Eq. (5.27) is reduced to:

$$\mathbf{f} = \begin{bmatrix} \cos(\frac{\pi}{8})\mu_0 A_g N^2 \left(\dfrac{i_1^2}{\left(g_0 - x\cos(\frac{\pi}{8})\right)^2} - \dfrac{i_5^2}{\left(g_0 + x\cos(\frac{\pi}{8})\right)^2} \right) \\ \cos(\frac{\pi}{8})\mu_0 A_g N^2 \left(\dfrac{i_3^2}{\left(g_0 - y\cos(\frac{\pi}{8})\right)^2} - \dfrac{i_7^2}{\left(g_0 + y\cos(\frac{\pi}{8})\right)^2} \right) \end{bmatrix}. \tag{5.28}$$

Eq. (5.28) was obtained by using a symbolic computation code in Mathematica, which is shown in Appendix E.4.

Linearization of the force model

The forces of Eq. (5.27) depend on eight independent currents. For applications such as excitation and control, it is convenient to reduce the independent currents by wiring two consecutive coils in series and applying a bias current. This configuration is shown in Fig. 5.4. This current law is applied by using the current matrix $\mathbf{C}$:

$$\mathbf{i} = \mathbf{C}\hat{\mathbf{i}}, \tag{5.29}$$

where

$$\mathbf{C} = \begin{bmatrix} 1 & 0 & 1 \\ -\frac{\sqrt{2}}{2} & -\frac{\sqrt{2}}{2} & -1 \\ 0 & 1 & 1 \\ \frac{\sqrt{2}}{2} & -\frac{\sqrt{2}}{2} & -1 \\ -1 & 0 & 1 \\ \frac{\sqrt{2}}{2} & \frac{\sqrt{2}}{2} & -1 \\ 0 & -1 & 1 \\ -\frac{\sqrt{2}}{2} & \frac{\sqrt{2}}{2} & -1 \end{bmatrix}, \ \hat{\mathbf{i}} = \begin{bmatrix} i_x \\ i_y \\ i_0 \end{bmatrix}. \tag{5.30}$$

i_0 is the bias current and i_x, i_y are the current perturbations related to the forces along the x and y directions, respectively. The substitution of Eq. (5.29) gives the force model

$$\mathbf{f} = \begin{bmatrix} \hat{\mathbf{i}}^T\mathbf{C}^T\mathbf{i}^T\mathbf{N}^T\mathbf{R}^{-T}\mathbf{A}_x\mathbf{R}^{-1}\mathbf{N}\mathbf{C}\hat{\mathbf{i}} \\ \hat{\mathbf{i}}^T\mathbf{C}^T\mathbf{i}^T\mathbf{N}^T\mathbf{R}^{-T}\mathbf{A}_y\mathbf{R}^{-1}\mathbf{N}\mathbf{C}\hat{\mathbf{i}} \end{bmatrix}. \tag{5.31}$$

In order to obtain a linear force model, Eq. (5.27) is expanded in Taylor series. If small current and displacement perturbations are considered, the following equation

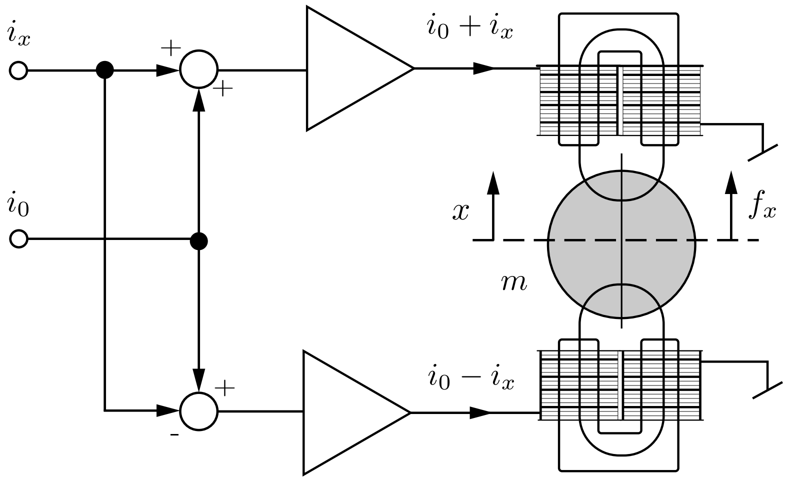

Figure 5.4: Magnetic actuator pair with differential configuration (modified from Schweitzer and Maslen [90])

holds:

$$\mathbf{f} \approx \begin{bmatrix} f_x(x_0, i_x) + \dfrac{\partial f_x(0, i_x)}{\partial i_{px}}(i_0 - i_x) + \dfrac{\partial f_x(x_0, i_x)}{\partial x}(x - x_0) \\ f_y(y_0, i_y) + \dfrac{\partial f_y(0, i_y)}{\partial i_{py}}(i_0 - i_y) + \dfrac{\partial f_y(y_0, i_y)}{\partial y}(y - y_0) \end{bmatrix}. \tag{5.32}$$

The actuator gain is defined as

$$\mathbf{K}_i \equiv \begin{bmatrix} \dfrac{\partial f_x}{\partial i_{px}} & \dfrac{\partial f_x}{\partial i_{py}} \\ \dfrac{\partial f_y}{\partial i_{px}} & \dfrac{\partial f_y}{\partial i_{py}} \end{bmatrix} = K_i \begin{bmatrix} 1 & 0 \\ 0 & 1 \end{bmatrix}, \tag{5.33}$$

where

$$K_i = 2\hat{\mathbf{i}}^T \mathbf{C}^T \mathbf{N}^T \mathbf{R}^{-T}(0,0) \mathbf{A}_x \mathbf{R}^{-1}(0,0) \mathbf{N}\mathbf{C} \tag{5.34}$$

$$= \frac{4\mu_0 A_g N^2 i_0}{g_0^2}. \tag{5.35}$$

The open loop stiffness is defined as

$$\mathbf{K}_q \equiv \begin{bmatrix} \dfrac{\partial f_x}{\partial x} & \dfrac{\partial f_x}{\partial y} \\ \dfrac{\partial f_y}{\partial x} & \dfrac{\partial f_y}{\partial y} \end{bmatrix} = \begin{bmatrix} K_{xx} & K_{xy} \\ K_{yx} & K_{yy} \end{bmatrix} = -\frac{\mu_0 A_g N^2}{g^3} \begin{bmatrix} 3i_x^2 + i_y^2 + 4i_0^2 & i_x i_y \\ i_x i_y & i_x^2 + 3i_y^2 + 4i_0^2 \end{bmatrix}, \tag{5.36}$$

where

$$K_{ij} = \hat{\mathbf{i}}_p^T \mathbf{C}^T \mathbf{N}^T \left(\frac{\partial \mathbf{R}^{-T}}{\partial j} \mathbf{A}_i \mathbf{R}^{-1} + \mathbf{R}^{-T} \mathbf{A}_i \frac{\partial \mathbf{R}^{-1}}{\partial j} \right) \mathbf{N}\mathbf{C}\hat{\mathbf{i}}_p, \quad \text{for } i, j \in \{x, y\}. \tag{5.37}$$

Thus,

$$\mathbf{K}_q = -\frac{\mu_0 A_g N^2}{g^3}\begin{bmatrix} 3i_x^2 + i_y^2 + 4i_0^2 & i_x i_y \\ i_x i_y & i_x^2 + 3i_y^2 + 4i_0^2 \end{bmatrix}. \tag{5.38}$$

If i_x and i_y are small perturbations, then

$$K_q = -\frac{4i_0^2 \mu_0 A_g N^2}{g_0^3}, \tag{5.39}$$

$$\mathbf{f} = \mu_o N^2 A_g \left(\frac{i_0}{g_0^2}\mathbf{i}_p - \frac{i_0^2}{g_0^3}\mathbf{q}\right). \tag{5.40}$$

This equation is used to perform the simulations using the model proposed in the next section. Note that in order to obtain a linear model, a bias current must be used. This must be taken into account because, if no bias current is supplied, the forces applied to the rotor may be nonlinear and harmonic distortions will appear, which is not desirable, since the identification method is based on characteristics of linear systems.

5.2.2 Effect of bias current on the rotor response

Linearity is an advantageous characteristic for parameters identification. When a linear system is excited with a single frequency component, the system respond with a proportional amplitude signal at the same frequency. When a nonlinear system is excited with a single frequency signal, other frequencies also appear in the response. This means that the energy applied leaks to other frequencies.

This linearity requirement is fulfilled by the rotor, bearings and seal. However, the electromagnetic model of the forces may become nonlinear if no bias current is applied. In order to illustrate these nonlinear effects, a multisine signal with 17 frequency component was applied to the rig's actuators with zero rotor speed. Fig. 5.5a shows the force from actuator A with a linearized model with bias current. The amplitude profile was chosen to excite the rotor with no contact between stator and rotor, as will be discussed in Chapter 6. The flat vibration response obtained is shown in Fig. 5.6a. On the other hand, if no bias current is used, the amplitude profile of the force is distorted and some additional frequency components are added, as shown in Fig. 5.6b. The vibration response of this force is shown in Fig. 5.5b. There are two important differences between both vibration responses. One of them, the amplitude is not flat anymore. However, the most important effect is the appearance of other frequency components of considerable amplitudes. Thus, the use of bias current improves the energy distribution along the desired frequency components.

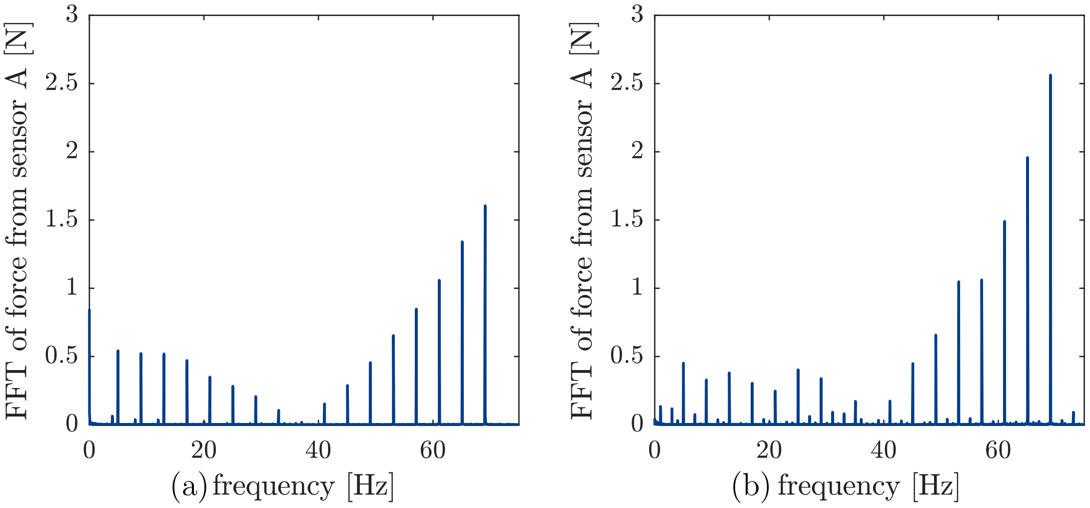

Figure 5.5: Excitation signal with (a) and without (b) bias currents in the magnetic actuators' coils.

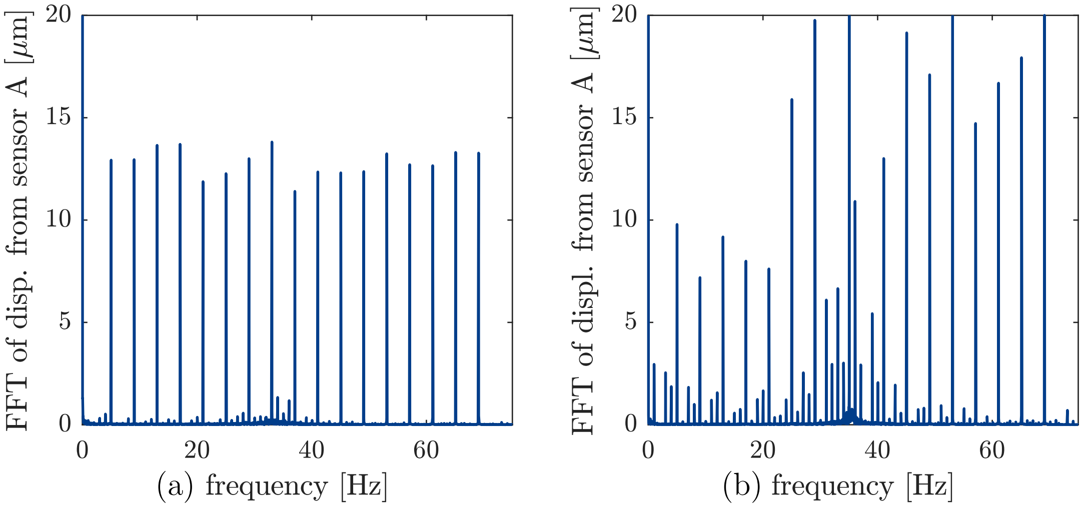

Figure 5.6: Experimental displacement response signal with (a) and without (b) bias currents in the magnetic actuators' coils.

Chapter 6

Identification methodology

6.1 Introduction

The parameter identification of a rotating machine is performed by applying excitation forces and measuring variables such as displacement, velocity and acceleration. Several excitation approaches have been applied: impulsive signals with instrumented hammers; and single harmonic, multisine and pseudorandom signals with hydraulic shakers and magnetic bearings (Nordmann [91], Lee [92], Kozanecka et al. [93], Wagner et al. [3], Wagner [94], Matros and Nordmann [95], Wagner and Pietruszka [96]). The use of contactless actuators to excite the rotor for identification purposes has been studied intensively during the last 25 years due to the advantages.

In this chapter, an identification methodology is applied to obtain the seal coefficients of the test rig by using magnetic actuators. The rotor is excited harmonically by the electromagnets and the rotor-seal relative displacement are measure by proximity sensors. Assuming a linear system, the seal forces are considered as a spring-damper system with stiffness and damping coefficients. The methodology is based on a frequency approach, in which all variables are transformed to the frequency domain by means of the Fourier transform. Moreover, an estimator is used to reduce the effect of the noise on the coefficients.

The identification scheme is shown in Fig. 6.1. In the first block, the excitation signals vector $\mathbf{v}$ are created in a LabView program. These are voltage signals and are connected to a power amplifier that drivers the coils of the electromagnetic actuators. This voltage set currents in each coil, represented by $\mathbf{i}_a$, and the electromagnetic forces $\mathbf{f}_a$ are applied to the rig. The displacement $\mathbf{u}$ of the rotor and current of each coil are transformed to a voltage level by displacement and current sensors, represented by $\mathbf{u}_s$ and $\hat{\mathbf{i}}_a$, respectively. All sensor readings are stored in text files that are later used to estimate the parameters vector

$\hat{\mathbf{p}} = [K_{xx}, K_{xy}, K_{yx}, K_{yy}, C_{xx}, C_{xy}, C_{yx}, C_{yy}]^T$. The identification methodology is divided in three important steps. First, the computation of a complex matrix that is directly related to the parameters of the seals. Then, an averaging method to deal with noisy measurements from sensors. Finally, the design of the excitation signal to distribute the energy suitably.

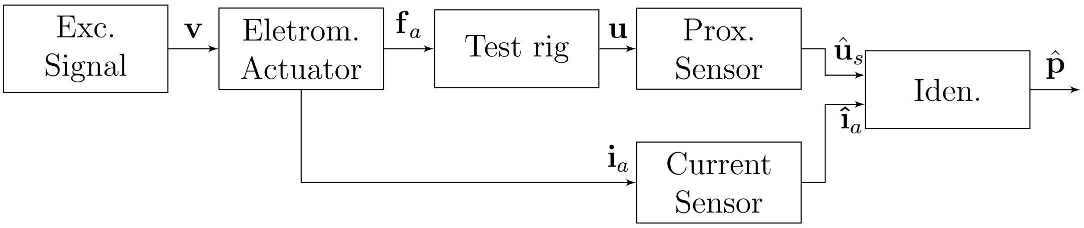

Figure 6.1: Block diagram of system excitation and parameter identification.

6.2 Annular gas seal model

Theoretical models of annular gas seals have been proposed mainly to compute the velocity and pressure fields of the flow inside the clearance, for different operating conditions. The pressure distribution is then integrated to determine the stiffness and damping coefficients. There are two common techniques to model the seals: A bulk-flow approach and CFD simulations. In the former, it is assumed that no shear stresses act inside the fluid but only on the boundaries, in the fluid-stator or fluid-rotor interfaces. In the latter, the fluid geometry is modeled in a CAD software, discretized in smaller subdomains, set some input variables and parameters, and then run a CFD simulation.

In general, the dynamics of the fluid between the rotor and seal depends on several parameters. Nevertheless, for a given operating condition and with small deflection of the rotor (less than $100\mu m$), the linear system

$$\begin{bmatrix} -f_{xs} \\ -f_{ys} \end{bmatrix} = \begin{bmatrix} K_{xx} & K_{xy} \\ K_{yx} & K_{yy} \end{bmatrix} \begin{bmatrix} u_{xs} \\ u_{ys} \end{bmatrix} + \begin{bmatrix} C_{xx} & C_{xy} \\ C_{yx} & C_{yy} \end{bmatrix} \begin{bmatrix} \dot{u}_{xs} \\ \dot{u}_{ys} \end{bmatrix} \tag{6.1}$$

is able to model the seal dynamics. K_{xx}, K_{yy}, C_{xx}, C_{yy} are the direct stiffness and damping coefficients, and K_{xy}, K_{yx}, C_{xy}, C_{yx} are the cross-coupled stiffness and damping coefficients. These parameters depend on different operating conditions such as rotor speed, pressure drop, gas density, inlet circumferential speed, clearance geometry, actuators frequency, etc. Moreover, it is common to consider the stiffness and damping matrices of Eq. (6.1) as skew-symmetric. In this case, Eq. (6.1) becomes

$$\begin{bmatrix} -f_{xs} \\ -f_{ys} \end{bmatrix} = \begin{bmatrix} K & k \\ -k & K \end{bmatrix} \begin{bmatrix} u_{xs} \\ u_{ys} \end{bmatrix} + \begin{bmatrix} C & c \\ -c & C \end{bmatrix} \begin{bmatrix} \dot{u}_{xs} \\ \dot{u}_{ys}, \end{bmatrix} \tag{6.2}$$

where K, k, C and c are obtained by averaging coefficients in Eq. (6.1), detailed in Chapter 6.

Eq. (6.1) can be represented in the frequency domain as

$$\begin{bmatrix} F_{xs} \\ F_{ys} \end{bmatrix} = \begin{bmatrix} H_{xx} & H_{xy} \\ H_{yx} & H_{yy} \end{bmatrix} \begin{bmatrix} U_{xs} \\ U_{ys} \end{bmatrix}, \tag{6.3}$$

where

$$H_{ij} = K_{ij} + i\omega C_{ij}, \ \text{ for } i = \{x, y\} \tag{6.4}$$

is the CDS of the seal with H_{xx} and H_{yy} representing the direct CDS and H_{xy} and H_{yx} the cross-coupled CDS. Parameters K_{xx}, K_{yy}, C_{xx}, C_{yy}, M_{xx}, and M_{yy} are called direct coefficients of the stiffness, damping and mass, while K_{xy}, K_{yx}, C_{xy}, C_{yx}, M_{xy} and M_{yx} are the cross-coupled coefficients of the stiffness, damping and mass, respectively. For gas seals, the mass does not affect the CDS considerable when compared to the mass of the rotor. In this case, the real part is directly related to stiffness coefficients and the imaginary part related to the damping multiplied by the excitation frequency. In the general case, the real part corresponds to a function in terms of the stiffness, mass and excitation frequency.

6.3 Identification method of the CDS

The seal CDS is obtained by exciting the rotor with the magnetic actuators and measuring the displacement at two points. Eq. (4.49) can be expressed as

$$\mathbf{H}(\omega_k)\mathbf{u}(\omega_k) = \mathbf{f}(\omega_k), \tag{6.5}$$

where $\mathbf{u} \in \mathbb{C}^{44\times1}$ and $\mathbf{f} \in \mathbb{C}^{44\times1}$ are vectors containing the displacements (linear and angular) and forces at each node, and $\mathbf{H} \in \mathbb{C}^{44\times44}$ is the CDS matrix

$$\mathbf{H}(\omega_k) = \left(-\omega^2\mathbf{M} + i\omega\left(\mathbf{C} + \mathbf{G}(\Omega)\right) + \mathbf{K}\right), \tag{6.6}$$

containing the mass, damping, stiffness and gyroscopic terms of the rotor, bearings and seals. Since the objective of the analysis is to obtain the seal coefficients, matrix $\mathbf{H}$ is rearranged to separate the effect of seals from that of the rotor and bearings.

Thus, the rearranged version of Eq. (6.5) is

$$\bar{\mathbf{H}}\bar{\mathbf{u}} = \bar{\mathbf{H}}_R \begin{bmatrix} \mathbf{u}_{s1} \\ \mathbf{u}_{s2} \\ \mathbf{u}_R \end{bmatrix} + \begin{bmatrix} \mathbf{H}_{s1} & \mathbf{0} & \mathbf{0} \\ \mathbf{0} & \mathbf{H}_{s2} & \mathbf{0} \\ \mathbf{0} & \mathbf{0} & \mathbf{0} \end{bmatrix} \begin{bmatrix} \mathbf{u}_{s1} \\ \mathbf{u}_{s2} \\ \mathbf{u}_R \end{bmatrix} = \begin{bmatrix} \mathbf{f}_{a1} \\ \mathbf{f}_{a2} \\ \mathbf{0} \end{bmatrix}, \tag{6.7}$$

where

$$\bar{\mathbf{H}}_R = \begin{bmatrix} \mathbf{H}_{R11} & \mathbf{H}_{R12} & \mathbf{H}_{R13} \\ \mathbf{H}_{R21} & \mathbf{H}_{R22} & \mathbf{H}_{R23} \\ \mathbf{H}_{R31} & \mathbf{H}_{R32} & \mathbf{H}_{R33} \end{bmatrix} \tag{6.8}$$

is the rearranged CDS matrix of the rotor and bearings, $\mathbf{u}_{s1} \in \mathbb{C}^{2\times1}$ and $\mathbf{u}_{s2} \in \mathbb{C}^{2\times1}$ are the displacement vector at the location of the proximity sensors, $\mathbf{u}_R \in \mathbb{C}^{40\times1}$ is the displacement vector of the remaining node's location, $\mathbf{f}_{a1} \in \mathbb{C}^{2\times1}$ and $\mathbf{f}_{a2} \in \mathbb{C}^{2\times1}$ are the actuators' forces, and $\mathbf{H}_{s1}$ and $\mathbf{H}_{s2}$ are the CDS matrices of the seals.

Although the seal forces are created at the test section of the rig (near the middle), the displacement and forces are only measured and applied at the sensors' and actuators' location (assuming that the forces are applied exactly at the proximity sensors). Thus, two set of parameters are obtained. As will be shown later, the seal parameters are defined as the average between $\mathbf{H}_{s1}$ and $\mathbf{H}_{s2}$.

Next, matrix $\bar{\mathbf{H}}_R$ is expressed in a compacted form and Eq. (6.7) turns to

$$\begin{bmatrix} \tilde{\mathbf{H}}_{R11} & \tilde{\mathbf{H}}_{R12} \\ \tilde{\mathbf{H}}_{R21} & \mathbf{H}_{R33} \end{bmatrix} \begin{bmatrix} \mathbf{u}_s \\ \mathbf{u}_R \end{bmatrix} + \begin{bmatrix} \mathbf{H}_{s12}\mathbf{u}_s \\ \mathbf{0} \end{bmatrix} = \begin{bmatrix} \mathbf{f}_a \\ \mathbf{0} \end{bmatrix}, \tag{6.9}$$

where

$$\tilde{\mathbf{H}}_{R11} = \begin{bmatrix} \mathbf{H}_{R11} & \mathbf{H}_{R12} \\ \mathbf{H}_{R12} & \mathbf{H}_{R22} \end{bmatrix}, \ \tilde{\mathbf{H}}_{R12} = \begin{bmatrix} \mathbf{H}_{R13} \\ \mathbf{H}_{R23} \end{bmatrix}, \ \tilde{\mathbf{H}}_{R21} = \begin{bmatrix} \mathbf{H}_{R31} & \mathbf{H}_{R32} \end{bmatrix}, \tag{6.10}$$
$$\mathbf{H}_{s12} = \begin{bmatrix} \mathbf{H}_{s1} & \mathbf{0} \\ \mathbf{0} & \mathbf{H}_{s2} \end{bmatrix}, \ \mathbf{u}_s = \begin{bmatrix} \mathbf{u}_{s1}^T & \mathbf{u}_{s2}^T \end{bmatrix}^T, \ \mathbf{f}_a = \begin{bmatrix} \mathbf{f}_{a1}^T & \mathbf{f}_{a2}^T \end{bmatrix}^T,$$

with $\tilde{\mathbf{H}}_{R11} \in \mathbb{C}^{4\times4}$, $\tilde{\mathbf{H}}_{R12} \in \mathbb{C}^{4\times40}$, $\tilde{\mathbf{H}}_{R21} \in \mathbb{C}^{40\times4}$, $\mathbf{H}_{R33} \in \mathbb{C}^{40\times40}$, $\mathbf{H}_{s12} \in \mathbb{C}^{4\times4}$, $\mathbf{u}_s \in \mathbb{C}^{4\times1}$ and $\mathbf{f}_a \in \mathbb{C}^{4\times1}$. Note that the displacement vector $\mathbf{u}_{s1}$ and $\mathbf{u}_{s2}$ are measured by the proximity sensors, and the actuators' forces $\mathbf{f}_{a1}$ and $\mathbf{f}_{a2}$ are measured indirectly by the current and proximity sensors. The displacements of the vector $\mathbf{u}_R$ are not measured, but they can be obtained from Eq. (6.9):

$$\mathbf{u}_R = -\mathbf{H}_{R33}^{-1}\tilde{\mathbf{H}}_{R21}\mathbf{u}_s = -\mathbf{H}_{R33}^{-1}\left(\tilde{\mathbf{H}}_{R31}\mathbf{u}_{s1} + \tilde{\mathbf{H}}_{R32}\mathbf{u}_{s2}\right). \tag{6.11}$$

Based on Eqs. (6.9) and (6.11), the equation that relates the matrix $\mathbf{H}_{s12}$ and vector

$\mathbf{u}_s$ and $\mathbf{f}_a$ is:

$$\left(\tilde{\mathbf{H}}_{R11} + \mathbf{H}_{s12} - \tilde{\mathbf{H}}_{R12}\mathbf{H}_{R33}^{-1}\tilde{\mathbf{H}}_{R21}\right)\mathbf{u}_s = \mathbf{f}_a. \tag{6.12}$$

Note that the only unknown matrix is $\mathbf{H}_{s12}$. However, algebraically, there are eight unknowns (four coefficients for each seal) but only 4 equations. In order to overcome the lack of information, the rotor is excited in two orthogonal direction and eight equations are obtained in total. With this approach, Eq. (6.12) turns to

$$\left(\tilde{\mathbf{H}}_{R11} + \mathbf{H}_{s12} - \tilde{\mathbf{H}}_{R12}\mathbf{H}_{R33}^{-1}\tilde{\mathbf{H}}_{R21}\right)\mathbf{U}_s = \mathbf{F}_a, \tag{6.13}$$

with

$$\mathbf{F}_a = \begin{bmatrix} \mathbf{f}_{a,11} & \mathbf{f}_{a,12} \\ \mathbf{f}_{a,21} & \mathbf{f}_{a,22} \end{bmatrix}, \; \mathbf{U}_s = \begin{bmatrix} \mathbf{U}_{s,11} & \mathbf{U}_{s,12} \\ \mathbf{U}_{s,21} & \mathbf{U}_{s,22} \end{bmatrix}. \tag{6.14}$$

The subscript ij means a quantity obtained along the i-direction for an excitation along the j-direction. Thus, Eq. (6.13) can be used to obtain the seal coefficients:

$$\mathbf{H}_{s12} = \mathbf{F}_a\mathbf{U}_s^{-1} + \tilde{\mathbf{H}}_{R12}\mathbf{H}_{R33}^{-1}\tilde{\mathbf{H}}_{R21} - \tilde{\mathbf{H}}_{R11}. \tag{6.15}$$

Note that the coefficients depends on the measurements and a previously known model of the rotor and bearings. In the next subsection, two-step procedure is used to avoid this dependency.

6.3.1 Baseline and overall test approach

When a test is performed, the CDS matrix $\mathbf{F}_a\mathbf{U}_s^{-1}$ contains the effects of the seals, rotor and bearings. If a test is performed previously without the effect of the seals, the CDS matrix will only contain the effects of the rotor and bearings. Intuitively, one can subtract both matrices to obtain only the effects related to the seals. Mathematically, a baseline and overall test matrices are defined:

$$(\mathbf{H}_s)_{\text{base}} \equiv \left(\mathbf{F}_a\mathbf{U}_s^{-1}\right)_{\text{base}} \longrightarrow \text{No pressure,} \tag{6.16}$$

$$(\mathbf{H}_s)_{\text{over}} \equiv \left(\mathbf{F}_a\mathbf{U}_s^{-1}\right)_{\text{over}} \longrightarrow \text{With pressure.} \tag{6.17}$$

The baseline CDS matrix can be obtained by removing the supply pressure.

Based on Eqs. (6.15), (6.16) and (6.17), the baseline and overall CDS matrices are

$$(\mathbf{H}_s)_{\text{base}} = \tilde{\mathbf{H}}_{R11} - \tilde{\mathbf{H}}_{R12}\mathbf{H}_{R33}^{-1}\tilde{\mathbf{H}}_{R21}, \tag{6.18}$$

$$(\mathbf{H}_s)_{\text{over}} = \tilde{\mathbf{H}}_{R11} + \mathbf{H}_{s12} - \tilde{\mathbf{H}}_{R12}\mathbf{H}_{R33}^{-1}\tilde{\mathbf{H}}_{R21}. \tag{6.19}$$

The seals' CDS matrix are obained by subtracting (6.18) from (6.19):

$$\mathbf{H}_{s12} = \mathbf{H}_s^{\text{over}} - \mathbf{H}_s^{\text{base}}. \tag{6.20}$$

Thus, the CDS of each seal is

$$\mathbf{H}_{s1} = \mathbf{F}_a \mathbf{U}_{s1}^{\text{over}-1} - \mathbf{F}_a \mathbf{U}_{s1}^{\text{base}-1}, \tag{6.21}$$

$$\mathbf{H}_{s2} = \mathbf{F}_a \mathbf{U}_{s2}^{\text{over}-1} - \mathbf{F}_a \mathbf{U}_{s2}^{\text{base}-1}. \tag{6.22}$$

As can be noted in Eq. (6.21), each CDS matrix is obtained with only the measurements from the overall and baseline tests, removing the dependency on the model of the rotor and bearings. This approach is also advantageous if any unexpected linear perturbation is present in the test.

Finally, both CDS matrices are averaged to obtain the seal CDS:

$$\mathbf{H}_s = \frac{\mathbf{H}_{s1} + \mathbf{H}_{s2}}{2}. \tag{6.23}$$

This equation is valid only if the rotor is excited with actuator in a symmetrical manner.

6.4 Estimation of the CDS matrix

Electronic devices such as sensors are susceptible of random errors or deviation of their readings, also known as noise. A measure of the quality of a sensor measurements is the Signal-to-Noise ratio (SNR). If the mean value of the noise is zero, several repetitions (or blocks) of the measurement can be taken and averaged to reduce the noise effects on the estimates. Estimators [97] can be used to reduce the noise effects on an FRF. Further details about estimators can be found in Pintelon and Schoukens [98]. In this thesis, the estimator is based on the power spectral density of the signals, similar to that used by Childs and Hale [99].

Based on Eq. (6.13), the relation between the CDS matrix, the force matrix and the displacement matrix is

$$\mathbf{F}(\omega_k) = \mathbf{H}(\omega_k)\mathbf{U}(\omega_k). \tag{6.24}$$

After several algebraic manipulations (see Appendix A), two important equations, relating spectral densities $\mathbf{S}_{uu}(\omega_k)$, $\mathbf{S}_{ff}(\omega_k)$ and $\mathbf{S}_{uf}(\omega_k)$, are obtained:

$$\mathbf{S}_{ff}(\omega_k) = \mathbf{H}^*(\omega_k)\mathbf{S}_{uu}(\omega_k)\mathbf{H}(\omega_k), \tag{6.25}$$

$$\mathbf{S}_{uf}(\omega_k) = \mathbf{S}_{uu}(\omega_k)\mathbf{H}(\omega_k). \tag{6.26}$$

These two equations are used to obtain the CDS matrix $\mathbf{H}$. One alternative is to multiply both sides of Eq. (6.26) by $\mathbf{S}_{uu}^{-1}$. This is called the H_1 estimator. A second alternative is to conjugate Eq. (6.26) and substitute $\mathbf{H}^*$ in Eq. (6.25). This gives the H_2 estimator. These methods are explained in the following section and a short proof is available in the Appendix B.

6.5 $\mathbf{H}_1$, $\mathbf{H}_2$ and $\mathbf{H}_3$ Estimators

For the calculation of the CDS matrix, the following disturbing noise model is considered:

$$\mathbf{U}(\omega_k) = \mathbf{U}_0(\omega_k) + \mathbf{N}_u(\omega_k), \tag{6.27a}$$

$$\mathbf{F}(\omega_k) = \mathbf{F}_0(\omega_k) + \mathbf{N}_f(\omega_k), \tag{6.27b}$$

where $\mathbf{U}$ and $\mathbf{F}$ are the measured displacement and force matrices, $\mathbf{U}_0$ and $\mathbf{F}_0$ are their exact value, and $\mathbf{N}_u$ and $\mathbf{N}_f$ are zero-mean disturbing noises.

There are several approaches in the literature to compute the CDS matrix in Eq. (6.24). The H_1 estimator is used when the SNR at the input is greater than that at the output. It is defined as

$$\mathbf{H}_1(\omega_k) = \left(\frac{1}{N_b}\sum_{l=1}^{N_b}\mathbf{F}(\omega_k)^{(l)}\mathbf{F}^*(\omega_k)^{(l)}\right)\left(\frac{1}{N_b}\sum_{l=1}^{N_b}\mathbf{U}(\omega_k)^{(l)}\mathbf{F}^*(\omega_k)^{(l)}\right)^{-1}. \tag{6.28}$$

The H_2 estimator is used when the SNR at the output is greater than that at the input. Its equation is

$$\mathbf{H}_2(\omega_k) = \left(\frac{1}{N_b}\sum_{l=1}^{N_b}\mathbf{F}(\omega_k)^{(l)}\mathbf{U}^*(\omega_k)^{(l)}\right)\left(\frac{1}{N_b}\sum_{l=1}^{N_b}\mathbf{U}(\omega_k)^{(l)}\mathbf{U}^*(\omega_k)^{(l)}\right)^{-1}. \tag{6.29}$$

Finally, the H_3 estimator is obtained from the average between the H_1 and H_2 estimators:

$$\mathbf{H}_3(\omega_k) = \frac{\mathbf{H}_1(\omega_k) + \mathbf{H}_2(\omega_k)}{2}. \tag{6.30}$$

Details about the estimators can be found in Appendix B. It is important to remark that the forces and displacements in the frequency domain are obtained by applying a discrete-time Fourier transform, which is implemented computationally with a fast Fourier transform (FFT). Special attention should be given to certain parameters of the FFT such as the sampling frequency, number of samples, frequency resolution and leakage.

6.5.1 Errors in the Estimates

Since noise in the measurements create random errors, the CDS must be computed along with confidence intervals. In this thesis, the standard deviation is used. According to Bendat [100], Pintelon [98] and Cloud [101], the standard deviations of the magnitude and phase of the estimator in Eq. (6.30) are

$$\sigma(|H_{ij}(\omega_k)|) = \frac{\sqrt{1-\gamma_{ij}^2(\omega_k)}}{\gamma_{ij}(\omega_k)\sqrt{2N_b}} H_{ij}(\omega_k) \;\; , \;\; \sigma(\angle H_{ij}(\omega_k)) = \frac{\sqrt{1-\gamma_{ij}^2(\omega_k)}}{\gamma_{ij}(\omega_k)\sqrt{2N_b}}, \tag{6.31}$$

where γ_{ij} is the coherence function between the force and displacement signals, and N_b the number of data blocks. The errors for stiffness and damping coefficients are estimated by propagating the standard deviation to the real and imaginary parts of the CDS. Thus, by assuming an asymptotic normal distribution, the estimates of the CDS with a confidence interval of 99.7% is

$$|H_{ij}(\omega_k)| - 3\sigma(|H_{ij}(\omega_k)|) \leq |H_{ij}(\omega_k)| \leq |H_{ij}(\omega_k)| + 3\sigma(|H_{ij}(\omega_k)|) \tag{6.32}$$

$$\angle H_{ij}(\omega_k) - 3\sigma(\angle H_{ij}(\omega_k)) \leq \angle H_{ij}(\omega_k) \leq \angle H_{ij}(\omega_k) + 3\sigma(\angle H_{ij}(\omega_k)) \tag{6.33}$$

This equation is also used to compute the confidence interval of the stiffness and damping coefficients in Chapter 6.

6.6 Excitation signal

Excitation signal must be properly designed to obtain measurements with high SNR. This is no simple task when dealing with rotordynamic systems that have small gaps between their parts. A high excitation energy may cause a rotor-stator contact. An alternative is to use a single harmonic signal that excites one component frequency. One of the advantages of using this type of signal is that it has a high SNR value [102]. A frequency interval can be excited by performing several tests with different sine waves. Nonetheless, a considerable amount of time would be expended at the end of all tests, which is not viable in this rig. Another alternative is to excite the system with random signals, which have a robust behavior with non-linear distortions. However, their leakage limitations demands a high quantity of repetitions to obtain accurate results [103], especially in higher frequencies. A more appropriate alternative is to excite harmonically with different single frequencies simultaneously, which can reduce the overall test time and better distribute the energy along the frequency. This type of signal is formed by the sum of several sine waves of different frequency, phase and amplitude [104]. It is defined as

$$S = \sum_{k=1}^{N_f} A_k \cos(2\pi f_k t + \phi_k), \tag{6.34}$$

where N_f is the number of frequency components (also known as harmonics or tones) and A_k, f_k, and ϕ_k are the k-th excited amplitude, frequency and phase angle, respectively. For the tests, 17 frequencies were selected, below and beyond the first critical speed (35 Hz), avoiding the excitation of their first four multiples. The chosen frequencies are according equation

$$f_k = 4k + 1, \text{ for } k = 1, 2, \ldots, 17. \tag{6.35}$$

According to Eq. (6.34), each tone has two unknown parameters: amplitude and phase. They must be carefully designed to avoid poor coefficient estimates as a result of low SNR. Regarding the amplitude, it was established in such a way that the displacement signal amplitudes, in the frequency domain, remain flat. The excitation amplitude profile was experimentally obtained by computing the magnitude of the CDS at baseline condition. Since the CDS is the inverse of the FRF shown in Fig. 4.6, the responses are expected to be constant. In this approach, the excitation amplitudes near the critical speeds are lower than those far from then. Regarding the phase, an algorithm proposed by Guillaume et al. [105] was used. The intention with this signal is to reduce the Crest-Factor (CF), which is the ratio of the l_∞ norm of the signal to its root-mean-square value. If the CF is reduced, small peaks of the signal are reduced and the energy can be better distributed. The phases are determined by an iterative minimization strategy based on Gauss-Newton method and Levenberg-Marquardt algorithm. At the first iteration, the phases are set according to the formula proposed by Schroeder [106], i.e. $\phi_k = -\pi k^2/N_b$, which gives a CF of 2.78.

In Fig. 6.2 the original (CF=2.78) and modified (CF=1.62) signals are plotted. They are based on the work on Diaz et al. [29]. In the time domain, the maximum peaks are reduced but the signal has the same amount of energy. In the frequency domain, the amplitude of each tone is not modified. However, the phases are different and are responsible for reducing the CF. Moreover, the amplitudes are not constant. Higher amplitudes are give to those frequencies where the natural responses of the rotor is lower.

In rotating machines with small gaps between rotating and stationary parts, the excitation signal is an important aspect to improve measurements. A properly choice of phases is desirable since more energy can be applied to the system as a result of the decrease of some peaks. This means that the SNR is improved. Also,

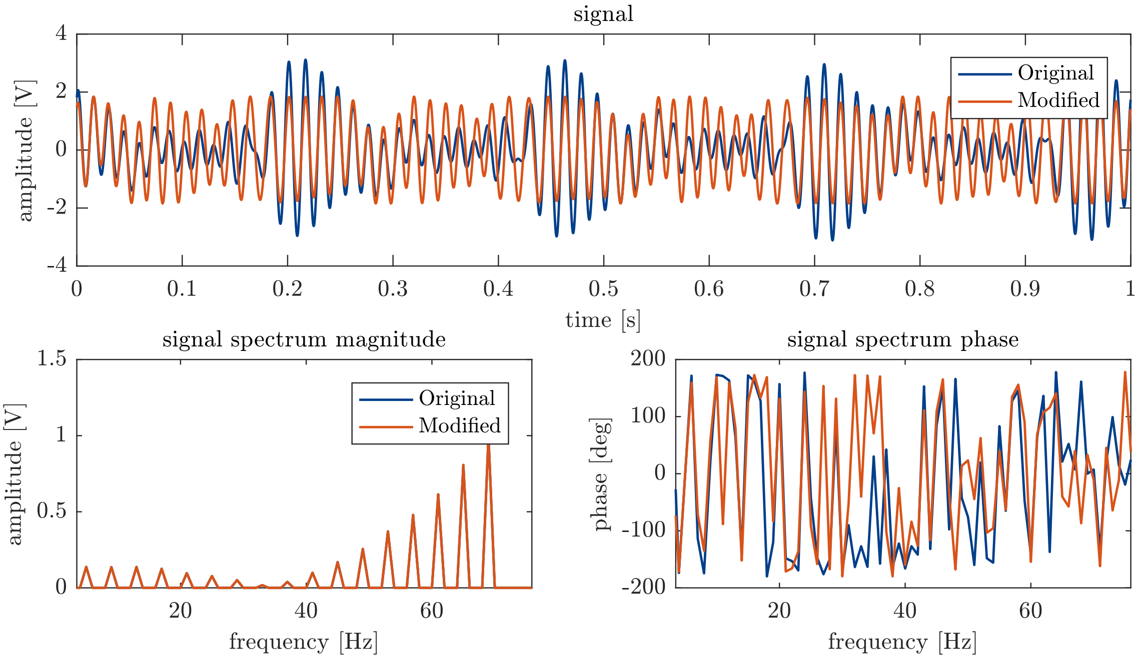

Figure 6.2: Original and modified excitation signal using the algorithm proposed by Guillaume et al. [105]. Signal with 17 tones: $f_k = 4k + 1$, for $k = 1, 2, \ldots, 17$

the amplitude design is relevant to avoid rotor-stator contact, which is easily excited by frequencies near the first critical speed. If an excitation signal with a flat profile is used, the vibrations near the first critical speed would limit the allowed excitation energy due to the maximum shaft lateral displacement. In the next section, it is shown that constant displacement amplitudes are produced by the excitation profile. This tends to give the same SNR to all displacement measurements.

6.7 Experimental results and discussion

In this section, experimental results of the identification methodology are shown. The tests were performed with an average input pressure of 0.3 MPa (3 bar), atmospheric pressure in the discharge port, pre-swirl ring of 30° and a rotor speed of 4500 RPM. Data acquisition of displacements, forces, currents and voltages were performed using a sample rate of 5.12 kHz and 5120 samples. This sets a frequency resolution of 1 Hz. Also, 20 blocks of measurements were used for the averaging process of the estimates. For comparison purposes, three excitation signals are applied: multisine, random and single harmonic signals.

6.7.1 Noise in the measurements

The measurement errors presented in this thesis only considers random errors. The distribution of the measurements is an important characteristic to assess the uncertainty in the parameter estimation. Normal or gaussian noise is widely used in the literature due to its statistical properties. However, some analyses consider this type of distribution without any justification. In order to show some evidence to use normal distribution in this thesis, Fig. 6.3 shows the histograms of one of the proximity and current sensors for a stationary rotor test with no excitation. Both sensors showed normal distributions with the parameters shown in Tab. 6.1.

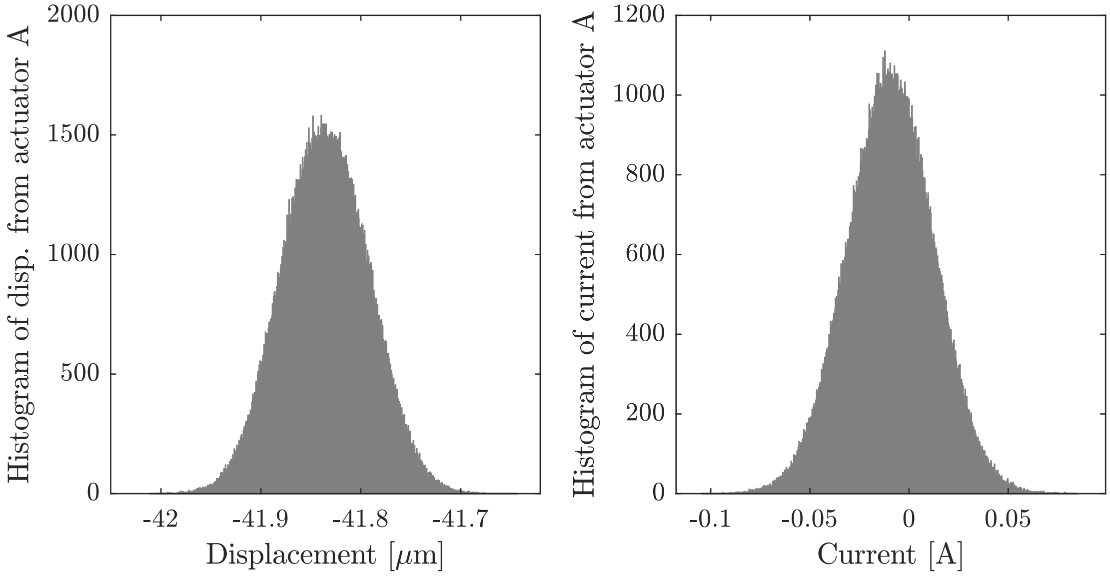

Figure 6.3: Histograms of one of the proximity and current sensors.

	Mean value	Std. dev.	Units
Proximity sensor	41.83	0.043	μm
Current sensor	0.0092	0.0217	A

Table 6.1: Statistics of the histograms of one of the proximity and current sensors.

6.7.2 High, low and differential pressure

During an excitation along one of the axis, both baseline and overall tests are performed consecutively. Fig. 6.4 shows the inlet (High), outlet (Low) and drop (Differential) pressures for both the baseline (Figs. 6.4a and 6.4c) and overall (Figs. 6.4b and 6.4d) tests. The vertical lines correspond to each measurement block. During the baseline test, the inlet and outlet ports are at atmospheric pressure because a valve is blocking the pressure from the compressor; the high pressures from the figures correspond to the pressure before the valve. When the valve is opened, the high pressure starts to decay linearly. The low pressure raised immediately after the valve was opened, but also decays over time. This pressure drop occurs because the amount of air flux is out of the compressor's capacity. For this reason, during the overall test, a short amount of time is available to acquire the signals before both the high and low pressures are balanced. The parameters obtained are related to the equivalent parameters for the pressure range 0.50-0.56 MPa (5.6-5.0 bar).

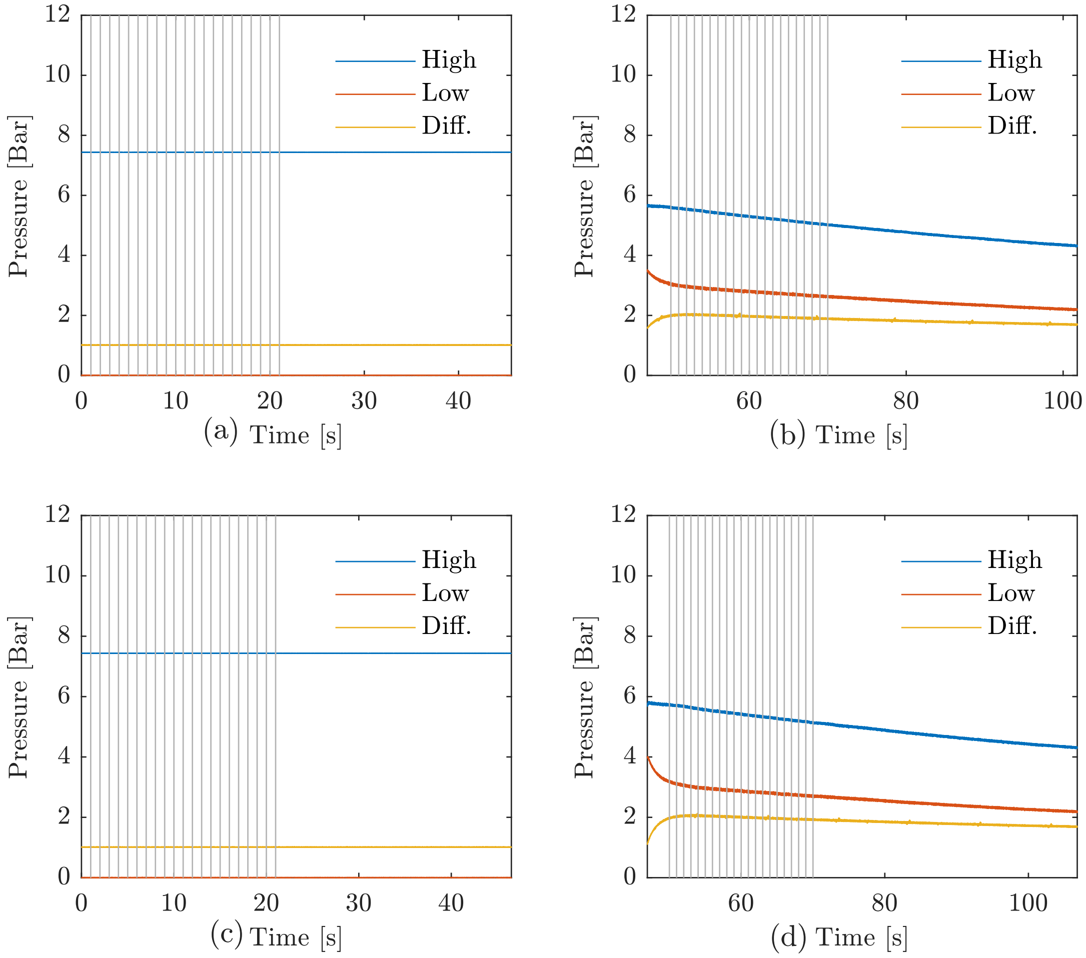

(a) Time [s] (b) Time [s]

(c) Time [s] (d) Time [s]

Figure 6.4: High, low and differential pressures.

6.7.3 Multisine excitation

The first signal used to excite the rotor is the 17-tone multisine shown in Fig. 6.2 from section Sec. 6.6.

Excitation, force, current and displacement signals

Fig. 6.5 shows the excitation voltage, force, current and displacement signals, in time and frequency domain, of one actuator. They were taken during a baseline test and with an excitation along the x direction. Fig. 6.5a shows the excitation voltage during 400 ms. In Fig. 6.5b, the amplitude profile of the excitation is shown. When this excitation is applied to the coils of the actuator, Fig. 6.5c is obtained. The spectrum of the force in Fig. 6.5d is similar to that of the excitation in Fig. 6.5b.

The current of the actuator in Figs. 6.5e and 6.5f also showed similar behavior as the excitation and force signals. In Fig. 6.5g the displacements of the seal (mean value between sensors A and B), along the x and y directions, are plotted. Although an excitation along the x direction was applied, a small response in the other direction is also obtained. This can be attributed to residual unbalance and crossed-couple terms in the system. This effect is better observed in the spectrum of Fig. 6.5h, where small amplitudes are obtained in the y direction. The amplitude profile of the displacements was a design objective to improve the SNR. If an excitation with constant amplitudes were adopted, the SNR would be low for frequencies far from the critical speed.

Coherence between force and displacement signals

In order to assess the quality of the excitation signal, the magnitude-squared coherence function is used. It is defined as

$$\gamma = \frac{|S_{fu}(\omega)|^2}{S_{ff}(\omega)S_{uu}(\omega)}, \tag{6.36}$$

where S_{ff} and S_{uu} are the autospectral density functions of the force and displacement, and S_{fu} the cross-spectral density function between them. It is a function that varies between zero (no coherence) and one (full coherence). Basically, it represents the part of the output power (displacement) that was excited by the input (force).

Fig. 6.6 shows two coherence function for the baseline and overall test. γ_{xx} corresponds to the direct coherence (excitation and response along the x-direction). γ_{xy} is the cross-coupled coherence function (excitation along the x-direction and response along the y-direction). For both tests, the direct coherence was equal to one at all frequencies, except at the critical speed. The cross-coupled coherence showed values much lower than one and decreasing with the frequency. This means that the energy applied to the system was in great measure used to excite the direct coefficients. Due to the low cross-coupled effects of the system, the low coherence was expected.

CDS of the overall system coefficients

Before showing the results of the seal coefficients, the results of the overall tests are shown. This corresponds basically to the rotor, bearings and seal dynamics over the frequency. Fig. 6.7 shows the magnitude of the direct and cross-coupled CDS coefficients for the excitation signal in Fig. 6.5. It was computed at both seals' location and averaged. The direct CDS obtained is a typical function from

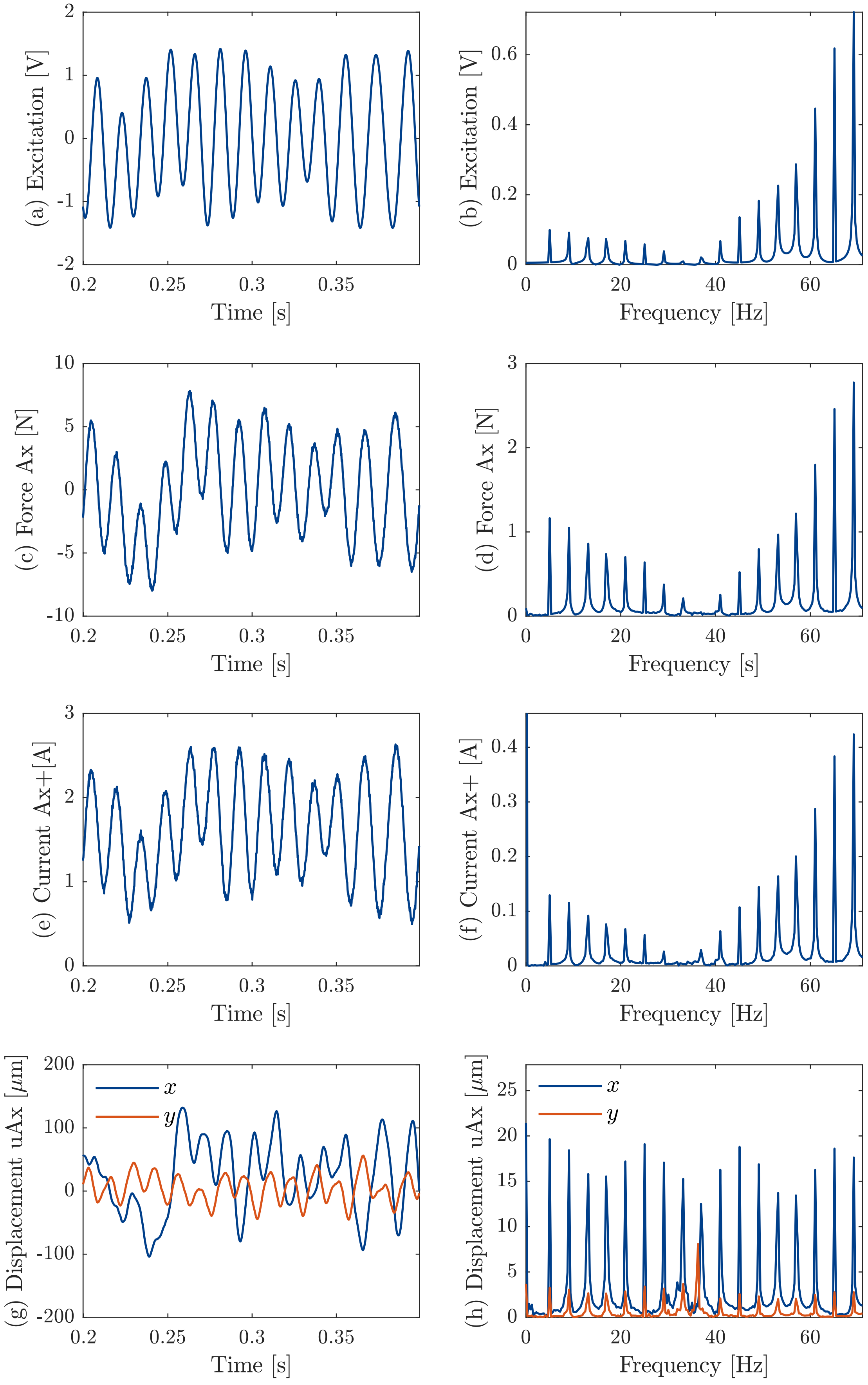

Figure 6.5: Excitation, force, current and displacement signals for a multisine excitation.

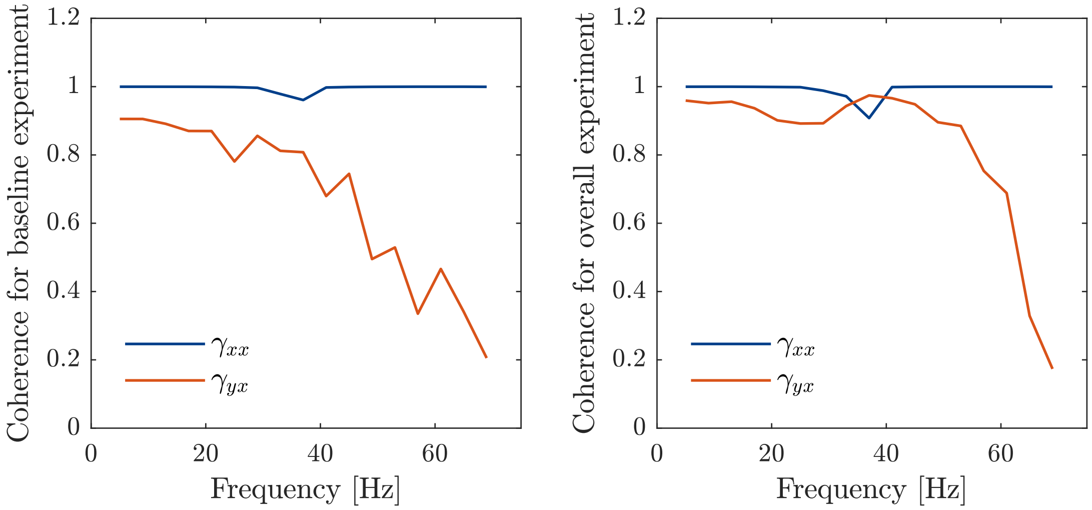

Figure 6.6: Coherence function of the baseline and overall tests for a multisine excitation.

rotordynamic systems where lower amplitudes are near the critical speed. At low frequencies, the stiffness has more influence on the dynamics. The mass and damping effects increase with the frequency. Also, the cross-coupled CDS exhibited negligible values with respect to the direct parts.

Another important characteristic of the CDS are its real and imaginary parts. According to Eq. (6.4), the real part corresponds to $K - M\omega^2$, which is a quadratic function. The results for the direct and cross-coupled parts are shown in Fig. 6.8. As expected, the direct part decrease with the frequency and crosses zero at the critical speed. The cross-coupled part is negligible and varies slowly with the frequency.

The imaginary part of the CDS contains the damping terms. It is shown in Fig. 6.9. The direct part increases almost linearly with the frequency. The cross-coupled remained around zero.

Seal coefficients

The results of the identification of the seals coefficients are based on the baseline approach. After performing both the baseline and overall tests, the Fig. 6.10 is obtained. The direct stiffness in Fig. 6.10a shows a trend to increase when the frequency is higher, which means a hardening effect of the overall system. As a result, the critical speed is slightly increased. The cross-coupled stiffness in Fig. 6.10c presented negligible variations with the frequency and its amplitudes are small compared to the direct coefficient. Regarding the damping coefficients, they exhibited small amplitudes. The direct damping in Fig. 6.10b shows an increasing behavior with the frequency and with negative values at low frequencies. In the case of the cross-coupled damping in Fig. 6.10d, its amplitudes remained near zero, with no relevant effects to the system. In general, the seal studied in this thesis only ex-

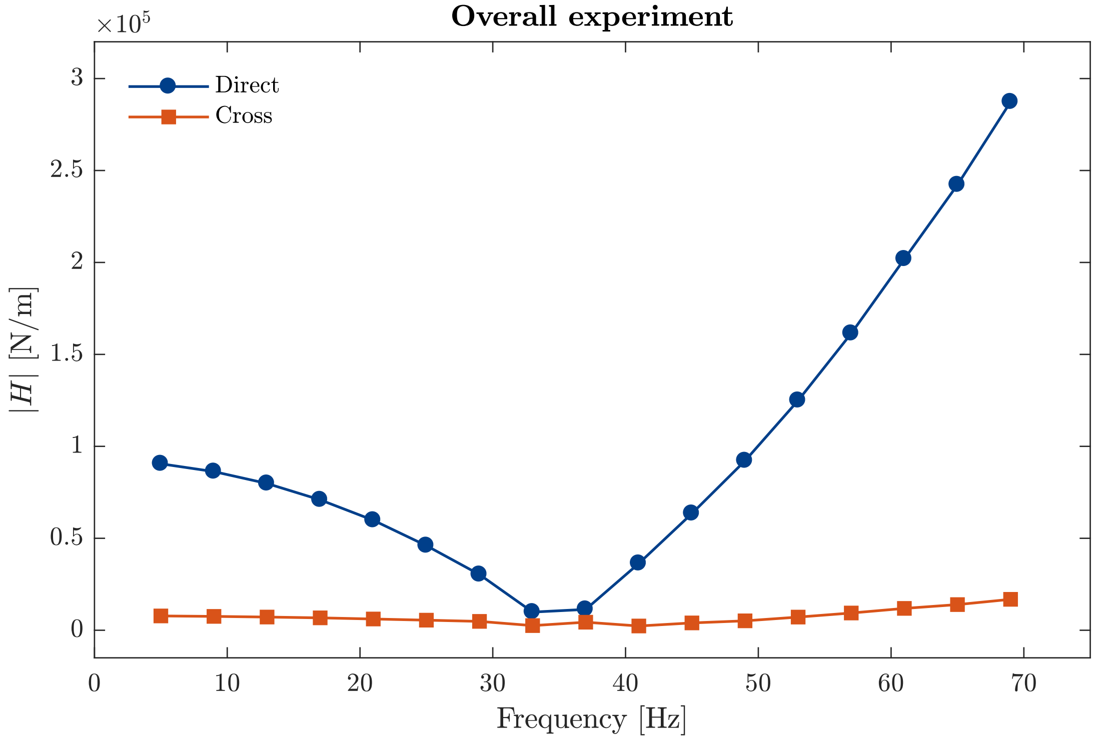

Figure 6.7: Magnitude of the direct and cross-coupled CDS.

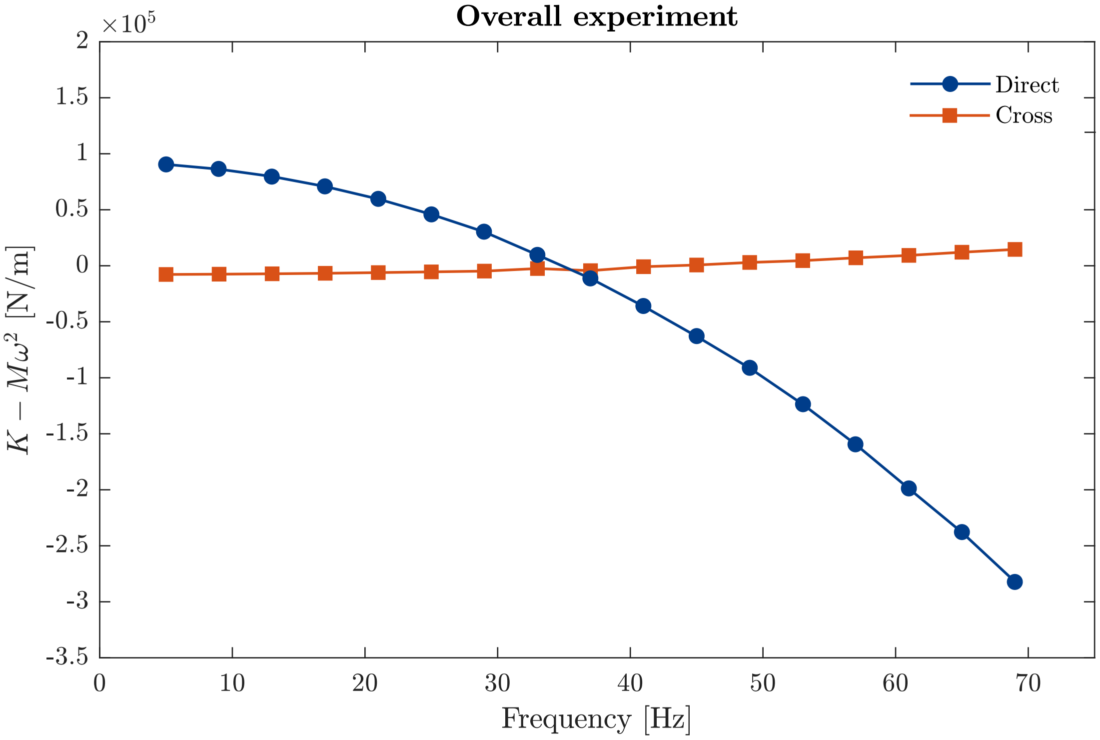

Figure 6.8: Real part of the overall CDS.

hibited a stiffening effect and no instability issues were observed. Nevertheless, the cross-coupled stiffness has to be taken into account when changing the operating condition (e.g. pressure, fluid, speed of rotation, etc.), since it may destabilize the system.

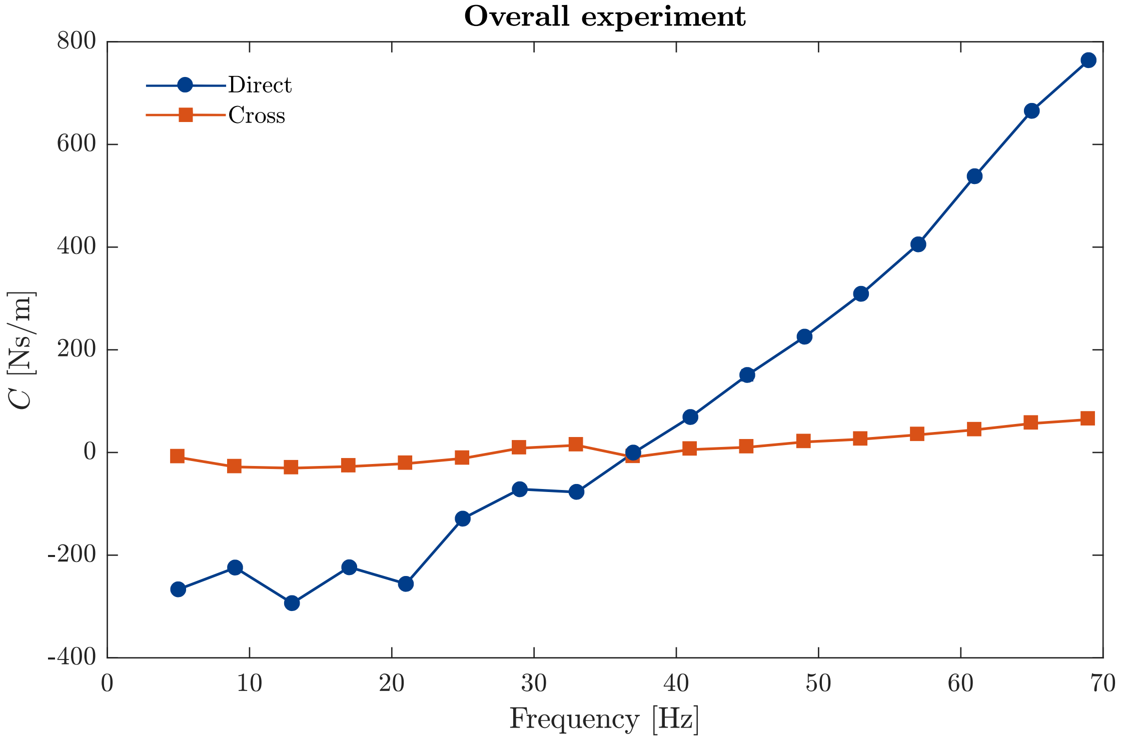

Figure 6.9: Imaginary part of the overall CDS.

Although the estimator used in this work improves the computation of the CDS, it is of great importance to take into consideration the error of each estimate. The error of direct stiffness remained low for all the excited frequencies. Nevertheless, the error of the cross-coupled stiffness was considerably high, specifically at the higher frequencies (e.g. at 69 Hz). In other words, the identification method at those frequencies returned poor estimates. This is so because the coherence between the force and displacements, for both baseline and overall tests, was high for the direct CDS and low for the cross-coupled CDS. Similar results were seen on the damping coefficients. The error of the direct damping is relatively slow, except for the first frequencies (e.g. 5 Hz). The cross-coupled damping presented better estimates at the center frequencies. As before, the bad estimates were found where the coherence between the force and displacement were low. In order to reduce the error of the estimates, more averages should be taken.

6.7.4 White noise excitation

For comparison purposes, the seal coefficients were obtained also with a white noise excitation.

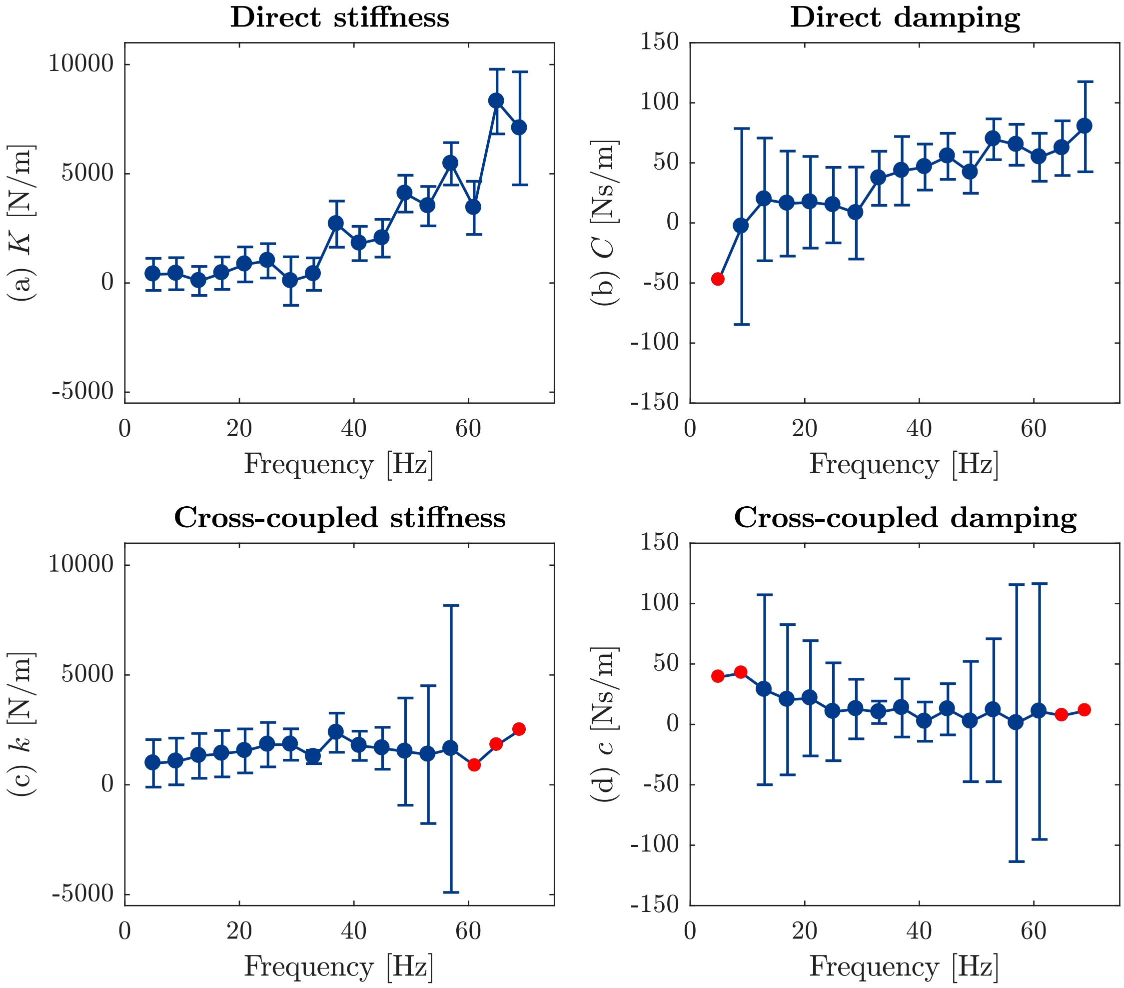

Figure 6.10: Direct and cross-coupled coefficients of the seal obtained with a multisine excitation. The error bars of each estimate correspond to an interval with 99.7% of confidence. Red dots correspond to estimates with a confidence interval out of the figure scale.

Histogram of the excitation

The histogram of the excitation and force signals are shown in Fig. 6.11. Both signals are normally distributed. This type of signal is widely used for identification in several research fields. However, it has some strong disadvantages. In this thesis, the energy distribution of this signal is discussed.

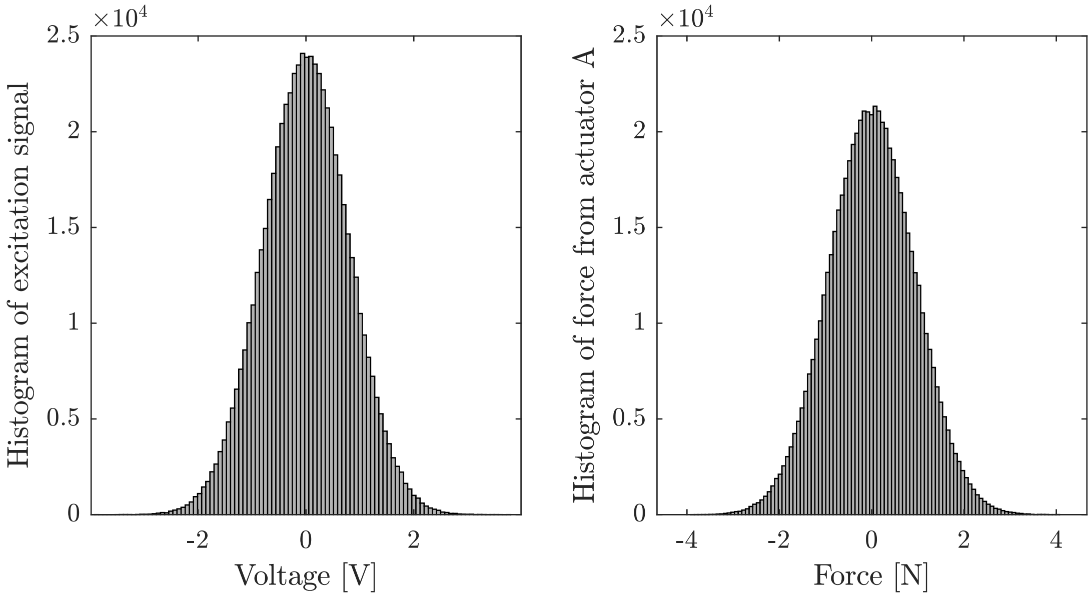

Figure 6.11: Histograms of the excitation signal and force from Actuator A.

Excitation, force, current and displacement signals

Fig. 6.12 show the excitation, force, displacement and current signals in time and frequency domain, for an excitation along the x-axis. The amplitude of the excitation was selected such that no rotor-stator contact occurs. The energy is distributed almost evenly along the frequency range. However, the spectrum of the displacement along the excited axis exhibits higher values near the critical speed. This is a major drawback because it means that the maximum excitation energy depends strongly on the amplitudes near the critical speed. This causes a poor excitation at other frequencies, which means low SNR values.

Coherence function

The quality of the excitation is quantitatively assessed by the coherence functions shown in Fig. 6.13. As expected the direct coherence has low values, especially at the higher frequencies.

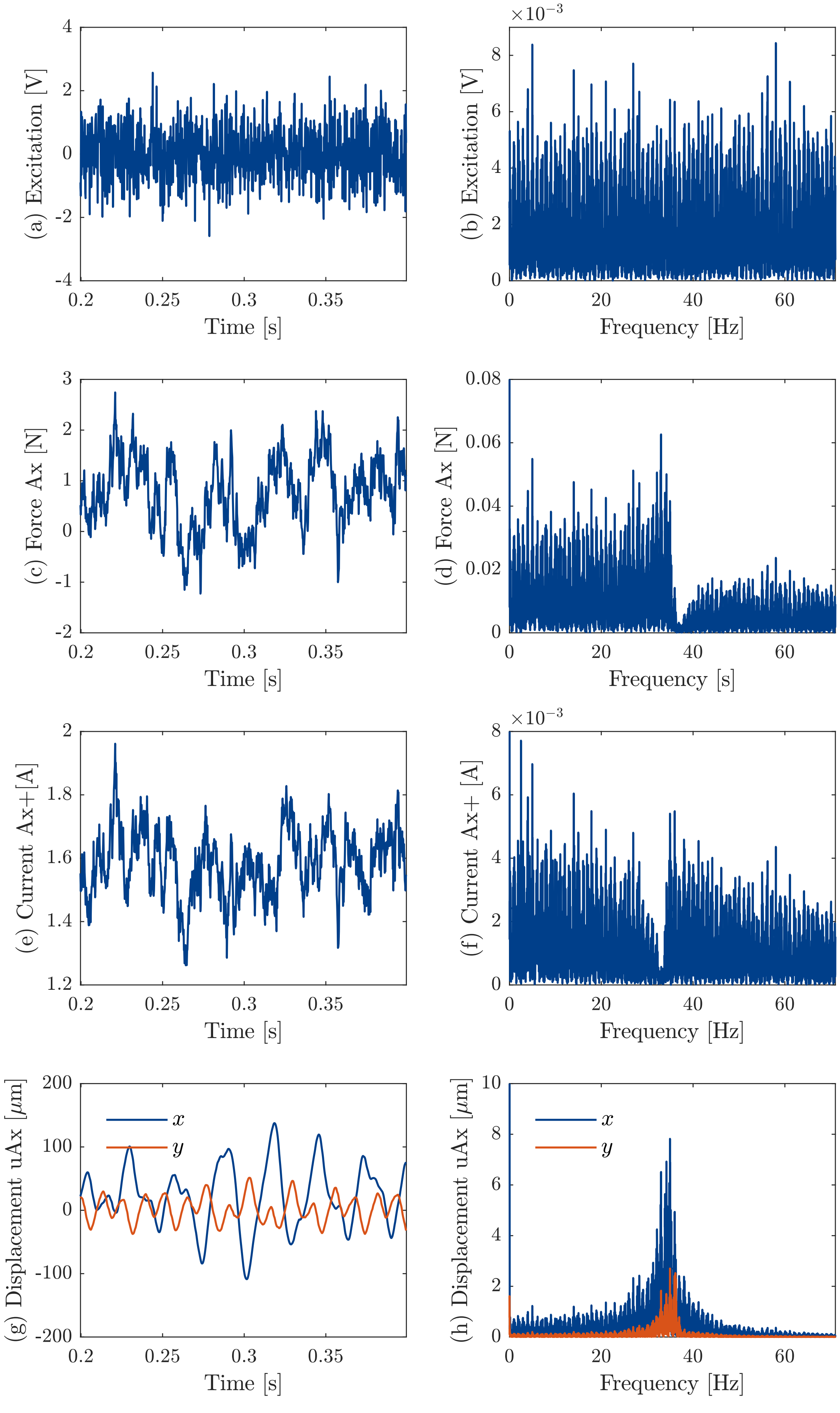

Figure 6.12: Excitation, force, current and displacement signals for a white noise excitation.

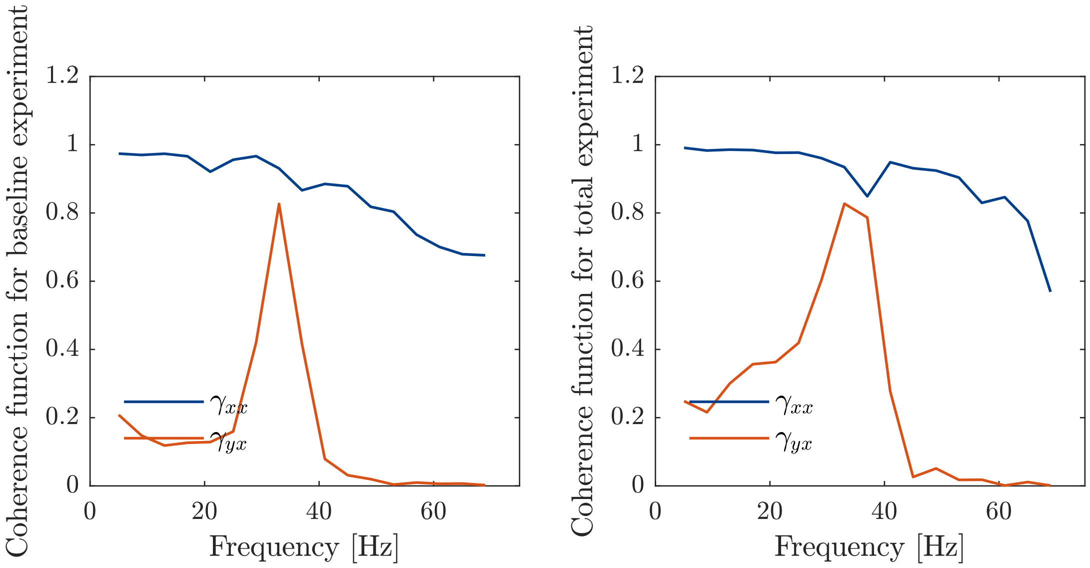

Figure 6.13: Coherence function of the baseline and overall tests for a white noise excitation.

Seal coefficients

The seal coefficients are shown in Fig. 6.14. With the excitation and response signals of Fig. 6.12, the coefficients obtained showed a high uncertainty. The only way to reduce it is to increase the number of measurement blocks. However, as was discussed before, the test time is limited by the pressure drop of the compressor. For this reason, a multisine signal is a better excitation signal in this case.

6.7.5 Single harmonic excitation

One further excitation signal was applied for comparison purposes. It is a harmonic excitation, with the energy concentrated in only one frequency component. This characteristic makes this type of signal appropriate to increase the SNR at a certain frequency. However, a drawback of this signal is discussed below.

Excitation, force and displacement signals

In Fig. 6.15, the excitation, force, current and displacement signals are shown for an excitation of 69 Hz and along the x-axis. The spectra of the excitation, force and currents presented only one frequency harmonic. However, the displacement signal has also one peak near the critical speed. This peak appears in any excitation due to the resonance characteristic at this frequency in the presence of small perturbations.

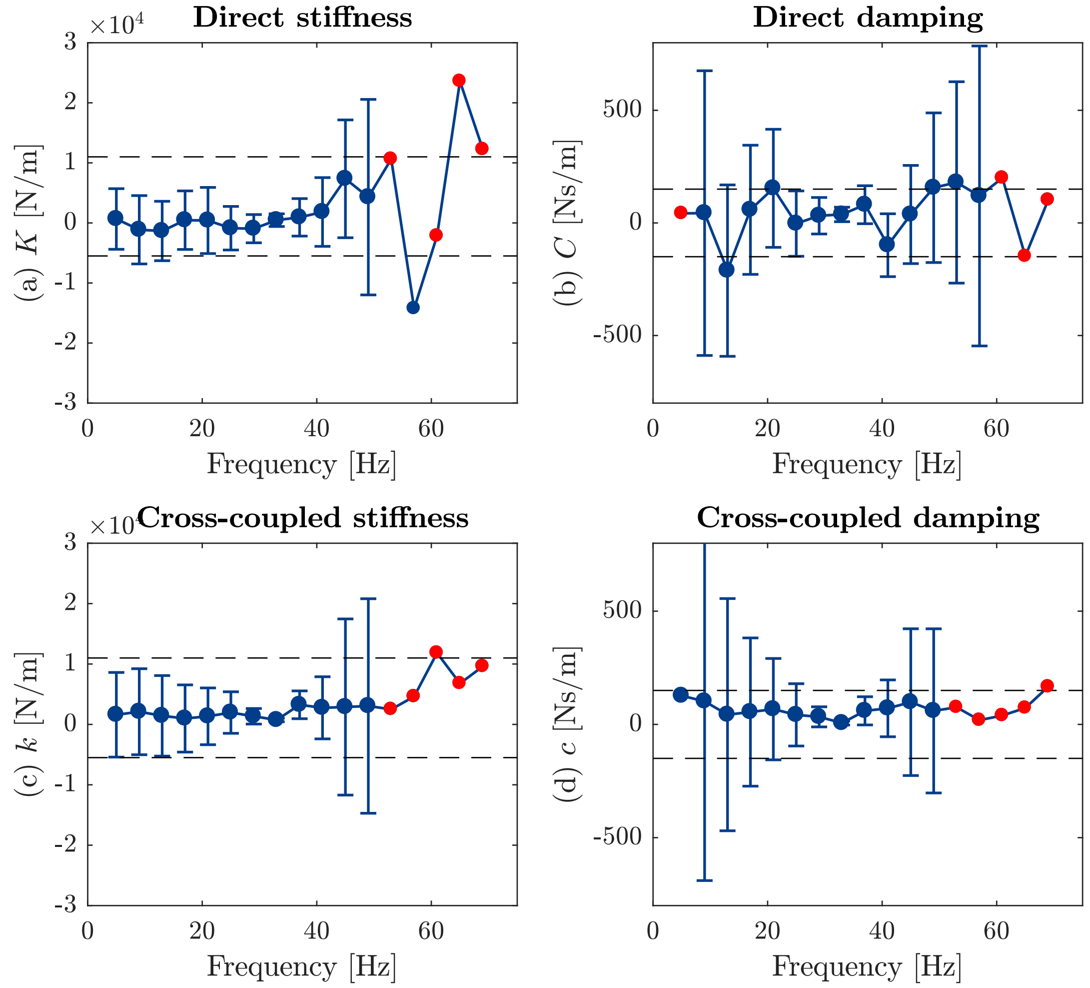

Figure 6.14: Direct and cross-coupled coefficients of the seal obtained with a white noise excitation. The error bars of each estimate correspond to an interval with 99.7% of confidence. Red dots correspond to estimates with a confidence interval out of the figure scale.

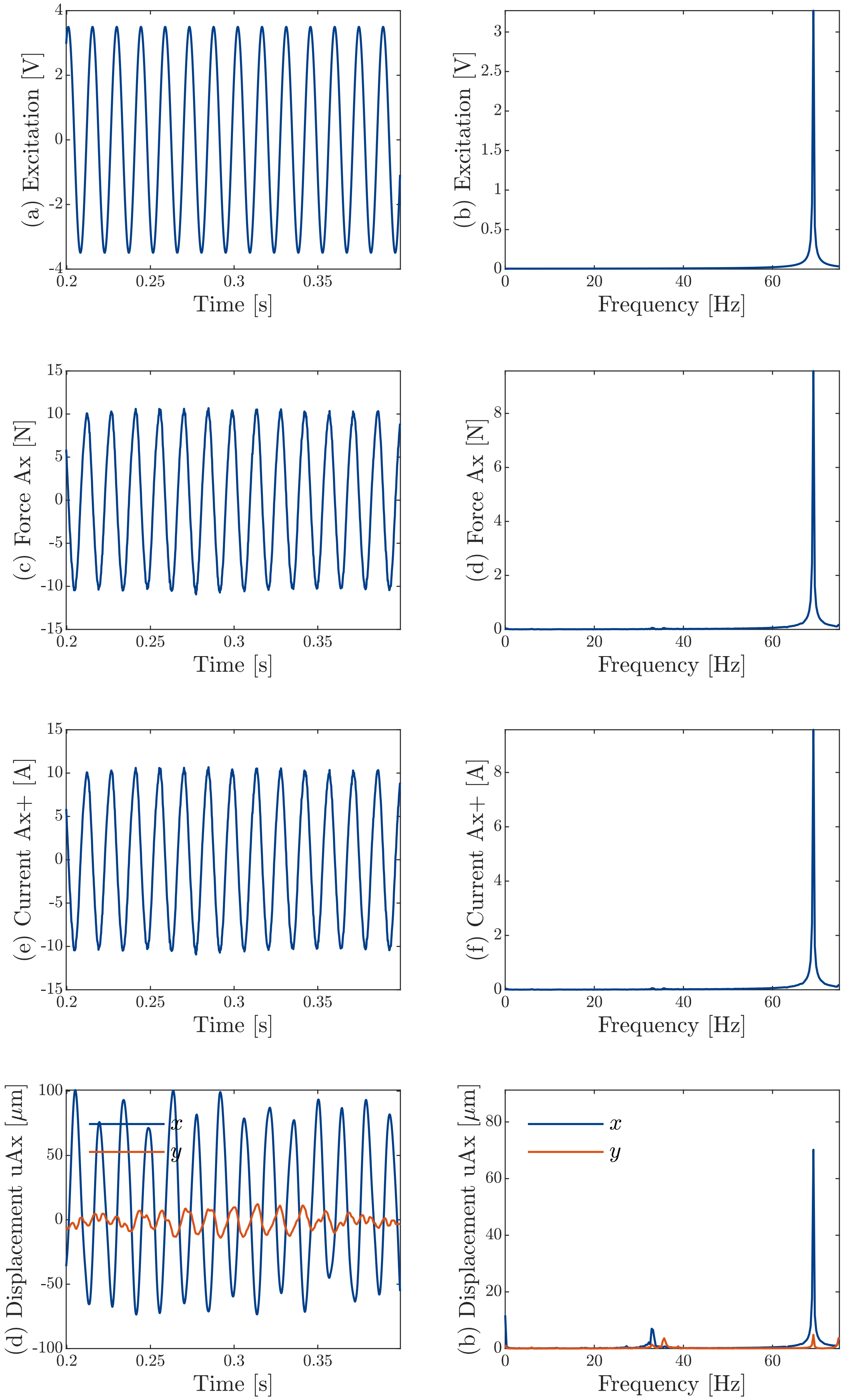

Figure 6.15: Excitation, force, current and displacement signals for a single harmonic excitation.

Coherence function

The coherence functions are shown in Fig. 6.16. As expected, the direct coherence is near the unity at all frequency. Even with low cross-coupled terms, this signal managed to increase the coherence. Only at the last two frequencies the cross-coupled coherence is low, possibly for a measuring error.

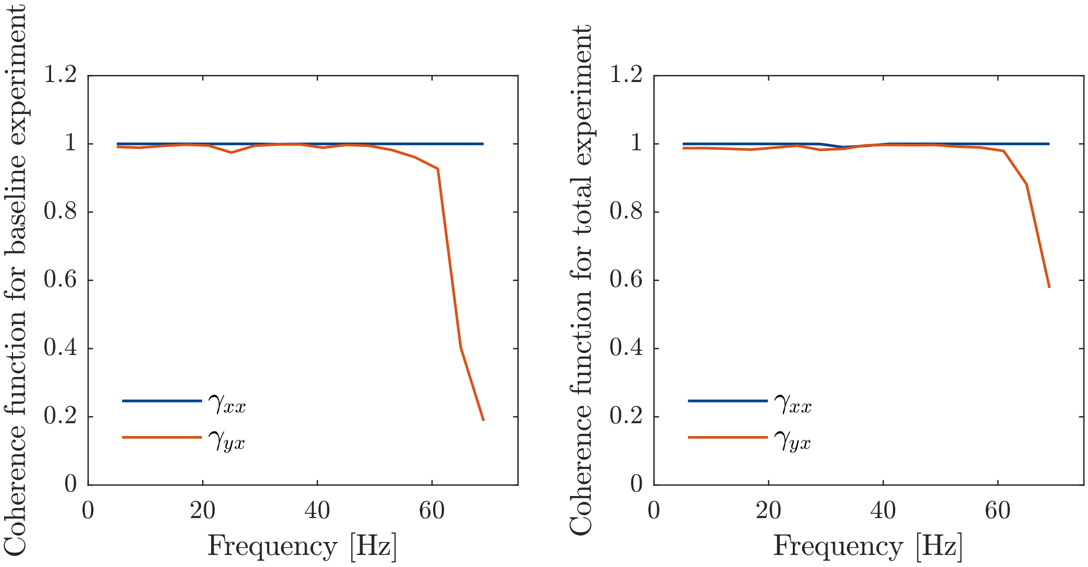

Figure 6.16: Coherence function of the baseline and overall tests for a single harmonic excitation.

Seal coefficients

The seal coefficients are shown in Fig. 6.17. All coefficients showed a low uncertainty, except at those frequencies with a low coherence. For these reason, this type of signal is of extreme importance in the identification method. It serves as a benchmark for other excitation signals, such as the multisine or white. Although it is a signal that returned a high coherence, the total duration of all the tests is a drawback and a motivation to use a multisine. Due to the compressor limitations, the duration of all the 17 tests were completed approximately in 12 hours. On the other hand, the multisine approach was performed in a shorter time (1 hour approximately). Thus, the multisine signal is recommended when the duration of an experiment is restricted.

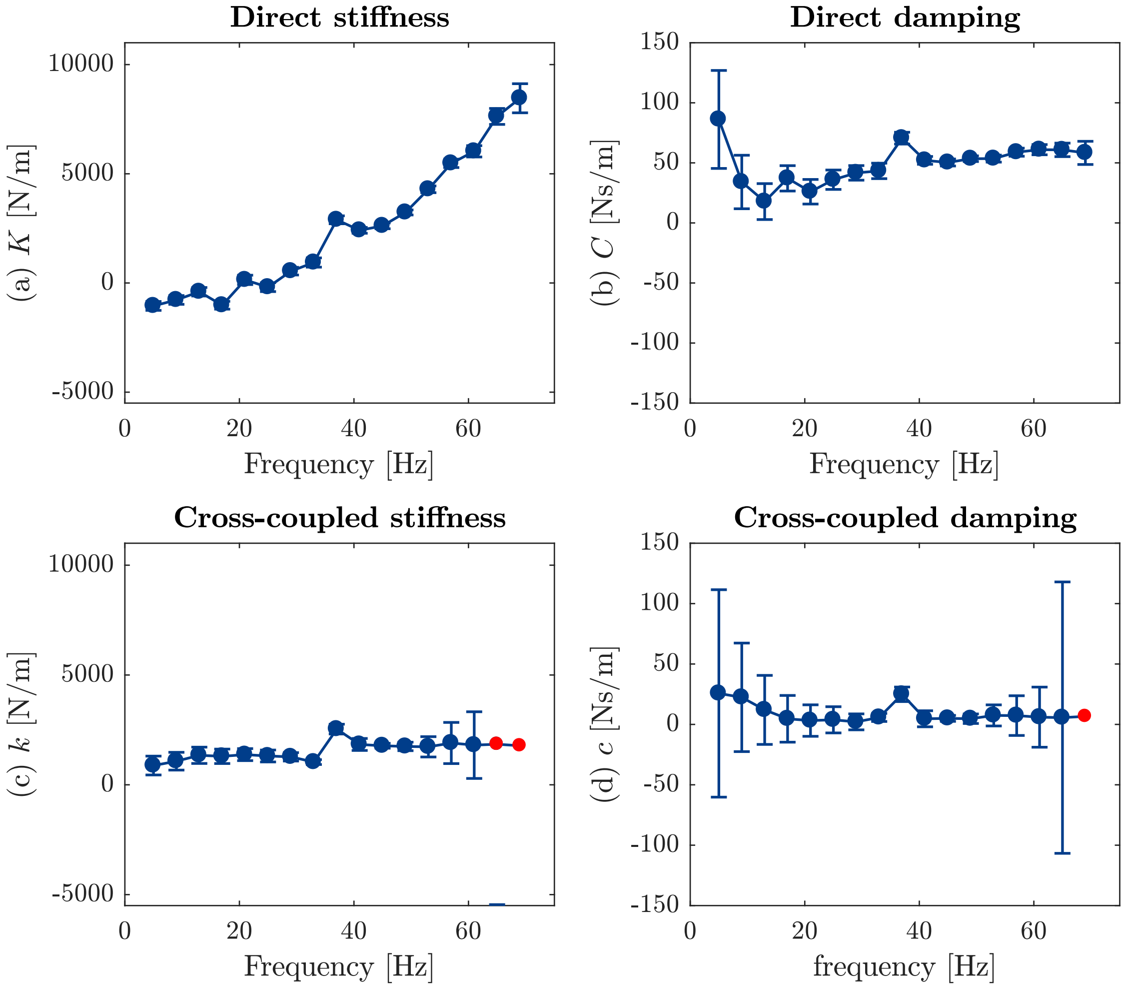

Figure 6.17: Direct and cross-coupled coefficients of the seal obtained with a single harmonic excitation. The error bars of each estimate correspond to an interval with 99.7% of confidence. Red dots correspond to estimates with a confidence interval out of the figure scale.

Chapter 7

System with rotor-stator contact

An investigation of the motion type is performed in a simplified model representing the test rig. This type of machine operates with small clearances to reduce fluid leakage and to improve its performance. However, this fact increases the chance of a rotor-stator contact when the vibration eventually exceed the clearance. As a consequence, contact forces are developed at the contact surfaces and the dynamics is affected. Depending on some parameters, the machine may change its operating condition dramatically.

Components of rotating machines, such as seals or bearings, contain small clearances between the stator and rotor that turns the machine susceptible of contact between them. Specifically, annular gas seals are designed to reduce the leakage from a higher-pressure stage to a lower-pressure stage. During normal operation, rotor and seals do not touch each other. Eventually, beyond the nominal capacity or abnormal condition, the seals contact the rotor and the phenomenon of rubbing occurs. This event must be avoided or minimized, because contact forces may damage the machine or reduce its lifespan. Thus, the study of the rotor behavior under different rubbing conditions provides relevant information for preventive, predictive and/or corrective maintenance.

In some cases, the contact only causes wear of the parts but may change the dynamics of the machine. For example, when the rotor rubs slightly with a seal, the clearance may be increase because of the material removal; the parameters of the seal may change considerably and also the dynamics of the overall machine. In other cases, severe damage may occur as a result of high contact and friction forces. In any case, the effects of the rubbing must be well understood to diminish the risk of hazardous events.

The rubbing can be divided into two effects: thermal deformation and contact forces. In the former, which is not considered in this thesis, a non-uniform temperature distribution causes a bending in the rotor. In the latter, which is addressed here, normal and tangential forces are applied to both parts. The interaction between the stator and rotor leads to a nonlinear system that cannot be solved analytically. Moreover, the due to the abrupt change of some parameters after the contact, some nonlinear analysis, such as perturbation methods, are not valid. Thus, numerical integration is used to solve the system for certain set of parameters. In this thesis, a numerical integration based on Runge-Kutta of fourth-order algorithm was implemented in Matlab. Moreover, the system equations are nondimensionalized to avoid numerical integration problems due to high stiffness values.

The rotor vibration presents different type of motion depending on the system parameters. This motion is visualized by plotting orbits and frequency spectra. Since the rotor speed is an important parameter in rotating machines, its influence on the vibration is assessed. Moreover, the spectrogram based on the short-time FFT is used to analyze the vibration of the test rig experimentally.

7.1 System Equations

The model of the test rig with the rotor-stator contact is shown in Fig. 7.1. It consists of a Jeffcott rotor and a flexible stator. The rotor has an unbalanced mass m_R, stiffness k_R and external viscous damping b_R. The stator has a mass m_S, stiffness k_S and external viscous damping b_S. Due to the unbalance of the disk, forces f_{ux} are f_{uy} are considered. There is a small concentric clearance s between the cylindrical surfaces of disk and stator. If the clearance is not surpassed by the disk's displacements, the rotor behaves like a simple Jeffcott rotor, with a linear dynamics. When the disk displacement is greater than the clearance, the rotor rubs the stator and contact forces are applied at the surface of contact. These forces are in terms of stiffness k_C and viscous damping b_C. Moreover, they are decomposed as tangential and normal components. The normal force depends on the minimum thickness d, while the tangential force depends on the friction coefficient μ_f between the contact surfaces. Finally, eccentricities x_{S0} and y_{S0} of the stator are considered. Considering the displacement vectors $\mathbf{u}_R = [u_{Rx}, u_{Ry}]^T$ and $\mathbf{u}_S = [u_{Sx}, u_{Sy}]^T$, the equations that represent the dynamics of both the rotor and stator are:

$$m_R\ddot{\mathbf{u}}_R + b_R\dot{\mathbf{u}}_R + k_R\mathbf{u}_R = \mathbf{f}_u - \mathbf{f}_c + \mathbf{f}_s, \tag{7.1}$$

$$m_S\ddot{\mathbf{u}}_S + b_S\dot{\mathbf{u}}_S + k_S(\mathbf{u}_S - \mathbf{u}_{S0}) = \mathbf{f}_c - \mathbf{f}_s, \tag{7.2}$$

where $\mathbf{f}_u$, $\mathbf{f}_c$ and $\mathbf{f}_s$ are the unbalance, contact and seal forces, respectively. The unbalance force is given by

$$\mathbf{f}_u = m_R r_u \Omega^2 \begin{bmatrix}\cos(\Omega t + \varphi_0) & \sin(\Omega t + \varphi_0)\end{bmatrix}^T \tag{7.3}$$

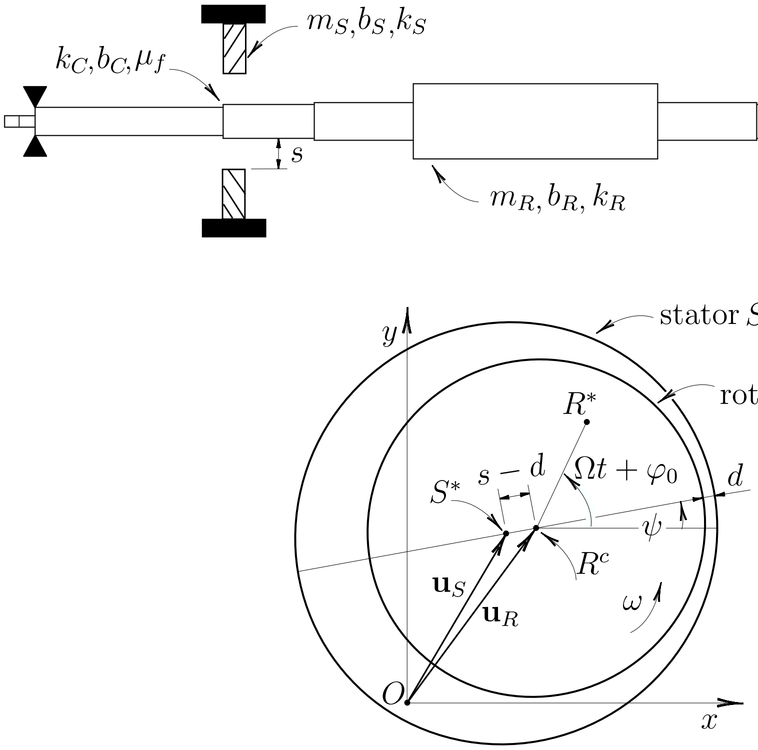

Figure 7.1: Model of the rotor-stator contact.

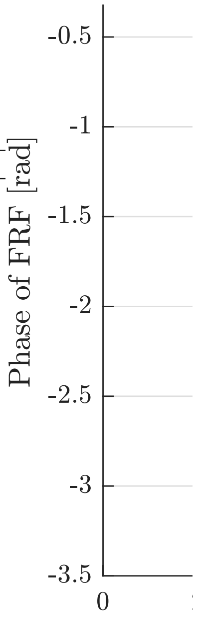

Figure 4.7: Pl
computed at ı

The contact forces are modeled according to several works in the literature, such as Ehehalt et al. [107], Alber and Markert [108], Sawicki et al. [109] and Jacquet-Richardet et al. [110]. They can be decomposed as the normal and tangential forces

$$\mathbf{f}_c = \mathbf{f}_{cn} + \mathbf{f}_{ct}. \tag{7.4}$$

The normal force depends on the indentation (negative value of d) between rotor and stator. It is defined by

$$\mathbf{f}_{cn} = \left\langle -k_C d - b_C \langle \dot{d} \rangle \right\rangle \langle -d \rangle^0 \begin{bmatrix} \cos\psi & \sin\psi \end{bmatrix}^T \tag{7.5}$$

where k_C is the contact stiffness, b_C is the contact damping and ψ is the angle that defines the direction of the minimal thickness d. Since the contact force only acts when d is equal or less than zero, the discontinuous function

$$\langle x \rangle^c = \begin{cases} x^p, & \text{for } x > 0, \\ 0, & \text{otherwise,} \end{cases} \tag{7.6}$$

is used.

Assuming a Coulomb friction between the surfaces, the tangential force is

$$\mathbf{f}_{ct} = \mu_f \mathbf{f}_{cn} = \mu_f \left\langle -k_C d - b_C \langle \dot{d} \rangle \right\rangle \langle -d \rangle^0 \begin{bmatrix} -\sin\psi & \cos\psi \end{bmatrix}^T . \tag{7.7}$$

The angle ψ and thickness d can be determined geometrically. Based on Fig. 7.1, the kinematic relations

$$\mathbf{u}_A = \mathbf{u}_R + \begin{bmatrix} r_u \cos(\Omega t + \varphi_0) & r_u \sin(\Omega t + \varphi_0) \end{bmatrix}^T , \tag{7.8}$$

$$\mathbf{u}_A = \mathbf{u}_S + \begin{bmatrix} (s-d)\cos\psi & (s-d)\sin\psi \end{bmatrix}^T , \tag{7.9}$$

hold, and they are determined by

$$\psi = \tan^{-1}\left(\frac{y_R + r_u \sin(\Omega t + \varphi_0) - y_S}{x_R + r_u \cos(\Omega t + \varphi_0) - x_S} \right), \tag{7.10}$$

$$d = s - \sqrt{(x_R + r_u \cos(\Omega t + \varphi_0) - x_S)^2 + (y_R + r_u \sin(\Omega t + \varphi_0) - y_S)^2}. \tag{7.11}$$

7.1.1 Dimensionless equations

The equations of motion are nondimensionalized to reduce the number of parameters and to void numerical problems related to stiff systems. The following change of variables are used:

$$\begin{aligned}
&\tau = \omega_R t,\ \eta = \frac{\Omega}{\omega_R},\ \nu_R = \frac{b_R}{\sqrt{m_R k_R}},\ \nu_S = \frac{b_S}{\sqrt{m_R k_R}},\ \nu_C = \frac{b_C}{\sqrt{m_R k_R}},\\
&\kappa = \frac{k_S}{k_R},\ \rho = \frac{m_S}{m_R},\ \kappa_C = \frac{k_C}{k_R},\ \sigma = \frac{r_u}{s},\ \hat{u}_{Rx} = \frac{u_{Rx}}{s},\ \hat{u}_{Ry} = \frac{u_{Ry}}{s},\ \hat{x}_S = \frac{x_S}{s},\\
&\hat{y}_S = \frac{y_S}{s}.
\end{aligned} \tag{7.12}$$

Using Eq. (7.12) in Eqs. (7.1)-(7.5), the following new system equations are obtained:

$$\hat{\mathbf{u}}_R'' + \nu_R \hat{\mathbf{u}}_R' + \hat{\mathbf{u}}_R = \hat{\mathbf{f}}_u - \hat{\mathbf{f}}_c, \tag{7.13}$$

$$\rho \hat{\mathbf{u}}_S'' + \nu_S \hat{\mathbf{u}}_S' + \kappa(\hat{\mathbf{u}}_S - \hat{\mathbf{u}}_{S0}) = \hat{\mathbf{f}}_c, \tag{7.14}$$

where

$$\hat{\mathbf{f}}_c = \frac{1}{s} \left\langle -\kappa_C d - \nu_C \langle \dot{d} \rangle \right\rangle \langle -d \rangle^0 \begin{bmatrix} \cos\psi - \mu_f \sin\psi & \sin\psi + \mu_f \cos\psi \end{bmatrix}^T , \tag{7.15}$$

$$\hat{\mathbf{f}}_u = \sigma \eta^2 \begin{bmatrix} \cos(\eta\tau + \varphi_0) & \sin(\eta\tau + \varphi_0) \end{bmatrix}^T . \tag{7.16}$$

The scaling of the time t by the natural frequency of the rotor ω_R is important to avoid problems with numerical methods when solving the nonlinear equations. In the left-hand side of Eq. (7.13), the nondimensionalized rotor stiffness is the unity. Hence, the solution of the equations is not affected by high rotor stiffness. On the other hand, in Eq. (7.14), the nondimensionalized stator stiffness is the ratio between the rotor and stator stiffness. In this case, the nondimensionalized stator stiffness is not the unity. However, if both stiffness coefficients are in the same order of magnitude, the ratio would be small compared to both stiffness coefficients.

7.2 Tools for analysis

7.2.1 Poincaré section

The Poincaré section can better identify periodic, quasi-periodic and chaotic motion. It can be obtained by sampling the state variables at the times $t_n = 2\pi n/\Omega + t_0$. This yields a sequence of values that corresponds to points in the phase plane. The pattern of the points correspond to different type of vibration. If only one point is obtained, the response is a synchronous or period-1 motion. n points means a subharmonic or period-n motion. When points form a closed curve, it corresponds to a quasi-periodic motion with two incommensurable frequencies. Finally, when a quasi-periodic motion with more than two incommensurable frequencies is obtained, the points are scattered over the phase plane and it can be a strong evidence of chaotic motion (see Moon [111]).

7.2.2 Full spectrum

The frequency analysis of a rotor's orbit can be performed by applying the DFT to the signals in two different ways. If the DFT is applied to each signal individually, it is called a half spectrum. Since they are computed separately, no relative information between the signals is obtained. On the other hand, a full spectrum can be used to decompose the orbits into forward orbits (precessions in the direction of rotation) and backward orbits (processions in the opposite direction of rotation). The visualization of such orbits is of great importance for detecting and identifying rubbing.

The first step to determine the full spectrum is to consider the motion's orbit as the complex function

$$u(t) = u_x(t) + iu_y(t) = U_x \cos(\omega t + \phi_x) + iU_y \sin(\omega t + \phi_y), \tag{7.17}$$

where u_x and u_y are the signals from two orthogonal proximity sensors, U_x and U_y

are their amplitudes, and ϕ_x and ϕ_y are their phases. Eq. (7.17), rewritten as sums of complex exponentials, turns to

$$\begin{aligned} U =& \frac{U_x}{2}\left(e^{i(\omega t+\phi_x)} + e^{-i(\omega t+\phi_x)}\right) + i\frac{U_y}{2}\left(e^{i(\omega t+\phi_y)} - e^{-i(\omega t+\phi_y)}\right), && (7.18)\\ U =& e^{i\omega t}\left(\frac{U_x}{2}e^{i\phi_x} + i\frac{U_y}{2}e^{i\phi_y}\right) + e^{-i\omega t}\left(\frac{U_x}{2}e^{-i\phi_x} - i\frac{U_y}{2}e^{-i\phi_y}\right). && (7.19)\end{aligned}$$

The coefficients that are multiplied by $e^{i\omega t}$ and $e^{-i\omega t}$ correspond to the parameters of the forward (FW) and backward (BW) orbits, respectively. Thus, Eq. (7.18) is written as

$$U = e^{i\omega t}U_{FW}e^{i\phi_{FW}} + e^{-i\omega t}U_{BW}e^{i\phi_{BW}}, \tag{7.20}$$

where

$$\begin{aligned} U_{FW}e^{i\phi_{FW}} =& \frac{1}{2}\left(U_x e^{i\phi_x} + iU_y e^{i\phi_y}\right), && (7.21)\\ =& \frac{1}{2}\left(U_x \cos\phi_x + iU_x \sin\phi_x + iU_y \cos\phi_y - U_y \sin\phi_y\right), && (7.22)\\ U_{BW}e^{i\phi_{BW}} =& \frac{1}{2}\left(U_x e^{-i\phi_x} - iU_y e^{-i\phi_y}\right), && (7.23)\\ =& \frac{1}{2}\left(U_x \cos\phi_x - iU_x \sin\phi_x - iU_y \sin\phi_y + U_y \cos\phi_y\right). && (7.24)\end{aligned}$$

Thus, by considering the complex orbit from Eq. (7.17), the amplitudes and phases of the forward and backward components for a frequency ω are obtained. Since the Fourier transform decomposes a signal into amplitudes and phases of different frequencies, the forward and backward components of a motion can be represented by

$$U(\omega) = \mathcal{F}\left\{u_x + iu_y\right\}, \tag{7.25}$$

which is known as the full spectrum of the orbit.

7.2.3 Full spectrogram

The Fourier transform decomposes a signal into a sum of complex exponentials, providing that the signal is stationary over a range of time. In a rotating machine, the spectrum is useful to analyze the response at a fixed operating condition such as pressure drop or rotating speed. However, if some parameters are changing with time, the response may not be stationary anymore. In such cases, different methods are available to overcome this situation. One straightforward approach is to use a window function in the DFT small enough to guarantee the stationarity of the signal. This is called the discrete short-time Fourier transform and is defined as

$$U\left[n,k\right] = \sum_{m=-\infty}^{\infty} u[m]w[n-m]e^{-i2\pi kn/N}, \tag{7.26}$$

where w is the window function, n is the n-th time sample, k the k-th frequency component and m the length of the window. This transformation is also called spectrogram.

For contact detection, the spectrogram is very useful to determine the time interval where the contact began. Also, depending on the dominant frequency components, the type of the rubbing can be identified.

7.3 Type of responses

Depending on the value of the parameters in Eq. (7.12), the equations of motion in Eqs. (7.13)-(7.16) exhibit different types of vibration, namely forward, backward, subharmonic, superharmonic, sidebands and chaotic vibration. Each of them can be identified and analyzed by the aforementioned tools.

Three simulations are performed to show these types of vibration. A fourth order Runge-Kutta method [112] was implemented in Matlab to integrate the equations. Part of the code is shown in Appendix E.1. The parameters of the simulations are shown in Tab. 7.1.

Parameter	Symbol	Value			Units
		(Sim. 1)	(Sim. 2)	(Sim. 3)	
Concentric clearance	s	$4\cdot10^{-5}$	$5.8\cdot10^{-5}$	0.004	m
Unbalance radius	σ	0.5	0.3448	0.5	-
rotor-stator mass	ρ	0.01	0.17	3	-
Static eccentricity	$\hat{\mathbf{u}}_{S0}$	$[0,0]^T$	$[0.8276,0]^T$	$[0,0]^T$	-
Friction coefficient	μ_f	0.3	0.1	0.3	-
rotor-stator stiffness	κ	3	1.64	5	-
Rotor damping	ν_R	0.1	0.0240	0.1	-
Stator damping	κ_C	0	0.0220	0.1	-
Contact damping	ν_C	3	3	3	-
Initial rotation phase	φ_0	0	0	0	rad

Table 7.1: Parameters of the simulations.

7.3.1 Simulation 1 (Forward and backward whirl vibration)

The first simulation was performed to show the forward and backward whirl motion. Fig. 7.2 shows the magnitudes ($\hat{U}_R$), stator ($\hat{U}_S$) and rotor-stator ($\hat{U}_{RS}$) orbit from

0 to $3\omega_R$. Before $\Omega/\omega_R = 0.8208$ Hz, the rotor's response in Fig. 7.2a corresponds to synchronous vibration. Then, when the amplitude surpasses the clearance s, the contact occurs and the amplitude of vibration is spread out inside an envelope. Two regions with high and low vibration amplitude can be identified. Similar behavior is seen in the stator response in Fig. 7.2b, except for the non-contact state, where the stator vibration is zero. Since the proximity sensors are located in the stator, they are able to measure only the relative distance between the rotor and stator. This relative vibration is shown in Fig. 7.2c. A value less than s corresponds to a non-contact state, while a value beyond it represents a penetration of the rotor in the stator.

The previous results suggest the existence of a low and high vibration state during rubbing. Fig. 7.3 shows graphical information of one frequency from each interval. Fig. 7.3a shows the orbit of the relative vibration $\hat{u}_{RS}$, along with a Poincaré section, at $\eta = 0.9061$. The motion is restrained between a circular strip with a rosette-like form. The Poincaré section encloses a portion of the orbit, not including the center. These patterns are related to two different frequencies components, as shown in the full spectrum of Fig. 7.3c. The positive frequency $\eta_{\mathrm{F}}/\eta = 1$ is the synchronous component, while the negative frequency $\eta_{\mathrm{F}}/\eta = -1.39$ corresponds to the backward whirl component. However, since the amplitude of the synchronous is higher, the motion is considered a forward whirl type. Similarly, Fig. 7.3b shows the orbit with a Poincaré section at $\eta = 1.5586$ Hz. Although the motion is also restricted to a circular strip, the Poincaré section encloses the center of the orbit. The full spectrum in Fig. 7.3d shows two different frequencies but the amplitude of the negative component $\eta_{\mathrm{F}}/\eta = -1.17$ is greater than the synchronous vibration. Thus, this motion is considered a backward whirl. An analysis of the vibration during a machine run-up is carried out by means of the spectrogram, as shown in Fig. 7.4. The continuous straight red line corresponds to the synchronous vibration. The forward and backward whirl vibrations can be easily identified in this type of graphical representation.

7.3.2 Simulation 2 (Subharmonic, superharmonic and chaotic vibration)

Subharmonic, superharmonic and chaotic vibration may occur when the rotor and stator are statically misaligned. The results for this case are shown in Fig. 7.5. The magnitudes of the stator and rotor's vibration in Figs. 7.5a and 7.5b reached higher amplitudes than the forward and backward whirls. The rotor indentation during rubbing, shown in Fig. 7.5c is also higher than in Simulation 1.

Three types of vibration were identified in the relative amplitudes. They are

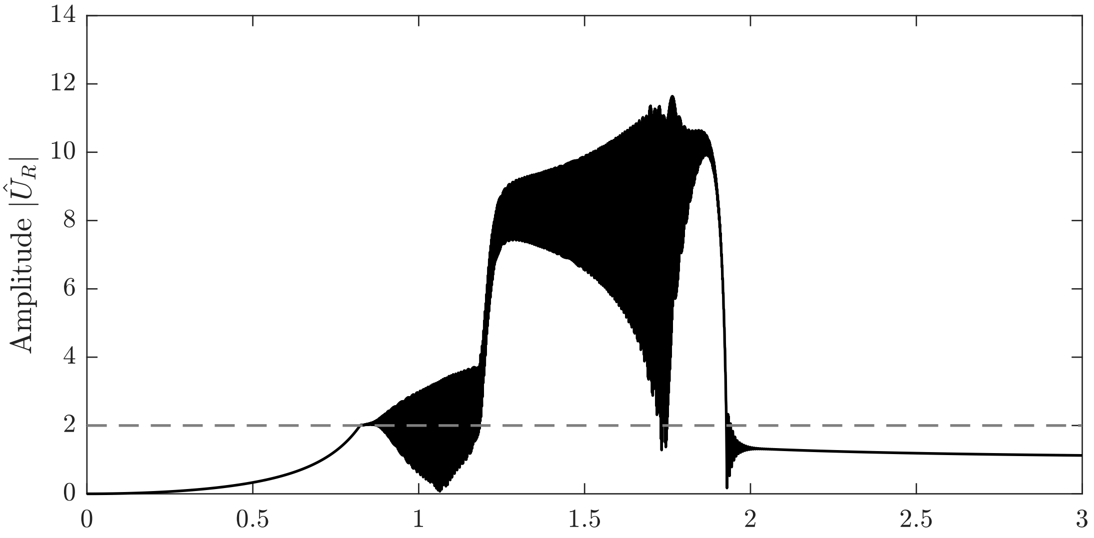

(a) Dimensionless frequency η

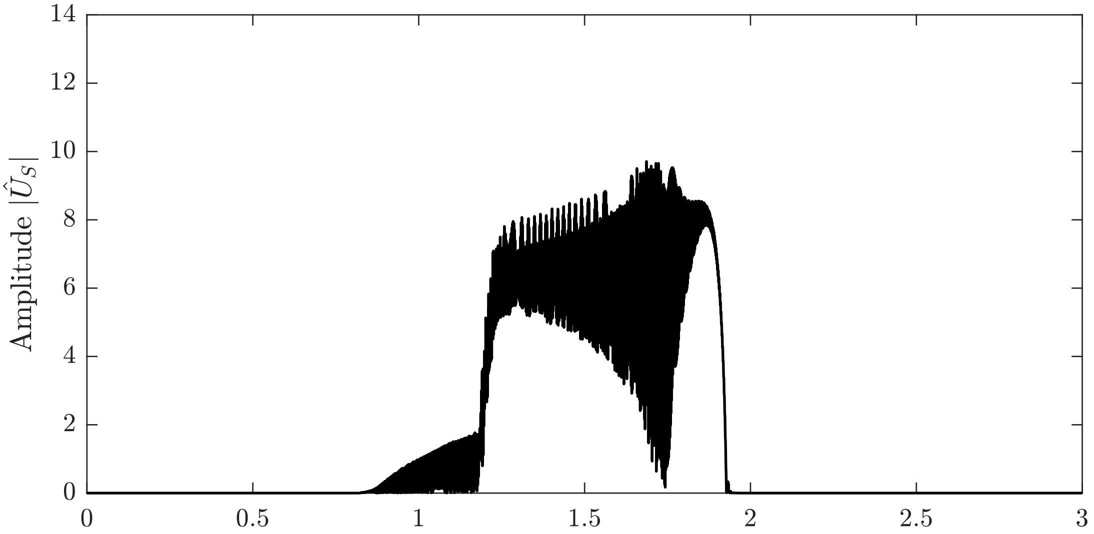

(b) Dimensionless frequency η

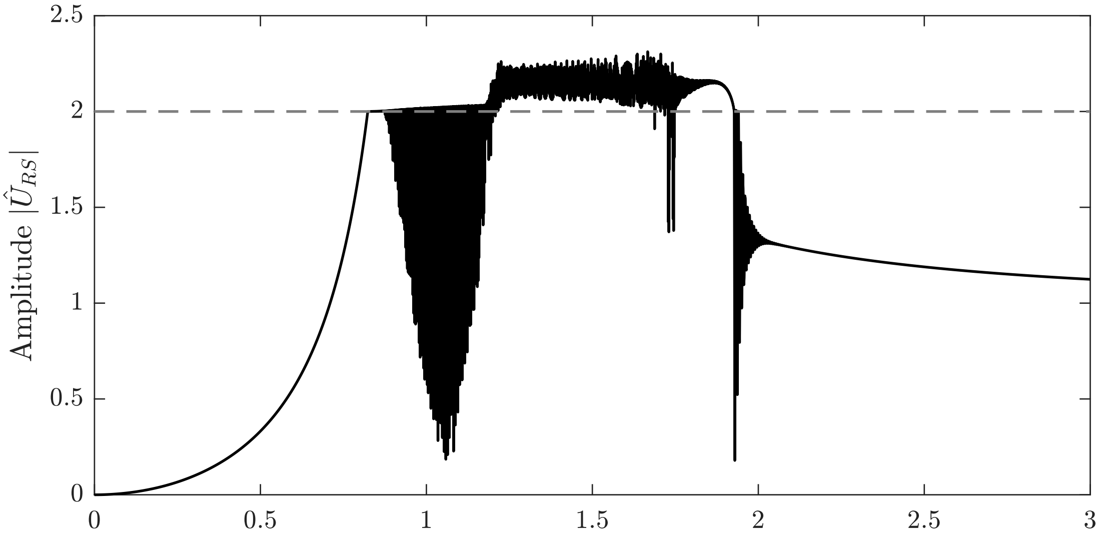

(c) Dimensionless frequency η

Figure 7.2: Magnitude of the rotor, stator and rotor-stator displacement with forward and backward vibration.

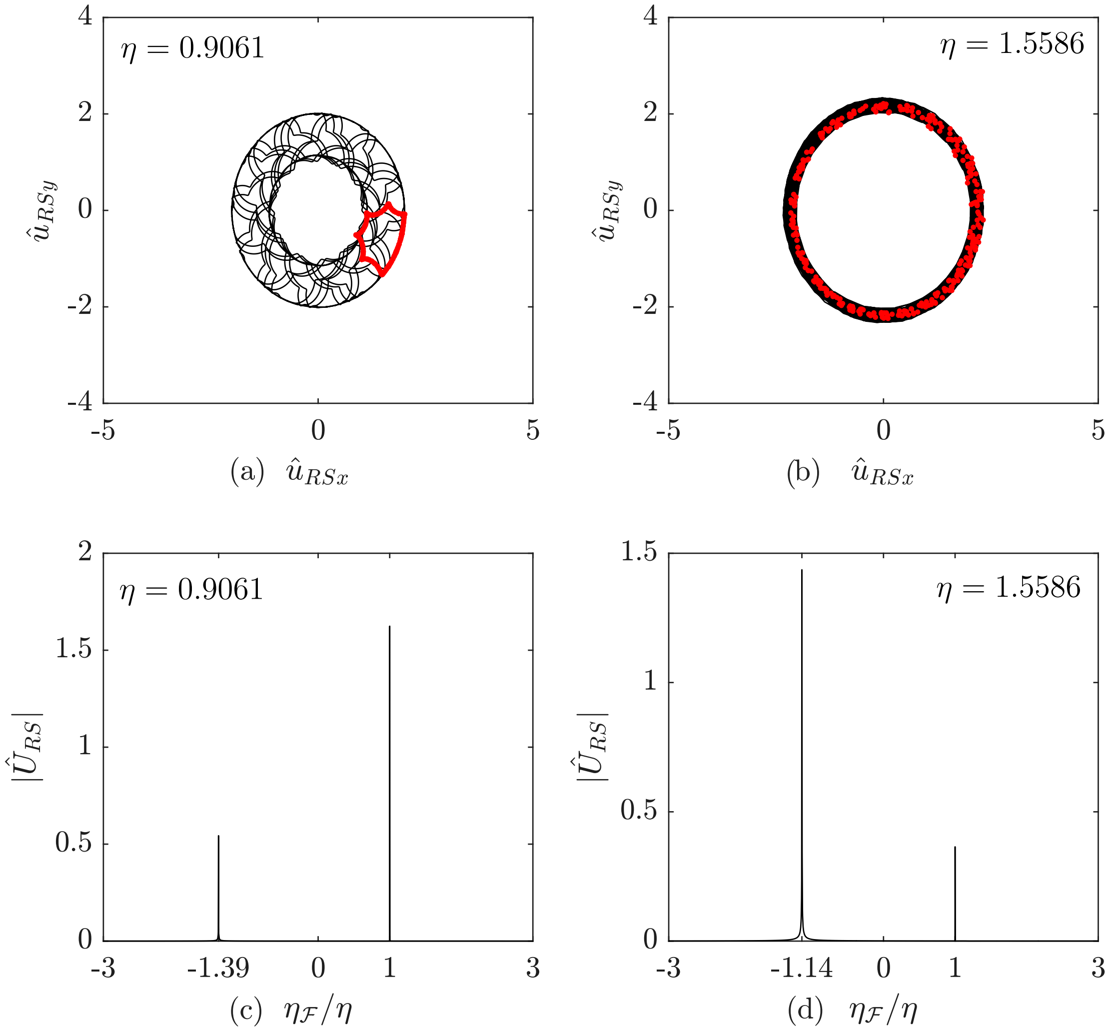

Figure 7.3: Orbits and full spectrum of the rotor-stator displacement with forward and backward vibration.

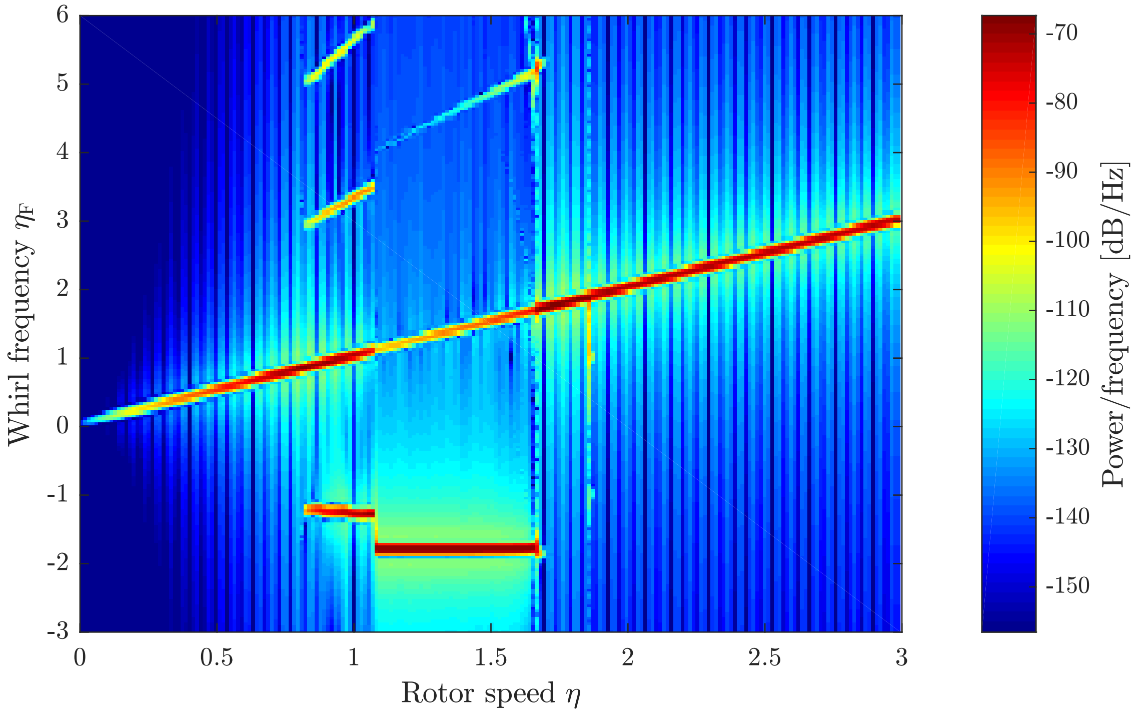

Figure 7.4: Full spectrogram of the rotor-stator displacement with forward and backward vibration.

shown in Fig. 7.6. For $\eta = 1.2071$, the orbit in Fig. 7.6a exhibits a simpler form with a punctual Poincaré section. In the full spectrum from 7.6c, five frequency components were found. The greatest amplitude component is the synchronous vibration. The superharmonic vibrations $\eta_{\mathrm{F}} = \pm 2\eta$ were found. Also, a vibration around $\eta_{\mathrm{F}} = 0$ was present. For $\eta = 2.5202$, the Poincaré sections of the orbit in Fig. 7.6b forms a dispersed pattern, suggesting an evidence of chaotic vibration. The frequency components are shown in Fig. 7.6d. The vibration contains components spread along an interval, not only at discrete values. This is also an evidence of chaotic motion. Moreover, the subsynchronous vibrations $\eta_{\mathrm{F}} = \pm 0.5\eta$ were found. The spectrogram in Fig. 7.7 reveals the three types of vibration during a machine run-up. Also, the transition between chaotic and periodic motion (sub and superharmonic) is also visible.

7.3.3 Simulation 3 (Vibration with sidebands)

Another type of motion arises when the eigenfrequency of the stator is slightly higher than the first critical speed of the rotor. The amplitude of vibrations are shown in Fig. 7.8. In this case, the rotor and stator's vibration, shown in Figs. 7.8a and 7.8b, do not spread out after the contact. It remains at a simple vibration until $\eta = 1.259$. After that frequency, a different motion is set. Similar results can be observed in the relative amplitude in Fig. 7.8c. The types of motion for two frequencies are shown in Fig. 7.9. The orbits at $\eta = 1.2707$ and $\eta = 1.3667$, in Figs. 7.9c and 7.9d , are circular and the Poincaré section encloses a portion of the orbit, but not in a circular pattern. For both frequencies, the full spectrum exhibits the synchronous vibration with smaller components around, or sidebands. Moreover, the spacing of the sidebands decreases with the frequency. The spectrogram with the different motions type is shown in Fig. 7.10

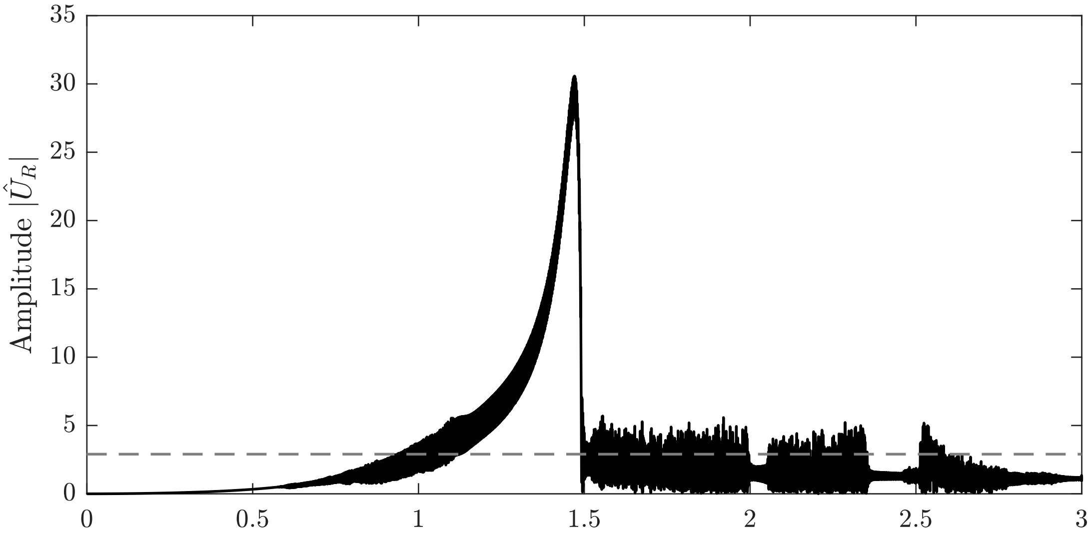

(a) Dimensionless frequency η

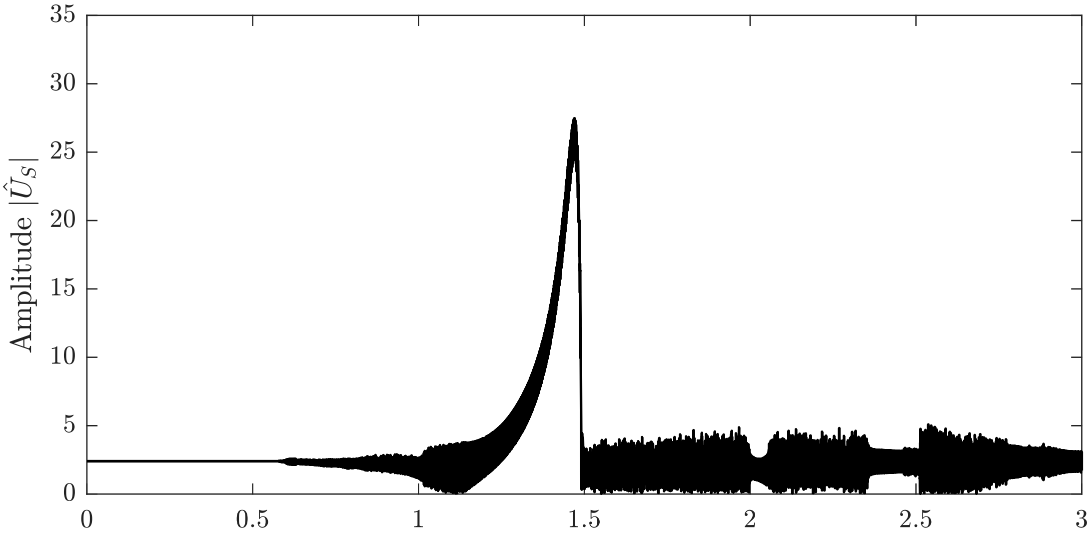

(b) Dimensionless frequency η

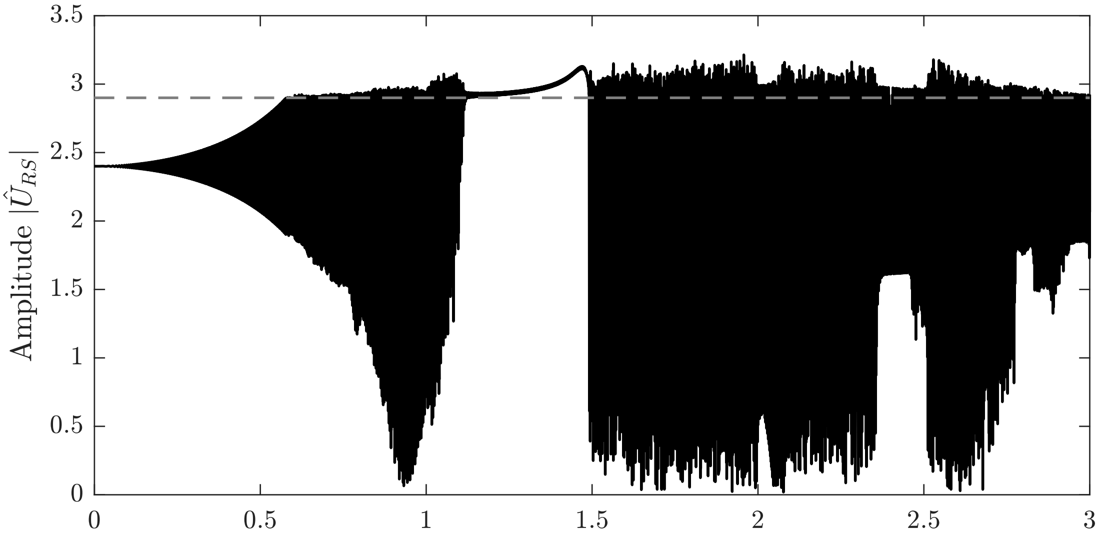

(c) Dimensionless frequency η

Figure 7.5: Magnitude of the rotor, stator and rotor-stator displacement with subharmonic, superharmonic and chaotic vibration.

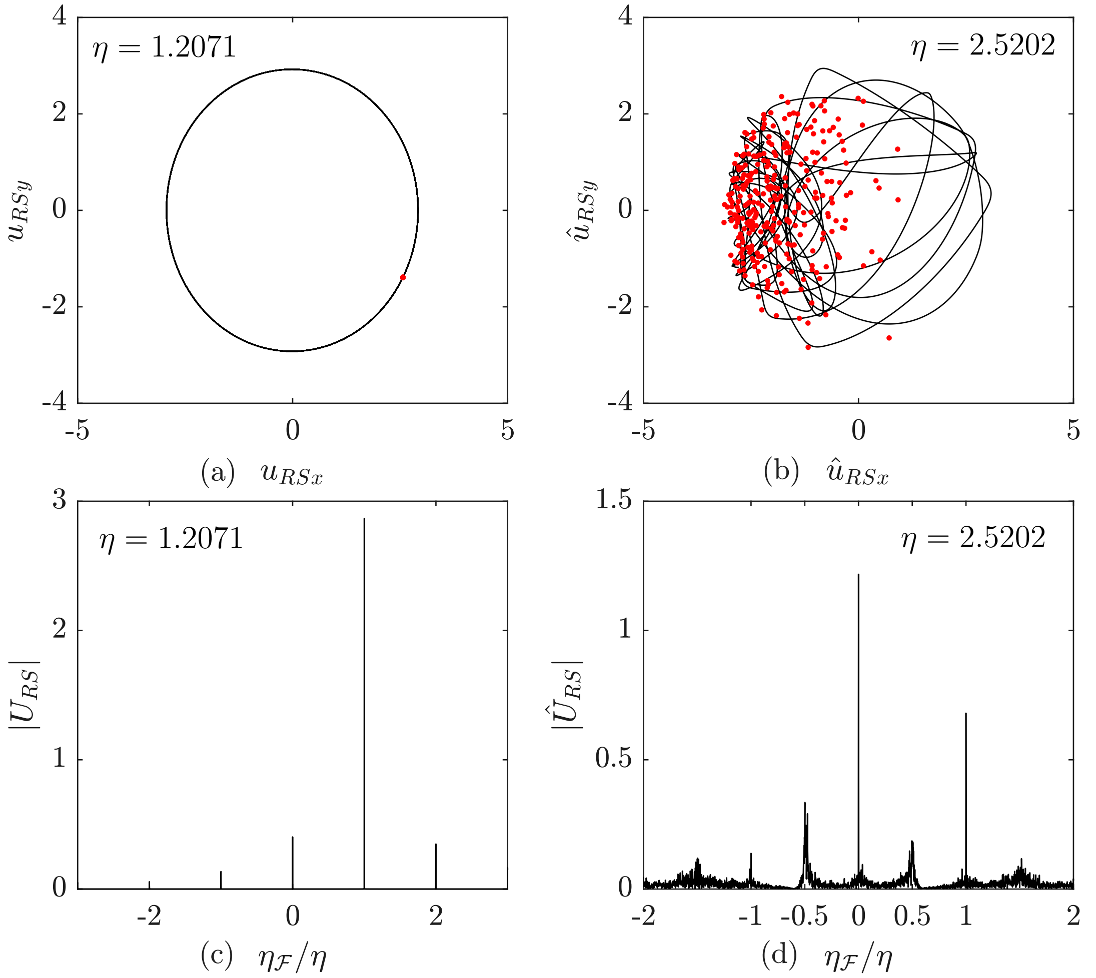

Figure 7.6: Orbits and full spectrum of the rotor-stator displacement with subharmonic, superharmonic and chaotic vibration.

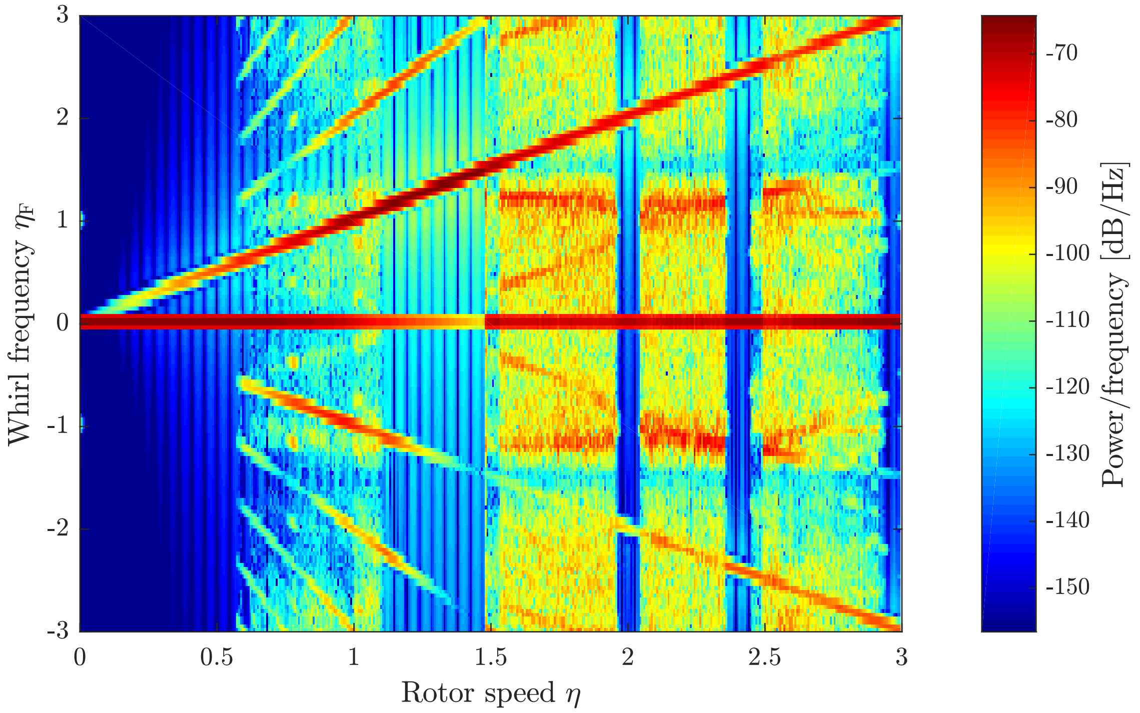

Figure 7.7: Full spectrogram of the rotor-stator displacement with subharmonic, superharmonic and chaotic vibration.

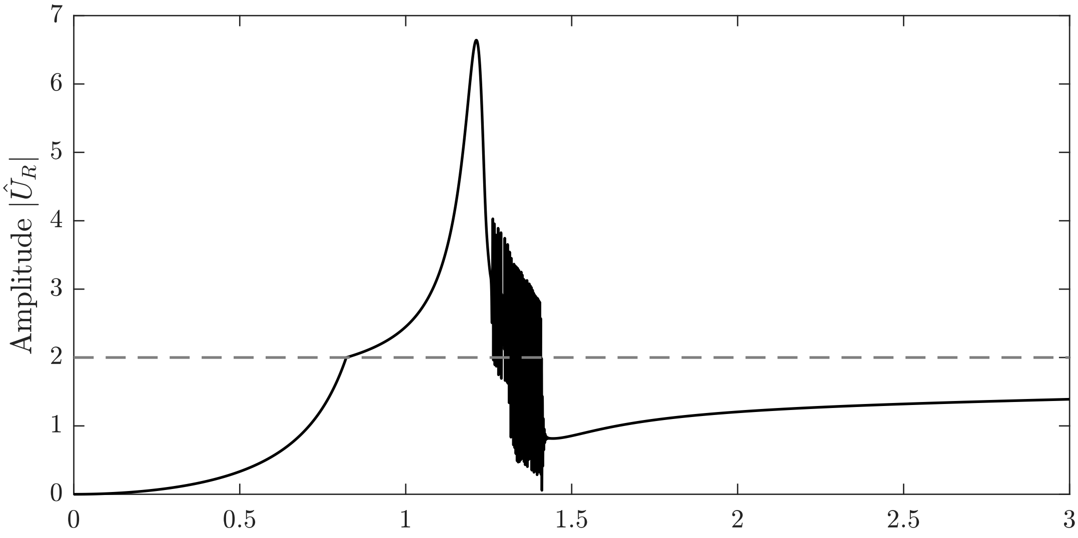

(a) Dimensionless frequency η

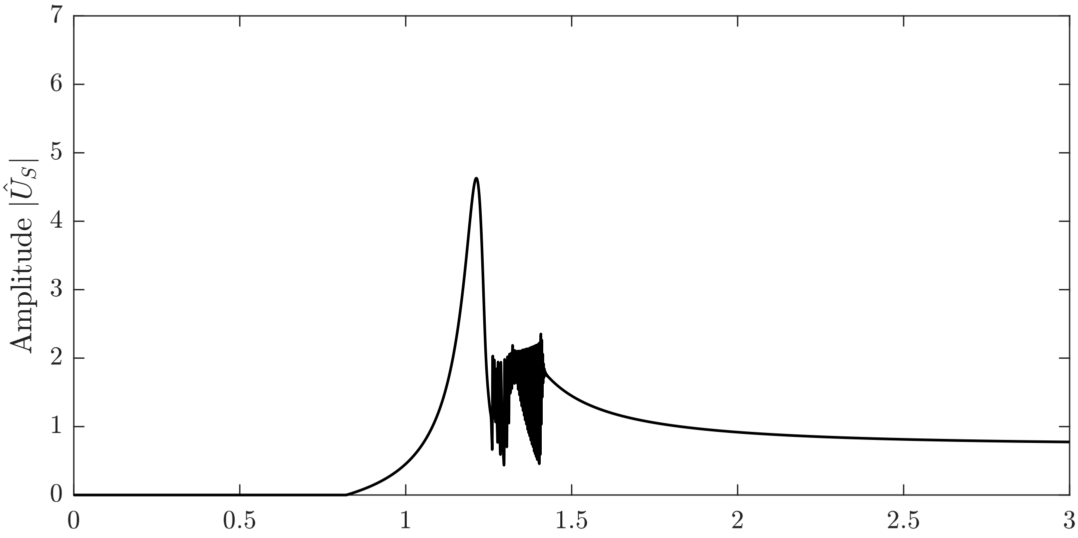

(b) Dimensionless frequency η

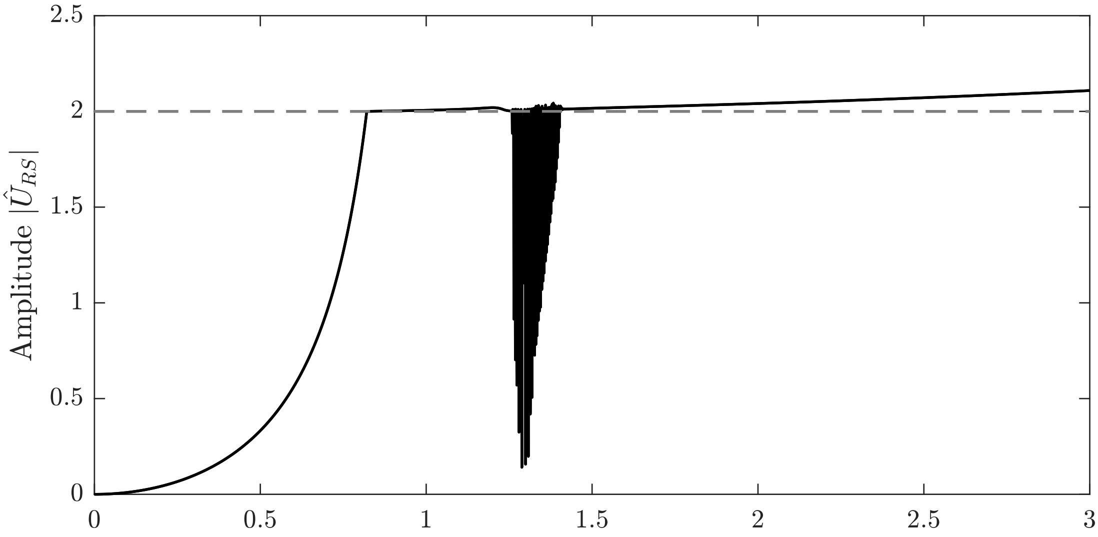

(c) Dimensionless frequency η

Figure 7.8: Magnitude of the rotor, stator and rotor-stator displacement with sidebands vibration.

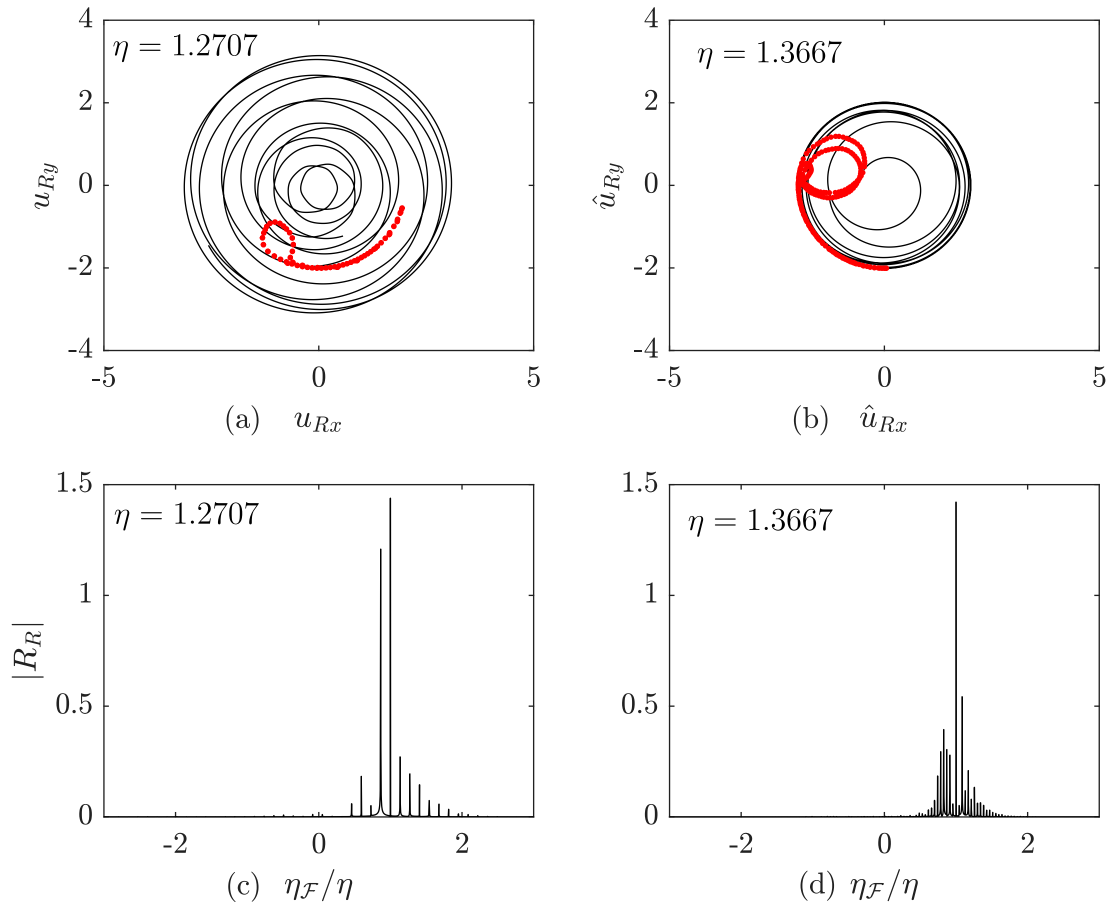

(a) u_{Rx} (b) $\hat{u}_{Rx}$

(c) $\eta_{\mathcal{F}}/\eta$ (d) $\eta_{\mathcal{F}}/\eta$

Figure 7.9: Orbits and full spectrum of the rotor-stator displacement with sidebands vibration.

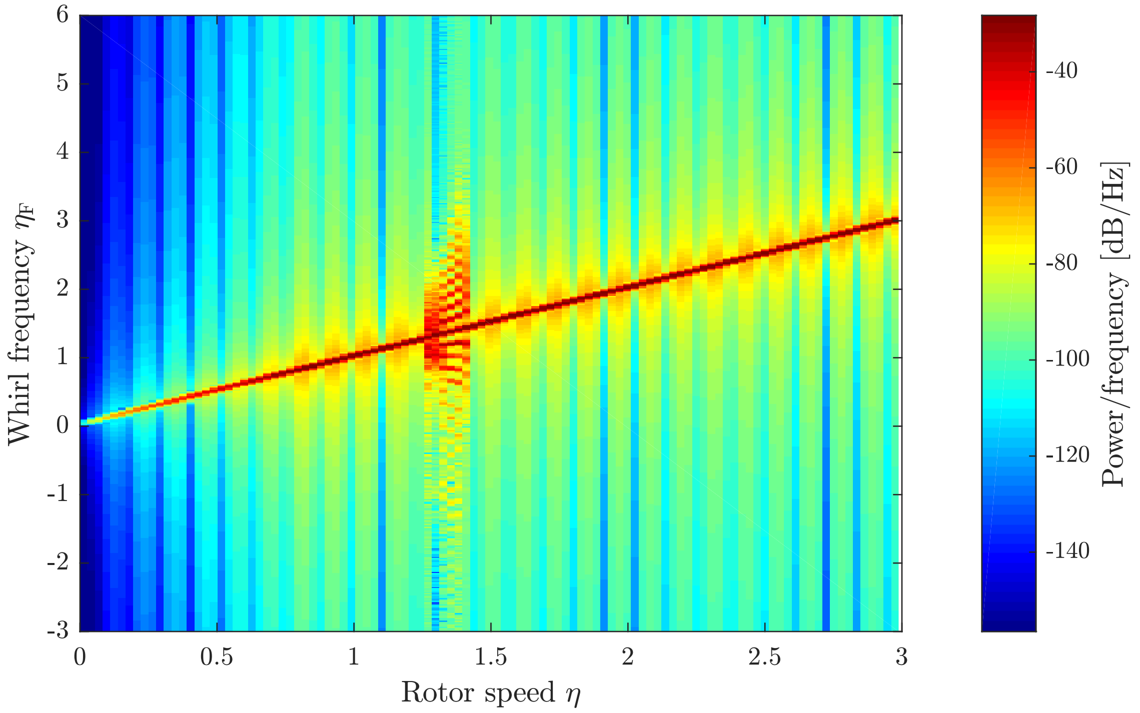

Figure 7.10: Full spectrogram of the rotor-stator displacement with sidebands vibration.

7.4 Discussion

The analysis of the rubbing in rotors leads to complex mathematical models due to the discontinuous model of the forces. Although a simplified model was considered, the numerical integrator used to solve the equations may take a high computational time depending on the time-step. If additional degrees of freedom are added, that time may increase considerably. Moreover, the number of parameters to consider increases the complexity of the analysis. Thus, in this work, the mathematical model was as simplified as much as possible.

The nondimensionalization of the equations applied to the equations was performed for two reasons. One of them is the reduction of the number of parameters. This can simplify some analysis without loss of generality. Also, the dimensionless time introduces a time scaling that enhance the performance of the numerical integration when high stiffness values are considered. This type of system may cause a bad numerical condition due to the small step size needed to capture the dynamics.

The tools for analysis used in this work were chosen due to the simplicity and practicality of their implementation; characteristics that are considered in industrial applications. The orbits combined with the Poincaré map are rather convenient to visualize the type of vibration of the machine. For quantitative analysis, the full spectrum yields the amplitude of each frequency component present in the motion. In the case of monitoring the machine when varying a parameter such as the rotor speed, time-frequency methods can be implemented. Among the most used are the FFT and Wavelets. The frequency and time resolution is better handled by the Wavelets. The FFT depends on the uncertainty principle; a high time resolution leads to a low frequency resolution and vice-versa. However, the fast implementation of the FFT makes the spectrum-base method rather useful in the industry.

The simulations showed similar results to those observed in the literature; the forward, backward, subsynchronous, supersynchronous and chaotic motion appeared. The difference of this work from the literature lies on the use of a nondimensional model, the use of a relative rotor-stator displacement and the use of full spectrogram to detect forward and backward precessions. As stated before, the nondimensional model is convenient to both reduce the number of parameters and to change the time scale of the system in order to avoid a bad numerical condition. The simulation of the orbits from the rotor or stator, individually, could not be observed in an experimental set up if the stator stiffness is within the order of magnitude of that of the rotor stiffness; the relative rotor-stator displacement is a more realistic measure. The use of the full spectrum to account for the forward and backward orbits were introduced by Bently and Muszynska. Since the contact simulations showed $0X$, $1X$, $-1X$, and other components, it is a useful tool to analyze the data. For nonstationary tests like run-ups and rundowns, a full spectrogram is a better tool. Although the full spectrum cascades or waterfall plots have been widely used, a spectrogram is a compact representation of the same plots.

One of the main drawbacks of the model is the number of parameters to be determined in the real machine. In this work, similar values obtained from the literature were used to verify the model. Among the most parameters are the stiffness and damping coefficients. For some values of this parameter, the numerical integration may not converge. For future works, this parameter must be determined experimentally from some properties of the material such as elasticity and hardness.

In Appendix D, preliminary experimental results of the test rig's orbits are shown. The frequencies $-1X$, $1X$ and $0X$ revealed by the spectrogram are similar to the Simulation 2. Thus, there might be a static misalignment between stator and rotor. For future works, the parameters of the model will be identified from the vibration measurements.

Chapter 8

Rotordynamic system with anisotropy and nonlinearity

In this chapter, a theoretical analysis of a flexible rotor with an annular seal is performed base on the work of Maldonado et al. [26]. The system equations obtained have a periodic stiffness matrix and nonlinear terms. A Floquet theory is used to plot stability charts for different levels of anisotropy. For the nonlinear terms, a method known as normal forms is applied. It is based on several coordinate transformations that takes the original equations to a simpler form.

The system studied is composed of an anisotropic rotor, two asymmetrical bearings, a disk and two nonlinear spring-damper systems, as shown in Fig. 8.1. The stiffness matrix of the rotor and bearings were taken from [113] and the nonlinearities were added. The nonlinear stiffness and damping can model some fluid-induced forces that are created in some components, such as annular gas seals, of rotating machinery. Considering the Fig. 8.1, the system equations are

$$\mathbf{M}\ddot{\mathbf{u}} + \mathbf{K}(t)\mathbf{u} + \mathbf{f}_{nk}(\mathbf{u}) + \mathbf{f}_{nc}(\dot{\mathbf{u}}) = \mathbf{f}_g + \mathbf{f}_u(t), \tag{8.1}$$

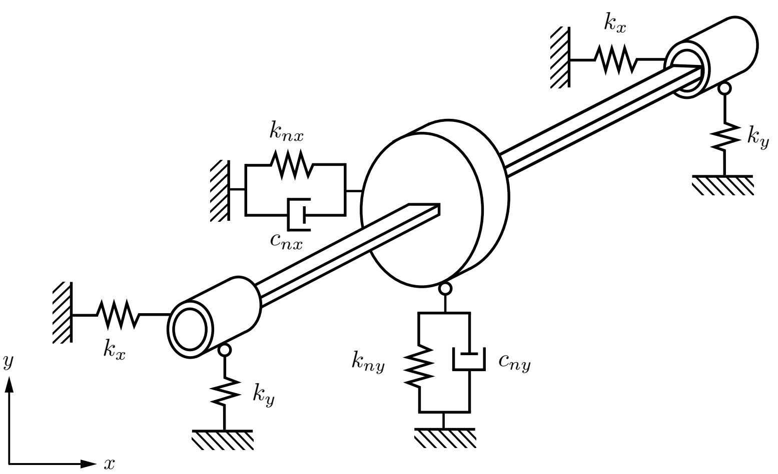

Figure 8.1: Rotordynamic system with a flexible anisotropic rotor, a disk, 2 bearings and two set of nonlinear spring-dampers at the disk (based on Gasch and Pfützner[113], and Maldonado et al. [26])

where

$$\mathbf{M} = \begin{bmatrix} m_d & 0 & 0 & 0 \\ 0 & m_d & 0 & 0 \\ 0 & 0 & 2m_b & 0 \\ 0 & 0 & 0 & 2m_b \end{bmatrix}, \mathbf{K}(t) = \begin{bmatrix} \mathbf{K}_r(t) & -\mathbf{K}_r(t) \\ -\mathbf{K}_r(t) & \mathbf{K}_r(t) + \mathbf{K}_b \end{bmatrix}, \mathbf{f}_g = \begin{bmatrix} 0 \\ m_d g \\ 0 \\ 2m_b g \end{bmatrix},$$

$$\mathbf{K}_r(t) = \begin{bmatrix} k_\zeta \cos^2 \Omega t + k_\eta \sin^2 \Omega t & (k_\zeta - k_\eta) \cos \Omega t \sin \Omega t \\ (k_\zeta - k_\eta) \cos \Omega t \sin \Omega t & k_\zeta \sin^2 \Omega t + k_\eta \cos^2 \Omega t \end{bmatrix}, \mathbf{f}_u(t) = \varepsilon m_d \Omega^2 \begin{bmatrix} \cos \Omega t \\ \sin \Omega t \\ 0 \\ 0 \end{bmatrix},$$

$$\mathbf{u}(t) = \begin{bmatrix} u_x \\ u_y \\ u_{xb} \\ u_{yb} \end{bmatrix}, \mathbf{K}_b = 2 \begin{bmatrix} k_x & 0 \\ 0 & k_y \end{bmatrix}, \mathbf{f}_{nk} = \begin{bmatrix} k_{nx} u_x^3 \\ k_{ny} u_y^3 \\ 0 \\ 0 \end{bmatrix}, \mathbf{f}_{nc} = \begin{bmatrix} c_{nx} \dot{u}_x^3 \\ c_{ny} \dot{u}_y^3 \\ 0 \\ 0 \end{bmatrix}. \tag{8.2}$$

$\mathbf{M}$ is the mass matrix with the mass of the disk m_d and mass of the bearing m_b along its main diagonal. $\mathbf{K}(t)$ is the stiffness matrix in terms of the rotor stiffness matrix $\mathbf{K}_r(t)$ and the stiffness of bearings $\mathbf{K}_b$. $\mathbf{f}_{nk}$ and $\mathbf{f}_{nc}$ are the nonlinear stiffness and damping forces in terms of the parameters k_{nx}, k_{ny}, c_{nx}, c_{ny}. Parameters k_ζ, k_η are the rotor stiffness in the rotating frame (along its principal axes of inertia). $\mathbf{f}_g$ is the gravity force vector due to the mass of the disk and bearings. $\mathbf{f}_u(t)$ is the unbalance force vector applied by a small eccentricity ε in the disk. $\mathbf{u}(t)$ is the displacement vector comprising the displacements of the center of disk u_x, u_y, and the displacements of the bearings u_{xb}, u_{yb}.

Since the rotor is asymmetric, its stiffness matrix $\mathbf{K}_r(t)$, w.r.t. an inertial frame, is time dependent and has a periodic behavior, i.e., $\mathbf{K}_r(t) = \mathbf{K}_r(t+T)$, with $T = \pi/\Omega$ as the period of the parametric excitation. On the other hand, the bearing stiffness $\mathbf{K}_b$ is constant.

8.0.1 Assumptions and system simplifications

The previous equations consider the mass of the bearings. Nevertheless, if the mass of the disk is much larger than that of the bearings, one may assume that the latter is negligible to the system behavior. This fact, in an inertial frame, yields the simpler system

$$\mathbf{M}_d\ddot{\mathbf{u}}_d + \tilde{\mathbf{K}}(t)\mathbf{u}_d + \tilde{\mathbf{f}}_{nk}(\mathbf{u}_d) + \tilde{\mathbf{f}}_{nc}(\dot{\mathbf{u}}_d) = \tilde{\mathbf{f}}_g + \tilde{\mathbf{f}}_u(t), \tag{8.3}$$

where

$$\begin{aligned}
&\mathbf{M}_d = \begin{bmatrix} m_d & 0 \\ 0 & m_d \end{bmatrix}, \mathbf{u}_d = \begin{bmatrix} u_x \\ u_y \end{bmatrix}, \tilde{\mathbf{f}}_g = \begin{bmatrix} 0 \\ m_d g \end{bmatrix}, \tilde{\mathbf{f}}_u(t) = \varepsilon m_d \Omega^2 \begin{bmatrix} \cos\Omega t \\ \sin\Omega t \end{bmatrix}, \\
&\tilde{\mathbf{K}}(t) = \mathbf{K}_r(t) - \mathbf{K}_r(t)\left(\mathbf{K}_r(t) + \mathbf{K}_b\right)^{-1}\mathbf{K}_r(t)\ , \tilde{\mathbf{f}}_{nk} = \begin{bmatrix} k_{nx}u_x^3 \\ k_{ny}u_y^3 \end{bmatrix}, \tilde{\mathbf{f}}_{nc} = \begin{bmatrix} c_{nx}\dot{u}_x^3 \\ c_{ny}\dot{u}_y^3 \end{bmatrix}.
\end{aligned} \tag{8.4}$$

The stiffness matrix $\mathbf{K}$ has the form

$$\tilde{\mathbf{K}}(t) = \begin{bmatrix} \dfrac{c_1 + c_2\cos\tilde{\Omega}t}{c_3 + c_4\cos\tilde{\Omega}t} & \dfrac{c_2\sin\hat{\Omega}t}{c_3 + c_4\cos\tilde{\Omega}t} \\[2ex] \dfrac{c_2\sin\tilde{\Omega}t}{c_3 + c_4\cos\tilde{\Omega}t} & \dfrac{c_5 - c_2\cos\tilde{\Omega}t}{c_3 + c_4\cos\tilde{\Omega}t} \end{bmatrix}, \tag{8.5}$$

where

$$\begin{aligned}
&\tilde{\Omega} = 2\Omega, \\
&c_1 = 2k_xk_yk_\eta + 2k_yk_\eta k_\zeta + k_xk_yk_\zeta, \\
&c_2 = 2k_xk_yk_\zeta - 2k_xk_yk_\eta, \\
&c_3 = 4k_xk_y + k_xk_\zeta + k_yk_\zeta + k_xk_\eta + k_yk_\eta + k_\eta k_\zeta, \\
&c_4 = k_xk_\zeta + k_yk_\eta - k_yk_\zeta - k_xk_\eta, \\
&c_5 = 2k_xk_yk_\eta + 2k_xk_\eta k_\zeta + k_xk_yk_\zeta.
\end{aligned} \tag{8.6}$$

For the purpose of this work, the gravity and unbalance forces are considered null for the nonlinear analysis of Section 8.2. For the Floquet theory of Section 8.1, only unbalance force is taken into account. Thus, the final system equations are

$$\mathbf{M}_d\ddot{\mathbf{u}}_d + \tilde{\mathbf{K}}(t)\mathbf{u}_d + \tilde{\mathbf{f}}_{nk}(\mathbf{u}_d) + \tilde{\mathbf{f}}_{nc}(\dot{\mathbf{u}}_d) = \tilde{\mathbf{0}}. \tag{8.7}$$

Eq. (8.3) corresponds to a system with nonlinearities, caused by the cubic stiffness and damping of the seal, and periodic stiffness matrix, due to the anisotropy between rotor and bearings. If the seal forces are neglected, the system reduces to a linear system with periodic coefficient parameters. These type of systems can be solved by Floquet theory, as will be shown in the next section. Specifically, the stability of the system for different levels of asymmetry are investigated. When the nonlinearities are taken into account, a different analysis is performed in Section 8.2. The fixed points of the system, near a certain rotor speed, are computed by a method known as normal forms.

8.1 Linear analysis

In this section, a linear analysis of system given by Eqs. (8.3)-(8.7) is carried out by assuming no seal forces. The stability of the linear system is assessed for different values of rotor anisotropy k_ζ/k_η and bearings anisotropy k_x/k_y. Stability maps are built by employing the Floquet theory.

8.1.1 First-order Form

The first step is to set the nonlinear stiffness and damping parameters k_{nx}, k_{ny}, c_{nx} and c_{ny} to zero in Eq. (8.7) and, then, express the system into a first-order form by using the vector state

$$\mathbf{q} = \begin{bmatrix} q_1 & q_2 & q_3 & q_4 \end{bmatrix}^T = \begin{bmatrix} u_x & \dot{u}_x & u_y & \dot{u}_y \end{bmatrix}^T . \tag{8.8}$$

Thus, Eq. (8.7) assumes the form

$$\begin{aligned}
\dot{q}_1 &= q_2, \\
\dot{q}_2 &= -\frac{1}{m_d}\left(\frac{c_1 + c_2\cos\tilde{\Omega}t}{c_3 + c_4\cos\tilde{\Omega}t} q_1 + \frac{c_2\sin\tilde{\Omega}t}{c_3 + c_4\cos\tilde{\Omega}t} q_3 - \varepsilon m_d \Omega^2 \cos\Omega t\right), \\
\dot{q}_3 &= q_4, \\
\dot{q}_4 &= -\frac{1}{m_d}\left(\frac{c_2\sin\tilde{\Omega}t}{c_3 + c_4\cos\tilde{\Omega}t} q_1 + \frac{c_5 - c_2\cos\tilde{\Omega}t}{c_3 + c_4\cos\tilde{\Omega}t} q_3 - \varepsilon m_d \Omega^2 \sin\Omega t\right).
\end{aligned} \tag{8.9}$$

Since these equations are in the form $\dot{\mathbf{q}} = \mathbf{A}(t)\mathbf{q} + \mathbf{f}(t)$, with

$$\mathbf{A}(t) = \mathbf{A}(t+T), \tag{8.10}$$

they represent a linear system with periodic coefficients. The stability analysis of this system is assessed by the Floquet theory, as shown in the following subsection.

Also, note that if the rotor anisotropy is null, i.e., $k_\zeta = k_\eta$, then $c_2 = 0$ and the system is not time-periodic anymore. In this case, the natural eigenfrequencies are

$$\omega_1 = \sqrt{\frac{1}{m_d}}\sqrt{\frac{3k_x k_y k_\zeta + 2k_y k_\zeta^2}{4k_x k_y + 2k_x k_\zeta + 2k_y k_\zeta + k_\zeta^2}}, \tag{8.11}$$

$$\omega_2 = \sqrt{\frac{1}{m_d}}\sqrt{\frac{3k_x k_y k_\zeta + 2k_x k_\zeta^2}{4k_x k_y + 2k_x k_\zeta + 2k_y k_\zeta + k_\zeta^2}}. \tag{8.12}$$

8.1.2 Floquet theory

The stability of the linear system in Eq. (8.9) in terms of the rotor speed Ω, the rotor stiffness k_ζ and k_η as well as the bearings stiffness k_x and k_y is analyzed. With the fundamental solution matrix $\mathbf{\Phi}(t)$, the solution at the time $t + T$ is given by

$$\mathbf{\Phi}(t+T) = \mathbf{\Phi}(t)\mathbf{\Phi}^{-1}(0)\mathbf{\Phi}(T), \tag{8.13}$$

where $\mathbf{\Phi}^{-1}(0)\mathbf{\Phi}(T)$ is called *monodromy matrix* [114]. According to the Floquet theory, the stability of the trivial solution is defined by the largest characteristic multiplier given by the eigenvalue of the monodromy matrix with the largest magnitude.

In this way, given a monodromy matrix with the eigenvalues $\lambda_1, \lambda_2, \ldots, \lambda_n$, the stability of the trivial solution is as follows:

(1) If all the characteristic multipliers are less than one, then the trivial solution is asymptotically stable.

(2) If all the characteristic multipliers are less than or equal to one, then the trivial solution is weakly stable.

(3) If at least one characteristic multiplier is greater than one, then the trivial solution is unstable.

The monodromy matrix is obtained by integrating Eq. (8.9) over one period with initial conditions such that $\mathbf{\Phi}(0) = \mathbf{I}$. Since the monodromy matrix represents the map $\mathbf{q}(t) \longmapsto \mathbf{q}(t+T)$, only the values at time $t+T$ of the integration are needed. In order to reduce the number of system parameters, the dimensionless quantities

$$\hat{k}_r = \frac{k_\zeta - k_\eta}{k_\zeta + k_\eta}\ , \quad \hat{k}_b = \frac{k_x - k_y}{k_x + k_y}\ , \quad \hat{\Omega} = \Omega/\omega\ , \quad \text{for } k_\zeta \geq k_\eta,\ k_x \geq k_y, \tag{8.14}$$

are introduced. The rotation speed is nondimensionalized by the frequency

$$\omega = \sqrt{\frac{k_\zeta + k_\eta}{2m_d}}, \tag{8.15}$$

which corresponds to the natural eigenfrequency when rigid bearings are considered. In Fig. 8.2, the greatest Floquet multiplier is shown for a certain set of parameters. The peaks correspond to a resonance condition. ω_1/ω and ω_2/ω correspond to fundamental parametric resonances, and $(\omega_1+\omega_2)/(2\omega)$ to a combination parametric resonance.

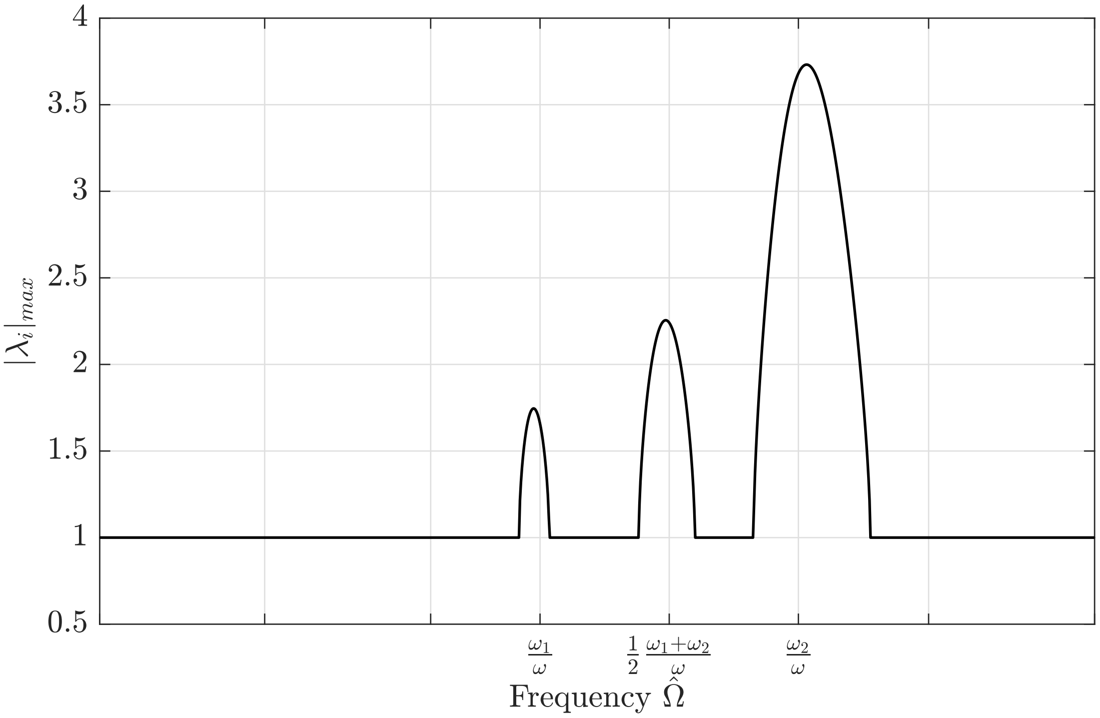

Figure 8.2: Greatest Floquet multiplier showing the fundamental and combination parametric resonance.

Stability maps

Based on these parameters, stability maps are constructed by computing the characteristic multipliers for each triple $\hat{k}_r$, $\hat{k}_b$, $\hat{\Omega}$. Figs. 8.3 and 8.4 show stability maps for different levels of rotor and bearings anisotropy in terms of the dimensionless frequency $\hat{\Omega}$. In each of the figures, stable and unstable regions can be observed. The unstable region is composed of three tongues and the affected area depends on the level of anisotropy. Fig. 8.3 shows that the bearings' anisotropy separates the tongues and stability areas between them are created. Note that the widest instability area occurs when $\hat{k}_r = 1$ and that the origins of the tongues tend to merge when decreasing $\hat{k}_b$. This result is in agreement with Gasch and Pfützner [113]. On the other hand, Fig. 8.4 shows that the rotor anisotropy also modifies the origins of the tongues. However, the stable areas between them are reduced and the unstable area is widened considerably. Thus, if the set of parameters lies in a stable region close to the tongues, a small variation of the anisotropy may destabilize the system.

Far from that region, the instability due to a small variation of the bearings or the rotor stiffness is less likely to occur. This result is important when defining safe operating conditions of a rotating machine. Also, since bearings may change their stiffness (e.g. due to wear) it is advisable to identify and monitor these parameters. The origins of the tongues in Fig. 8.3 are located along the axis $\hat{k}_r = 0$, which corresponds to the isotropic rotor case when $k_\zeta = k_\eta$. Based on Eqs. (8.11)-(8.12), the origins of the tongues are

$$\hat{\Omega} = \frac{\omega_1}{\omega}, \tag{8.16}$$

$$\hat{\Omega} = \frac{\omega_2}{\omega}, \tag{8.17}$$

$$\hat{\Omega} = \frac{1}{2}(\frac{\omega_1 + \omega_2}{\omega}). \tag{8.18}$$

Recalling from Eq. (8.6) that the parametric excitation frequency $\tilde{\Omega}$ is twice the rotation speed Ω, the fundamental parametric resonances $\tilde{\Omega} \approx 2\omega_1$ and $\tilde{\Omega} \approx 2\omega_2$ are excited through the rotation speeds $\Omega = \omega_1$ and $\Omega = \omega_2$, respectively. This means that the system has an external excitation resonance as well as fundamental parametric excitation. Thus, a nonlinear analysis around the fundamental frequencies is performed in the next section.

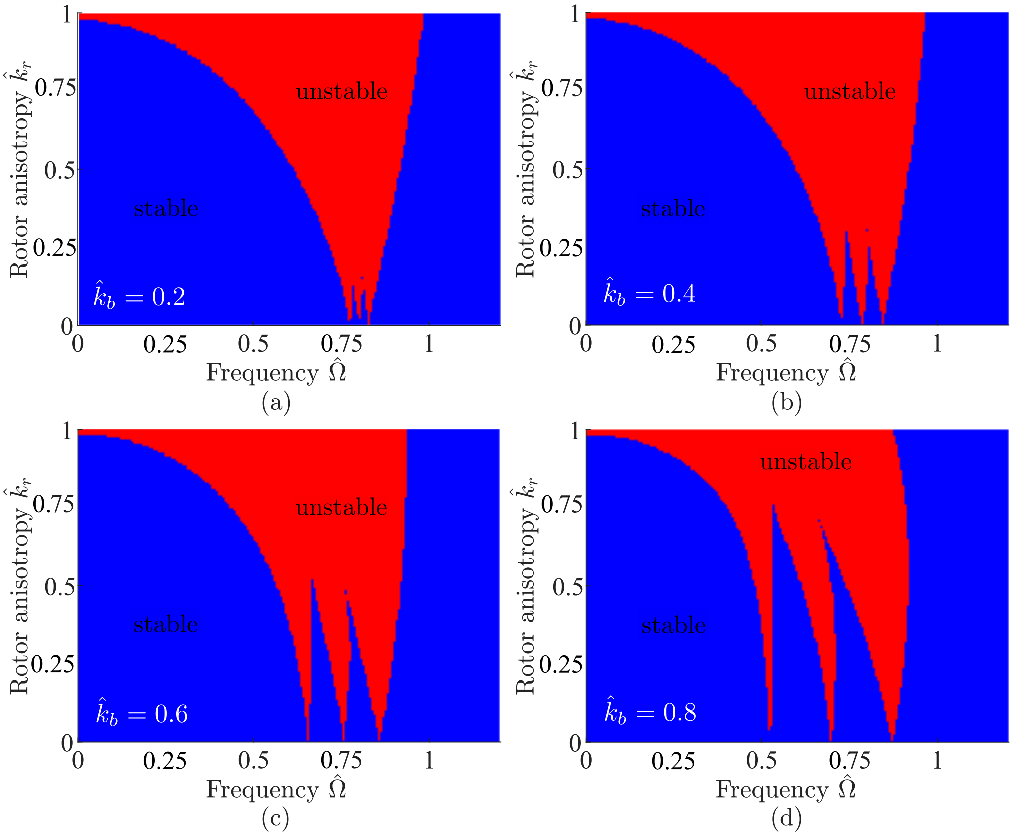

(a) (b) (c) (d)

Figure 8.3: Stability maps computed via the Floquet theory for $m_d = 1$ kg, $\omega = 1$ rad/s and $\hat{k}_b = 0.2$(a), 0.4(b), 0.6(c), 0.8(d)

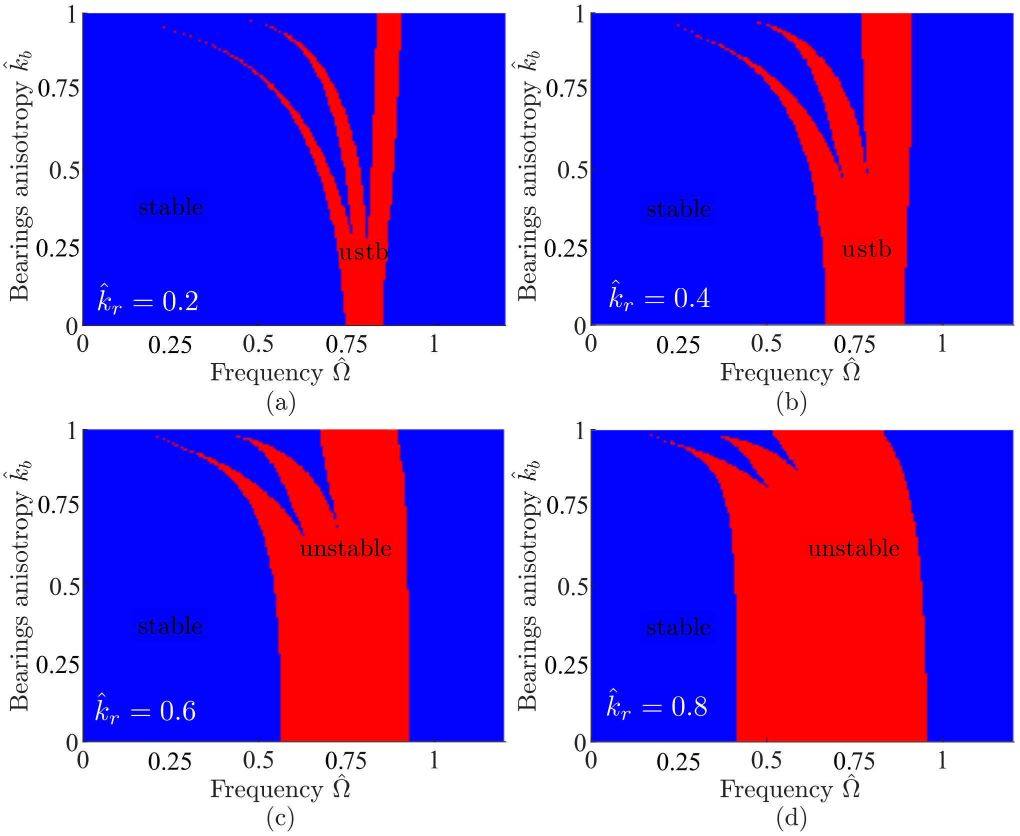

(a) (b) (c) (d)

Figure 8.4: Stability maps computed via the Floquet theory for $m_d = 1$ kg, $\omega = 1$ rad/s and $\hat{k}_r = 0.2$(a), 0.4(b), 0.6(c), 0.8(d)

8.2 Nonlinear analysis

In this section, the nonlinear stiffness and damping parameters are taken into account. The main objective is to find and analyze the fixed points of Eq. (8.7) by using the method of normal forms. The analysis is based on References [66, 77, 115].

8.2.1 First-order form

The method of normal forms requires a first-order representation of the equations and a polynomial form of nonlinearities with time-independent parameters. To do so, the transformation

$$\mathbf{q} = \begin{bmatrix} q_1 & q_2 & q_3 & q_4 & q_5 & q_6 \end{bmatrix}^T = \begin{bmatrix} u_x & \dot{u}_x & u_y & \dot{u}_y & e^{i\tilde{\Omega}t} & e^{-i\tilde{\Omega}t} \end{bmatrix}^T, \tag{8.19}$$

is used in Eq. (8.7). Note that the two complex exponentials are introduced to eliminate the time-dependency, creating an autonomous system. Nevertheless, increasing the states of the system leaves the entries of the stiffness matrix of Eq. (8.5) in a fraction form. Thus, multivariate Taylor series are used to expand the system equations up to the third order. The expanded equations take the form

$$\dot{\mathbf{q}} = \mathbf{f}(\mathbf{q}) = \mathbf{A}\mathbf{q} + \mathbf{f}_2(\mathbf{q}) + \mathbf{f}_3(\mathbf{q}), \tag{8.20}$$

where $\mathbf{A} = \left.\frac{\partial \mathbf{f}}{\partial \mathbf{q}}\right|_{\mathbf{q}=0}$ and $\mathbf{f}_2(\cdot)$, $\mathbf{f}_3(\cdot)$ contain all the terms of degree 2 and 3, respectively. Eq. (8.20) assumes the form

$$\begin{aligned}
\dot{q}_1 =& q_2,\\
\dot{q}_2 =& -\frac{1}{m_d}\left(\omega_1^2 q_1 + \frac{c_2c_3^2 - c_1c_4}{2c_3^2}(q_5+q_6)q_1 + \frac{c_2}{2c_3}(q_5-q_6)q_3 + \frac{c_1c_4^2 - c_3c_2c_4}{4c_3^3}(q_5+q_6)^2 q_1 + \right.\\
&\left.\frac{c_2c_4}{4c_3^2}(q_6^2 - q_5^2)q_3 + k_{nx}q_1^3 + c_{nx}q_2^3\right),\\
\dot{q}_3 =& q_4,\\
\dot{q}_4 =& -\frac{1}{m_d}\left(\omega_2^2 q_3 - \frac{c_2c_3^2 + c_4c_5}{2c_3^2}(q_5+q_6)q_3 + \frac{c_2}{2c_3}(q_5-q_6)q_1 + \frac{c_3c_2c_4 + c_4^2c_5}{4c_3^3}(q_5+q_6)^2 q_3 + \right.\\
&\left.\frac{c_2c_4}{4c_3^2}(q_6^2 - q_5^2)q_1 + k_{nx}q_1^3 + c_{nx}q_2^3\right),\\
\dot{q}_5 =& \tilde{\Omega} q_5 i,\\
\dot{q}_6 =& -\tilde{\Omega} q_6 i.
\end{aligned} \tag{8.21}$$

Note that after the introduction of complex exponentials the system is autonomous, i.e., there is no explicit dependency on time in the equations. However, the system's dimension increased and the equations became complex.

In order to simplify the equations, the matrix $\mathbf{A}$ can be expressed in its simplest form using the modal transformation $\mathbf{q} = \mathbf{R}\mathbf{x}$, where $\mathbf{R}$ is the modal matrix, in which columns are formed by the eigenvectors of the linear system. Thus, the equation of motion is transformed to

$$\dot{\mathbf{x}} = \mathbf{\Lambda}\mathbf{x} + \mathbf{R}^{-1}\mathbf{f}_2(\mathbf{x}) + \mathbf{R}^{-1}\mathbf{f}_3(\mathbf{x}), \tag{8.22}$$

where

$$\mathbf{\Lambda} = \mathrm{diag}(\omega_2 i, -\omega_2 i, \omega_1 i, -\omega_1 i, \tilde{\Omega} i, -\tilde{\Omega} i) \tag{8.23}$$

is a diagonal matrix and $\mathbf{f}_2(\cdot)$ and $\mathbf{f}_3(\cdot)$ are polynomial functions of order 2 and 3, respectively. Eq. (8.22) can be rewritten in a matrix form as

$$\dot{\mathbf{x}} = \mathbf{f}(\mathbf{x}) = \mathbf{\Lambda}\mathbf{x} + \mathbf{F}_2\mathbf{x}^2 + \mathbf{F}_3\mathbf{x}^3, \tag{8.24}$$

where $\mathbf{x}^2$, $\mathbf{x}^3$ are 21×1 and 56×1 vectors, and $\mathbf{F}_2$, $\mathbf{F}_3$ are 6×21 and 6×56 matrices, respectively. Note that the notation

$$\mathbf{x}^i = \begin{bmatrix} x_1^{m_{11}} x_2^{m_{12}} \cdots x_n^{m_{1n}} \\ x_1^{m_{21}} x_2^{m_{22}} \cdots x_n^{m_{2n}} \\ \vdots \\ x_1^{m_{k1}} x_2^{m_{k2}} \cdots x_n^{m_{kn}} \\ \vdots \end{bmatrix} \tag{8.25}$$

represents a vector with the monomials of degree i

$$x_1^{m_{k1}} x_2^{m_{k2}} \cdots x_n^{m_{kn}} \quad , \quad \text{with} \sum_{l=1}^{n} m_{kl} = i \quad , \quad \text{for} \;\; i = 1, 2, 3. \tag{8.26}$$

8.2.2 Normal form transformation

The main objective of the normal form transformation is to eliminate as many quadratic and cubic terms in Eq. (8.21) as possible. The number of eliminated terms depends on a special resonance condition. After the transformation is applied, a simpler set of equations is obtained and some analyses are easier to carry out. The following steps are according to Hochlenert [115].

The equations in normal form are expressed as

$$\dot{\mathbf{y}} = \mathbf{h}(\mathbf{y}) = \mathbf{\Lambda}\mathbf{y} + \mathbf{H}_2\mathbf{y}^2 + \mathbf{H}_3\mathbf{y}^3. \tag{8.27}$$

The near-identity transformation that takes Eq. (8.21) to Eq. (8.27) is of the type

$$\mathbf{x} = \mathbf{g}(\mathbf{y}) = \mathbf{y} + \mathbf{G}_2\mathbf{y}^2 + \mathbf{G}_3\mathbf{y}^3. \tag{8.28}$$

The transformation leaves the linear part unchanged. On the other hand, the monomials vectors $\mathbf{y}^2$, $\mathbf{y}^3$ are multiplied by matrices $\mathbf{H}_2$, $\mathbf{H}_3$, defining the remaining nonlinear terms. These matrices depend on $\mathbf{F}_2$, $\mathbf{F}_3$, $\mathbf{G}_2$, $\mathbf{G}_3$, and are chosen so that as many nonlinear terms are eliminated as possible.

The objective is to determine matrices $\mathbf{G}_i$ and $\mathbf{H}_i$. First, Eq. (8.28) is subtituted in Eq. (8.24) and equated to the time derivative of Eq. (8.28). This gives

$$\begin{gathered}\left(\mathbf{I} + \frac{\partial(\mathbf{G}_2\mathbf{y}^2)}{\partial\mathbf{y}} + \frac{\partial\left(\mathbf{G}_3\mathbf{y}^3\right)}{\partial\mathbf{y}} + \cdots\right)\left(\boldsymbol{\Lambda}\mathbf{y} + \mathbf{H}_2\mathbf{y}^2 + \mathbf{H}_3\mathbf{y}^3 + \cdots\right) = \boldsymbol{\Lambda}\left(\mathbf{y} + \mathbf{G}_2\mathbf{y}^2 + \right. \\ \left. \mathbf{G}_3\mathbf{y}^3 + \cdots\right) + \mathbf{F}_2\left(\mathbf{y} + \mathbf{G}_2\mathbf{y}^2 + \mathbf{G}_3\mathbf{y}^3 + \cdots\right)^2 + \mathbf{F}_3\left(\mathbf{y} + \mathbf{G}_2\mathbf{y}^2 + \mathbf{G}_3\mathbf{y}^3 + \cdots\right)^3\end{gathered} \tag{8.29}$$

By equating the monomials of the same degree (except for the trivial equation of degree 1) on both sides, the matrices $\mathbf{H}_2$, $\mathbf{H}_3$ can be obtained as

$$\mathbf{H}_2\mathbf{y}^2 = \mathbf{F}_2\mathbf{y}^2 + \boldsymbol{\Lambda}\mathbf{G}_2\mathbf{y}^2 - \frac{\partial\left(\mathbf{G}_2\mathbf{y}^2\right)}{\partial\mathbf{y}}\boldsymbol{\Lambda}\mathbf{y}, \tag{8.30a}$$

$$\mathbf{H}_3\mathbf{y}^3 = \tilde{\mathbf{F}}_3\mathbf{y}^3 + \boldsymbol{\Lambda}\mathbf{G}_3\mathbf{y}^3 - \frac{\partial\left(\mathbf{G}_3\mathbf{y}^3\right)}{\partial\mathbf{y}}\boldsymbol{\Lambda}\mathbf{y}, \tag{8.30b}$$

where

$$\tilde{\mathbf{F}}_3\mathbf{y}^3 := \mathbf{F}_3\mathbf{y}^3 + 2\mathbf{F}_2\left(\mathbf{y}\left(\mathbf{G}_2\mathbf{y}^2\right)\right) - \frac{\partial\left(\mathbf{G}_2\mathbf{y}^2\right)}{\partial\mathbf{y}}\mathbf{H}_2\mathbf{y}^2. \tag{8.31}$$

The last term of each equation involving a partial derivative can be determined as

$$\begin{aligned}\frac{\partial(\mathbf{G}_i\mathbf{y}^i)}{\partial\mathbf{y}}\boldsymbol{\Lambda}\mathbf{y} &= \mathbf{G}_i\begin{bmatrix}\frac{\partial\mathbf{y}^i}{\partial y_1} & \cdots & \frac{\partial\mathbf{y}^i}{\partial y_6}\end{bmatrix}\boldsymbol{\Lambda}\mathbf{y} \\ &= \mathbf{G}_i\begin{bmatrix}\vdots & & \vdots & & \vdots \\ \cdots & m_{kj}\left(y_1^{m_{k1}}\cdots y_j^{m_{kj}-1}\cdots y_6^{m_{k6}}\right) & \cdots \\ \vdots & & \vdots & & \vdots\end{bmatrix}\boldsymbol{\Lambda}\mathbf{y} \\ &= \mathbf{G}_i\begin{bmatrix}\ddots & & \mathbf{0} \\ & \sum_{l=1}^{6} m_{kl}\lambda_l & \\ \mathbf{0} & & \ddots\end{bmatrix}\mathbf{y}^i, \quad \text{for} \quad i = 2, 3.\end{aligned} \tag{8.32}$$

Using Eq. (8.32) in Eq. (8.30), the equations

$$H_{2,jk} = F_{2,jk} + \left\{ \lambda_j - \sum_{l=1}^{6} m_{kl}\lambda_l \right\} G_{2,jk} \quad , \quad \text{for} \quad j = 1, \dots, 6 \tag{8.33a}$$

$$H_{3,jk} = \tilde{F}_{3,jk} + \left\{ \lambda_j - \sum_{l=1}^{6} m_{kl}\lambda_l \right\} G_{3,jk} \quad , \quad \text{for} \quad j = 1, \dots, 6 \tag{8.33b}$$

are obtained.

The idea of the transformation is to choose such $G_{2,jk}$ and $G_{3,jk}$ that $H_{2,jk}$ and $H_{3,jk}$ become zero. It is possible for all nonlinear terms which do not fulfill the resonance condition

$$\lambda_j = \sum_{l=1}^{6} m_{kl}\lambda_l \quad , \quad \text{with} \quad \sum_{l=1}^{6} m_{kl} = i \quad , \quad \text{for} \quad i = 1, 2, 3. \tag{8.34}$$

If the resonance condition is fulfilled, the corresponding nonlinear terms cannot be eliminated, i.e., the terms are called resonant. Considering this condition, two cases are used to determine the normal form of the system equations, as shown in Tab. 8.1. It has to be noted that due to parametric excitation, the resonant terms depend on the excitation frequency, so that for each specific values of excitation frequency a separate normal form has to be derived.

Resonance condition not fulfilled	Resonance condition fulfilled
$G_{2,jk} = \dfrac{F_{2,jk}}{\sum_{l=1}^{6} m_{kl}\lambda_l - \lambda_j}$	$G_{2,jk} = 0$
$G_{3,jk} = \dfrac{\tilde{F}_{3,jk}}{\sum_{l=1}^{6} m_{kl}\lambda_l - \lambda_j}$	$G_{3,jk} = 0$
$H_{2,jk} = 0$	$H_{2,jk} = F_{2,jk}$
$H_{3,jk} = 0$	$H_{3,jk} = \tilde{F}_{3,jk}$

Table 8.1: Values of matrices $G_{2,jk}$, $G_{3,jk}$, $H_{2,jk}$, $H_{3,jk}$

8.2.3 System equations in normal form

The normal form of Eq. (8.21) for the combination resonances $\tilde{\Omega} \approx 2\omega_1$ and $\tilde{\Omega} \approx 2\omega_2$ is computed based on the cases of Tab. 8.1. These frequencies also correspond to $\Omega \approx \omega_1$ and $\Omega \approx \omega_2$, which are the external resonances discussed in Section 8.1.

For the fundamental resonance frequency $\tilde{\Omega} \approx 2\omega_1$, the equations in normal form are

$$
\begin{aligned}
\dot{y}_1 &= \omega_2 y_1 i + (f_1 + f_2 i) y_1^2 y_2, \\
\dot{y}_2 &= -\omega_2 y_2 i + (f_1 - f_2 i) y_1 y_2^2 + f_3 y_2 y_5 y_6 i, \\
\dot{y}_3 &= \omega_1 y_3 i + f_4 y_4 y_5 i + (f_5 + f_6 i) y_3^2 y_4, \\
\dot{y}_4 &= -\omega_1 y_4 i + f_7 y_3 y_6 i + (f_5 - f_6 i) y_3 y_4^2 + f_8 y_4 y_5 y_6 i, \\
\dot{y}_5 &= \tilde{\Omega} y_5 i, \\
\dot{y}_6 &= -\tilde{\Omega} y_6 i,
\end{aligned}
\tag{8.35}
$$

where $f_1, \ldots, f_8$ are real constants that depend on the system parameters.

For the fundamental resonance frequency $\tilde{\Omega} \approx 2\omega_2$, the equations in normal form are

$$
\begin{aligned}
\dot{y}_1 &= \omega_2 y_1 i + g_1 y_2 y_5 i + (g_2 + g_3 i) y_1^2 y_2, \\
\dot{y}_2 &= -\omega_2 y_2 i + g_4 y_1 y_6 i + (g_2 - g_3 i) y_1 y_2^2 + g_5 y_2 y_5 y_6 i, \\
\dot{y}_3 &= \omega_1 y_3 i + (g_6 + g_7 i) y_3^2 y_4 + g_8 y_3 y_5 y_6 i, \\
\dot{y}_4 &= -\omega_1 y_4 i + (g_6 - g_7 i) y_3 y_4^2 + g_9 y_4 y_5 y_6 i, \\
\dot{y}_5 &= \tilde{\Omega} y_5 i, \\
\dot{y}_6 &= -\tilde{\Omega} y_6 i,
\end{aligned}
\tag{8.36}
$$

where $g_1, \ldots, g_9$ are real constants that depend on the system parameters.

In both cases, the number of nonlinear terms from the second and fourth equations is less than in Eq. (8.21). Note that the system is still complex and the first four equations still depend on y_5 and y_6, which are the complex exponentials of the periodic stiffness. In the following subsection, a polar coordinate transformation is applied to eliminate this dependency and to obtain a real system.

8.2.4 Normal form in polar coordinates

Eqs. (8.35) and (8.36) can be simplified by means of a further transformation. By using the polar coordinates

$$
y_1 = r_1 e^{i\varphi_1},\ y_2 = r_1 e^{-i\varphi_1},\ y_3 = r_2 e^{i(\varphi_2 + \frac{1}{2}\tilde{\Omega} t)},\ y_4 = r_2 e^{-i(\varphi_2 + \frac{1}{2}\tilde{\Omega} t)}, \tag{8.37}
$$

the normal form for the fundamental resonance frequency $\tilde{\Omega} \approx 2\omega_1$ is

$$\begin{aligned}
\dot{r}_1 &= e_1 c_{nx} r_1^3, \\
\dot{\varphi}_1 &= e_2 k_{nx} r_1^2 + e_3, \\
\dot{r}_2 &= e_4 c_{ny} r_2^3 + e_5 \sin(2\varphi_2) r_2, \\
\dot{\varphi}_2 &= e_6 k_{ny} r_2^2 + e_7 \cos(2\varphi_2) + e_8 - \frac{\tilde{\Omega}}{2},
\end{aligned} \tag{8.38}$$

where $e_1, \ldots, e_8$ are real constants.

For the fundamental resonance frequency $\tilde{\Omega} \approx 2\omega_2$, using the polar coordinates

$$y_1 = r_1 e^{i(\varphi_1 + \frac{1}{2}\tilde{\Omega} t)},\ y_2 = r_1 e^{-i(\varphi_1 + \frac{1}{2}\tilde{\Omega} t)},\ y_3 = r_2 e^{i\varphi_2},\ y_4 = r_2 e^{-i\varphi_2}, \tag{8.39}$$

the normal form is written as

$$\begin{aligned}
\dot{r}_1 &= d_1 c_{nx} r_1^3 + d_2 \sin(2\varphi_1) r_1, \\
\dot{\varphi}_1 &= d_3 k_{nx} r_1^2 + d_4 \cos(2\varphi_1) + d_5 - \frac{\tilde{\Omega}}{2}, \\
\dot{r}_2 &= d_6 c_{ny} r_2^3, \\
\dot{\varphi}_2 &= d_7 k_{ny} r_2^2 + d_8,
\end{aligned} \tag{8.40}$$

where $d_1, \ldots, d_8$ are real constants.

In both cases, there are some advantages of this representation in contrast to Eqs. (8.35) and (8.36): the number of nonlinear terms is smaller, it was possible to obtain an autonomous real system, and two of the equations are decoupled. For $\tilde{\Omega} \approx 2\omega_1$ in Eq. (8.38), only variables r_2, φ_2 are coupled. On the other hand, for $\tilde{\Omega} \approx 2\omega_2$ in Eq. (8.40), r_1, φ_1 are coupled. It is also relevant to note that $\tilde{\Omega}$ only affects the coupled variables. The procedure to obtain Eqs. (8.38) and (8.40) is detailed in Appendix E.2.

8.2.5 Fixed points

Normal form transformation

The fixed points of Eqs. (8.38) and (8.40) are computed by zeroing the derivatives and solving for each variable. Thus, from Eq. (8.40), the fixed points for $\tilde{\Omega} \approx 2\omega_2$ are obtained from the set of equations

$$d_1 c_{nx} r_1^3 + d_2 \sin(2\varphi_1) r_1 = 0, \tag{8.41a}$$

$$d_3 k_{nx} r_1^2 + d_4 \cos(2\varphi_1) + d_5 - \frac{\hat{\Omega}}{2} = 0. \tag{8.41b}$$

It is a set of equation with three solutions: $\{r_1^{(1)}, \varphi_1^{(1)}\}$, $\{r_1^{(2)}, \varphi_1^{(2)}\}$ and $\{r_1^{(3)}, \varphi_1^{(3)}\}$. One of the solutions is

$$r_1^{(1)} = 0, \tag{8.42a}$$

$$\varphi_1^{(1)} = \frac{1}{2}\cos^{-1}\left(\frac{\hat{\Omega}/2 - d_5}{d_4}\right). \tag{8.42b}$$

The remaining solutions are obtained by solving the set of equations

$$d_1 c_{nx}\left(r_1^{(2,3)}\right)^2 + d_2\sin(2\varphi_1^{(2,3)}) = 0, \tag{8.43a}$$

$$d_3 k_{nx}\left(r_1^{(2,3)}\right)^2 + d_4\cos(2\varphi_1^{(2,3)}) + d_5 - \frac{\hat{\Omega}}{2} = 0. \tag{8.43b}$$

The stability of these solutions can be assessed by computing eigenvalues of the Jacobian matrix

$$\mathbf{J}_{\omega_2} = \begin{bmatrix} 3d_1c_{nx}r_1^2 + d_2\sin(2\varphi_1) & 2d_2\cos(2\varphi_1)r_1 \\ 2d_2k_{nx}r_1 & -2d_4\sin(2\varphi_1) \end{bmatrix}. \tag{8.44}$$

Similarly, the fixed points for $\tilde{\Omega} \approx 2\omega_1$ are obtained from the set of equations

$$\begin{aligned} e_4c_{ny}r_2^3 + e_5\sin(2\varphi_2)r_2 &= 0, \\ e_6k_{ny}r_2^2 + e_7\cos(2\varphi_2) + e_8 - \frac{\hat{\Omega}}{2} &= 0, \end{aligned} \tag{8.45}$$

with the solutions $\{r_2^{(1)}, \varphi_2^{(1)}\}$, $\{r_2^{(2)}, \varphi_2^{(2)}\}$ and $\{r_2^{(3)}, \varphi_2^{(3)}\}$ obtained from

$$r_2^{(1)} = 0, \tag{8.46a}$$

$$\varphi_2^{(1)} = \frac{1}{2}\cos^{-1}\left(\frac{\hat{\Omega}/2 - e_8}{e_7}\right), \tag{8.46b}$$

and

$$\begin{aligned} e_4c_{ny}\left(r_2^{(2,3)}\right)^2 + e_5\sin(2\varphi_2^{(2,3)}) &= 0, \\ e_6k_{ny}\left(r_2^{(2,3)}\right)^2 + e_7\cos(2\varphi_2^{(2,3)}) + e_8 - \frac{\hat{\Omega}}{2} &= 0. \end{aligned} \tag{8.47}$$

In this case, the Jacobian matrix is

$$\mathbf{J}_{\omega_1} = \begin{bmatrix} 3e_4c_{ny}r_2^2 + e_5\sin(2\varphi_2) & 2e_5\cos(2\varphi_2)r_2 \\ 2e_6k_{ny}r_2 & -2e_7\sin(2\varphi_2) \end{bmatrix}. \tag{8.48}$$

The solution of Eqs. (8.45) and (8.47) form the 3-dim spaces r_2-φ_2-$\tilde{\Omega}$ and r_1-

φ_1-$\tilde{\Omega}$, valid only near the fundamental resonance frequencies $2\omega_1$ and $2\omega_2$. The results are shown in Figs. 8.5-8.7. The curves are composed of stable (solid lines) and unstable points (dashed lines). The stability is determined by computing the Jacobian matrices (8.44) and (8.48). If the real part of one eigenvalue is less than zero, the point is stable, otherwise it is unstable. The figures also show the influence of the nonlinear stiffness and damping coefficients. Figs. 8.5a and 8.6a show that the nonlinear stiffness has a hardening effect, and the curve bends to the right as the nonlinear stiffness is increased. On the other hand, Figs. 8.5b and 8.6b show that the nonlinear damping attenuates the amplitude of vibration. The bearings and the rotor anisotropy change the amplitude and the bifurcation point of the nontrivial fixed points, as shown in Fig. 8.7. Depending on how the rotor speed is varied, different paths are traversed by the fixed points. During a run-up, starting with $\tilde{\Omega}$ below a fundamental resonance frequency, the trivial solution is the only stable point. Near a fundamental resonance frequency, the trivial solution loses stability and a bifurcation causes a separation into two branches, one stable and the other unstable. Thus, the fixed point jumps up to the stable branch of nontrivial solutions. Hereafter, when increasing the rotor speed, the fixed point loses stability and jumps down to trivial solution branch again. During the run-down, starting above a fundamental resonance frequency, the same behavior occurs but at different frequencies, as can be seen in the figures. The bifurcation only occurs at the turning points seen in the figures.

Numerical integration

The results obtained from the normal form transformation are verified by a numerical integration from Eq. (8.21). A fourth-order Runge-Kutta integrator is used to obtain the solutions to unfolded system equation

$$\begin{aligned} \dot{\mathbf{q}} &= \mathbf{f}(\mathbf{q}, \Omega), \quad \text{for } \Omega \approx 2\omega_1, \Omega \approx 2\omega_2 \\ \dot{\Omega} &= \varepsilon, \end{aligned} \tag{8.49}$$

where ε is a small constant representing the variation of the rotor speed.

Figs. 8.8 adn 8.9 shows the solutions of the state variable q_2 and q_3 during a run-up, starting below the corresponding fundamental resonance frequency, and run-down, starting above it. The vibrations are attracted to the stable fixed points obtained through the normal form method. The points were the solutions jump from a low to high vibration level are related to the jump phenomena common in systems with parametric excitation. Note that the unstable branches, obtained by the normal form method, cannot be observed by the numerical integration. Near the unstable points, the solutions are repelled to a stable fixed point. When an initial

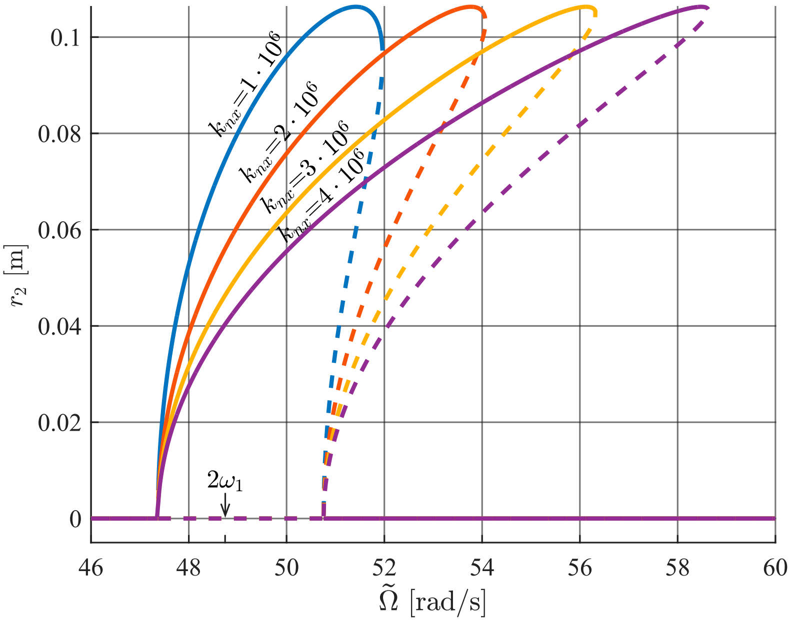

(a) $k_x = 5 \cdot 10^2$N/m, $k_y = 1.75 \cdot 10^3$N/m, $k_\eta = 2 \cdot 10^3$N/m, $k_\zeta = 10^3$N/m, $m = 1kg$, $c_{nx} = c_{ny} = 50$Ns/m.

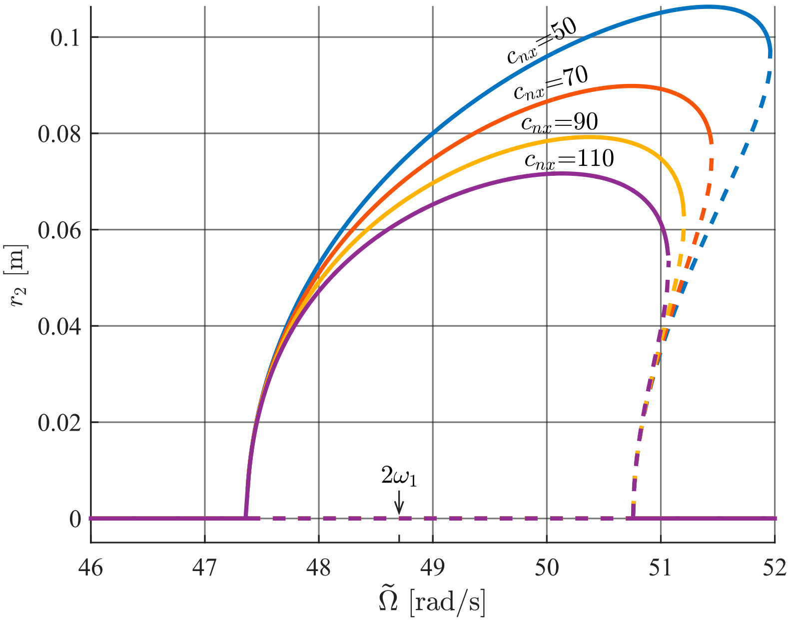

(b) $k_x = 5 \cdot 10^2$N/m, $k_y = 1.75 \cdot 10^3$N/m, $k_\eta = 2 \cdot 10^3$N/m, $k_\zeta = 10^3$N/m, $m = 1kg$, $k_{nx} = k_{ny} = 10^6$N/m.

Figure 8.5: Fixed point for different values of c_{nx} and k_{nx}. The solid lines are stable points and the dashed lines are unstable points. (a) Fixed point curve bending for $\hat{\Omega} \approx 2\omega_1$ on the plane r_2-$\hat{\Omega}$ when varying k_{nx}. (b) Fixed point curve damping for $\hat{\Omega} \approx 2\omega_1$ on the plane r_2-$\hat{\Omega}$ when varying c_{nx}.

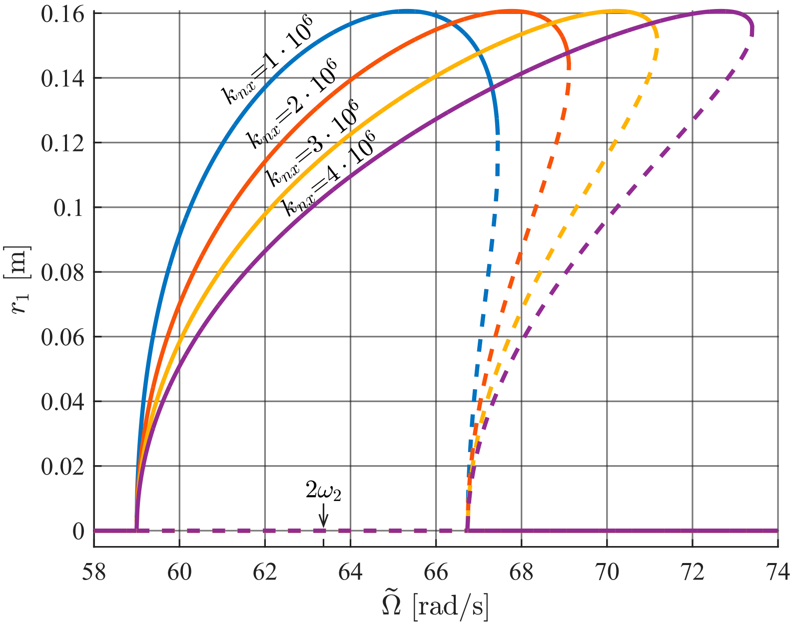

(a) $k_x = 5 \cdot 10^2$N/m, $k_y = 1.75 \cdot 10^3$N/m, $k_\eta = 2 \cdot 10^3$N/m, $k_\zeta = 10^3$N/m, $m = 1$ kg, $c_{nx} = c_{ny} = 50$Ns/m.

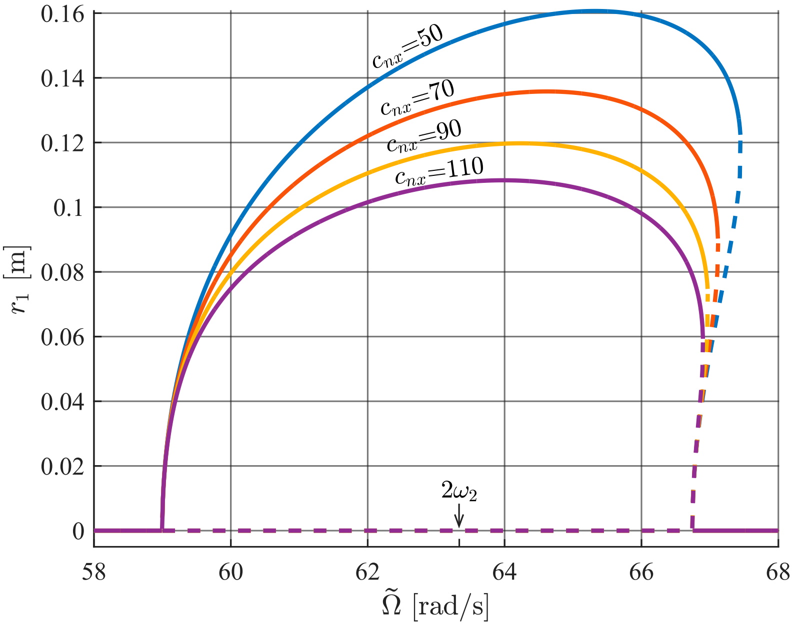

(b) $k_x = 5 \cdot 10^2$N/m, $k_y = 1.75 \cdot 10^3$N/m, $k_\eta = 2 \cdot 10^3$N/m, $k_\zeta = 10^3$N/m, $m = 1$ kg, $k_{nx} = k_{ny} = 10^6$N/m.

Figure 8.6: Fixed point for different values of c_{ny} and k_{ny}. The continuous lines are stable points and the dashed lines are unstable points. (a) Fixed point curve bending for $\hat{\Omega} \approx 2\omega_2$ on the plane r_1-$\hat{\Omega}$ when varying k_{nx}. (b) Fixed point curve damping for $\hat{\Omega} \approx 2\omega_2$ on the plane r_1-$\hat{\Omega}$ when varying c_{nx}.

condition is given outside the unstable orbit, the solution tends to the nontrivial solution. Inside this orbit, the solution tends to the trivial solution.

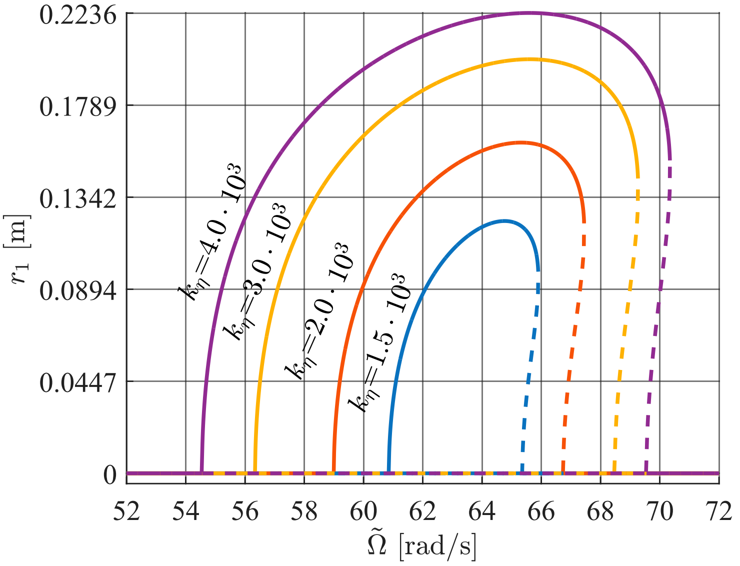

(a) $k_x = 0.5 \cdot 10^3$N/m, $k_y = 1.75 \cdot 10^3$N/m, $k_\zeta = 10^3$N/m, $m = 1$ kg, $k_{nx} = k_{ny} = 10^6$N/m, $c_{nx} = c_{ny} = 50$Ns/m.

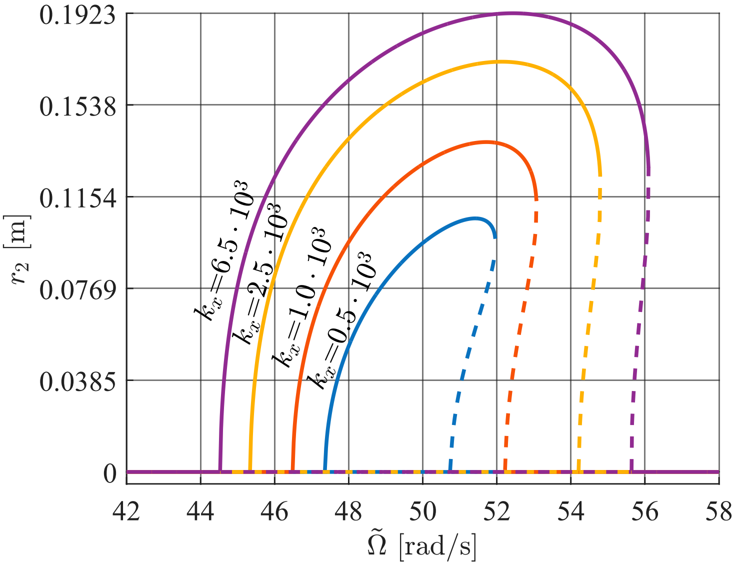

(b) $k_y = 1.75 \cdot 10^3$N/m, $k_\eta = 2 \cdot 10^3$N/m, $k_\zeta = 10^3$N/m, $m = 1$ kg, $k_{nx} = k_{ny} = 10^6$N/m, $c_{nx} = c_{ny} = 50$Ns/m.

Figure 8.7: Fixed point for different values of k_x and k_η. The continuous lines are stable points and the dashed lines are unstable points. (a) Effect of the rotor asymmetry on the fixed point curve for $\hat{\Omega} \approx 2\omega_2$ on the plane r_1-$\hat{\Omega}$ when varying k_η. (b) Effect of the bearings asymmetry on the fixed point curve for $\hat{\Omega} \approx 2\omega_1$ on the plane r_2-$\hat{\Omega}$ when varying k_x.

Verification

Since the fixed points of the system in normal form are related to amplitudes of the limit cycles of the original system, the maximum amplitudes of the periodic solutions obtained by the integration of Eq. (8.49) are considered. Moreover, both

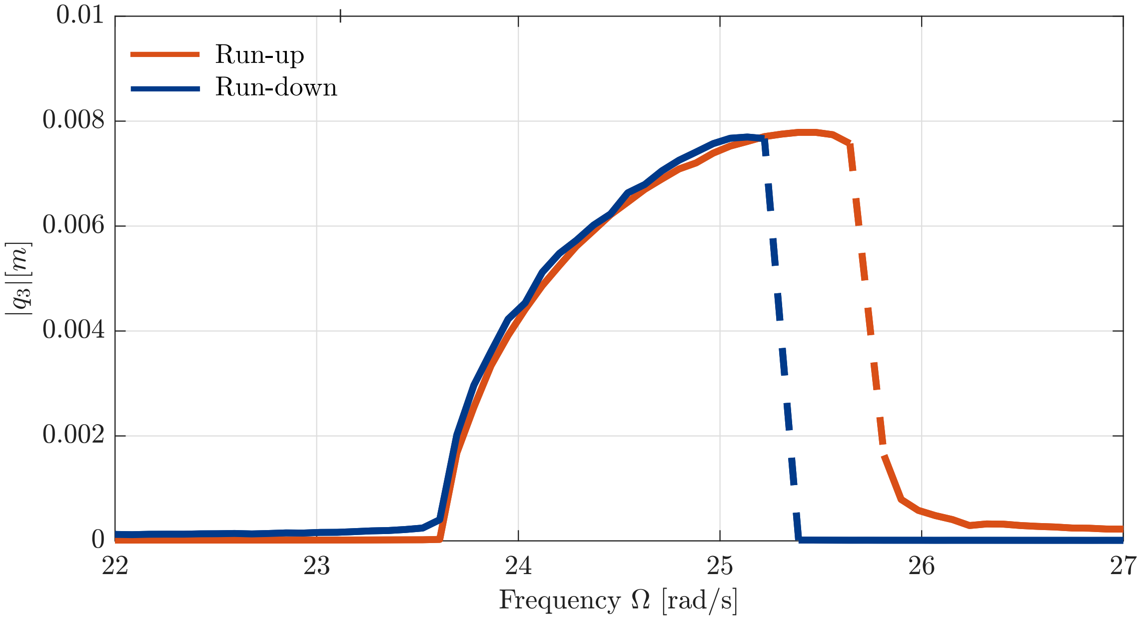

Figure 8.8: Numerical integration of variable q_3 during a run-up and run-down for $\tilde{\Omega} \approx 2\omega_1$, $k_x = 5 \cdot 10^2$N/m, $k_y = 1.75 \cdot 10^3$N/m, $k_\eta = 2 \cdot 10^3$N/m, $k_\zeta = 10^3$N/m, $m = 1$ kg, $k_{nx} = k_{ny} = 1 \cdot 10^6$N/m, $c_{nx} = c_{ny} = 500$Ns/m.

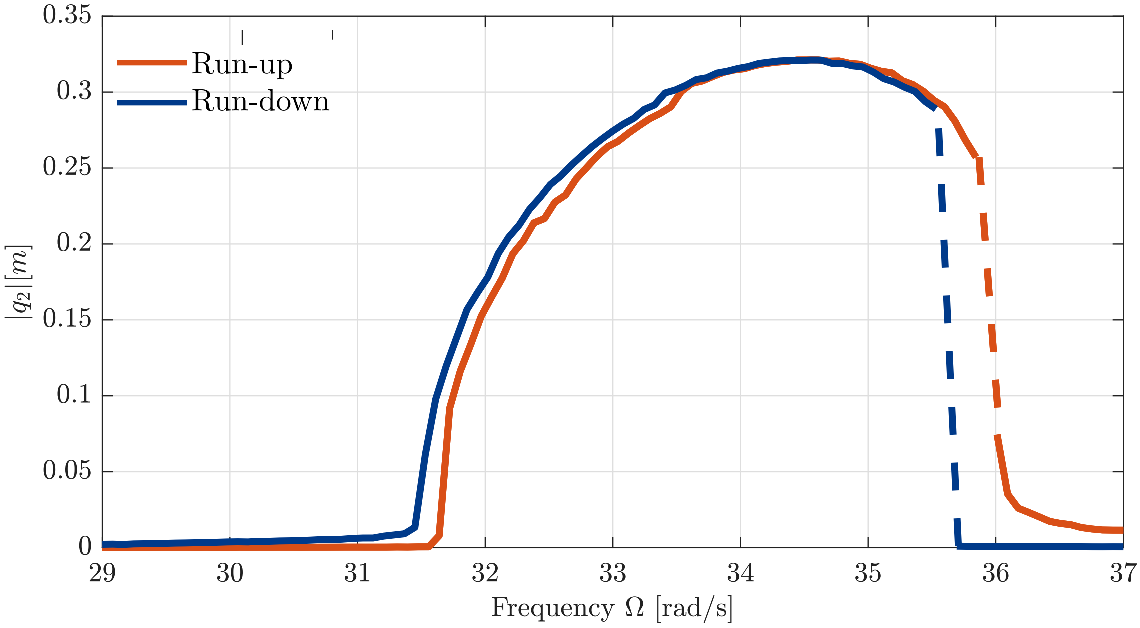

Figure 8.9: Numerical integration of variable q_2 during a run-up and run-down for $\tilde{\Omega} \approx 2\omega_2$, $k_x = 5 \cdot 10^2$N/m, $k_y = 1.75 \cdot 10^3$N/m, $k_\eta = 2 \cdot 10^3$N/m, $k_\zeta = 10^3$N/m, $m = 1$ kg, $k_{nx} = k_{ny} = 1 \cdot 10^6$N/m, $c_{nx} = c_{ny} = 500$Ns/m.

solutions must be in the same coordinate systems. Thus, Eqs. (8.28),(8.38) and (8.40) are used to express both solutions in the same coordinate system. In this case, the physical coordinates (coordinates of the original system) are used. The results in Fig. 8.10 shows a good agreement between the normal forms method and the numerical integration. Figs. 8.8 and 8.9 show the jump phenomena during the run-up and run-down due to the unstable fixed points.

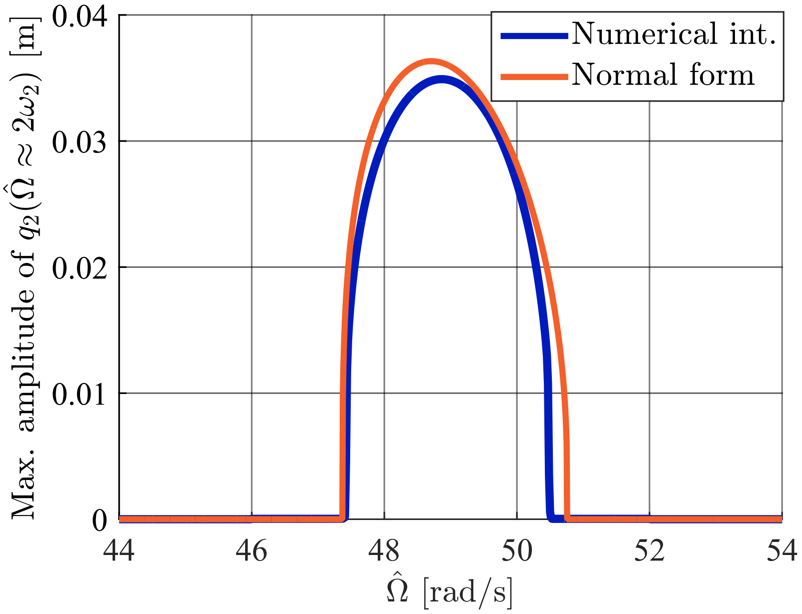

(a)

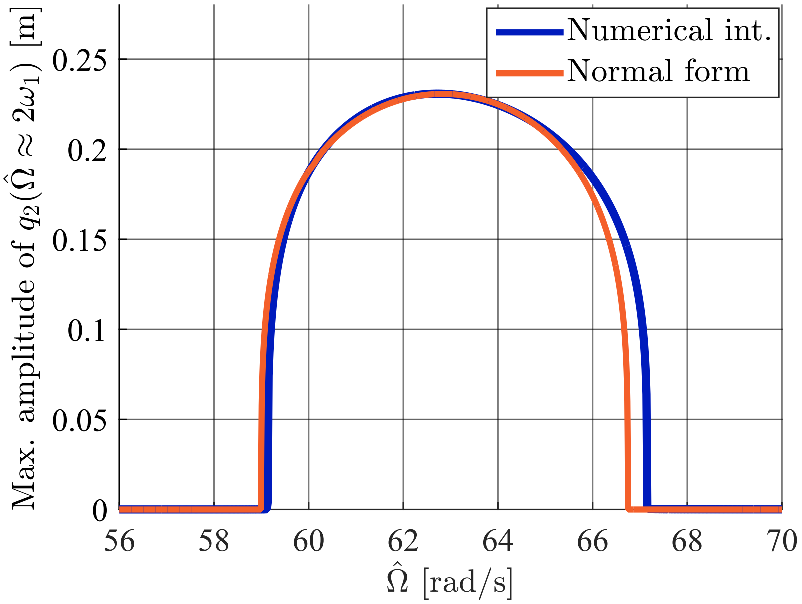

(b)

Figure 8.10: Comparison between the normal forms and the numerical integration for $\hat{\Omega} \approx 2\omega_1$ (a) and $\hat{\Omega} \approx 2\omega_2$ (b) with $k_x = 5 \cdot 10^2$N/m, $k_y = 1.75 \cdot 10^3$N/m, $k_\eta = 2 \cdot 10^3$N/m, $k_\zeta = 10^3$N/m, $m = 1$ kg, $k_{nx} = k_{ny} = 2 \cdot 10^4$N/m, $c_{nx} = c_{ny} = 100$Ns/m.

8.3 Discussion

Stability maps is one of the most important tools in rotating machinery because one can predict the behavior of the system with the modification of a parameter value. Similarly, fixed points are also relevant because the mathematical model of components such as bearings and seals are linearized around these points. If the value of any parameter changes (by wear or a different operating condition), the fixed points may become unstable and the linear equations would not be valid anymore. Thus, parameters such as the bearings' anisotropy, rotor anisotropy, and nonlinear stiffness and damping should be identified and monitored. In an experimental rig or machine, this can be carried out by proximity sensors and accelerometers measuring the transverse vibration of the rotor. This vibration, combined with an identification method, can be used to determine the stiffness of the rotor and of the bearings. With these parameters, the position of the operating point on the stability maps of Figs. 8.3-8.4 as well as the distance from instability can be determined. On the other hand, the experimental version of Fig. 8.10 can be obtained by taking the maximum amplitude of the vibration during a slow run-up and run-down. If an abrupt change in the amplitude of vibration occurs, it can be attributed to the jump phenomenon of Figs. 8.5-8.7. As seen before, such behavior comes from the presence of cubic stiffness and damping in the seal. In this case, the bifurcation points that cause the jump must be taken into consideration because if the machine is working near these points with a low vibration level, a small variation in the rotor speed would increase (or decrease) the vibration dramatically.

Even though the intention of this work was not to show the advantage of the normal forms over other methods, it is remarkable to show the basic idea of simplifying the system via coordinate transformations and order approximations applied to the equations of motion itself without making assumptions on the kind of solutions [75]; the method can be readily implemented by using symbolic computation. Also, as stated by Guckenheimer and Holmes [78], the normal form reveals some hidden symmetries useful for further analysis. Moreover, no references in the literature were found regarding normal forms applied to rotordynamics, particularly to bearings and seals. This is a motivation since a different analysis of such systems may bring new insights to the field. In the case of this thesis, asymmetries and cubic nonlinearities created nontrivial fixed points with frequency jumps. It is important to note that the method is based on polynomial expansions and truncations that makes the result valid only under those assumptions. Different results might be obtained by considering higher order terms. The analysis of a larger system by means of the normal form transformation is possible, but most probably not feasible due to the high complexity of analytical expressions involved. Therefore, the method is preferably applied to a smaller or reduced model in order to investigate specific effects or qualitative influence of a few chosen parameters in detail.

Chapter 9

Conclusions

In this thesis, three problems of rotordynamics were investigated. They are related to the dynamics of a test rig for the identification of annular gas seal coefficients. In the first problem, the coefficients were obtained by means of a transfer function (CDS matrix) between the forces and displacements measurements. Three excitation signals were tested and the results showed that the multisine signal is adequate for this type of machine. During the tests, the rotor vibration eventually exceeded the maximum clearance and a rotor-stator contact problem arouse. Since this phenomenon may damage the machine, a theoretical investigation was performed to know the consequences of this condition. Three simulations showed different asynchronous vibration and they were analyzed by different tools. The intention was to show that the contact condition can be detected by means of graphical information. Only preliminary experimental results of the rig's vibration was shown. Three harmonics were observed with the full spectrum and full spectrogram. Finally, the last problem was related to the nonlinear dynamics of a system, representing the rig, with anisotropy and a seal with cubic stiffness and damping. Although the problem was only analyzed theoretically, it is important to know the behavior of the rig with such conditions. Moreover, the method of the normal forms was introduced and applied to determine the influence of certain parameters on the system response. Below are shown specific conclusions, contributions and expected future work from the three problems.

9.1 Annular gas seal test rig

Conclusions

The construction of a test rig for annular gas seals involves the integration of the following aspects: rotordynamics, electromagnetism, instrumentation, identification of parameters and design of excitation signals. In order to obtain satisfactory measurements, each aspect must be correctly designed and implemented.

The dynamic characteristics of the rotor must be known a priori to guarantee a well energy distribution of the excitation signal. The finite element method used to model the rotor was able to predict the two first critical speeds. This information is important to define the operating speed and excitation frequency range.

The use of magnetic actuators to excite the rotor is an interesting approach and a widely used technique. Although the equations involved in the phenomena are complex, a simplified model is reasonable to both design the magnetic actuators and model the electromagnetic forces. Although this type of actuators brings some advantages, the model must be correctly linearized in order to avoid nonlinear effects. This can be done by applying a bias current and considering small displacements around the magnetic center of the actuators.

The CDS matrix method showed satisfactory results when identifying the equivalent stiffness and damping coefficients of the overall system. Each entry of the CDS was computed by using the H_3 estimator to account for both the noise in the displacement and force sensors. The shape of the absolute value, real part and imaginary part of the CDS are in accordance with the literature. It is important to remark that the estimates of the coefficients must be computed along with an estimate about their error. This gives an insight about the uncertainty of the coefficients at each frequency.

Regarding the amplitude limitation between the rotor and seal, the design of the excitation signal was able to better distribute the energy in two important aspects. First, the signal was composed of several tones that excite the system at different frequencies simultaneously. If all the individual tones are summed with the same phase, several overshoots would appear in the response. This was avoided by modifying the phases with an iterative method proposed in the literature. Thus, the overshoots were diminished and more energy can be transferred to the rotor without rubbing the seal. The second aspect is related to the natural vibration of the rotor. If the amplitudes of the excitation signal in the frequency domain are constant, the displacement response would be high at the critical speeds and low far from them (considering frequencies around the first critical speed). Thus, low SNR would be found around those small amplitudes and, consequently, poor estimates would be obtained. To overcome this issue, the amplitude of each tone from the excitation signal is designed so that the displacement responses is flat. In this case, the SNR would be higher, reaching better estimates.

The coefficients were obtained by applying the CDS matrix method with a two-step approach. A baseline set of measurements, with no pressure drop, determined the effects of the rotor and bearings. In the pressurized test, the effects of the rotor, bearings and seals are obtained. By subtracting the two tests one another, the effects of the seals were readily obtained. It is relevant to note that this is only true if all the effects coming from different components are linear. The results found using this method was according to several references in the literature. The direct stiffness increased with the excitation frequency with low error, which correspond to a hardening effect. The direct damping increased with the excitation frequency and high relative errors were found in the low frequencies. Both the cross-coupled stiffness and damping exhibited small values and high errors at some frequencies. High errors were found where the coherence between the excitation force and seal displacements were low.

Contributions

Currently, there are few test rigs for testing annular gas seals. In Brazil, there is no similar machine. This thesis showed some characteristics of a small-scale rig built in the Acoustics and Vibration Laboratory. This type of machine are of great relevance, especially in Brazil, since the Brazilian Petroleum Corporation (Petrobras) has interest in developing a real-scale machine to test seals from centrifugal compressors used in oil extraction. Currently, there is a partnership between Petrobras and UFRJ to develop such machine and one of the objective of this thesis is to build a small-scale rig to understand the dynamics and to test the identification algorithms that will be used in the bigger machine. Moreover, different theoretical models can be proposed and validated experimentally. This widens different studies in the rotordynamic field such as finite element methods, nonlinear dynamics, active magnetic bearings, monitoring and diagnosis, signal excitation design, rotor-stator rub, bulk-flow, CFD, among others.

Most of the available test rigs uses a rigid rotor, with an operating condition below the first critical speed, however, centrifugal compressors may work above it. In this thesis, a test rig with flexible rotor was considered and the excitation signal was applied below and above the first critical speed. This was a challenge in two aspects. First, the first critical speeds is always excited and the tones of the excitation must be void it. Since it is a flexible rotor, the vibration at that frequency may exceed the maximum value allowed and the rotor would rub the seal. Secondly, the excitation frequency must be carefully designed to avoid rubbing for all frequencies. In this thesis, the amplitude profile of the excitation frequency was chosen so that the amplitudes of the displacement remain flat. Thus, a high SNR was reached in contrast to an excitation with a flat profile.

The results obtained in this work are of great relevance in the industry of rotating machines, especially in Brazil. Only few rigs test annular seals around the world. This is the first step towards the improvement of centrifugal compressors' performance. The direct and cross-coupled coefficients of the seal were successfully obtained, showing that the design, instrumentation, identification method and excitation signals are sufficient to extract some preliminary results.

Future Works

One of the main drawbacks of the rig is the drop of the inlet pressure due to limitations from the air compressor used for the tests. Since it could not maintain the pressure constant, only a small part of the test, with an almost constant pressure, was used in the identification method. For future works, a compressor with a higher capacity should be used.

Although the coefficients were obtained with displacement and force measurements, rotordynamic instabilities may come mainly from the circumferential speed between the rotor and seal; this variable was not measured in this work. Thus, a pitot probes should be installed for future tests.

In this work, the electromagnets were used as shakers whilst ball bearings were used as support. A more interesting configuration would be use active magnetic bearings to both excite and support the rotor.

The use of other type of fluid, such as nitrogen or carbon dioxide, with a high pressure would be an interesting and more realistic case. It is intended to carry out this condition on bigger test rig.

9.2 Type of responses of a rotor-stator contact and the the detection in a test rig for annular gas seals

9.3 Conclusions

The analysis of the type of motion in a rotating machine is relevant in the diagnosis of failures. For certain operating conditions, the machine may exhibit vibration in asynchronous frequencies that could trigger an instability. One common problem in rotating machines with small clearances is the rotor-stator contact. In this thesis, a an analysis was performed to determine the type of motion in a test rig for annular gas seals.

As an effort to represent the system with as few degrees of freedom as possible, a lumped-element model was used. The results obtained were similar to the information available in the literature. The simulations showed different types of motion: forward, backward, subsynchronous, supersynchronous and chaotic vibrations. However, in this work, the equations were nondimensionalized to reduce the value of the time steps. Moreover, the relative rotor-stator displacement was chosen to analyze the system's vibration since it is the variable measured experimentally.

The tools to analyze the rotor vibration were chosen due to their simplicity in the practical implementation. The orbit with a superimposed Poincaré map gave an insight about the type of vibration. A single harmonic orbit is represented by one point the Poincaré map. When a forward and backward motions are present, the Poincaré map appears as closed paths around the orbit. A diffuse set of points in the Poincaré map is an indication of a multiperiodic or chaotic motion. At a certain frequency, the full spectrum can reveal more information. The forward/backward motion appears in the positive/negative frequency range. The dominant motion is the peak with the higher amplitude. During an acceleration or deceleration, the type of motion can be assessed by the full spectrogram. This type of plot is useful to detect, within a margin of error determined by the time window of each spectrum, a variation in the type of motion. Thus, the red curves are related to the different frequency components present in the vibration. Although in this work, the full spectrogram captured a change in the orbits due to a rotor-stator contact, it can be used to detect a modification of the motion due to other parameters.

The motion observed in the test rig revealed similar frequency components to those in Section 7.3. As expected, only one positive frequency ($1X$) is seen initially. Then, when the clearance is surpassed, the rub occurs and the motion is represented by three frequencies: $0X$, $1X$ and $-1X$. Thus, when performing a pressurized experiment on the rig, special attention must paid to the frequencies around these values.

Contributions

In the theoretical part, a computational code was developed to easily observe the influence of different parameters on the vibration. Although this model was already investigated by other authors, the intention is to show that it can be used for predicting the vibration in a test rig.

This thesis showed that classical tools such as orbits, Poincaré maps, power spectra and spectrograms are useful to assess and detect the vibration during rotor-stator contact. The experiments showed that when the vibration of the rotor rig rises significantly, the contact forces create a motion with the components 0X, 1X and -1X. The methods exposed in the thesis can be implemented in any rotating machine for the diagnosis of a failure due to rotor-stator contact.

Future Works

The parameters of the rotor-contact model will be identified in order to validate the results. This can be implemented by using a nonlinear fit or by using probabilistic approaches such as the Bayesian inference.

Experimental results from pressurized tests will be performed to see the influence on the vibration during contact.

9.4 Anisotropy and nonlinearities analysis of a rotor via Floquet and normal forms

Conclusions

In many mechanical systems, anisotropy and nonlinearity are present and its assessment is relevant to keep the machine under safe conditions. This thesis dealt with an asymmetric rotor, asymmetric bearings and an annular seal with nonlinear stiffness and damping. Stability and the behavior of the fixed points were assessed.

The Floquet theory was used to assess the the stability of the linearized dynamics of the system. Stability maps were created and they provided graphical insight about the safe operating regions, where small variations of the rotor or bearings anisotropy are allowed without making the system unstable. Three tongues of instability were observed. Depending on the level of anisotropy, the instability areas may increase or decrease. For a constant anisotropy level, the rotor may pass through instability areas during an acceleration. These tongues also were useful to find the nontrivial fixed points when a stiffness and damping is added to the system.

When a seal with cubic nonlinear stiffness and damping is considered, a more complex dynamics is obtained. The method of the normal forms was applied to compute the near-identity transformation in which the resonant terms are eliminated systematically. This fact simplified the complexity of the equations. The fixed points of the system were computed and they showed stable and unstable branches. During a rotor run-up or rundown, the fixed points traverse different paths due to the different location of the bifurcation on each path. Since no integration is required, the influence of the nonlinear parameters were assessed. The nonlinear stiffness showed a hardening effect by bending the curve to the right. On the other hand, the nonlinear damping had an attenuation effect on the amplitude of vibration when increased. The rotor and bearings asymmetries modified the bifurcation points and amplitudes of the fixed points. For verification purposes, the comparison between the fixed points, obtained using the method of normal forms method, and the maximum amplitude of limit cycles in physical coordinates, obtained by direct numerical integration of the original equations, were compared and showed a good agreement.

Contributions

Stability charts showed the importance of quantifying the level of asymmetry in a rotordynamic system. In practice, some components may exhibit anisotropic characteristics, such as rotors or bearings. These charts are a reference to maintain a safe operating condition without damaging the machine.

A method for analyzing nonlinearities in a rotordynamic system was applied. This is a novelty in the annular seals field, since many authors considers only linear stiffness and damping coefficients. Nevertheless, this work shows that if the seal exhibits cubic parameters, different fixed points are established and a jump phenomena occur near the fundamental resonances.

This behavior is relevant in rotating machines since the fixed points are used to linearize the equations. If they are unstable, the linear equations are not valid anymore. Also, the abrupt change in the amplitude at the bifurcation points should be taken into consideration in the design or operating stage of the machine by identifying the value of the nonlinear parameters and asymmetry.

The normal form of a nonlinear system is not a new concept. However, the systematic method that takes a nonlinear system with smooth nonlinearities into a simpler system has been studied recently. In this thesis, this method was successfully applied to a rotordynamic system to determine the influence of some parameters. Moreover, the computational code developed in Mathematica is able to compute the normal forms of a system of differential equations of first order with general smooth nonlinear stiffness and damping.

Future Works

Since the method of the normal forms can be applied to any system with smooth nonlinearities, other components from rotating machines can be analyzed. The Mathematica code will be used to determine the influence of other parameters such as a cross-coupled stiffness and damping.

Bibliography

[1] WHALEN, J., ALLEN, J., CARDELL, J., et al. "POLYMER SEAL USE IN CENTRIFUGAL COMPRESSORS–TWO USERS'EXPERIENCES OVER 15 YEARS". In: *Middle East Turbomachinery Symposia. 2013 Proceedings.* Turbomachinery Laboratory, Texas A&M Engineering Experiment Station, 2013.

[2] TIWARI, R. *Rotor systems: analysis and identification.* CRC Press, 2017.

[3] WAGNER, N. G., STEFF, K., GAUSMANN, R., et al. "Investigations on the dynamic coefficients of impeller eye labyrinth seals". In: *Proceedings of the Thirty-Eighth Turbomachinery Symposium, Houston, TX, September*, pp. 14–17, 2009.

[4] VANNARSDALL, M., CHILDS, D. W. "Static and rotordynamic characteristics for a new hole-pattern annular gas seal design incorporating larger diameter holes", *Journal of Engineering for Gas Turbines and Power*, v. 136, n. 2, 2014.

[5] EHEHALT, U., ALBER, O., MARKERT, R., et al. "Experimental observations on rotor-to-stator contact", *Journal of Sound and Vibration*, v. 446, pp. 453–467, 2019.

[6] RANKINE, W. M. "On the centrifugal force of rotating shafts", *Van Nostrand's Eclectic Engineering Magazine (1869-1879)*, v. 1, n. 7, pp. 598, 1869.

[7] DUNKERLEY, S. "On the whirling and vibration of shafts", *Proceedings of the Royal Society*, v. 185, pp. 229, 1895.

[8] JEFFCOTT, H. H. "The lateral vibration of loaded shafts in the neighbourhood of a whirling speed.—The effect of want of balance", *The London, Edinburgh, and Dublin Philosophical Magazine and Journal of Science*, v. 37, n. 219, pp. 304–314, 1919.

[9] FOPPL, A. "Das problem der laval'schen turbinenwelle", *Civilingenieur*, v. 41, pp. 248–250, 1895.

[10] NORONHA, R. F. D., UJIHARA, D. Y., REZENDE-TAPAJOZ, L. D., et al. "Applying CFD to Solve a Vibration Problem of a Compressor", 2015.

[11] IWATSUBO, T., TAKAHARA, K., KAWAI, R. "A new model of labyrinth seal for prediction of the dynamic force", *Rotordynamic Instability Problems in High-Performance Turbomachinery, College Station, TX, May*, pp. 28–30, 1984.

[12] CHILDS, D. W., KIM, C.-H. "Analysis and testing for rotordynamic coefficients of turbulent annular seals with different, directionally-homogeneous surface-roughness treatment for rotor and stator elements", 1985.

[13] CHILDS, D. W., SCHARRER, J. K. "Experimental rotordynamic coefficient results for teeth-on-rotor and teeth-on-stator labyrinth gas seals", *Journal of engineering for gas turbines and power*, pp. 599–604, 1986.

[14] DIETZEN, F. J., NORDMANN, R. "Calculating rotordynamic coefficients of seals by finite-difference techniques", *Journal of Tribology*, pp. 388–394, 1987.

[15] SYSSMANN, H. R. "Theory and measurements of labyrinth seal coefficients for rotor stability of turbocompressors", 1987.

[16] CHILDS, D. W., SCHARRER, J. K. "Theory versus experiment for the rotordynamic coefficient of labyrinth gas seals: part II—a comparison to experiment", *Journal of Vibration, Acoustics, Stress, and Reliability in Design*, v. 110, n. 3, pp. 281–287, 1988.

[17] KLEYNHANS, G. F., CHILDS, D. W. "The acoustic influence of cell depth on the rotordynamic characteristics of smooth-rotor/honeycomb-stator annular gas seals". In: *ASME 1996 International Gas Turbine and Aeroengine Congress and Exhibition*. American Society of Mechanical Engineers, 1996.

[18] YU, Z., CHILDS, D. W. "A comparison of experimental rotordynamic coefficients and leakage characteristics between hole-pattern gas damper seals and a honeycomb seal". In: *ASME 1997 International Gas Turbine and Aeroengine Congress and Exhibition*. American Society of Mechanical Engineers, 1997.

[19] CHILDS, D., ELROD, D., HALE, K. "Annular honeycomb seals: Test results for leakage and rotordynamic coefficients; comparisons to labyrinth and smooth configurations", *Journal of Tribology*, v. 111, n. 2, pp. 293–300, 1989.

[20] KWANKA, K., NAGEL, M. "Rotordynamic Coefficients of Short Labyrinth Gas Seals magel". In: *Rotordynamic Instability Problems in High-Performance Turbomachinery*, pp. 135–144, Texas A&M University, 1996.

[21] PICARDO, A., CHILDS, D. W. "Rotordynamic Coefficients for a Tooth-on-Stator Labyrinth Seal at 70 Bar Supply Pressures: Measurements Versus Theory and Comparisons to a Hole-Pattern Stator Seal", *Journal of Engineering for Gas Turbines and Power*, v. 127, n. 4, pp. 843–855, 2004.

[22] VANNINI, G., CIONCOLINI, S., CALICCHIO, V., et al. "Development of a High Pressure Rotordynamic Test Rig for Centrifugal Compressors Internal Seals Characterization". In: *Proceedings of the Fortieth Turbomachinery Symposium, Houston, TX, September*, pp. 12–15, 2011.

[23] VANNINI, G., MASALA, A., NERI, M. O., et al. "Full load testing of a 12.5 MW vertical high speed subsea motorcompressor". In: *Proceedings of the Fortieth Turbomachinery Symposium September*, pp. 12–15, 2011.

[24] CÔRTES, V. F. *Projeto de uma bancada de testes para selos labirintos em escala reduzida*. Master Thesis, Federal University of Rio de Janeiro, Rio de Janeiro, Brazil, 2017.

[25] MALDONADO, D., GODOY, D., CÔRTES, V., et al. "Simulation of a Test Rig and Identification of Annular Gas Seals Coefficients". In: Cavalca, K. L., Weber, H. I. (Eds.), *Proceedings of the 10th International Conference on Rotor Dynamics – IFToMM*, Mechanisms and Machine Science, pp. 157–176. Springer International Publishing, 2019.

[26] MALDONADO, D. J. G., KAREV, A., HAGEDORN, P., et al. "Analysis of a rotordynamic system with anisotropy and nonlinearity using the Floquet theory and the method of normal forms", *Journal of Sound and Vibration*, v. 453, pp. 201–213, 2019. doi: 10.1016/j.jsv.2019.04.006.

[27] MALDONADO, D. J. G., DIAZ, D. A. G., CÔRTES, V. F., et al. "On the Experimental Identification of Dynamical Characteristics of Annular Gas Seals". In: *Proceedings of the XVIII International Symposium on Dynamic Problems of Mechanics - DINAME*, Búzios, RJ, 2019.

[28] MALDONADO, D. J. G., RITTO, T. G., PINTO, F. A. N. C. "Identification of rotordynamic seal coefficients by means of impedance matrix and an optimization strategy". In: *Proceedings of the XVII International Symposium on Dynamic Problems of Mechanics, São Sebastião, SP, Brazil. ABCM*, 2017.

[29] DIAZ, D. A. G. *Metodologia de excitação para identificação de parâmetros dinâmicos de selos anulares.* Doctoral Thesis, Federal University of Rio de Janeiro, Rio de Janeiro, Brazil, 2019.

[30] DIAZ, D. A. G., PINTO, F. A. N. C., RITTO, T. G., et al. "Nonparametric identification of a small AMB test rig at several rotating speeds". In: *In the 16th International Symposium in Magnetic Bearings*, 2018.

[31] DIAZ, D. A. G., RITTO, T. G., MALDONADO, D. J. G., et al. "Stepped Sine and Multisine Signal Excitation for Identification in a Small AMB Test Rig". In: *In the 24th ABCM International Congress of Mechanical Engineering*, 2017.

[32] PINTO, F. A. N. C., RITTO, T. G., CÔRTES, V. F., et al. "Bancada experimental para identificação de parâmetros dinâmicos de selos anulares". In: *Encontro Nacional de Máquinas Rotativas*, Rio de Janeiro, 2018.

[33] ATKINS, K. E., PEREZ, R. X. "Influence Of Gas Seals On Rotor Stability Of A High Speed Hydrogen Recycle Compressor." 1988.

[34] SAN ANDRÉS, L., DE SANTIAGO, O. C. "Identification of Bearing Force Coefficients from Measurements of Imbalance Response of a Flexible Rotor". In: *ASME Turbo Expo 2004: Power for Land, Sea, and Air*, pp. 843–850. American Society of Mechanical Engineers, 2004.

[35] CHILDS, D., CHILDS, D. W. *Turbomachinery Rotordynamics: Phenomena, Modeling, and Analysis.* John Wiley & Sons, 1993.

[36] KERR, B. G. *Experimental and theoretical rotordynamic coefficients and leakage of straight smooth annular gas seals.* Doctoral Thesis, Texas A&M University, 2005.

[37] GUPTA, M. K., SOULAS, T. A., CHILDS, D. W. "New Steps to Improve Rotordynamic Stability Predictions of Centrifugal Compressors", pp. 843–848, 2007.

[38] FORTE, P., LATINI, F. "Theoretical Rotordynamic Coefficients of Labyrinth Gas Seals: a Parametric Study on a Bulk Model", *International Journal of Rotating Machinery*, v. 5, n. 1, pp. 67–76, 1999.

[39] KIM, K.-J., LEE, C.-W. "Identification of dynamic stiffness of squeeze film damper using active magnetic bearing system as an exciter". In: *International Sympositum on Stability Control of Rotating Machinery*, pp. 667–

677. The 2nd International Symposium on Stability Control of Rotating Machinery . . . , 2003.

[40] BURROWS, C. R., KUCUK, N. C., SAHINKAYA, M. N., et al. "Linearized squeeze-film dynamics: model structure and the interpretation of experimentally derived parameters", *Proceedings of the Institution of Mechanical Engineers, Part C: Mechanical Engineering Science*, v. 204, n. 4, pp. 263–272, 1990.

[41] LEE, Y. B., SHIN, S. K., RYU, K., et al. "Test results for leakage and rotordynamic coefficients of floating ring seals in a high-pressure, high-speed turbopump", *Tribology transactions*, v. 48, n. 3, pp. 273–282, 2005.

[42] TIWARI, R., LEES, A. W., FRISWELL, M. I. "Identification of dynamic bearing parameters: a review", *Shock and Vibration Digest*, v. 36, n. 2, pp. 99–124, 2004.

[43] EHRICH, F. F. "High Order Subharmonic Response of High Speed Rotors in Bearing Clearance", *Journal of Vibration, Acoustics, Stress, and Reliability in Design*, v. 110, n. 1, pp. 9–16, 1988.

[44] BLACK, H. F. "Interaction of a Whirling Rotor with a Vibrating Stator across a Clearance Annulus", *Journal of Mechanical Engineering Science*, v. 10, n. 1, pp. 1–12, 1968.

[45] ISAKSSON, J. L. *Dynamics of rotors influenced by rubbing contacts.* Division of Machine Design, Department of Mechanical Engineering, Linköping . . . , 1997.

[46] SAWICKI, J. T., PADOVAN, J., AL-KHATIB, R. "The Dynamics of Rotor with Rubbing". 1999.

[47] VON GROLL, G., EWINS, D. J. "A Mechanism of Low Subharmonic Response in Rotor/Stator Contact—Measurements and Simulations", *Journal of Vibration and Acoustics*, v. 124, n. 3, pp. 350–358, 2002.

[48] MUSZYNSKA, A., GOLDMAN, P. "Chaotic responses of unbalanced rotor/bearing/stator systems with looseness or rubs", *Chaos, Solitons & Fractals*, v. 5, n. 9, pp. 1683–1704, 1995.

[49] NORRICK, N., SIEGL, B., ALBER, O., et al. "Backward whirl during rotor-stator contact of gyroscopic rotors". In: *Proceedings of the 11th International Conference on Vibration Problems (ICOVP)*, 2013.

[50] EDWARDS, S., LEES, A. W., FRISWELL, M. I. "The influence of torsion on rotor/stator contact in rotating machinery", *Journal of Sound and Vibration*, v. 225, n. 4, pp. 767–778, 1999.

[51] BENTLY, D. E., YU, J. J., GOLDMAN, P., et al. "Full Annular RUB in Mechanical Seals, Part I: Experimental Results". 2002.

[52] LINGENER, A. "Experimental investigation of reverse whirl of a flexible rotor". In: *Proceedings of 3rd International Conference on Rotor dynamics,(1990-9)*, 1990.

[53] PRANDTL, L. "Beiträge zur Frage der kritischen Drehzahlen." *Polytechnisches Journal*, v. 333, pp. 179–182, 1918.

[54] FOOTE, W. R., PORITSKY, H., SLADE, J. J. "Critical speeds of a rotor with unequal shaft flexibilities, mounted in bearings of unequal flexibility", *Trans. ASME*, v. 10, pp. A77–A84, 1943.

[55] RODGERS, C. "On the vibration and critical speeds of rotors", *The London, Edinburgh, and Dublin Philosophical Magazine and Journal of Science*, v. 44, n. 259, pp. 122–156, 1922.

[56] YAMAMOTO, T., ŌTA, H. "On the Unstable Vibrations of a Shaft Carrying an Unsymmetrical Rotor", *Journal of Applied Mechanics*, v. 31, n. 3, pp. 515–522, 1964.

[57] NOAH, S. T., HOPKINS, G. R. "A Generalized Hill's Method for the Stability Analysis of Parametrically Excited Dynamic Systems", *Journal of Applied Mechanics*, v. 49, n. 1, pp. 217–223, 1982.

[58] GENTA, G. "Whirling of unsymmetrical rotors: A finite element approach based on complex co-ordinates", *Journal of Sound and Vibration*, v. 124, n. 1, pp. 27–53, 1988.

[59] JEI, Y. G., LEE, C. W. "Modal analysis of continuous asymmetrical rotor-bearing systems", *Journal of Sound and Vibration*, v. 152, n. 2, pp. 245–262, 1992.

[60] AFOLABI, D. "Elimination of periodic coefficients from the equations of motion of asymmetric shafts in anisotropic bearings", *Archive of Applied Mechanics*, v. 65, n. 6, pp. 415–424, 1995.

[61] ONCESCU, F., LAKIS, A. A., OSTIGUY, G. "Investigation of the stability and steady state response of asymmetric rotors, using the finite element

formulation", *Journal of Sound and Vibration*, v. 245, n. 2, pp. 303–328, 2001.

[62] HULL, E. H. "Shaft Whirling as Influenced by Stiffness Asymmetry", *Journal of Engineering for Industry*, v. 83, n. 2, pp. 219–226, 1961.

[63] IWATSUBO, T., TOMITA, A., KAWAI, R. "Vibrations of asymmetric rotors supported by asymmetric bearings", *Ingenieur-Archiv*, v. 42, n. 6, pp. 416–432, 1973.

[64] GANESAN, R. "Effects of bearing and shaft asymmetries on the instability of rotors operating at near-critical speeds", *Mechanism and Machine Theory*, v. 35, n. 5, pp. 737–752, 2000.

[65] MICKENS, R. E. *An introduction to nonlinear oscillations.* Cambridge University Press, 1981.

[66] NAYFEH, A. H. *The Method of Normal Forms.* John Wiley & Sons, ago. 2011.

[67] THOMSEN, J. J. *Vibrations and Stability: Advanced Theory, Analysis, and Tools.* 2 ed. Berlin Heidelberg, Springer-Verlag, 2003.

[68] DOHNAL, F. *Application of the averaging method on parametrically excited 2dof-systems.* Technical Report, Vienna University of Technology, Austria, 2003.

[69] VERHULST, F. *Nonlinear Differential Equations and Dynamical Systems.* Universitext. 2 ed. Berlin Heidelberg, Springer-Verlag, 1996.

[70] ELLIOTT, A. J., CAMMARANO, A., NEILD, S. A., et al. "Comparing the direct normal form and multiple scales methods through frequency detuning", *Nonlinear Dynamics*, v. 94, n. 4, pp. 2919–2935, 2018.

[71] HILL, T., NEILD, S., WAGG, D. "Comparing the direct normal form method with harmonic balance and the method of multiple scales", *Procedia Engineering*, v. 199, pp. 869–874, 2017.

[72] TROGER, H., STEINDL, A. *Nonlinear Stability and Bifurcation Theory: An Introduction for Engineers and Applied Scientists.* Wien, Springer-Verlag, 1991.

[73] JEZEQUEL, L., LAMARQUE, C. H. "Analysis of non-linear dynamical systems by the normal form theory", *Journal of Sound and Vibration*, v. 149, n. 3, pp. 429–459, 1991.

[74] NEILD, S. A., WAGG, D. J. "Applying the method of normal forms to second-order nonlinear vibration problems", *Proceedings of the Royal Society of London A*, v. 467, pp. 1141–1163, 2011.

[75] NEILD SIMON A., CHAMPNEYS ALAN R., WAGG DAVID J., et al. "The use of normal forms for analysing nonlinear mechanical vibrations", *Philosophical Transactions of the Royal Society A: Mathematical, Physical and Engineering Sciences*, v. 373, n. 2051, 2015.

[76] KAREV, A., HOCHLENERT, D., HAGEDORN, P. "Asynchronous parametric excitation, total instability and its occurrence in engineering structures", *Journal of Sound and Vibration*, v. 428, pp. 1–12, 2018.

[77] MURDOCK, J. *Normal Forms and Unfoldings for Local Dynamical Systems.* Springer Monographs in Mathematics. New York, Springer-Verlag, 2003.

[78] GUCKENHEIMER, J., HOLMES, P. *Nonlinear Oscillations, Dynamical Systems, and Bifurcations of Vector Fields.* New York, Springer, 2002.

[79] CHOW, S.-N., LI, C., WANG, D. *Normal Forms and Bifurcation of Planar Vector Fields.* 1 edition ed. Cambridge ; New York, Cambridge University Press, 1994.

[80] MASLEN, E. H. *Magnetic Bearings.* University of Virginia, 2000.

[81] ASTLEY, R. J. *Finite elements in solids and structures. An introduction.* Chapman & Hall (Springer), 1992.

[82] DAVIS, R., HENSHELL, R. D., WARBURTON, G. B. "A Timoshenko beam element", *Journal of Sound and Vibration*, v. 22, n. 4, pp. 475–487, 1972.

[83] INMAN, D. J. *Engineering Vibration.* 4 edition ed. Boston, Pearson, 2013. ISBN: 978-0-13-287169-3.

[84] PETYT, M. *Introduction to finite element vibration analysis.* Cambridge university press, 2010.

[85] THOMAS, D. L., WILSON, J. M., WILSON, R. R. "Timoshenko beam finite elements", *Journal of Sound and Vibration*, v. 31, n. 3, pp. 315–330, 1973.

[86] LALANNE, M., FERRARIS, G. *Rotordynamics prediction in engineering*, v. 2. Wiley, 1998.

[87] NELSON, H. D. "A finite rotating shaft element using Timoshenko beam theory", 1980.

[88] NELSON, H. D., MCVAUGH, J. M. "The dynamics of rotor-bearing systems using finite elements", *Journal of Engineering for Industry*, v. 98, n. 2, pp. 593–600, 1976.

[89] RITTO, T. G. *Numerical analysis of the nonlinear dynamics of a drill-string with uncertainty modeling.* PhD Thesis, Pontifícia Universidade Católica do Rio de Janeiro, 2010.

[90] SCHWEITZER, G., MASLEN, E. H. *Magnetic Bearings: Theory, Design, and Application to Rotating Machinery.* Springer Science & Business Media, 2009.

[91] NORDMANN, R. "Identification Techniques in Rotordynamics". In: *Diagnostics of Rotating Machines in Power Plants*, n. 352, International Centre for Mechanical Sciences, Springer Vienna, pp. 1–24, 1994.

[92] LEE, C.-W. "Mechatronics in Rotating Machinery". Vienna, Austria, 2006.

[93] KOZANECKA, D., KOZANECKI, Z., LECH, T., et al. "Application of active magnetic bearings for identification of the force generated in the labirynth seal", *Journal of Theoretical and Applied Mechanics*, v. 45, n. 1, pp. 53–60, 2007.

[94] WAGNER, N. G. "Dynamic labyrinth coefficients from a high-pressure full-scale test rig using magnetic bearings", *Rotordynamic Instability Problems in High-Performance Turbomachinery*, v. 95, 1996.

[95] MATROS, M., NORDMANN, R. "Dynamic characteristics of a hydrostatic bearing identified by active magnetic bearings", *Kaiserslautern Univ, Rotordynamic Instability Problems in High- Performance Turbomachinery 1996 p 23-28(SEE N 97-24525 01-37)*, 1997.

[96] WAGNER, N. G., PIETRUSZKA, W. D. "Identification of rotordynamic parameters on a test stand with active magnetic bearings". In: *Magnetic Bearings*, Springer, pp. 289–299, 1989.

[97] GUILLAUME, P. "Frequency response measurements of multivariable systems using nonlinear averaging techniques". In: *Quality Measurement: The Indispensable Bridge between Theory and Reality (No Measurements? No Science! Joint Conference - 1996: IEEE Instrumentation and Measurement Technology Conference and IMEKO Tec*, pp. 156–161, 1996.

[98] PINTELON, R., SCHOUKENS, J. *System Identification: A Frequency Domain Approach.* John Wiley & Sons, 2012.

[99] CHILDS, D., HALE, K. "A Test Apparatus and Facility to Identify the Rotordynamic Coefficients of High-Speed Hydrostatic Bearings", *Journal of Tribology*, v. 116, n. 2, pp. 337–343, 1994.

[100] BENDAT, J. S., PIERSOL, A. G. *Random Data: Analysis and Measurement Procedures.* John Wiley & Sons, 2011.

[101] CLOUD, C. H. *Stability of rotors suported by tilting pad journal bearings.* Doctoral Thesis, University of Virginia, Virginia, USA, 2007.

[102] LJUNG, L. *System identification - Theory for the User.* Prentice-Hall, 1999.

[103] SCHOUKENS, J., SWEVERS, J., PINTELON, R., et al. "Excitation design for FRF measurements in the presence of non-linear distortions", *Mechanical Systems and Signal Processing*, pp. 727–738, 2004.

[104] FRISWELL, M. I., PENNY, J. E. T. "Stepped multisine modal testing using phased components", *Mechanical Systems and Signal Processing*, pp. 145–156, 1990.

[105] GUILLAUME, P., SCHOUKENS, J., PINTELON, R., et al. "Crest-factor minimization using nonlinear Chebyshev approximation methods", *IEEE Transactions on Instrumentation and Measurement*, pp. 982–989, 1991.

[106] SCHROEDER, M. "Synthesis of low-peak-factor signals and binary sequences with low autocorrelation (Corresp.)", *IEEE Transactions on Information Theory*, pp. 85–89, 1970.

[107] EHEHALT, U., HAHN, E., MARKERT, R. "Motion patterns at rotor stator contact". In: *ASME 2005 International Design Engineering Technical Conferences and Computers and Information in Engineering Conference*, pp. 1031–1042. American Society of Mechanical Engineers, 2005.

[108] ALBER, O., MARKERT, R. "Rotor-Stator Contact – Overview of Current Research", *MATEC Web of Conferences*, v. 16, pp. 03001, 2014.

[109] SAWICKI, J. T., MONTILLA-BRAVO, A., GOSIEWSKI, Z. "Thermomechanical behavior of rotor with rubbing", *International Journal of Rotating Machinery*, v. 9, n. 1, pp. 41–47, 2003.

[110] JACQUET-RICHARDET, G., TORKHANI, M., CARTRAUD, P., et al. "Rotor to stator contacts in turbomachines. Review and application", *Mechanical Systems and Signal Processing*, v. 40, n. 2, pp. 401–420, 2013.

[111] MOON, F. C. *Chaotic Vibrations: An Introduction for Applied Scientists and Engineers*. 1 edition ed. New York, Wiley-VCH, 2004. ISBN: 978-0-471-67908-0.

[112] GRIFFITHS, D. F., HIGHAM, D. J. *Numerical Methods for Ordinary Differential Equations: Initial Value Problems*. Springer, nov. 2010.

[113] GASCH, R., PFÜTZNER, H. *Rotordynamik: Eine Einführung (Rotordynamics: An introduction)*. Springer-Verlag, 2013.

[114] HALE, P. J. K. *Ordinary Differential Equations*. Dover edition ed. Mineola, N.Y, 2009.

[115] HOCHLENERT, D. *Normalformen und Einzugsbereiche nichtlinearer dynamischer Systeme: Beispiele und technische Anwendungen (Normal forms and domains of attraction of nonlinear dynamical systems: examples and technical applications)*. Habilitation Thesis, Technische Universität Berlin, 2012.

Appendix A

Spectral density functions

The spectral density functions are used to relate the input and output measurements from a linear system. The equations shown below are based on the book of Bendat [100].

A.1 Definitions

The power spectral densities S_{ff} and S_{uu}, and cross-power spectral density S_{fu}, needed to compute the coherence function, are defined as

$$S_{uu}(\omega) = \int_0^\infty r_{uu}(\tau)e^{-i\omega\tau}\, d\tau, \tag{A.1}$$

$$S_{ff}(\omega) = \int_0^\infty r_{ff}(\tau)e^{-i\omega\tau}\, d\tau, \tag{A.2}$$

$$S_{fu}(\omega) = \int_0^\infty r_{fu}(\tau)e^{-i\omega\tau}\, d\tau, \tag{A.3}$$

$$S_{uf}(\omega) = \int_0^\infty r_{uf}(\tau)e^{-i\omega\tau}\, d\tau, \tag{A.4}$$

where r_{uu} and r_{ff} are autocorrelation functions, and r_{fu} is the cross-correlation function. They are defined as be

$$r_{uu}(\tau) = \int_0^\infty u(t)u(t+\tau)\, dt, \tag{A.5}$$

$$r_{ff}(\tau) = \int_0^\infty f(t)f(t+\tau)\, dt, \tag{A.6}$$

$$r_{fu}(\tau) = \int_0^\infty f(t)u(t+\tau)\, dt, \tag{A.7}$$

$$r_{uf}(\tau) = \int_0^\infty u(t)f(t+\tau)\, dt. \tag{A.8}$$

A.2 Estimation

Since the correlation functions are convolution integrals, the power and cross-power spectral densities can be estimated by the Fourier transform of each signal as follows:

$$\begin{aligned}
\hat{S}_{ff}(\omega_k) =& |F(\omega_k)|^2, && \text{(A.9)} \\
\hat{S}_{uu}(\omega_k) =& |U(\omega_k)|^2, && \text{(A.10)} \\
\hat{S}_{fu}(\omega_k) =& F^*(\omega_k)U(\omega_k). && \text{(A.11)}
\end{aligned}$$

A.3 Relation with the system response

Considering a linear system, represented by the system response $h(\tau)$, the relation between input $u(t)$ and output $f(t)$ is

$$f(t) = \int_0^\infty h(\tau)u(t-\tau)d\tau. \tag{A.12}$$

By using Eq. (A.12) in Eqs. (A.6) and (A.8), the relations between the correlation functions and system response are

$$\begin{aligned}
r_{ff}(\tau) &= \int_0^\infty \int_0^\infty \int_0^\infty h(\alpha)h(\beta)u(t-\beta)u(t+\tau-\alpha)\;d\alpha\;d\beta\;dt \\
&= \int_0^\infty \int_0^\infty h(\alpha)h(\beta)r_{uu}(\tau+\beta-\alpha)\;d\alpha\;d\beta && \text{(A.13)} \\
r_{uf}(\tau) &= \int_0^\infty \int_0^\infty h(\alpha)u(t)u(t+\tau-\alpha)\;d\alpha\;dt \\
&= \int_0^\infty h(\alpha)r_{uu}(\tau-\alpha)\;d\alpha && \text{(A.14)}
\end{aligned}$$

Now, by inserting the Eqs. (A.13)-(A.14) into Eqs. (A.2)-(A.4), the relations between the spectral densities and system response are

$$\begin{aligned}
S_{ff}(\omega) =& \int_0^\infty \int_0^\infty \int_0^\infty h(\alpha)h(\beta)r_{uu}(\tau+\beta-\alpha)e^{-i\omega\tau}\, d\alpha\, d\beta\, d\tau \\
=& S_{uu}(\omega) \int_0^\infty \int_0^\infty h(\alpha)h(\beta)e^{i\omega(\beta-\alpha)}\, d\alpha\, d\beta \\
=& S_{uu}(\omega)H(\omega) \int_0^\infty h(\beta)e^{i\omega\beta}\, d\beta \\
=& H(\omega)H^*(\omega)S_{uu}(\omega) \qquad \text{(A.15)} \\
S_{uf}(\omega) =& \int_0^\infty \int_0^\infty h(\alpha)r_{uu}(\tau-\alpha)e^{-i\omega\tau}\, d\alpha\, d\tau \\
=& S_{uu}(\omega) \int_0^\infty h(\alpha)e^{-i\omega\alpha}\, d\alpha \\
=& S_{uu}(\omega)H(\omega) \qquad \text{(A.16)}
\end{aligned}$$

A.4 Equations for multiple-input-multiple-output systems

For multiple-input-multiple-output systems, Eq. (A.12) turns

$$\mathbf{F}(\omega_k) = \mathbf{H}(\omega_k)\mathbf{U}(\omega_k), \qquad \text{(A.17)}$$

where $\mathbf{F}(\omega_k) \in \mathbb{C}^{N\times 1}$, $\mathbf{U}(\omega_k) \in \mathbb{C}^{N\times 1}$.

Also, the multidimensional version of Eqs. (A.15) and (A.16) is

$$\begin{aligned}
\mathbf{S}_{ff}(\omega_k) =& \mathbf{H}(\omega_k)^*\mathbf{S}_{uu}(\omega_k)\mathbf{H}(\omega_k) \qquad \text{(A.18)} \\
\mathbf{S}_{uf}(\omega_k) =& \mathbf{S}_{uu}(\omega_k)\mathbf{H}(\omega_k), \qquad \text{(A.19)}
\end{aligned}$$

where $\mathbf{S}_{ff}(\omega_k) \in \mathbb{C}^{N\times N}$, $\mathbf{S}_{uu}(\omega_k) \in \mathbb{C}^{N\times N}$ and $\mathbf{S}_{uf}(\omega_k) \in \mathbb{C}^{N\times N}$.

If a several experiments approach is adopted, then $\mathbf{F}(\omega_k) \in \mathbb{C}^{N\times N_b}$, $\mathbf{U}(\omega_k) \in \mathbb{C}^{N\times N_b}$, were N_b is the number of experiments (or blocks).

Appendix B

$\mathbf{H}_1$, $\mathbf{H}_2$ and $\mathbf{H}_3$ Estimators

A transfer function $\mathbf{H}_0$, which relates the output $\mathbf{F}_0$ and input $\mathbf{U}_0$ with the equation

$$\mathbf{F}_0(\omega_k) = \mathbf{H}_0(\omega_k)\mathbf{U}_0(\omega_k), \tag{B.1}$$

can be estimated from noisy input and output measurements. The model assumed for the measurements is

$$\mathbf{U}(\omega_k) = \mathbf{U}_0(\omega_k) + \mathbf{N}_u(\omega_k) \tag{B.2a}$$

$$\mathbf{F}(\omega_k) = \mathbf{F}_0(\omega_k) + \mathbf{N}_f(\omega_k) \tag{B.2b}$$

where $\mathbf{F}_0$ is the exact value of the force vector, $\mathbf{N}_f$ is a zero-mean disturbing noise, $\mathbf{U}_0$ is the exact value of the displacement vector and $\mathbf{N}_f$ a zero-mean disturbing noise. Thus, the model that relates the noisy outputs and inputs is

$$\mathbf{F}(\omega_k) = \mathbf{H}(\omega_k)\mathbf{U}(\omega_k). \tag{B.3}$$

The objective of the estimators is to take advantage of the properties of the disturbing noises so that $\mathbf{H}$ tends to $\mathbf{H}_0$. If the SNR at the input is much higher than that at the output, the H_1 estimator should be used. In the converse case, the H_2 estimator is more convenient. In any case, the H_3 estimator can be constructed from the mean value between the H_1 and H_2 estimators. The equations shown here are based on the books of Pintelon [98] and Bendat [100].

B.1 $\mathbf{H}_1$ Estimator

This estimator assumes that the disturbing noise affecting the force measurements is greater than the noise affecting the displacement measurements. The first step is to multiply both sides of Equation (B.3) by the complex conjugate of the displacements vector $\mathbf{U}^*(\omega_k)$:

$$\begin{aligned} \mathbf{F}\mathbf{U}^* &= \mathbf{H}\mathbf{U}\mathbf{U}^* \\ \left(\mathbf{F}_0 + \mathbf{N}_f\right)\left(\mathbf{U}_0^* + \mathbf{N}_u^*\right) &= \mathbf{H}\left(\mathbf{U}_0 + \mathbf{N}_u\right)\left(\mathbf{U}_0^* + \mathbf{N}_u^*\right) \\ \mathbf{F}_0\mathbf{U}_0^* + \mathbf{F}_0\mathbf{N}_u^* + \mathbf{N}_f\mathbf{U}_0^* + \mathbf{N}_f\mathbf{N}_u^* &= \mathbf{H}\left(\mathbf{U}_0\mathbf{U}_0^* + \mathbf{U}_0\mathbf{N}_u^* + \mathbf{N}_u\mathbf{U}_0^* + \mathbf{N}_u\mathbf{N}_u^*\right) \end{aligned} \tag{B.4}$$

Then, by assuming the properties (uncorrelated and independent disturbing noises)

$$\begin{aligned} \mathrm{E}\left[\mathbf{N}_f(\omega_k)\right] = \mathrm{E}\left[\mathbf{N}_u(\omega_k)\right] = \mathrm{E}\left[\mathbf{N}_f(\omega_k)\mathbf{N}_u^*(\omega_k)\right] &= 0, \\ \mathrm{E}\left[\mathbf{F}_0(\omega_k)\mathbf{N}_u^*(\omega_k)\right] = \mathrm{E}\left[\mathbf{N}_f(\omega_k)\mathbf{U}_0^*(\omega_k)\right] &= 0, \\ \mathrm{E}\left[\mathbf{U}_0(\omega_k)\mathbf{N}_u^*(\omega_k)\right] = \mathrm{E}\left[\mathbf{N}_u(\omega_k)\mathbf{U}_0^*(\omega_k)\right] &= 0, \\ \mathrm{E}\left[\mathbf{N}_u(\omega_k)\mathbf{N}_u^*(\omega_k)\right] &= \boldsymbol{\sigma}_u^2(\omega_k), \end{aligned} \tag{B.5}$$

and applying the Expectation operator E[·] to Equation (B.4), the following equation is obtained:

$$\mathrm{E}\left[\mathbf{F}_0\mathbf{U}_0^*\right] = \mathbf{H}\left(\mathrm{E}\left[\mathbf{U}_0\mathbf{U}_0^*\right] + \boldsymbol{\sigma}_u^2\right). \tag{B.6}$$

Thus, the H_1 estimator of the transfer function is

$$\mathbf{H}(\omega_k) = \frac{\mathrm{E}\left[\mathbf{F}_0(\omega_k)\mathbf{U}_0^*(\omega_k)\right]}{\mathrm{E}\left[|\mathbf{U}_0(\omega_k)|^2\right] + \boldsymbol{\sigma}_u^2(\omega_k)} = \mathbf{H}_0(\omega_k)\frac{\mathrm{E}\left[|\mathbf{U}_0(\omega_k)|^2\right]}{\mathrm{E}\left[|\mathbf{U}_0(\omega_k)|^2\right] + \boldsymbol{\sigma}_u^2(\omega_k)} \tag{B.7}$$

If the SNR of the displacement measurements are high enough, then the measured transfer function converges to the exact transfer function:

$$\mathbf{H}(\omega_k) = \mathbf{H}_0(\omega_k) \tag{B.8}$$

For implementation purposes, the Expectation operator applied to Equation (B.4) can be represented by the arithmetic mean between M measurements blocks. Thus, the transfer function is computed by the equation

$$\mathbf{H}(\omega_k) = \frac{\frac{1}{M}\sum_{l=1}^{M}\mathbf{F}^{(l)}(\omega_k)\mathbf{U}^{*(l)}(\omega_k)}{\frac{1}{M}\sum_{l=1}^{M}\mathbf{U}^{(l)}(\omega_k)\mathbf{U}^{*(l)}(\omega_k)}. \tag{B.9}$$

This equation is the division between the cross-spectral density from the force and displacement vectors, and the auto-spectral density of the displacement vector.

B.2 H_2 Estimator

This estimator assumes that the disturbing noise affecting the displacement measurements is greater than the noise affecting the force measurements. In this case, the both sides of Equation (B.3) are multiply by the complex conjugate of the forces vector $\mathbf{F}^*(\omega_k)$:

$$\begin{aligned}\mathbf{F}\mathbf{F}^* &= \mathbf{H}\mathbf{U}\mathbf{F}^* \\ \left(\mathbf{F}_0+\mathbf{N}_f\right)\left(\mathbf{F}_0^*+\mathbf{N}_f^*\right) &= \mathbf{H}\left(\mathbf{U}_0+\mathbf{N}_u\right)\left(\mathbf{F}_0^*+\mathbf{N}_f^*\right) \\ \mathbf{F}_0\mathbf{F}_0^*+\mathbf{F}_0\mathbf{N}_f^*+\mathbf{N}_f\mathbf{F}_0^*+\mathbf{N}_f\mathbf{N}_f^* &= \mathbf{H}\left(\mathbf{U}_0\mathbf{F}_0^*+\mathbf{U}_0\mathbf{N}_f^*+\mathbf{N}_u\mathbf{F}_0^*+\mathbf{N}_u\mathbf{N}_f^*\right)\end{aligned} \tag{B.10}$$

Then, by assuming the properties (uncorrelated and independent disturbing noise)

$$\begin{aligned}\mathrm{E}\left[\mathbf{N}_f(\omega_k)\right]=\mathrm{E}\left[\mathbf{N}_u(\omega_k)\right]=\mathrm{E}\left[\mathbf{N}_u(\omega_k)\mathbf{N}_f^*(\omega_k)\right] &=0 \\ \mathrm{E}\left[\mathbf{F}_0(\omega_k)\mathbf{N}_f^*(\omega_k)\right]=\mathrm{E}\left[\mathbf{N}_f(\omega_k)\mathbf{F}_0^*(\omega_k)\right] &=0, \\ \mathrm{E}\left[\mathbf{U}_0(\omega_k)\mathbf{N}_f^*(\omega_k)\right]=\mathrm{E}\left[\mathbf{N}_u(\omega_k)\mathbf{F}_0^*(\omega_k)\right] &=0, \\ \mathrm{E}\left[\mathbf{N}_f(\omega_k)\mathbf{N}_f^*(\omega_k)\right] &=\boldsymbol{\sigma}_f^2(\omega_k),\end{aligned} \tag{B.11}$$

and applying the Expectation operator E[·] to Equation (B.10), the following equation is obtained:

$$\mathrm{E}\left[\mathbf{F}_0\mathbf{F}_0^*\right]+\boldsymbol{\sigma}_f^2=\mathbf{H}\mathrm{E}\left[\mathbf{U}_0\mathbf{F}_0^*\right] \tag{B.12}$$

Thus, the H_2 estimator of the transfer function is

$$\mathbf{H}(\omega_k)=\frac{\mathrm{E}\left[|\mathbf{F}_0|^2\right]+\boldsymbol{\sigma}_f^2}{\mathrm{E}\left[\mathbf{U}_0\mathbf{F}_0^*\right]}=\mathbf{H}_0(\omega_k)\frac{\mathrm{E}\left[|\mathbf{F}_0|^2+\boldsymbol{\sigma}_f^2\right]}{\mathrm{E}\left[|\mathbf{F}_0|^2\right]} \tag{B.13}$$

If the SNR of the force measurements are high enough, then the measured transfer function converges to the exact transfer function:

$$\mathbf{H}(\omega_k)=\mathbf{H}_0(\omega_k) \tag{B.14}$$

For implementation purposes, the Expectation operator applied to Equation (B.10) can be represented by the arithmetic mean between M measurements blocks. Thus, the transfer function is computed by the equation

$$\mathbf{H}(\omega_k)=\frac{\dfrac{1}{M}\sum_{l=1}^{M}\mathbf{F}^{(l)}(\omega_k)\mathbf{F}^{*(l)}(\omega_k)}{\dfrac{1}{M}\sum_{l=1}^{M}\mathbf{U}^{(l)}(\omega_k)\mathbf{F}^{*(l)}(\omega_k)} \tag{B.15}$$

This equation is the division between the auto-spectral density of the force and the cross-spectral density from the displacement and force vectors.

B.3 H$_3$ Estimator

If the disturbing noise affects both the input and output considerably, the H_3 estimator can be used:

$$\mathbf{H}_3(\omega_k) = \frac{\mathbf{H}_1(\omega_k) + \mathbf{H}_2(\omega_k)}{2}. \tag{B.16}$$

B.4 Magnitude-squared coherence function

The magnitude-squared coherence function γ^2_{fu} estimates the amount of power that is transferred from input f to output u at a frequency ω, assuming a linear relation between them. It is defined as

$$\gamma^2_{fu}(\omega) = \frac{|S_{fu}(\omega)|^2}{S_{uu}(\omega)S_{yy}(\omega)}, \tag{B.17}$$

where S_{ff} and S_{uu} are the autospectral density of signals $f(t)$ and $u(t)$, respectively, and S_{fu} is the cross-spectral density between $f(t)$ and $u(t)$.

The coherence function always satisfies $0 \leq \gamma^2_{fu}(\omega) \leq 1$. For an ideal input output relation $\gamma^2_{fu}(\omega) = 1$. If the coherence is different than the unity, it is an evidence of noise in the signals, a nonlinear relation between signals or other inputs also transferring power to the output.

Appendix C

Final equations of the normal form

C.1 Normal form for $\tilde{\Omega} \approx 2\omega_1$

$$
\begin{aligned}
\dot{r}_1 =& -\frac{3c_{nx}}{2}r_1^3 \\
\dot{\varphi}_1 =& \frac{3605}{114} - \frac{238431095c_1^2}{49240108376\omega_2^2} + \frac{c_5}{4\omega_2} + \frac{1151568664451910843 8c_2^2}{12047081125691869247 57\omega_1\omega_2} + \frac{3k_{nx}r_1^2}{2\omega_1^3} \\
\dot{r}_2 =& -\frac{r_2(6\omega_1 c_{ny} r_2^2 + c_4\sin(2\varphi_2))}{4\omega_1} + \\
\dot{\varphi}_2 =& \frac{4306}{177} - \Omega - \frac{177c_4^2}{275584\omega_1^2} + \frac{c_6}{4\omega_1} + \frac{2113249341147139002 5c2^2}{24094162251383738495 14\omega_1\omega_2} - \frac{c_4\cos(2\varphi_2)}{4\omega_2} \\
&+ \frac{3k_{ny}r_2}{2\omega_1^3}
\end{aligned}
\tag{C.1}
$$

C.2 Normal from for $\tilde{\Omega} \approx 2\omega_2$

$$
\begin{aligned}
\dot{r}_1 =& \frac{r_1 c_1}{4\omega_2}\sin(2\varphi_1) + \frac{6c_{nx}\omega_2}{4\omega_2}{r_1}^2, \\
\dot{\varphi}_1 =& -\frac{57{c_1}^2}{115360{\omega_2}^2} - \frac{c_1}{4\omega_2}\cos(2\varphi 1) - \frac{1828966022067154705 4{c_2}^2}{23412338654817925610 27\omega_2\omega_2} \\
&+ \frac{c_5}{4\omega_2} + \frac{3k_{nx}}{2{\omega_2}^3}{r_1}^2 - \Omega + \frac{3605}{114}, \\
\dot{r}_2 =& -\frac{3}{2}c_{ny}{r_2}^3, \\
\dot{\varphi}_2 =& -\frac{3874305284848391760 5{c_2}^2}{46824677309635851220 54\omega_2\omega_1} + \frac{45856747{c_4}^2}{12310027094{\omega_1}^2} + \frac{c_6}{4\omega_1} \\
&+ \frac{3k_{ny}}{2{\omega_1}^3}{r_2}^2 + \frac{4306}{177}.
\end{aligned}
\tag{C.2}
$$

Appendix D

Preliminary experimental results of the rotor-stator contact of the test rig

A preliminary experimental investigation was carried out in a test rig used for the identification of annular gas seals. This machine is available in the Federal University of Rio de Janeiro (UFRJ), in the Acoustics and Vibration Laboratory (LAVI). The identification tests are based on the measurement of the rotor displacement when it is excited with magnetic bearings actuators. Eventually, during normal operations, the vibrations exceeded the clearance and a rotor-stator contact was recognized by tinkling sound. This condition is reached either by applying excessive excitation signal to the magnetic bearings' coils or by passing through a critical speed slowly. In any case, it is important to avoid this condition. In this thesis, the rub is analyzed by observing the vibration with time and frequency domain methods.

The experiments consist in a slow run-up of the rotor until a light rub is reached; the rotor is stopped short after the rub for safety reasons. The vibration of the rotor is obtained by a set of two orthogonal proximity probes. The data is acquired by National Instruments boards with a rate of 5128 samples/second and stored in a computer as a CSV file. The data is then postprocessed in Matlab.

The run-up acceleration is slow enough to assure stationarity inside a time window with short duration. Thus, orbits, Poincaré maps and full FFTs can be calculated. Moreover, a nonstationary analysis can also be applied by stacking several small FFTs and using a colormap to construct a full spectrogram. This time-frequency analysis is useful to observe a certain motion and the time interval where it changed to another type of motion.

Figure D.1 shows the full spectrogram for a run-up acceleration. The x axis correspond to the time interval of each time window and the y axis is the frequency

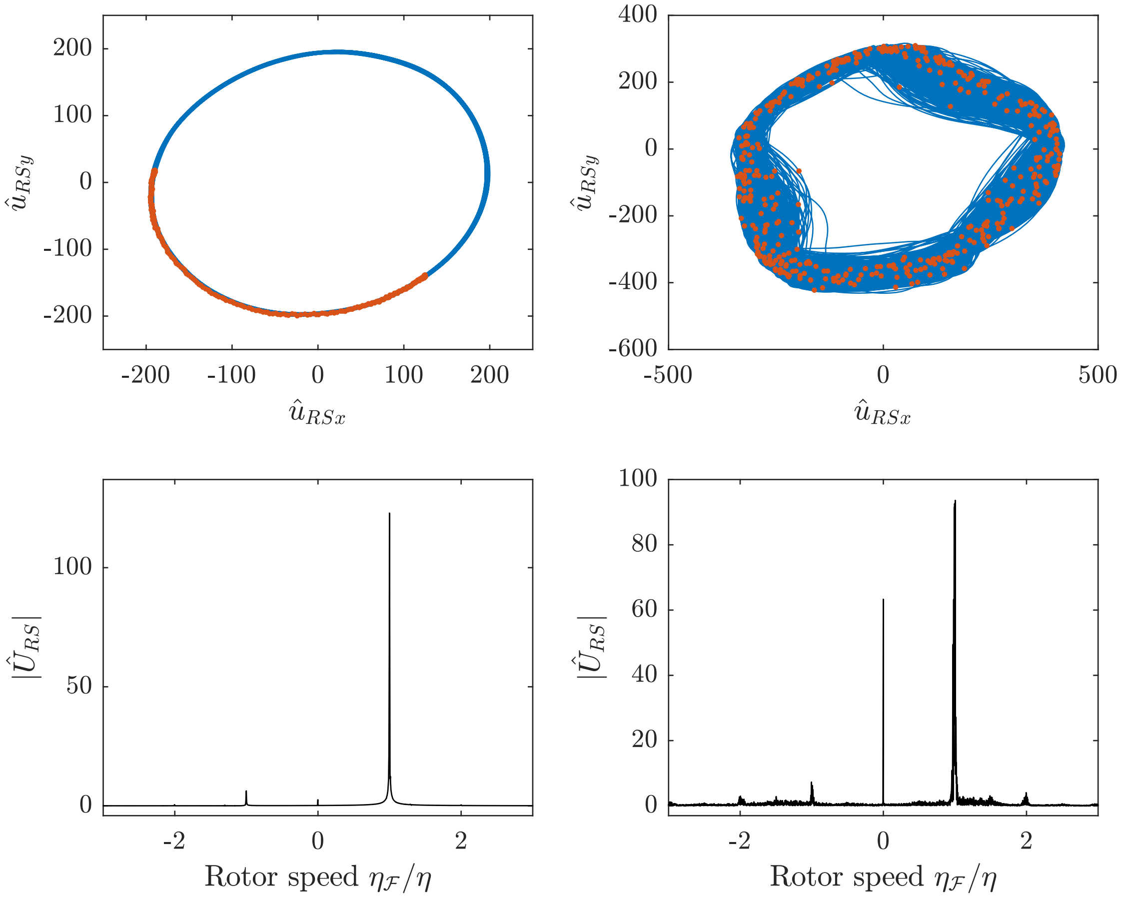

Figure D.1: Full spectrum of the vibration before (a, c) and after (b, d) the rotor-stator contact.

spectrum of the motion. The power spectral density is shown as a colormap. At start, only the forward precession is the dominant motion, as expected from the linear dynamics of a flexible rotor excited by unbalance forces. At 236 seconds, the vibration of the rotor exceeds the clearance and a different motion is set. Three frequency components can be observed as red lines, indicating high amplitude values with respect to other frequencies. One of the components is still the forward precession (1X). The new frequencies are the backward precession (-1X) and 0 Hz (0X). This behavior is similar to the Simulation 3 shown in Chapter 7.

The motion can be also analyzed by observing the orbits, Poincaré plots and full spectra at points before and after the rub. This is shown in Figure D.2. As expected, the orbit before the rub condition (Figure D.2a and c) is a well-defined closed path with the Poincaré map moving around it. The spectrum has a peak showing the dominant frequency component. In the rub condition (Figure D.2b and d), the three frequency components are clearly observed.

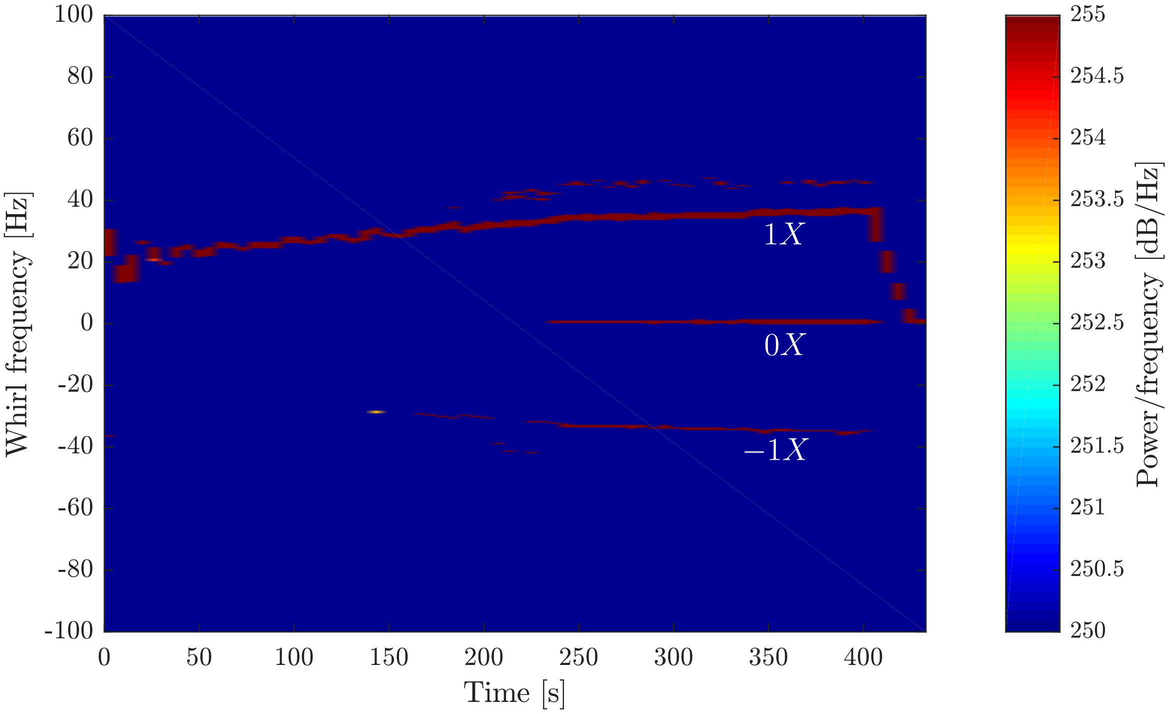

Figure D.2: Full spectrogram of the vibration of the rotor during a slow run-up.

Appendix E

Codes

E.1 Matlab code for the rotor-stator contact

```
function qd = rub4dof(t,q,s,eps_A,omega,m_s,m_r,r_u,x_stat,y_stat,mu_f,k_c,b_c,k_r,b_r,k_s,b_s,K,D,mf,tauz,b)
omega_r=sqrt(k_r/m_r);
q1 = q(1); q2 = q(2); q3 = q(3); q4 = q(4); q5 = q(5); q6 = q(6);
q7 = q(7); q8 = q(8);
aux = [q1+eps_A*cos(omega*t/omega_r)-q3;q5+eps_A*sin(omega*t/omega_r)-q7];
auxd = [q2-eps_A*sin(omega*t/omega_r)*omega/omega_r-q4;q6+eps_A*cos(omega*t/omega_r)*omega/omega_r-q8];
psi = ang(aux);
delta = s - norm(aux);
deltad = -(aux'*auxd)/norm(aux);
fux = m_r*r_u*omega^2*cos(omega*t/omega_r);
fuy = m_r*r_u*omega^2*sin(omega*t/omega_r);
fcx = koppl(-k_c*delta-b_c*koppl(deltad))*koppl(-delta)^0*(cos(psi)-mu_f*sin(psi));
fcy = koppl(-k_c*delta-b_c*koppl(deltad))*koppl(-delta)^0*(sin(psi)+mu_f*cos(psi));
fsx = -K_d*(q1-q3)-D_d*(q2-q4)-K_c*(q5-q7)-D_c*(q6-q8);
fsy = -K_d*(q5-q7)-D_d*(q6-q8)+K_c*(q1-q3)+D_c*(q2-q4);

q1d = q2;
q2d = (fux+fsx-fcx-b_r*q2*omega_r-k_r*q1)/(omega_r^2*m_r);
q3d = q4;
```

```
q4d =  (fcx-fsx-b_s*q4*omega_r-k_s*(q3-x_stat))/(m_s*omega_r^2);
q5d = q6;
q6d = (fuy+fsy-fcy-b_r*q6*omega_r-k_r*q5)/(m_r*omega_r^2);
q7d = q8;
q8d = (fcy-fsy-b_s*q8*omega_r-k_s*(q7-y_stat))/(m_s*omega_r^2);
qd = [q1d,q2d,q3d,q4d,q5d,q6d,q7d,q8d]';
end
```

E.2 Mathematica code for the normal form transformation

```
ClearAll["Global`*"]

(*Rotation Matrix - q'→q*)
R = {{Cos[Ω * t], -Sin[Ω * t]}, {Sin[Ω * t], Cos[Ω * t]}};

(*Mass matrix*)
M = {{m, 0}, {0, m}} ;

Kn = {{Keta , 0}, {0, Kzeta}};
(*Bearings stiffness matrix*)
Sl = 2 * {{Sv, 0}, {0, Sh}};

{{Keta, 0}, {0, Kzeta}}

Cn = {{Ceta , 0}, {0, Czeta}};

{{Ceta, 0}, {0, Czeta}}

(*Shaft Stiffness*)
Sw = FullSimplify[
   {{Szeta * Cos[Ω * t]^2 + Seta * Sin[Ω * t]^2, (Szeta - Seta) * Cos[Ω * t] * Sin[Ω * t]},
    {(Szeta - Seta) * Cos[Ω * t] * Sin[Ω * t], Szeta * Sin[Ω * t]^2 + Seta * Cos[Ω * t]^2}}];

Swapp = TrigReduce[Sw];

(*System Stiffness*)
K = FullSimplify[(Sw - Sw.Inverse[Sw + Sl].Sw)] ;

Klin = ReplaceAll[K, {Sin[2 * Ω * t] → 0, Cos[2 * Ω * t] -> 0}];

Kapp = Normal[Series[K, {Cos[2 * Ω * t], 0, 1}]];
```

```
Kapp2 =
  {{ω2^2 + c1 * Cos[2 t Ω] + c5 * Cos[2 t Ω]^2, c2 * Sin[2 t Ω] + c3 * Cos[2 t Ω] * Sin[2 t Ω]},
   {c2 * Sin[2 t Ω] + c3 * Cos[2 t Ω] * Sin[2 t Ω], ω1^2 + c4 * Cos[2 t Ω] + c6 * Cos[2 t Ω]^2}};


q[t_] = {q1[t], q2[t], q3[t], q4[t], q5[t], q6[t]};

System = {q'[t] == {q2[t],
      -1 * (Kapp2[[1, 1]] * q1[t] + Kapp2[[1, 2]] q3[t] +
          Kn[[1, 1]] * (q1[t])^3 + Cn[[1, 1]] * (q2[t])^3),
      q4[t],
      -1 * (Kapp2[[2, 1]] * q1[t] +
          Kapp2[[2, 2]] q3[t] + Kn[[2, 2]] * (q3[t])^3 + Cn[[2, 2]] * (q4[t])^3),
      2 ⅈ Ω q5[t],
      -2 ⅈ Ω q6[t]}};
System = FullSimplify[ReplaceAll[System,
    {Sin[2 * Ω * t] → (1 / 2) * (q5[t] - q6[t]), Cos[2 * Ω * t] → (1 / 2) * (q5[t] + q6[t])}]];
```

Eigenvectors Matrix

```
rechteSeite = #[[2]] - #[[1]] & /@ System;

rechteSeite = Flatten[rechteSeite];

ATilde = Coefficient[#, q[t]] & /@ rechteSeite;

rule = Table[q[t][[i]] → 0, {i, 1, Length[q[t]]}];

A = ATilde /. rule;

{Q, Adiag} = JordanDecomposition[A];

λ = Diagonal[Adiag];
λ = {λ[[4]], λ[[3]], λ[[6]], λ[[5]], λ[[2]], λ[[1]]};

Q = Transpose[
   {Q[[All, 4]], Q[[All, 3]], Q[[All, 6]], Q[[All, 5]], Q[[All, 2]], Q[[All, 1]]}];
```

Nonlinear with Diagonal Linear Part

```
x[t_] = {x1[t], x2[t], x3[t], x4[t], x5[t], x6[t]};

rule2 = Table[q[t][[i]] → (Q.x[t])[[i]], {i, 1, 6}];

rule3 = Table[q'[t][[i]] → (Q.x'[t])[[i]], {i, 1, 6}];

SystemJordan = FullSimplify[System /. rule2 /. rule3];

SystemJordan = Solve[SystemJordan, x'[t]];

SystemJordan = {x'[t] == Table[SystemJordan[[1, k, 2]], {k, 1, 6}]};
```

Matrix F2

```
k = 0; p = 0;

Do[Do[p = p + 1, {j, i, 6}], {i, 1, 6}]

ax = Table[0, {i, 1, p}];

Do[Do[ax[[k = k + 1]] = x[t][[i]] * x[t][[j]], {j, i, 6}], {i, 1, 6}]

rechteSeiteJordan = Flatten[#[[2]] - #[[1]] & /@ SystemJordan];

F2 = Coefficient[#, ax] & /@ rechteSeiteJordan;

rule = Table[x[t][[i]] → 0, {i, 1, Length[x[t]]}];

F2 = FullSimplify[F2 /. rule];
```

Resonant Condition

```
Ω = (1 * ω1 + 0 * ω2) / 1;

λ = ReplaceAll[λ, {ω2 → 3605 / 114, ω1 → 4306 / 177}];
```

Matrices G2 and H2

```
y[t_] = {y1[t], y2[t], y3[t], y4[t], y5[t], y6[t]}
{y1[t], y2[t], y3[t], y4[t], y5[t], y6[t]}

k = 0; p = 0;

Do[Do[p = p + 1, {j, i, 6}], {i, 1, 6}];

ay = Table[0, {i, 1, p}];

Do[Do[ay[[k = k + 1]] = y[t][[i]] * y[t][[j]], {j, i, 6}], {i, 1, 6}];

G2 = Table[0, {i, 1, Length[y[t]]}, {j, 1, Length[ay]}];

H2 = Table[0, {i, 1, Length[y[t]]}, {j, 1, Length[ay]}];

Do[
 {u = Table[0, {i, 1, Length[y[t]]}],
  Do[u[[i]] = Exponent[ay[[k]], y[t][[i]]], {i, 1, 6}],
  b = {0, 0, 0, 0, 0, 0},
  Do[{
    If[u.λ - λ[[j]] == 0, G2[[j, k]] = 0;
                                          F2[[j, k]]
     H2[[j, k]] = F2[[j, k]], G2[[j, k]] = ────────────;
                                          u.λ - λ[[j]]
     H2[[j, k]] = 0]}, {j, 1, 4}]}, {k, 1, Length[ay]}]

Do[H2[[i, All]] = F2[[i, All]], {i, 5, 6}];
```

Matrix F_3

```
p = 0; k = 0;

Do[Do[Do[p = p + 1, {l, j, 6}], {j, i, 6}], {i, 1, 6}]

bx = Table[0, {i, 1, p}];

Do[
 Do[Do[bx[[k = k + 1]] = x[t][[i]] * x[t][[j]] * x[t][[l]], {l, j, 6}], {j, i, 6}], {i, 1, 6}]

rechteSeiteJordan = Flatten[#[[2]] - #[[1]] & /@ SystemJordan];

F3 = Coefficient[#, bx] & /@ rechteSeiteJordan;
```

Matrix $\tilde{F}_3$: $F_3 y^3 = F_3 y^3 + 2 F_2(y(G_2 y^2)) - \frac{\partial(G_2 y^2)}{\partial y} H_2 y^2$

```
Jay = Transpose[Table[D[ay, y[t][[i]]], {i, 1, 6}]];

Ausdruck2 = G2.Jay.H2.ay;

Ausdruck1 = F2.Jay.G2.ay;

p = 0; k = 0;

Do[Do[Do[p = p + 1, {l, j, 6}], {j, i, 6}], {i, 1, 6}];

by = Table[0, {i, 1, p}];

Do[
 Do[Do[by[[k = k + 1]] = y[t][[i]] * y[t][[j]] * y[t][[l]], {l, j, 6}], {j, i, 6}], {i, 1, 6}]

KoeffizientenAusdruck1 = Coefficient[#, by] & /@ Ausdruck1;

KoeffizientenAusdruck2 = Coefficient[#, by] & /@ Ausdruck2;

F3Tilde = F3 + KoeffizientenAusdruck1 - KoeffizientenAusdruck2;
```

Matrices G3 and H3

```
G3 = Table[0, {i, 1, Length[y[t]]}, {j, 1, Length[by]}];

H3 = Table[0, {i, 1, Length[y[t]]}, {j, 1, Length[by]}];
```

```
Do[
  {u = Table[0, {i, 1, Length[y[t]]}],
   Do[u[[i]] = Exponent[by[[k]], y[t][[i]]], {i, 1, 6}],
   b = {0, 0, 0, 0, 0, 0},
   Do[{
     If[u.λ - λ[[j]] == 0, G3[[j, k]] = 0;
      H3[[j, k]] = F3Tilde[[j, k]], G3[[j, k]] = F3Tilde[[j, k]] / (u.λ - λ[[j]]);
      H3[[j, k]] = 0]}, {j, 1, 4}]}, {k, 1, Length[by]}];

Do[H3[[i, All]] = F3[[i, All]], {i, 5, 6}]

Λ = DiagonalMatrix[λ];
```

System $\dot{y} = \Lambda y + H_2 y^2 + H_3 y^3$

```
hOmega2 = Λ.y[t] + H2.ay + H3.by;
```

System $x = y + G_2 y^2 + G_3 y^3$

```
gOmega2 = y[t] + G2.ay + G3.by;

Clear[Ω]

rule4 = {y[t][[5]] → E^(2 I Ω t), y[t][[6]] → E^((-1) 2 I Ω t)};

hOmega2 = hOmega2 /. rule4;
```

System in Polar Coordinates

```
NormalformOmega2 = Table[y'[t][[i]] == hOmega2[[i]], {i, 1, Length[y[t]]}];

rule = {y1[t] → r1[t] E^(I (ϕ1[t]+Ω t)),
   y2[t] → r1[t]  E^(-I (ϕ1[t]+Ω t)), y3[t] → r2[t] E^(I (ϕ2[t])), y4[t] → r2[t] E^(-I (ϕ2[t]))};

rule2 = Table[D[rule[[i]], t], {i, 1, Length[rule]}];

NormalformPolarOmega2Tilde = NormalformOmega2 /. rule2 /. rule;

NormalformPolarOmega2Tilde = NormalformPolarOmega2Tilde;
FullSimplify[NormalformPolarOmega2Tilde];

Polarkoor[t_] = {r1[t], ϕ1[t], r2[t], ϕ2[t]};

NormalformPolarOmega2 = {0, 0, 0, 0};

k = {{2, 3, 4}, {1, 3, 4}, {1, 2, 4}, {1, 2, 3}};
```

E.3 Mathematica code for the finite element matrices $\mathbf{K}, \mathbf{M}, \mathbf{G}$

```
In[1389]:= ClearAll["Global`*"]

In[1390]:= SetAttributes[{Ee, ρ, Ie, γ, Le, Ae}, Constant];

In[1391]:= S = {{1, 0}, {0 , -1}};
           P = {{0, 1}, {0, 0}};

In[1419]:= N1 = (1/(1 + γ)) (1 + γ - γ/Le ξ - 3/Le^2 ξ^2 + 2/Le^3 ξ^3);
           N2 = (Le/(1 + γ)) ((2 + γ)/(2 Le) ξ - (4 + γ)/(2 Le^2) ξ^2 + 1/Le^3 ξ^3);
           N3 = (1/(1 + γ)) (γ/Le ξ + 3/Le^2 ξ^2 - 2/Le^3 ξ^3);
           N4 = (Le/(1 + γ)) (- γ/(2 Le) ξ - (2 - γ)/(2 Le^2) ξ^2 + 1/Le^3 ξ^3);
           Ne = {{N1, N2, 0, 0, N3, N4, 0, 0}, {0, 0, N1, -N2, 0, 0, N3, -N4}};
           Uek = {{ue1[t]}, {θe1[t]}, {ve1[t]}, {ϕe1[t]}, {ue2[t]}, {θe2[t]}, {ve2[t]}, {ϕe2[t]}};

In[1399]:= B = -15 (1 + γ)^2 Le 2 Integrate[
              Transpose[D[Ne, ξ]].S.P.S.D[Ne, ξ] + (γ Le^2)/12 Transpose[D[Ne, ξ]].S.P.S.D[Ne, {ξ, 3}] +
               (γ Le^2)/12 Transpose[D[Ne, {ξ, 3}]].S.P.S.D[Ne, ξ] +
               ((γ Le^2)/12)^2 Transpose[D[Ne, {ξ, 3}]].S.P.S.D[Ne, {ξ, 3}], {ξ, 0, Le}];

In[1400]:= rule = {36 → G01, -36 → -G01, 3 Le - 15 γ Le → G02, -(3 Le - 15 γ Le) → -G02,
              (4 Le^2 + 5 γ Le^2 + 10 γ^2 Le^2) → G03, -(4 Le^2 + 5 γ Le^2 + 10 γ^2 Le^2) → -G04,
              -Le^2 - 5 γ Le^2 + 5 γ^2 Le^2 → G04, -(-Le^2 - 5 γ Le^2 + 5 γ^2 Le^2) → -G04};
           G = Expand[Simplify[B - Transpose[B]]] /. rule // MatrixForm;

In[1402]:= M1 = (840 (1 + γ)^2)/Le Integrate[Transpose[Ne]. Ne, {ξ, 0, Le}];
           M2 = 30 (1 + γ)^2 Le Integrate[Transpose[(γ Le^2)/12 D[Ne, {ξ, 3}] + D[Ne, {ξ, 1}]] .
              ((γ Le^2)/12 D[Ne, {ξ, 3}] + D[Ne, {ξ, 1}]), {ξ, 0, Le}];
```

```
In[16]:= rule1 = {(312 + 588 γ + 280 γ^2) → M01, (44 Le + 77 γ Le + 35 γ^2 Le) -> M02,
           -(44 Le + 77 γ Le + 35 γ^2 Le) → -M02, (108 + 252 γ + 140 γ^2) → M03,
           (-26 Le - 63 γ Le - 35 γ^2 Le) → M04, 26 Le + 63 γ Le + 35 γ^2 Le → -M04,
           8 Le^2 + 14 γ Le^2 + 7 γ^2 Le^2 → M05, -6 Le^2 - 14 γ Le^2 - 7 γ^2 Le^2 → M06, 36 → M07,
           -36 → -M07, 3 Le - 15 γ Le → M08, -3 Le + 15 γ Le → -M08, 4 Le^2 + 5 γ Le^2 + 10 γ^2 Le^2 → M09,
           -4 Le^2 - 5 γ Le^2 - 10 γ^2 Le^2 → -M09, -Le^2 - 5 γ Le^2 + 5 γ^2 Le^2 → M10};
         M = ((ρ Ae Le)/(840 (1 + γ)^2)).MatrixForm[Expand[M1] /. rule1] +
           ((ρIe)/(30 (1 + γ)^2 Le)).MatrixForm[Expand[Simplify[M2]] /. rule1];

In[18]:= K1 = (1 + γ) Le^3 Integrate[Transpose[D[Ne, {ξ, 2}]].D[Ne, {ξ, 2}], {ξ, 0, Le}];
         K2 = (1 + γ) Le^3 ((γ Le^2)/12) Integrate[Transpose[D[Ne, {ξ, 3}]].D[Ne, {ξ, 3}], {ξ, 0, Le}];

In[20]:= rule3 = {12 → K01, -12 → -K01, 6 Le → K02, -6 Le → -K02, 4 Le^2 + Le^2 γ → K03,
           -(4 Le^2 + Le^2 γ) → -K03, 2 Le^2 - γ Le^2 → K04, (2 Le^2 - γ Le^2) → -K04};
         K = (Ee.Ie)/((1 + γ) Le^3).MatrixForm[Expand[Simplify[K1 + K2]]] /. rule3;
```

Stiffness Matrix

```
In[22]:= K

                         ( K01   K02    0     0   -K01   K02    0     0  )
                         ( K02   K03    0     0   -K02   K04    0     0  )
                         (  0     0    K01  -K02   0      0   -K01  -K02 )
            Ee.Ie        (  0     0   -K02   K03   0      0    K02   K04 )
Out[22]= ------------- . ( -K01  -K02   0     0    K01  -K02    0     0  )
         Le^3 (1 + γ)    ( K02   K04    0     0   -K02   K03    0     0  )
                         (  0     0   -K01   K02   0      0    K01   K02 )
                         (  0     0   -K02   K04   0      0    K02   K03 )
```

Mass matrix

In[23]:= **M**

Out[23]=

$$\frac{\text{Ae Le}\,\rho}{840\,(1+\gamma)^2}.\begin{pmatrix} M01 & M02 & 0 & 0 & M03 & M04 & 0 & 0 \\ M02 & M05 & 0 & 0 & -M04 & M06 & 0 & 0 \\ 0 & 0 & M01 & -M02 & 0 & 0 & M03 & -M04 \\ 0 & 0 & -M02 & M05 & 0 & 0 & M04 & M06 \\ M03 & -M04 & 0 & 0 & M01 & -M02 & 0 & 0 \\ M04 & M06 & 0 & 0 & -M02 & M05 & 0 & 0 \\ 0 & 0 & M03 & M04 & 0 & 0 & M01 & M02 \\ 0 & 0 & -M04 & M06 & 0 & 0 & M02 & M05 \end{pmatrix} +$$

$$\frac{\rho \text{Ie}}{30\,\text{Le}\,(1+\gamma)^2}.\begin{pmatrix} M07 & M08 & 0 & 0 & -M07 & M08 & 0 & 0 \\ M08 & M09 & 0 & 0 & -M08 & M10 & 0 & 0 \\ 0 & 0 & M07 & -M08 & 0 & 0 & -M07 & -M08 \\ 0 & 0 & -M08 & M09 & 0 & 0 & M08 & M10 \\ -M07 & -M08 & 0 & 0 & M07 & -M08 & 0 & 0 \\ M08 & M10 & 0 & 0 & -M08 & M09 & 0 & 0 \\ 0 & 0 & -M07 & M08 & 0 & 0 & M07 & M08 \\ 0 & 0 & -M08 & M10 & 0 & 0 & M08 & M09 \end{pmatrix}$$

Gyroscopic matrix

In[24]:= **G**

Out[24]//MatrixForm=

$$\begin{pmatrix} 0 & 0 & -G01 & G02 & 0 & 0 & G01 & G02 \\ 0 & 0 & -G02 & G03 & 0 & 0 & G02 & G04 \\ G01 & G02 & 0 & 0 & -G01 & G02 & 0 & 0 \\ -G02 & -G03 & 0 & 0 & G02 & -G04 & 0 & 0 \\ 0 & 0 & G01 & -G02 & 0 & 0 & -G01 & -G02 \\ 0 & 0 & -G02 & G04 & 0 & 0 & G02 & G03 \\ -G01 & -G02 & 0 & 0 & G01 & -G02 & 0 & 0 \\ -G02 & -G04 & 0 & 0 & G02 & -G03 & 0 & 0 \end{pmatrix}$$

E.4 Mathematica code for the electromagnetic forces

```
In[65]:= ClearAll["Global`*"]

In[66]:= theta = Table[i * Pi / 4 - Pi / 8, {i, 0, 7}];
         i = Transpose[{{i1, -i1, i3, -i3, i5, -i5, i7, -i7}}];
         ii2 = Transpose[{{ix, iy, i0}}];
         g1 = g - Cos[theta[[1]]] x - Sin[theta[[1]]] y;
         g2 = g - Cos[theta[[2]]] x - Sin[theta[[2]]] y;
         g3 = g - Cos[theta[[3]]] x - Sin[theta[[3]]] y;
         g4 = g - Cos[theta[[4]]] x - Sin[theta[[4]]] y;
         g5 = g - Cos[theta[[5]]] x - Sin[theta[[5]]] y;
         g6 = g - Cos[theta[[6]]] x - Sin[theta[[6]]] y;
         g7 = g - Cos[theta[[7]]] x - Sin[theta[[7]]] y;
         g8 = g - Cos[theta[[8]]] x - Sin[theta[[8]]] y;
         R = {{-g1, g2, 0, 0, 0, 0, 0, 0}, {0, -g2, g3, 0, 0, 0, 0, 0},
             {0, 0, -g3, g4, 0, 0, 0, 0}, {0, 0, 0, -g4, g5, 0, 0, 0},
             {0, 0, 0, 0, -g5, g6, 0, 0}, {0, 0, 0, 0, 0, -g6, g7, 0}, {0, 0, 0, 0, 0, 0, -g7, g8},
             {mu0 Ag, mu0 Ag, mu0 Ag, mu0 Ag, mu0 Ag, mu0 Ag, mu0 Ag, mu0 Ag}};
         CC = {{Cos[theta[[1]]], Sin[theta[[1]]], 1}, {-Cos[theta[[2]]], -Sin[theta[[2]]], -1},
             {Cos[theta[[3]]], Sin[theta[[3]]], 1}, {-Cos[theta[[4]]], -Sin[theta[[4]]], -1},
             {Cos[theta[[5]]], Sin[theta[[5]]], 1}, {-Cos[theta[[6]]], -Sin[theta[[6]]], -1},
             {Cos[theta[[7]]], Sin[theta[[7]]], 1}, {-Cos[theta[[8]]], -Sin[theta[[8]]], -1}};
         Nm = {{1, -1, 0, 0, 0, 0, 0, 0}, {0, 1, -1, 0, 0, 0, 0, 0}, {0, 0, 1, -1, 0, 0, 0, 0},
             {0, 0, 0, 1, -1, 0, 0, 0}, {0, 0, 0, 0, 1, -1, 0, 0}, {0, 0, 0, 0, 0, 1, -1, 0},
             {0, 0, 0, 0, 0, 0, 1, -1}, {0, 0, 0, 0, 0, 0, 0, 0}};

         Ay = DiagonalMatrix[Table[Sin[theta[[i]]], {i, 1, 8}]];
         Ax = DiagonalMatrix[Table[Cos[theta[[i]]], {i, 1, 8}]];
         R2 = ReplaceAll[R, {y → 0}];
         R3 = ReplaceAll[R, {x → 0}];

In[77]:= Fx = FullSimplify[Chop[ReplaceAll[Transpose[i].Transpose[Nm].
              Transpose[Inverse[R]].Ax.Inverse[R].Nm .i, {y → 0, i3 → 0, i7 → 0}]]]
```

Out[77]=

$$\left\{\left\{\frac{\left(2+\sqrt{2}\right) g \left(\text{i1}^2+\text{i5}^2\right) x+2 g^2 (\text{i1}-\text{i5}) (\text{i1}+\text{i5}) \mathrm{Cos}\left[\frac{\pi}{8}\right]+2 (\text{i1}-\text{i5}) (\text{i1}+\text{i5}) x^2 \mathrm{Cos}\left[\frac{\pi}{8}\right]^3}{\left(g^2-x^2 \mathrm{Cos}\left[\frac{\pi}{8}\right]^2\right)^2}\right\}\right\}$$

```
In[78]:= Fy = FullSimplify[Chop[ReplaceAll[Transpose[i].Transpose[Nm].
              Transpose[Inverse[R]].Ay.Inverse[R].Nm .i, {x → 0, i1 → 0, i5 → 0}]]]
```

Out[78]=

$$\left\{\left\{\frac{\left(2+\sqrt{2}\right) g \left(\text{i3}^2+\text{i7}^2\right) y+2 g^2 (\text{i3}-\text{i7}) (\text{i3}+\text{i7}) \mathrm{Cos}\left[\frac{\pi}{8}\right]+2 (\text{i3}-\text{i7}) (\text{i3}+\text{i7}) y^2 \mathrm{Cos}\left[\frac{\pi}{8}\right]^3}{\left(g^2-y^2 \mathrm{Cos}\left[\frac{\pi}{8}\right]^2\right)^2}\right\}\right\}$$